
This is an electronic reprint of the original article.
This reprint may differ from the original in pagination and typographic detail.

Castellanos Durán, J. S.; Milanovic, N.; Korpi-Lagg, A.; Löptien, B.; van Noort, M.; Solanki, S. K.

The MODEST catalog of depth-dependent spatially coupled inversions of sunspots observed by Hinode/SOT-SP

Published in:
Astronomy and Astrophysics

DOI:
[10.1051/0004-6361/202449269](https://doi.org/10.1051/0004-6361/202449269)

Published: 01/07/2024

Document Version
Publisher's PDF, also known as Version of record

Please cite the original version:
Castellanos Durán, J. S., Milanovic, N., Korpi-Lagg, A., Löptien, B., van Noort, M., & Solanki, S. K. (2024). The MODEST catalog of depth-dependent spatially coupled inversions of sunspots observed by Hinode/SOT-SP. *Astronomy and Astrophysics*, 687, 1-85. Article A218. <https://doi.org/10.1051/0004-6361/202449269>

The MODEST catalog of depth-dependent spatially coupled inversions of sunspots observed by Hinode/SOT-SP

J. S. Castellanos Durán^{1,2}, N. Milanovic¹, A. Korpi-Lagg^{1,3}, B. Löptien¹, M. van Noort¹, and S. K. Solanki^{1,4}

¹ Max Planck Institute for Solar System Research, Justus-von-Liebig-Weg 3, 37077 Göttingen, Germany
e-mail: castellanos@mps.mpg.de

² Georg-August-Universität Göttingen, Friedrich-Hund-Platz 1, 37077 Göttingen, Germany

³ Department of Computer Science, Aalto University, PO Box 15400, 00076 Aalto, Finland

⁴ School of Space Research, Kyung Hee University, Yongin 446-101, Gyeonggi, Republic of Korea

Received 18 January 2024 / Accepted 22 February 2024

ABSTRACT

We present a catalog that contains depth-dependent information about the atmospheric conditions inside sunspot groups of all types. The catalog, which we named MODEST, is currently composed of 944 observations of 117 individual active regions with sunspots and covers all types of features observed in the solar photosphere. We used the SPINOR-2D code to perform spatially coupled inversions of the Stokes profiles observed by Hinode/SOT-SP at high spatial resolution. SPINOR-2D accounts for the unavoidable degradation of the spatial information due to the point spread function of the telescope. The sunspot sample focuses on complex sunspot groups, but simple sunspots are also part of the catalog for completeness. Sunspots were observed from 2006 to 2019, covering parts of solar cycles 23 and 24. The catalog is a living resource, as with time, more sunspot groups will be included.

Key words. polarization – catalogs – Sun: atmosphere – Sun: magnetic fields – Sun: photosphere – sunspots

1. Introduction

Sunspots are magnetic structures that are comparatively cool and hence dark in continuum images with respect to their surroundings; they form the hearts of active regions (ARs; for a review see, e.g., Solanki 2003; Borrero & Ichimoto 2011). They play a central role in and are often used as tracers of solar magnetic activity. Although sunspots have been studied for over four centuries, many of their properties are still not well known or understood. In an effort to change this, we have created a new catalog of high resolution maps of physical parameters within sunspots and in their surroundings.

The thermal, magnetic field, and dynamic properties of magnetic features in the lower solar atmosphere, such as sunspots, pores, and plage regions, are encoded in the intensity and polarization properties of the solar spectrum. The polarization state of sunlight is fully described by the Stokes profiles, where the intensity of the light is represented by Stokes $I(\lambda)$, the linear polarization by Stokes $Q(\lambda)$ and $U(\lambda)$, and the circular polarization by Stokes $V(\lambda)$.

It is necessary to solve an inverse problem to retrieve the conditions in the solar atmosphere from the measured Stokes parameters (see del Toro Iniesta & Ruiz Cobo 2016, for a review). These so-called inversions use as input the atomic data relevant to the transitions underlying the spectral lines in the solar spectrum. In a first step, a model of the solar atmosphere is formulated. The complexity of this model varies depending on the type of available observations and the level of detail of the involved physical processes. Then the radiative transfer equation of polarized light is solved to produce synthetic Stokes profiles that are compared with the observations. The model is iteratively modified until the synthetic Stokes profiles match the observations.

The χ^2 -merit function is usually used as a quantitative measure of the quality of the fit.

The atmospheric conditions retrieved from an inversion depend on the simplifications employed in the atmospheric model underlying the inversions. The atmosphere recovered for a given model does not have to resemble the true stratification of the solar atmosphere at the analyzed location. Inversions are usually done by integrating the radiative transfer equation numerically, and the propagation of numerical errors is intrinsic. Different physical parameters might leave very similar imprints in the observable (the polarization state and intensity of light), which can lead to ambiguities. It is customary to use the χ^2 -merit function as a metric of how well the atmospheric model resembles the observations. However, there is no guarantee that the χ^2 -hypersurface has a single minimum, and so the final result can, in some ill-posed cases, depend on the initial guess. Taken together, the above points make inversions a fine art that require experience and a thorough interpretation of the obtained results.

The plane-parallel Milne-Eddington (ME) approximation is the simplest atmospheric model. Inversion codes that apply to this approximation are extremely useful when quick inversions are needed (e.g., Borrero et al. 2011). This model is commonly used because a ME-type atmosphere has an analytical solution (Unno 1956; Rachkovsky 1962, 1967). As a result, inversion codes that rely on ME-type atmospheres can be almost straightforwardly turned into pipelines to retrieve information on some atmospheric properties at the average height of formation of the spectral lines. Milne-Eddington inversions can also be used to infer chromospheric magnetic fields and line-of-sight velocities for the He I triplet at 10830 Å as they are formed in a thin layer (e.g., Rüedi et al. 1995; Lagg et al. 2004, 2009; Sowmya et al. 2022). Milne-Eddington inversions are a fast and convenient tool

for finding the average atmospheric parameters over the height range in which the spectral line is formed when inverting large datasets. In particular for data taken by the Spectro-Polarimeter (SP; Ichimoto et al. 2008) on board the Japanese Hinode solar mission (Kosugi et al. 2007), the ME inversion is part of the standard data processing pipeline (Level-2 data product). The code used by the Hinode consortium is the Milne-Eddington gRid Linear Inversion Network (MERLIN; Skumanich & Lites 1987). MERLIN inversions of Hinode data are provided by the [Community Spectropolarimetric Analysis Center](#) (2006).

Different parts of an absorption line are formed at different heights in the solar atmosphere. The core of the line forms in higher layers than its wings. Any variation or gradient in the atmosphere where the line is formed can leave an imprint on its shape and polarization. For example, gradients in the velocity and the magnetic field result in asymmetric or even complex Stokes profiles (Solanki & Pahlke 1988; Solanki & Montavon 1993), which are ubiquitous (Solanki & Stenflo 1984; Sigwarth et al. 1999). Unfortunately, by construction, the ME inversions fail to model the observed Stokes profiles when such gradients along the line of sight exist since they can only reproduce simple profiles without asymmetries, a significant shortcoming given the strong asymmetries almost invariably present outside sunspot umbrae.

Depth-dependent codes are commonly used in solar physics to model stratified atmospheres, for example SIR (Ruiz Cobo & del Toro Iniesta 1992), NICOLE (Socas-Navarro et al. 1998, Socas-Navarro et al. 2015), SPINOR (Solanki 1987; Frutiger et al. 2000), globin (Vukadinović et al. 2024), and SNAPI (Milić & van Noort 2018), among others. Such height-stratified inversions are able to retrieve variations of the physical conditions with optical depth (for a review see, e.g., de la Cruz Rodríguez & van Noort 2017). However, depending on the photospheric features of interest, the model used to interpret the observations might need to be adjusted. For example, the formation height of the same spectral line can differ by hundreds of kilometers between the quiet Sun and sunspots (see, e.g., Fig. 2 of Smitha et al. 2021a). This large difference requires a change in the grid locations where the atmospheric parameters are determined.

Typically, it is difficult to obtain excellent fits to all pixels inside the field of view (FOV) if a single atmospheric model is used. Different features, such as the quiet Sun, plage, penumbrae, and umbrae, are customarily modeled with different settings for the atmospheric parameters (e.g., Collados et al. 1994; Bellot Rubio et al. 2003). Depth-dependent, spatially coupled inversions (hereafter, coupled inversions) were proposed to resolve this and other problems (van Noort 2012; van Noort et al. 2013). They account for the parasitic light coming from adjacent pixels due to the unavoidable blurring caused by the point spread function (PSF) of the telescope. The coupled inversions applied to Hinode Solar Optical Telescope (SOT) SP data have been used to study different features of the solar photosphere, including the umbral dots (Riethmüller et al. 2013), the Wilson depression (Löptien et al. 2020a), the umbra–penumbra boundary (Löptien et al. 2020b), light bridges (Lagg et al. 2014; Castellanos Durán et al. 2020), penumbral filaments (van Noort et al. 2013; Tiwari et al. 2013), and counter Evershed flows (Siu-Tapia et al. 2017, 2019; Castellanos Durán et al. 2023).

The concept behind coupled inversions was recently generalized by de la Cruz Rodríguez (2019) to account for observations taken by different facilities that may have different spatial or spectral resolutions or are rotated relative to each

other (see, e.g., Rouppe van der Voort et al. 2020, for a multi-observatory dataset to which such inversions could be applied). To our knowledge, there is only one existing photospheric catalog of depth-dependent inversions, which mainly focuses on simple sunspots and covers ~ 50 Hinode/SOT-SP scans (see, e.g., Löptien et al. 2018).

In this work we present the Max-Planck Open Database of Elaborate inversions of Sunspots (MODEST). The MODEST catalog of sunspot groups covers different types of ARs with sunspots, including the most complex ones. Figure 1 shows examples of different ARs that are part of MODEST. For many ARs, MODEST also provides some (limited) temporal coverage as they cross the solar disk. MODEST is one of the first catalogs of stratified sunspots inversions to both use the same atmospheric model for all observations and be able to fit all types of features observed on the Sun with one set of free atmospheric parameters. The MODEST catalog will enable statistical studies of depth-dependent conditions inside a large variety of sunspots.

2. Data and sunspot sample

2.1. Data calibration

The MODEST catalog uses spectropolarimetric data taken by the SP (Ichimoto et al. 2008) attached to the SOT (Tsuneta et al. 2008) on board Hinode (Kosugi et al. 2007). Hinode/SOT-SP performs high spectral and spatial resolution spectropolarimetric observations of the solar photosphere in the line pair Fe I 6301.5 Å and 6302.5 Å. The magnetic sensitivity of these lines, given by the effective Landé factor (g_{eff}), is 1.67 and 2.5, respectively (cf. Solanki & Stenflo 1985). Table 1 summarizes the atomic parameters of these transitions.

Hinode/SOT-SP has a spectral sampling of 21.5 mÅ, while the spatial resolution varies depending on the observing mode, with the “fast” mode having $0''.297 \times 0''.32$ pixel size and the “normal” mode $0''.149 \times 0''.16$. The fast mode decreases the time needed to scan a given area on the solar surface, to the detriment of the spatial resolution with respect to the normal mode. Depending on the science case, either mode can be more suitable, and therefore the sample of sunspots presented here contains observations taken in both modes. The data were calibrated using the standard `sp_prep` routines that are part of the Solarsoft package and were reduced using the nominal Hinode/SOT-SP pipeline (Lites & Ichimoto 2013). In addition, all data were checked for continuum polarization that is sometimes observed in Stokes $Q(\lambda)$, $U(\lambda)$ and $V(\lambda)$ (see Fig. 1 in Okamoto & Sakurai 2018). If such an offset was found in the polarization, we removed the offset by requiring the continuum polarization to be zero. No additional correction to account for gray spectral stray light was applied (see Appendix A). In addition, for some particularly large Hinode/SOT-SP scans, we did not invert the full scan but instead manually centered the sunspot group and cut the scan in the spatial plane (see Sect. 3.4).

2.2. Sample of sunspots

Since coupled inversions are computationally expensive, we could only include a small subset of Hinode observations in the MODEST database. We made use of the Lockheed Martin Solar and Astrophysics Laboratory (LMSAL) database¹ Hinode/SOT-SP to select the sample of sunspot groups to invert. This database contains ME inversions of all Hinode/SOT-SP observations,

¹ <http://sot.lmsal.com/data/sot/level2d/>

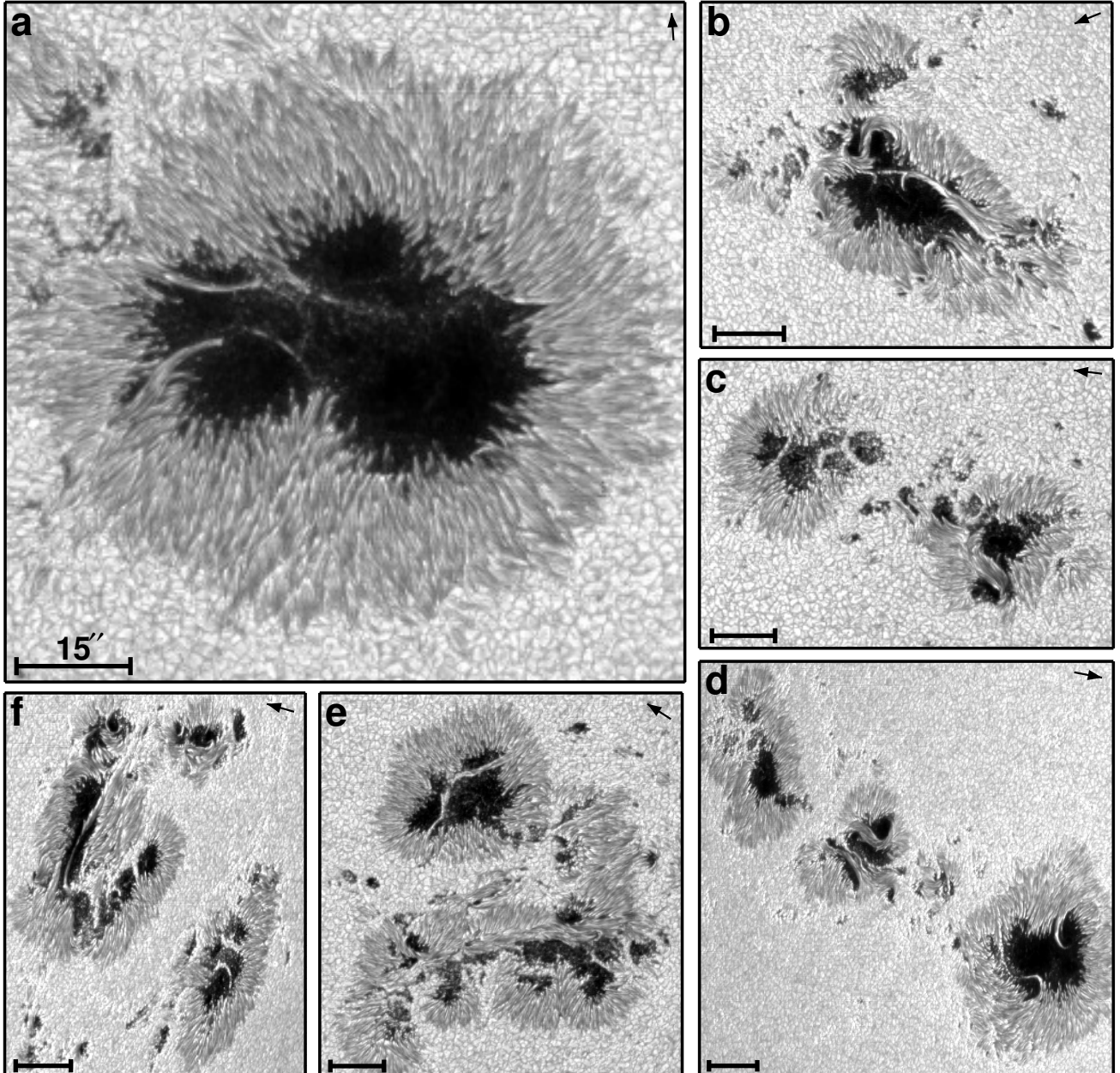


Fig. 1. Best-fit continuum images of sunspot groups included in MODEST. Panels display continuum images of the sunspot groups AR 11943 (2014 January 7; (a)), AR 11726 (2013 April 23; (b)), AR 12645 (2017 April 3; (c)), AR 11295 (2011 September 24; (d)), AR 12242 (2014 December 19; (e)), and AR 12673 (2017 September 8; (f)). Bars at the bottom left have a length of $15'' \approx 10\,800$ km (no foreshortening correction applied). Arrows in the top-right part of each image mark the direction of solar disk center.

Table 1. Atomic information of the observed spectral lines.

Element	Wavelength (Å)	Lower level	Upper level	g_{lower}	g_{upper}	g_{eff}	$\log(g_l^* f)$	Energy lower [eV]	Abundance	1st ionization potential [eV]	2nd ionization potential [eV]
Fe I	6301.5012	$z\,{}^5P_2^0$	—	$e\,{}^5D_2$	1.83	1.5	1.67	-0.745	3.654	7.50	7.9024
Fe I	6302.4936	$z\,{}^5P_1^0$	—	$e\,{}^5D_0$	2.50	—	2.50	-1.203	3.687		16.1879

which were performed with the MERLIN code. However, this database does not specify whether individual scans include a specific AR or not. On the date we started selecting our sample (2019 July 27), more than 22 000 scans were available.

We started by creating an initial list of all ARs with sunspots that were visible on the Sun from the date when Hinode started

observing until 2019 July 27. Here we used the Solar Regions Summaries (SRS)² made by the Space Weather Prediction Center. These are daily reports about all visible ARs on the Sun. For each visible AR with sunspots, the SRS reports contain the

² <ftp://ftp.swpc.noaa.gov/pub/warehouse>

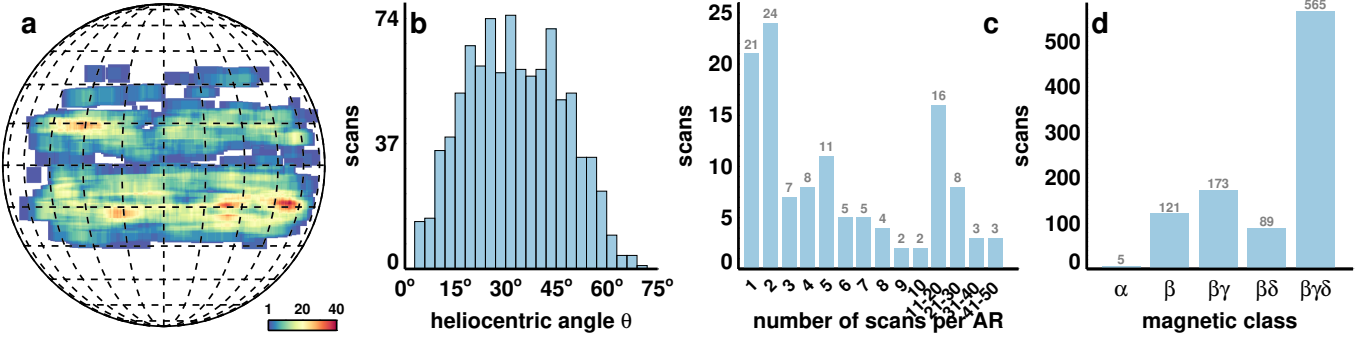


Fig. 2. Characteristics of the sample of sunspots in the archive. (a) Location of all scans on the solar disk. The color gives the number of scans observed at roughly the same location on the disk. (b) Heliocentric angle of the center of each FOV. (c) Number of scans of a given sunspot group (or part of it). (d) Magnetic classification of the sunspot group, with each scan counted separately.

NOAA number, the estimated area, the latitude and longitude, the modified Zürich class (McIntosh 1990), magnetic sunspot class (Hale et al. 1919; Künzel 1960, 1965), among others. If an AR was observed for more than one day, it occurs more than once on the initial list. To see which of these ARs were observed by Hinode/SOT-SP, we used the SOT planning files³. We kept only ARs that were visible on dates that appeared in the SOT planning files or that had a NOAA number that was mentioned in those. Finally, we also excluded all regions that had an estimated sunspot area smaller than 100 MSH, where MSH stands for a millionth of the solar hemisphere (i.e., $1 \mu\text{SH} = (6'3'')^2$). This filtering reduced the number of scans that we investigated further, from more than 22 000 to about 9 100.

These conditions could not completely exclude other types of Hinode/SOT-SP observations that were performed on the same day as an observation of a suitable AR, however. These scans were excluded in the subsequent filtering process. Sunspots can be identified easily in maps of the magnetic field strength. Hence, to select only scans that include sunspots, we made use of maps of the magnetic field strength provided by the MERLIN inversions in the LMSAL Level-2 database. With the help of the ME inversions, we checked for each scan in our sample if it had at least one connected region, where the inferred magnetic field strength was greater than 2 kG, and where the area of the region was larger or equal to $(10'')^2$.

This approach did not work well for wide scans that included the limb. Sometimes the MERLIN inversion assigns very strong magnetic fields to the parts of the FOV outside the limb (usually 5 kG, which is the upper limit in the MERLIN code), which would be falsely classified as sunspots by our approach. Consequently, we removed scans including the limb from the sample, by checking if the center of the connected region is too close to or even outside the limb (if its central pixel lies at a radius greater than the disk radius minus $50''$, which corresponds to $\mu \approx 0.35$). After applying these conditions, we were left with a sample of about 4500 “suitable” scans. Unfortunately, some of these scans still contained off-limb regions, since the coordinates of the center of the FOV in the Level-2 data header were not always accurate (cf. Fouhey et al. 2023) or the scans were too wide.

Initially, MODEST was conceived to study statistically super-strong magnetic fields observed in sunspots (cf. Okamoto & Sakurai 2018; Castellanos Durán et al. 2020). For this reason, we sorted the suitable scans of sunspot groups in descending order, according to the number of pixels inside the

connected regions that had magnetic field strength of exactly 5 kG, which is the maximum value allowed for the magnetic field strength in the MERLIN inversions. From this point on, we inspected each of the remaining scans manually before deciding whether to invert it or not. This step reduced the number of scans by another factor of ~ 4 .

As we were originally interested in complex sunspots with very strong magnetic fields, in particular in bipolar light bridges, the current MODEST sample focuses on complex ARs with sunspots, in particular δ groups. To increase the usability of our catalog also for other studies involving sunspots, we later added scans of α and β spots, and we will continue to do so in the future. Figure 2 shows a summary of the current sample of sunspot groups that are part of MODEST. As of now, MODEST consists of 944 scans of 117 individual ARs with sunspots (either in whole or part of them), and most of the inverted scans contain multiple sunspots. Figure 2a) displays the density of all scans projected onto the solar disk. Figure 2b) shows the heliocentric angle of the center of each scan. Multiple scans were inverted for many ARs to provide information on the temporal evolution of at least some of the ARs. Figure 2c) compiles the number of scans that cover a given AR, or part of it. Figure 2d) arranges all sunspot groups in terms of their magnetic class.

The current MODEST sample covers ARs located roughly within $\pm 60^\circ$ in longitude and $\pm 25^\circ$ in latitude of the solar disk. Table D.1 summarizes the sample of the scans inverted so far, namely information about the inverted scans – the OBS_ID, NOAA number, date, time, type of the Hinode scan (either fast, with a pixel size of $\sim 0'32$, or normal, with $\sim 0'16$), coordinates of the FOV, the μ -value (cosine of the heliocentric angle), the number of tiles that the FOV was divided into (see below), the size and area of the FOV, the Zürich classification, and the magnetic classification of the AR.

3. Inversion approach

3.1. Spatially coupled inversions

In this work, we applied the so-called spatially coupled inversions (van Noort 2012; van Noort et al. 2013), which make use of the knowledge of the telescope PSF to remove its effects at the same time as obtaining information on the solar atmosphere from the measured Stokes profiles. The recorded images at the entrance slit of the SP are the result of the convolution of the undisturbed solar image with the PSF of the aplanatic 50-cm $f/9$ Gregorian telescope. The PSF includes the effects of the spider holding the M2 mirror and the central obscuration (see Fig. 10 in

³ <https://sot.lmsal.com/operations/timeline/>

van Noort 2012). As a result of this convolution, the information of a given pixel is distributed over its surroundings. To account for these effects, van Noort (2012) proposed including the effects of the PSF in the inversion procedure.

The inversions are performed using the SPINOR code (Frutiger et al. 2000). SPINOR fits the spectropolarimetric observations with a stratified model of the solar atmosphere. SPINOR uses the STOPRO routines that solve the radiative transfer equation of polarized light (Solanki 1987), and employs the Levenberg-Marquardt minimization algorithm (Levenberg 1944; Marquardt 1963) to fit the synthetic Stokes profiles to the observed ones. The module for spatially coupled inversions in the SPINOR code can be activated when the PSF of the instrument is known (SPINOR-2D inversions).

Table 1 summarizes the atomic parameters used in the inversion procedure, where g_{lower} and g_{upper} are the Landé factors of the lower and upper energy levels of the considered transitions, and $\log(g_{\text{J}}^* f)$ is the weighted oscillator strength of the line. The Landé factors are calculated from the atomic configuration assuming LS coupling. The effective (triplet) Landé factors are shown for completeness but are not used during the inversion.

3.2. Node position and free parameters

The number of free parameters in the atmospheric model is related (1) to the number of nodes placed at different depths at which the parameters are determined, and (2) to the physical quantities that play a role in the formation of the spectral line. A larger number of free parameters generally improves the quality of the fit. This can come at the cost of the uniqueness of the solution, in particular, if some free parameters are not sufficiently independent of each other. For the MODEST catalog, we use 16 free parameters to model a stratified solar photosphere. The temperature (T), magnetic field strength (B), inclination (γ), azimuth (φ), and line-of-sight velocity (v_{LOS}) each contribute three free parameters located at different optical depths. The micro-turbulence (v_{micro}) was modeled without depth dependence (one free parameter) as the χ^2 -hypersurface is relatively insensitive to depth-dependent changes due to micro-turbulence velocities (Frutiger et al. 2000). We convolve the synthetic profile with the measured SP spectral transmission profile, which has a full width at half maximum of 24.3 mÅ and extended wings, so no other parameter was necessary to account for the broadening of the Fe I line pair.

The node positions were located at $\log \tau_c = 0.0, -0.8$, and -2.0 , where τ_c represents the continuum optical depth at 5000 Å. The position of the top node at $\log \tau_c = -2.0$ was chosen following Danilovic et al. (2016) as large parts of the FOV might be filled with the quiet Sun. These authors demonstrated that this node position is well suited under quiet-Sun conditions, but it also does not adversely affect the retrieved atmospheres for complex profiles (see the discussion in Sect. 4.1; cf. Figs. 4–6). The atmospheric stratification is computed from the coarse three-node grid onto a fine depth grid with a sampling of $\Delta \log(\tau) = 0.05$ using a spline approximation (see Frutiger 2000). The atmosphere was extrapolated using a linear function based on the slope of the spline interpolated between the nodes for optical depths ranging between $\log \tau_c < -6.0$ and $\log \tau_c > 1.5$.

3.3. Inversion strategy

Selecting a balanced inversion strategy helps avoid getting stuck in a local minimum in the χ^2 -hypersurface. There may be extreme cases where any of the retrieved parameters can

have an extreme value, for example $v_{\text{LOS}} > 7 \text{ km s}^{-1}$ (the photospheric sound speed) or $B > 4 \text{ kG}$. In addition, gradients of the v_{LOS} and the magnetic field, at different heights where the lines are formed, can create complex Stokes profiles (Solanki & Montavon 1993).

To account for these possibilities, each observation was inverted ten times as suggested by van Noort et al. (2013). After each inversion run, the output atmosphere for each pixel was smoothed with the surrounding neighbors if the solution in the pixel reached a local minimum in the χ^2 -hypersurface (see below). Then, that smoothed atmosphere was used as the initial condition for the next inversion run applied to the same set of pixels. In the first inversion run, for the initial conditions we give the average quiet-Sun conditions, weakly magnetized and at rest (e.g., Danilovic et al. 2016). We used quiet-Sun conditions to initialize the inversions, as 68.2% of the pixels inside the FOVs belong to the quiet Sun, an AR plague, or the network.

The number of maximum iterations allows us to find the best match between the observed and synthetic Stokes vector increases in each inversion run. The first inversion run has a maximum of 10 iterations, and this number is increased after each inversion run up to 100 iterations (van Noort 2012).

The allowed ranges (“limits”) of the atmospheric parameters during the first run were chosen to cover typical values that contain quiet-Sun, penumbral, and umbral regions (see below). In the subsequent runs, the parameter space was slowly increased. This allowed the adequately fitting of ever more complex profiles while ensuring that the fits to simple Stokes profiles remained of high quality. In particular, to avoid the inversion reaching extreme values the limits for the magnetic field strength and v_{LOS} were smoothly increased for each inversion run. For the first three runs B and v_{LOS} were limited to $B \leq 3 \text{ kG}$ and $|v_{\text{LOS}}| \leq 5 \text{ km s}^{-1}$. This limit accounts for the subsonic pixels in the quiet-Sun, penumbrae, and the not-too-dark parts of umbrae (i.e., in umbral dots and the diffuse background; e.g., Socas-Navarro et al. 2004; Riethmüller et al. 2008, 2013). This limit covers the values reached in the majority of the pixels. If a larger value of either of these quantities is required to reproduce a particular set of Stokes profiles, the inversion saturates at this limit, but the saturated value is then used as an input for the next inversion run.

During inversion runs 4 and 5, the v_{LOS} limits start covering the supersonic regime to $|v_{\text{LOS}}| \leq 8 \text{ km s}^{-1}$ and $\leq 10 \text{ km s}^{-1}$ and the maximum field strength is increased such that $B \leq 5 \text{ kG}$. The last five inversion runs are devoted to finding the best fits for extreme cases for the supersonic line-of-sight velocities (e.g., del Toro Iniesta et al. 2001; van Noort et al. 2013; Esteban Pozuelo et al. 2016; Siu-Tapia et al. 2017) and super-strong magnetic field strengths (van Noort et al. 2013; Okamoto & Sakurai 2018; Siu-Tapia et al. 2019; Castellanos Durán 2022), while further loosening the limits in each run. In the last run, the maximum values for the magnetic field strength and line-of-sight velocity were set to 15 kG and 30 km s⁻¹, respectively.

During a given inversion run, the global minimum of the χ^2 -hypersurface can be located inside the allowed parameter space or not, depending on the complexity of the atmosphere. When increasing the limits of the parameters in the next inversion run, the previously fitted atmosphere is only affected if the “real” global minimum of the χ^2 -hypersurface was not part of the parameter space. Then the next inversion run will improve the solution by increasing the size of the χ^2 -hypersurface in each step until the real global minimum is part of the parameter space. However, by extending limits the global minimum

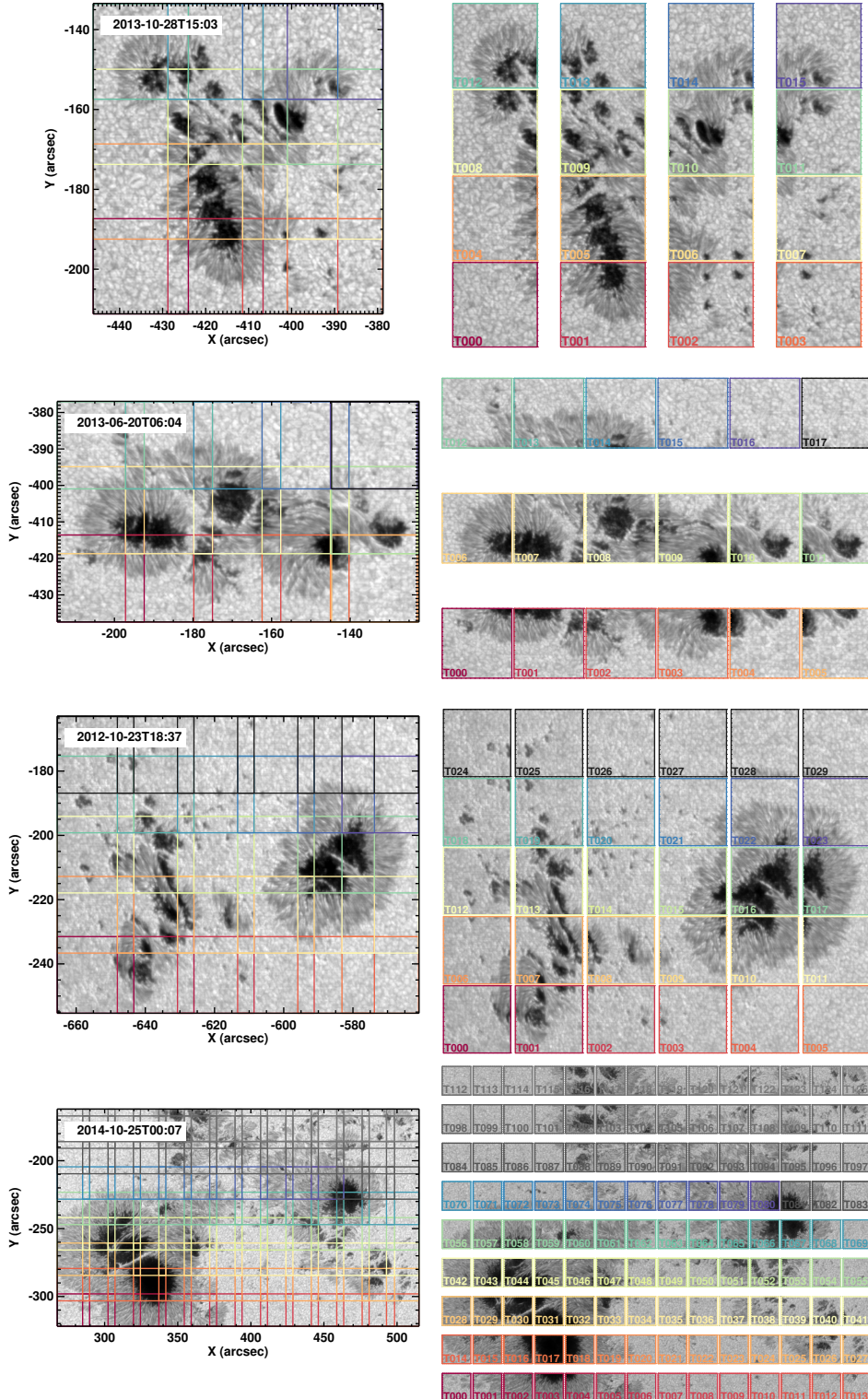


Fig. 3. Illustration of the division of the FOV into tiles for the coupled inversions. From top to bottom: continuum maps of AR 11882, AR 11775, AR 11560, and AR 12192 as observed by Hinode/SOT-SP. Colored lines mark the location of the tiles into which the FOV is divided (left). Notice that the tiles are designed to overlap. The right column shows the individual continuum maps of each individual tile.

for a given atmosphere does not change the solution if it represents the global minimum also in the increased parameter search space.

In addition, if the previous best-fit atmosphere was stuck in a local minimum, we helped the inversion leave it by starting the new inversion run with an offset given by the invert-smooth-invert approach. This approach assumes that adjacent pixels may have relatively similar atmospheres. Consequently, when using the smoothed atmosphere as an input of the next inversion run,

the inversion is likely to find the global minimum easier, avoiding getting stuck in a local minimum. Furthermore, every time the inversion is restarted, the so-called Marquardt parameter is also reset (see, e.g., Eq. (4) of van Noort 2012). The Marquardt parameter is used to find the minimum in a χ^2 -hypersurface, since it regulates the amount of linearization assumed by the algorithm. We helped the algorithm leave the local minimum by resetting the Marquardt parameter. The effect of the invert-smooth-invert approach can be directly seen working in the quiet

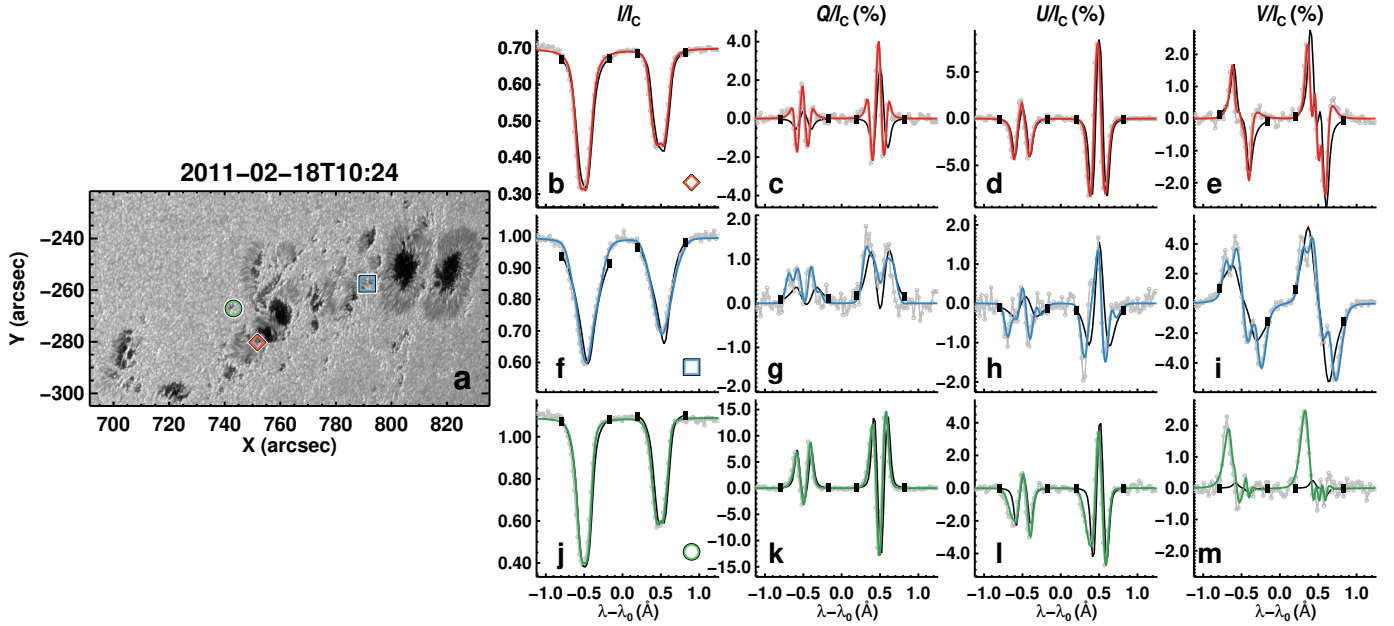


Fig. 4. Fits obtained by the coupled inversions to the observed Stokes profiles. Panel a shows the continuum image of AR 11158 when it was located at $\mu \approx 0.6$. Columns 2 to 5 show the observed Stokes profiles (dotted gray lines), the retrieved fits obtained by the coupled inversions (colored lines), and the ME inversion by MERLIN (black lines). Vertical black bars mark the spectral windows that MERLIN uses for the Level-2 inversions. The locations of the plotted profiles are marked on the continuum images with colored symbols. $\lambda_0 = 6302 \text{ \AA}$.

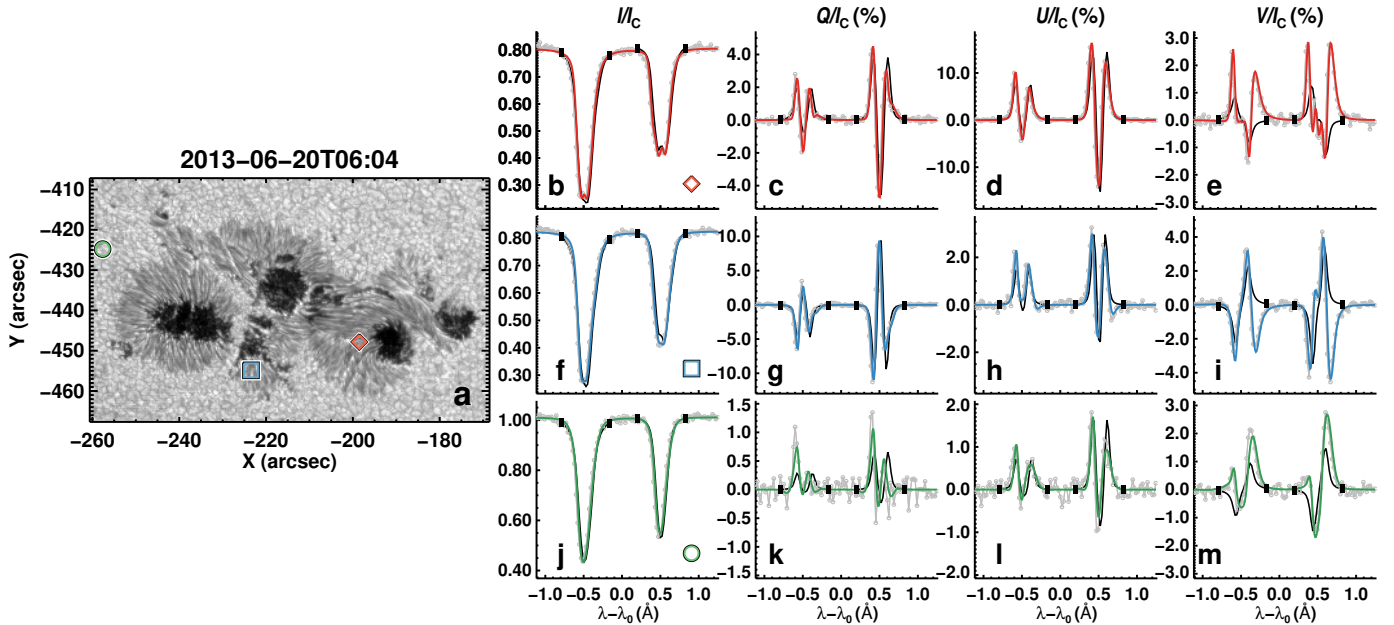


Fig. 5. Same as Fig. 4 but for a sunspot group belonging to AR 11775 when it was located at $\mu \approx 0.8$. $\lambda_0 = 6302 \text{ \AA}$.

Sun, where the low signal-to-noise tends to retrieve noisy maps. Other spatial-regularization schemes are found in the literature (see, e.g., [de la Cruz Rodríguez 2019](#)), but they have not been implemented in the SPINOR code yet. The opted simple spatial-regularization invert-smooth-invert scheme is applied after each inversion run. Therefore, it is straightforwardly applied to any other type of inversion that uses a gradient-based minimization (e.g., SIR inversions) to fit synthetic Stokes profiles to the observed ones.

As suggested by [van Noort et al. \(2013\)](#), data were up-sampled before the inversion by a factor of 2 in Fourier space to keep the noise level constant (see Fig. 5 in [van Noort et al.](#)

[2013](#) for illustration). The up-sampled data are then inverted by the coupled inversions, which means that the number of pixels inside the same FOV is four times larger than for the original sampling. For normal [fast] maps, the approximate pixel size is $0''.16$ [$0''.32$]. The inversion is done on up-sampled pixels with a size of $0''.08$ [$0''.16$]. The output of the coupled inversion is later down-sampled with the same procedure in Fourier space to return to the nominal scale of the observed FOV (i.e., the final pixels again have a size of $0''.16$ [$0''.32$]). The up-sampled inversions are not presented as a default in the current catalog, but are available on request. The up-sampling (and later down-sampling) steps are needed to fit substructures that are below

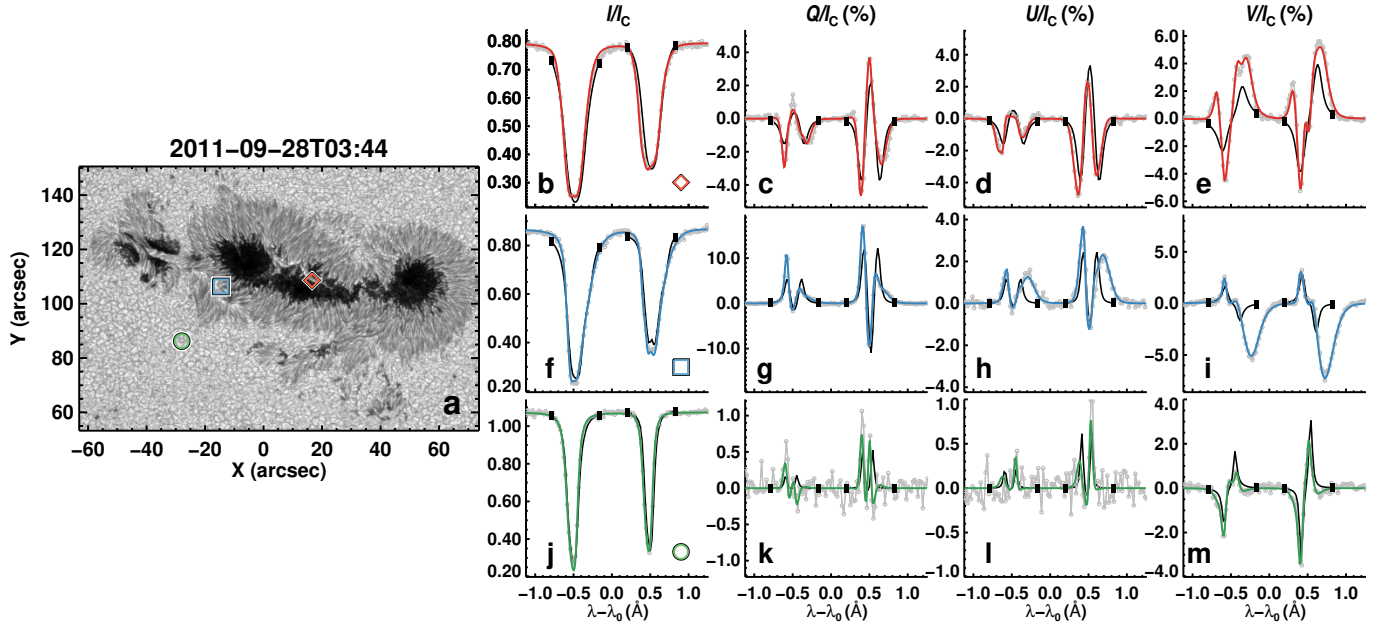


Fig. 6. Same as Fig. 4 but for a sunspot group belonging to AR 11302 when it was located at $\mu \approx 1.0$. $\lambda_0 = 6302 \text{ Å}$.

the pixel size but which affect the observed Stokes profiles. As explained by van Noort et al. (2013), this approach is similar to having multiple atmospheres within the pixel that are assigned different filling factors. Since these atmospheres or components are coupled by the PSF, this allows the coupled inversions to infer the atmospheric conditions up to the diffraction limit of the telescope when the PSF of the optical system is known and the data are reordered without seeing disturbances. van Noort (2017) describe how to estimate the PSF and restore solar spectra when observations are taken by a ground-based facility.

3.4. Tiling the FOV

During the inversion, a minimization procedure is applied to find the best match between the observed Stokes profiles and the synthetic Stokes profiles that are obtained after the solution of the radiative transfer equation of polarized light for a given atmospheric model. In the classic pixel-to-pixel inversions, every pixel inside the FOV is treated independently. This implies that the size of the matrices needed to be inverted during the minimization procedure is independent of the size of the FOV. Hence, classic inversions are fast and easy to parallelize, and not very demanding in terms of memory usage.

For coupled inversions, all profiles within the FOV must be inverted simultaneously. The coupling of the solutions between the pixels rapidly increases the size of the matrices needing to be inverted during the minimization procedure with the number of pixels, N . The size of the matrix computations roughly increases $\propto N^3$, which places greater demands on computer memory with increasing size of the scan (see further details in van Noort 2012).

The number of pixels in the scans selected for MOD-EST ranges from $N_{\text{smallest}} \sim 8500$ ($\approx 22'' \times 36''$; fast mode) to $N_{\text{largest}} \sim 591\,000$ ($\approx 125'' \times 110''$; normal mode). In addition, after up-sampling the number of pixels increases by a factor of 4. Many of the scans are much too large to be handled in one go. One solution is to split the larger scans into sufficiently overlapping tiles. In addition, we were able to use three different computing facilities to perform our inversions. However, this also

implied that we had to account for the differences between the facilities such as the type of processors, the available storage, the maximum runtime per job, and the read/write I/O characteristics among others. We chose to divide all scans into tiles of the same size based on all these constraints and for consistency. We obtained good results by dividing each up-sampled FOV into tiles of 150×150 spatial pixels resulting in a maximum memory usage of 2 GBytes per tile (see Fig. 3). Maps on the left side of Fig. 3 mark the location of each tile within the FOV, where different colors represent each tile. We note the overlap between tiles.

We performed tests by varying the overlapping area between tiles to determine how much overlap is needed to ensure that there are no discontinuities when stitching the atmospheres retrieved in the individual tiles together. These tests allowed us to ensure that the overlap between the tiles was at least twice the width of the core of the PSF that covers most of the power in Fourier space. A conservative value for this overlap was chosen to be 16 pixels. This was done to ensure a homogeneous quality of inversion after all the tiles (now containing the best-fit profiles and resulting atmospheres) are arranged in their original positions (see also Appendix B).

Maps on the right side of Fig. 3 show each tile within the FOV that then was inverted. After the inversion, tiles were stitched together by removing the outer added edge between neighboring tiles. No boundary or edge effects were visible after putting together the tiles on the large map. No smoothing at the boundaries was required, indicating that the independent inversions of the adjacent tiles found the same global minimum for the pixels located in both tiles, and that the chosen overlap of 16 pixels was sufficiently large.

Appendix B shows a quantitative test on the effects of tiling the FOV. A scan of AR 11748 was inverted without tiling the FOV on a so-called fat node with large memory. This scan contains all types of features (umbrae, penumbras, and quiet Sun) at the location where the tiles are put together. The inversion was carried out following the same steps as presented in Sects. 3.1–3.3. As the last step, the whole FOV was down-sampled to its original size, thus reversing the Fourier

Table 2. Features covered by the sample.

Pixels	Fast mode		Normal mode		Total	
	(Num. px)	(Percent.)	(Num. px)	(Percent.)	(Num. px)	(Percent.)
Quiet Sun/plage/network	9.1×10^7	68.8%	6.2×10^6	60.6%	9.7×10^7	68.2%
Penumbra	3.3×10^7	25.1%	3.2×10^6	31.8%	3.6×10^7	25.6%
Warm umbra	7.1×10^6	5.4%	6.6×10^5	6.5%	7.7×10^6	5.5%
Cold umbra	9.1×10^5	0.7%	1.2×10^5	1.1%	1.0×10^6	0.7%
Masked	7.6×10^4	0.06%	1.9×10^4	0.18%	9.4×10^4	0.07%
Total	1.3×10^8	100.0%	1.0×10^7	100.0%	1.4×10^8	100.0%

up-sampling procedure mentioned above. This inversion was then compared with the nominal “tiled” MODEST inversion (Fig. B.1). This test demonstrates that the effects of tiling the FOV are negligible.

4. Results

The MODEST catalog contains the atmospheric conditions of sunspot groups that were located roughly within a longitude of $\pm 60^\circ$ and $\pm 25^\circ$ in latitude on the solar disk. MODEST started out focusing on the more complex sunspot groups (Fig. 2d). Later, simpler sunspots were added. All ARs with sunspots were observed by Hinode/SOT-SP and span the last part of solar cycle 23, and almost the full cycle 24. Currently, MODEST is composed of 944 scans of 117 individual ARs with sunspots (or parts of these ARs). The inverted scans frequently show multiple sunspots. The total number of spatial xy -pixels is 1.4×10^8 , and the total number of data points⁴ that was fitted is 6.3×10^{10} .

In December 2006, still in the early stages of the mission, a hardware failure in the X band at 8.4 GHz reduced the down-link transmission bandwidth between Hinode and ground stations considerably. In terms of data volume, fast mode scans, with a spatial sampling of $0''.32$, are considerably smaller than normal scans with a spatial sampling of $0''.16$. Due to the technical problem with the X band, the majority of the Hinode/SOT-SP scans are therefore taken in fast mode (the fifth column in Table D.1 lists whether the scan was taken in fast or normal mode).

Table 2 summarizes the total number of xy -pixels covering different solar features depending on whether they were observed in fast or normal mode, and the combined total. Roughly 69% of the areas of the scans observe quiet-Sun, AR plage, and network regions surrounding sunspot groups, while 25% of the pixels cover sunspot penumbrae and 5% belong to sunspots umbrae. In addition, Figs. D.1–D.44 show a mosaic of the best-fit continuum images as well as the line-of-sight magnetograms of the current sample of MODEST (see also the summary in Table D.1).

The following subsections present examples taken from the catalog. They include examples of typical fits to the observed Stokes vectors at different μ -values of different solar structures, the retrieved atmospheric maps for different ARs, as well as the intrinsic limitations of the Fe I pair at 6302 Å, comparison with the standard Level-2 data product and the 6302 Å lines when observed in cold umbrae.

⁴ One data point is considered to be a monochromatic Stokes profile value. A typical xy -pixel has 444 data points, which corresponds to a full Stokes vector at a given wavelength ($I, Q, U, V(\lambda)$) times ~ 111 spectral wavelength positions covered by each Stokes profile. The number of wavelength positions may vary depending on the observing mode.

4.1. Modeling of the observed Stokes vector

The spatially coupled inversions apply a one-component depth-dependent atmospheric model to each pixel of an FOV, irrespective of the type of (photospheric) solar features observed. Figures 4–6 show three scans at μ -values of 0.6, 0.8, and 1.0, respectively. They show the best-fit continuum image of the scan, as well as the Stokes profiles and the best fits obtained by the MODEST inversions from three pixels within the FOV. These pixels were selected on the basis of the complexity of their observed Stokes spectra from the quiet Sun, the penumbrae, and/or a light bridge. For comparison, the standard MERLIN inversions, which are part of the Hinode/SOT-SP pipeline (Level-2 data product), are also shown. Figures 4–6 corroborate that, regardless of the μ -value of the scan and the photospheric feature, the spatially coupled inversions can retrieve fairly good fits to the sometimes very complex observed Stokes vector using a single atmospheric model. Further examples of typical good fits to complex atmospheres obtained by coupled inversions have been presented by van Noort et al. (2013), Siu-Tapia et al. (2017, 2019), and Castellanos Durán et al. (2020, 2023).

4.2. Physical parameters of the atmospheres

In this section we present examples of the maps of atmospheric physical parameters contained in the MODEST catalog. An inverted normal mode scan is shown in Fig. 7 and a fast mode scan in Fig. 8.

The magnetic field is in the line-of-sight reference frame. To transform the magnetic vector to the local reference frame, the intrinsic ambiguity of the magnetic field’s azimuth must be taken into account. Tests have been performed with the available techniques (Leka et al. 2009); however, the disambiguation is currently not part of the MODEST pipeline (see Sect. 5.3).

Atmospheric maps show emblematic features observed in the solar photosphere. For example, outside the sunspot, the upflows in the granules and downflows in the intergranular lanes are clearly visible (panel m), as is the concentration of the magnetic field in the intergranular lanes. Also, the well-known drop in the magnetic field strength of the sunspots from inside the umbra toward the outer parts of the penumbra is clearly visible. The magnetic field decreases with height and the magnetic field canopy is observed when comparing panels d and f. The temperature variation between penumbral spines and intra-spines is clearly visible (panels a–c; see also, e.g., Schmidt et al. 1992; Lites et al. 1993; Title et al. 1993; Langhans et al. 2005), which is associated with changes in the magnetic field inclination (panels g–h, cf. Tiwari et al. 2013). The normal Ever-shed flow pattern is seen as a blueshift in the center-side penumbra and as a redshift in the limb-side penumbra (Fig. 8m

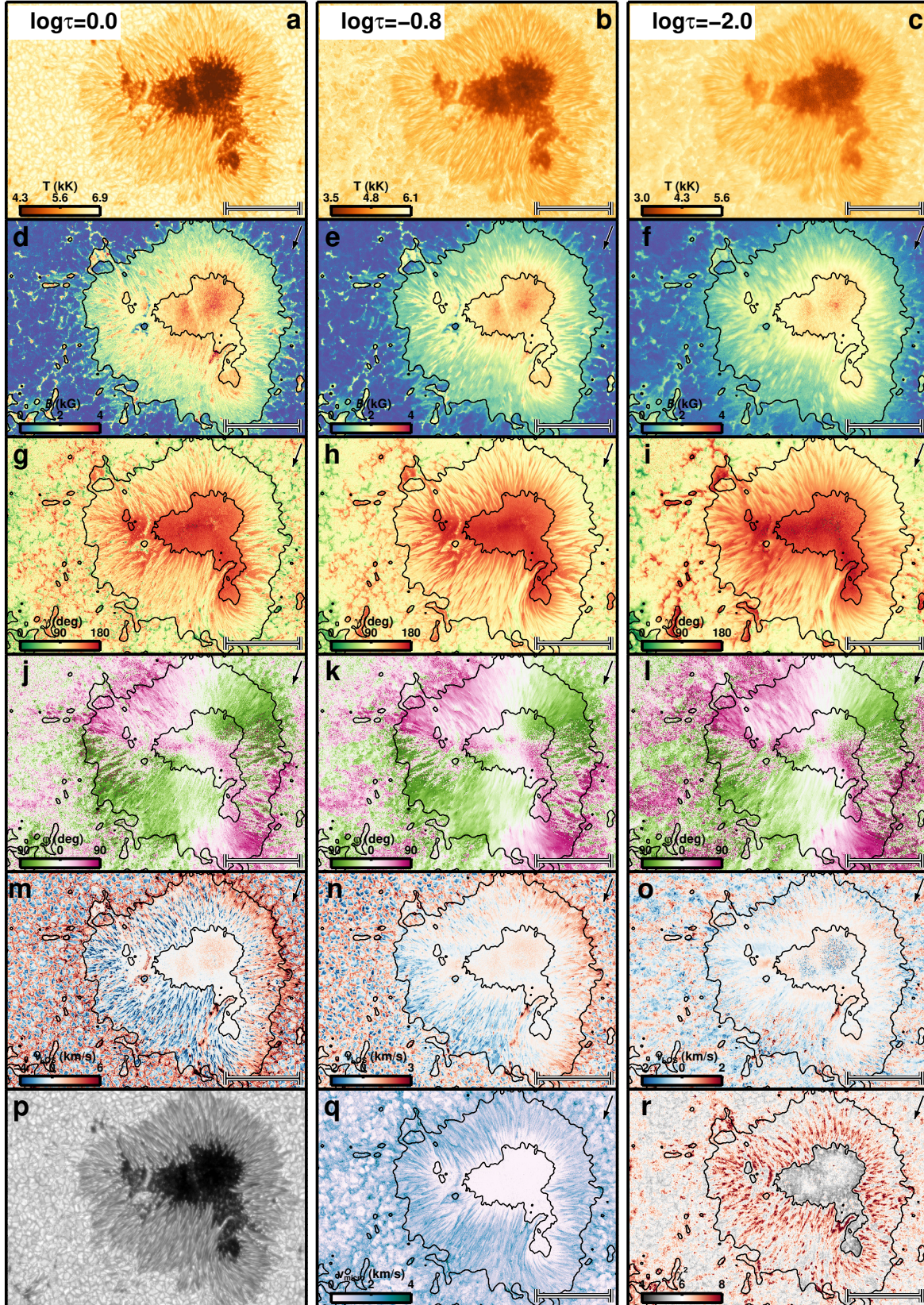


Fig. 7. Depth-dependent atmospheric conditions retrieved by the coupled inversions of AR 10953 (2007 May 1). The first five rows show, from top to bottom, maps of the temperature, magnetic field strength, inclination, azimuth, and line-of-sight velocity. The columns show, from left to right, these quantities retrieved at $\log \tau = 0, -0.8$, and -2.0 , i.e., at the bottom, middle, and top nodes. In the bottom row, panels p–r display the best-fit continuum, micro-turbulence, and χ^2_{reg} maps. This scan was observed in normal mode with a pixel size of $0''.16$. The FOV is composed of 8×10 tiles.

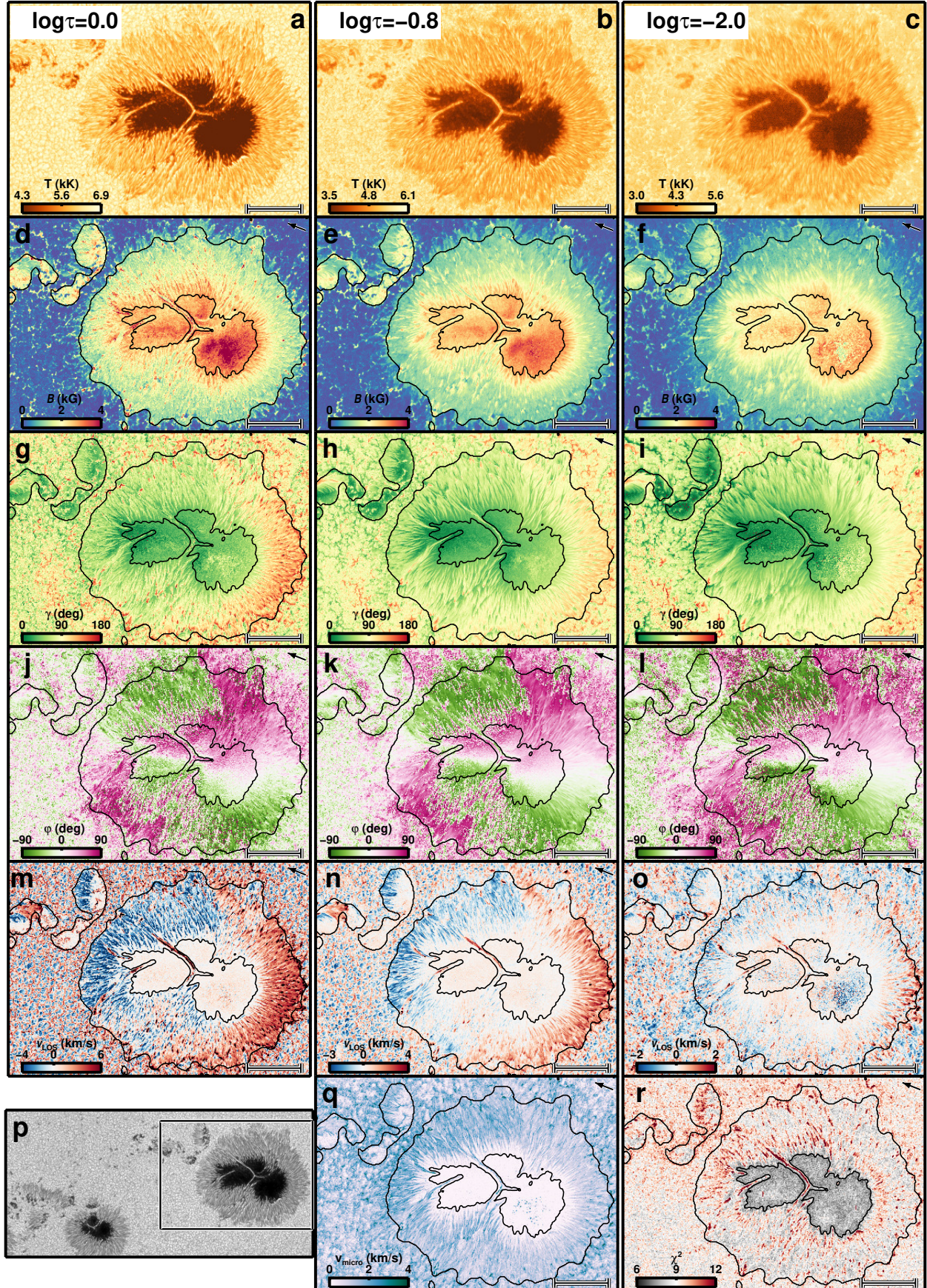


Fig. 8. Same as Fig. 7 but for part of AR 11944 (2014 January 9). This scan was observed in fast mode with a pixel size of $0''.32$. The black rectangle in panel p marks the FOV covered by the other panels. The full FOV is composed of 13×6 tiles.

in Fig. 8, cf. Evershed 1909). The same panel (Fig. 8m) also shows elongated counter Evershed flows associated with a filamentary light bridge (cf. Castellanos Durán et al. 2021), as well as small-scale penumbral downflows (cf. Katsukawa & Jurčák 2010; Jurčák & Katsukawa 2010; van Noort et al. 2013).

5. Discussion

5.1. Comparison with the standard Level-2 inversions

We present two examples of the depth-dependent atmospheric conditions retrieved using coupled inversions and compare them with the standard Level-2 ME inversions that are a part of the Hinode/SOT-SP pipeline. Figure 9 is a normal-mode scan, while Fig. 10 presents a fast-mode scan. The panels in Figs. 9 and 10 show the best-fit continuum image (a), χ^2 map (b), magnetic field strength (c), line-of-sight velocity (d), magnetic field inclination (e), and the magnetic field azimuth (f). Each panel is diagonally split into two halves, with the top-left half showing the results of the 2D coupled inversions presented in this paper. All these maps show the results for the middle node ($\log \tau_c = -0.8$), which is best suited for comparison with ME results (cf. Orozco Suárez et al. 2010). The bottom-right halves of the same panels show the same atmospheric quantities returned by the Level-2 ME inversions of the complementary part of the same dataset. The continuum images in panels a have slightly different brightnesses in the two halves, likely because the SPINOR and MERLIN codes normalize the observed Stokes profiles differently during the inversion. This should not affect the rest of the parameters, however.

Not seen in the examples shown here is that coupled inversions provide depth-dependent information that a ME inversion cannot provide by design. This is a qualitative difference between the atmospheres provided in the MODEST database and those obtained by inversions with MERLIN.

Equally important is the relative goodness of fit, or χ^2 . For direct comparison of the standard Level-2 with the coupled inversion, the χ^2 maps were estimated by adopting the generic form of the merit function:

$$\chi^2 = \frac{1}{4N_\lambda - \varrho} \sum_{i=1}^{N_\lambda} \sum_{j=1}^4 \frac{w_j^2}{\sigma_j^2} (I_{ij}^{\text{obs}} - I_{ij}^{\text{syn}})^2, \quad (1)$$

where j stands for the four Stokes profiles, i runs over the number of the observed wavelength points (N_λ), ϱ represents the number of free parameters of each inversion⁵, w_j is the weight applied to each Stokes profile, σ_j is the noise in the observed Stokes profile, and I_{ij}^{syn} and I_{ij}^{obs} are synthetic and observed Stokes profiles. In addition, χ^2 values were estimated only within the two spectral windows that MERLIN fits (black lines in Figs. 4–6), and we use the same weights that MERLIN assumes. Even though these assumptions may favor the MERLIN inversions, the χ^2 values obtained by coupled inversion are significantly smaller (see panel b in Figs. 9 and 10).

The superior visibility of the fine-scale structure from the SPINOR coupled inversions is evident. This difference is best visible in fast-mode scans (e.g., Fig. 10), but is also present for the normal-mode maps. One sign of the removal of the spatial degradation by the PSF by the coupled inversion is the enhanced contrast in the best-fit continuum map when comparing both

inversions (panels a), as can be seen from Figs. 9 and 10. In addition, in the outer part of the penumbra, the Level-2 continuum maps show a “halo” in the outer penumbra boundary that extends into the surrounding granulation. This spatial contamination between different solar features is absent in the coupled inversions. This is a direct consequence of the smearing by the PSF. Other atmospheric maps show comparable results at large scales, but on the smaller scales, the coupled inversions retrieve finer structures.

This smearing by the telescope PSF makes the Level-2 inversions look spatially smoother over scales of the PSF width. Inverting these smeared maps with Level-2 inversions maintains this smearing and results in apparently smoother maps. The 2D inversions act like a deconvolution of these smeared maps, bringing back the original fine structure with higher contrast in all physical quantities (see for example Fig. 11 of van Noort 2012, and compared Figs. 3 and 4 of Castellanos Durán et al. 2020).

5.2. Molecular blends in the coolest parts of sunspot umbrae

In the comparatively cool environment of sunspot umbrae, diatomic molecules can form. Due to the large number of possible molecular transitions, molecular spectral lines appear as bands in many spectral regions (e.g., Berdyugina & Solanki 2002; Asensio Ramos et al. 2004). Of particular importance in the spectral window around 6302 Å are transitions of the CaH and TiO diatomic molecules (Berdyugina 2011, see also Berdyugina et al. 2003, 2005).

Larger sunspots harbor darker and hence cooler umbrae (e.g., Mathew et al. 2007). In large dark umbrae the molecular blends are the strongest. Figure 11 shows five selected Stokes profiles arising along a line from the edge to the center of the umbra of a sunspot (AR 10930) that was located near the disk center. The main sunspot of AR 10930 is one of the largest spots in the sample. The pixels with the plotted profiles were chosen to sample umbra from warm ($I_c \approx 0.4 I_{qs}$; marked with the darkest blue color) to cold ($I_c \lesssim 0.15 I_{qs}$; marked with the lightest blue color). Only the most prominent molecular blends are marked. At the lowest umbral temperatures, the Fe I line pair is of similar strength as the molecular lines, making it difficult for the inversion code to find the correct solution. We also show the observed Stokes vector and the obtained best fits. The blending molecular lines can make the identification of the correct position and splitting of the Fe I line pair at 6302 Å difficult for the inversion code, potentially leading to errors in the field strength or the otherwise very robustly determined velocity. In Fig. 11v, the Stokes V of the Fe I line at 6302 Å shows a “wiggle” that the code sometimes fits by adding complexity to the atmosphere (e.g., unrealistically large line-of-sight velocities in umbrae). This wiggle is thought to have a molecular origin, as it is not seen in the Fe I line at 6301 Å. Also, the continuum level is suppressed to an unknown value due to a molecular blend that appears at ≈ 6300.3 Å. In addition to the molecular blends, the Fe I line pair 6302 Å weaken in the coldest parts of umbrae due to their relatively high excitation potentials, making these lines not very sensitive to low temperatures (Smitha et al. 2021a). The issues presented by the appearance of molecular lines must be taken into account when analyzing the cold regions in sunspots. The user of the catalog must be aware of this issue and should use the inversion results from the regions where the spectra are affected by molecular lines with caution, or use masking techniques to avoid them completely.

⁵ The number of free parameters of the stratified-MODEST inversions and the ME-Level-2 inversions are $\varrho_{\text{MODEST}} = 16$ (Sect. 3.2) and $\varrho_{\text{MERLIN}} = 11$.

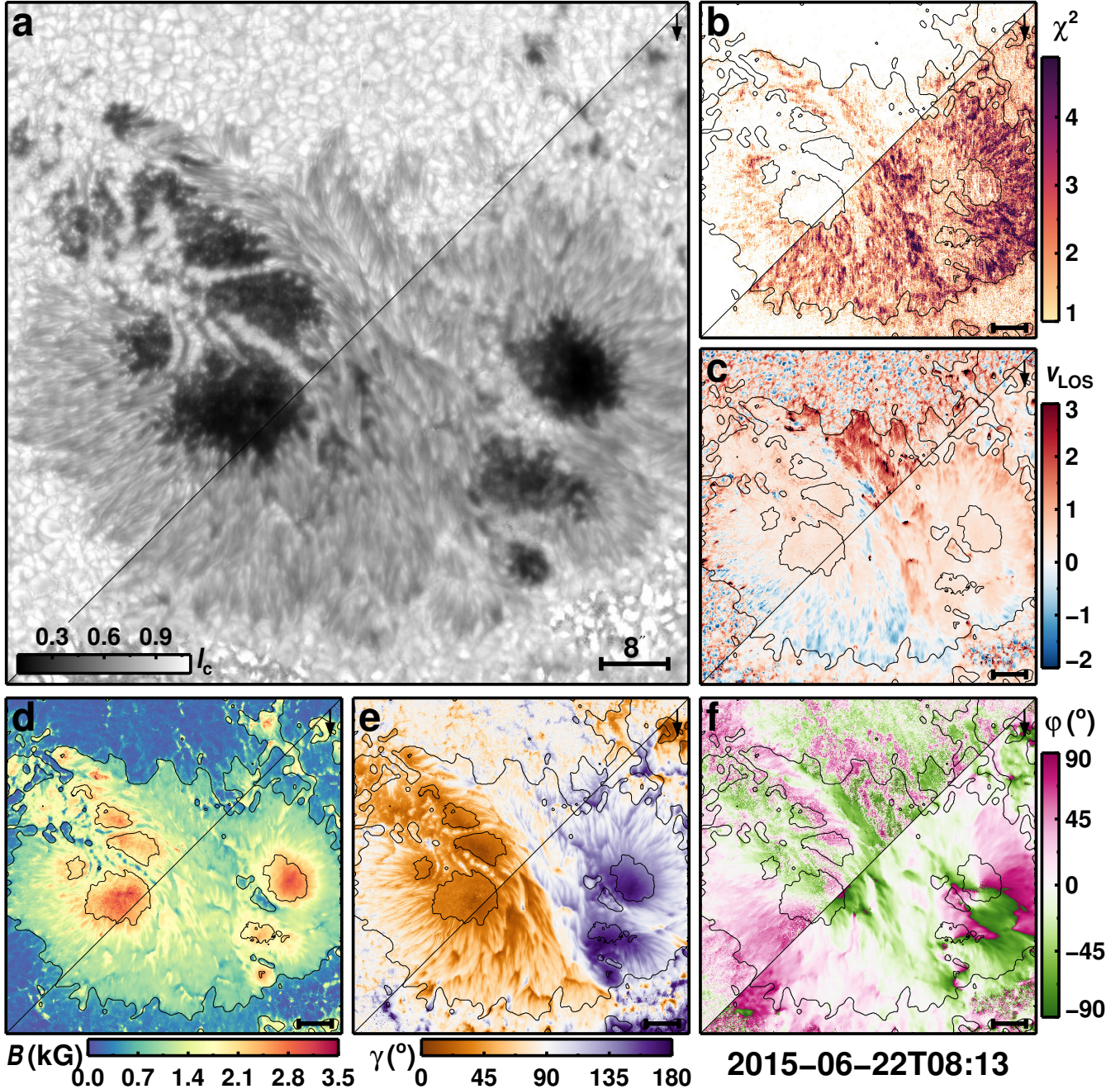


Fig. 9. Atmospheric maps of AR 12371 obtained with the spatially coupled inversions at the middle node ($\log \tau = -0.8$; top-left half of each panel) and MERLIN (Level-2; bottom-right half). Panel a shows the best-fit continuum map. The atmospheric parameters retrieved by both inversion schemes are shown in the panels: (b) χ^2 map, (c) line-of-sight velocity, (d) magnetic field strength, (e) magnetic field inclination relative to the line of sight, and (f) azimuth relative to the line of sight. Atmospheric maps at the middle node were used for the coupled inversions. Horizontal bars on the bottom-right mark $8''$. This scan was observed in normal mode with a pixel size of $0''.16$.

Fortunately, umbral regions cold enough to form strong molecular lines do not appear too often on the Sun. In fact, pixels with low intensities, $I_c < 0.15 I_{qs}$, where molecular blends are sufficiently prominent to start affecting the inversion results, represent just 11.7% of all umbral pixels ($I_c \leq 0.5 I_{qs}$), and fewer than 0.7% of the pixels that are part of the MODEST catalog. All the same, these 11% of the umbrae are also the coldest and hence likely the parts with the strongest field strengths (see the relationship between temperature and field strength studied by, e.g., Kopp & Rabin 1992; Solanki et al. 1993; Mathew et al. 2004), so that the properties of the strongest-field umbral regions

may not be so reliable in MODEST as other parts of the pg sunspots.

5.3. 180° disambiguation of the magnetic field

Measurements of the magnetic field based on the Zeeman effect have an intrinsic 180° ambiguity in the azimuthal angle of the component of the magnetic field transverse to the light-of-sight. Single-height-disambiguation techniques exist to solve the 180° ambiguity through minimizing a given parameter of the system (e.g., electric currents, free energy, etc.; for a review, see

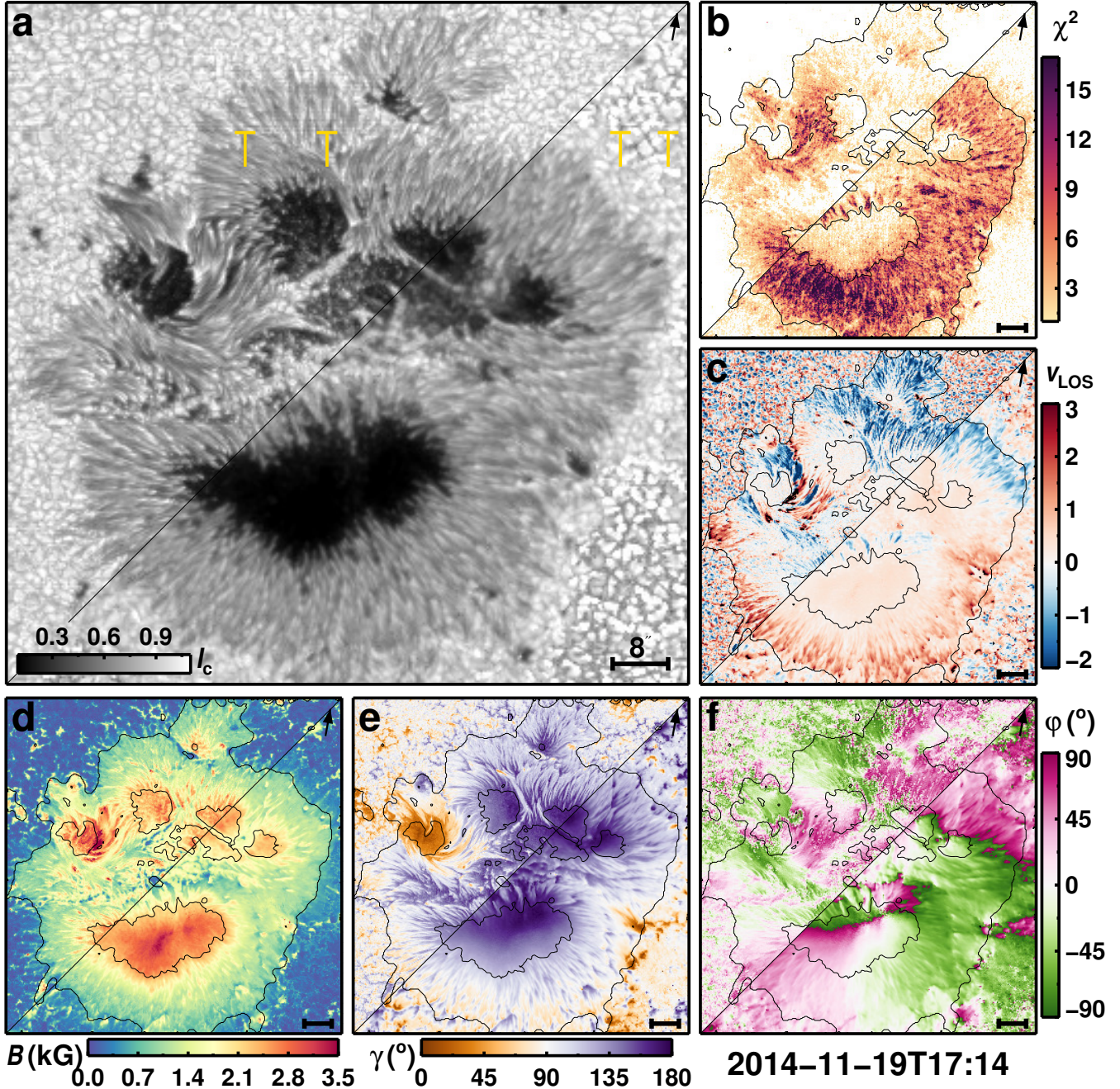


Fig. 10. Same as Fig. 9 but for part of AR 12209. This scan was observed in fast mode with a pixel size of $0''.32$.

Leka et al. 2009). These single-height techniques are currently, to some extent, considered to be straightforward and they have been already automated for the ME-based inversions part of the SDO/HMI (Borrero et al. 2011) and Hinode/SOT-SP standard data products. These techniques work especially well in simple configurations but tend to struggle in more complex ARs. For example, the disambiguation techniques undergo problems in highly sheared regions and complex polarity inversion lines, which are present in many ARs.

Another more recently developed technique combines observations taken with different view-angles by two instruments – for example SO/PHI (Solanki et al. 2020) on board Solar Orbiter (Müller 2020) and Hinode/SOT-SP or SDO/HMI. This technique solves the 180° ambiguity by geometrical considerations without the need of minimizing any parameter (Valori et al. 2022,

2023). However, this technique also solves the 180° ambiguity at a single optical depth only, because of the limited number of wavelength points recorded by SO/PHI.

There is currently no standard technique available to properly disambiguate height-stratified inversions. Hence, current methods find the minimum of a given parameter for one height but these techniques do not find the global minimum for a stratified inversion. To avoid this problem, it is customary to disambiguate the data node by node, but that can easily result in inconsistent disambiguation for the different layers. If the sunspot is located close to the disk center and it is a relatively regular sunspot, the disambiguation can be applied to the middle node and the same solutions can then be consistently applied to the other nodes. This choice assumes that the magnetic field does not change dramatically with height, which cannot be assumed

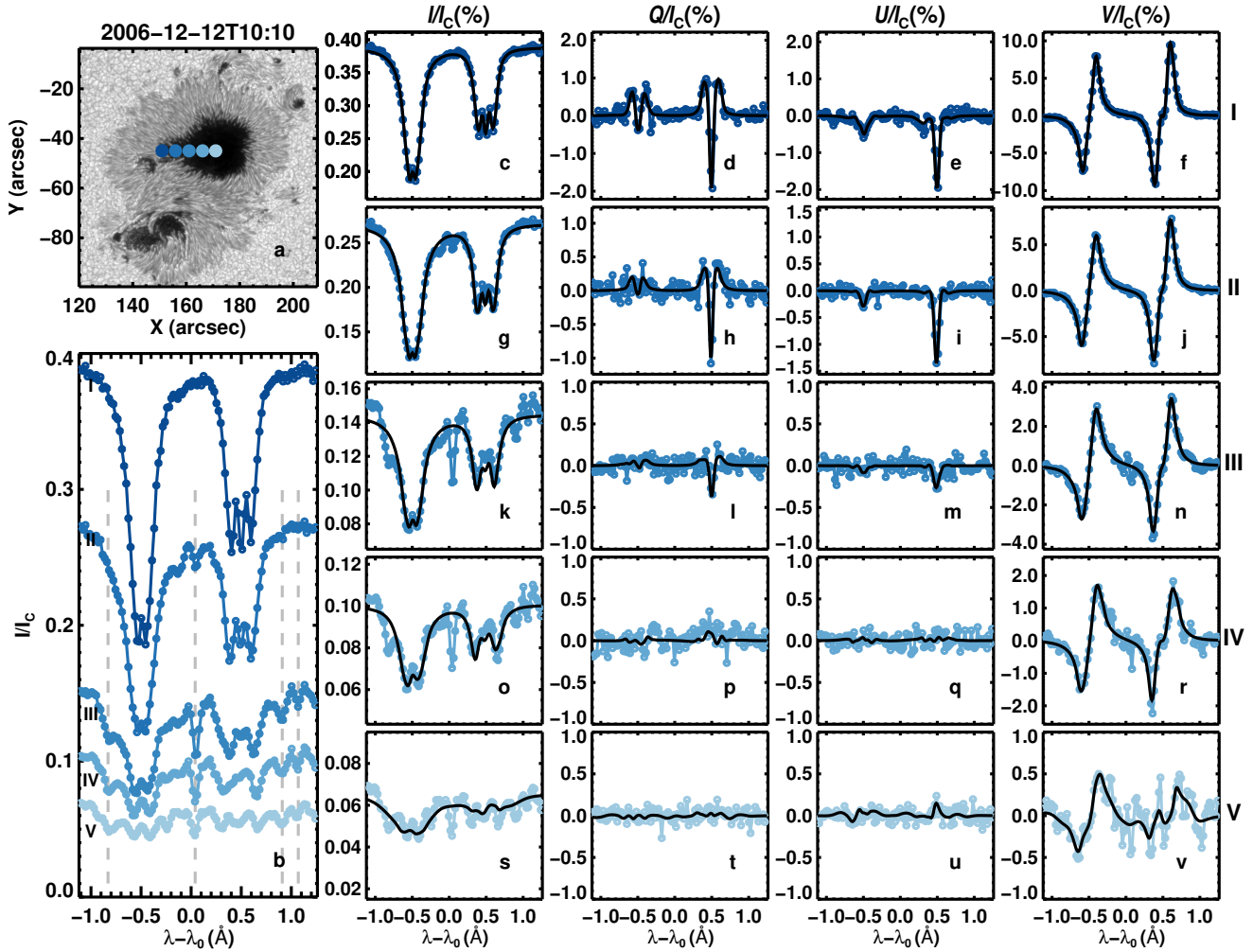


Fig. 11. Hinode/SOT-SP observations of AR 10930 observed almost at disk center ($\mu = 0.99$). Panel a shows the continuum image. Blue circles overplotted on the continuum image mark the locations inside the umbra of the spectra plotted in the remaining panels, color-coded according to the region they were observed in. Lighter blue represents darker and cooler umbral regions, where blends with molecular lines appear. Panel b shows the five normalized Stokes $I(\lambda)$ profiles. The spectra are displayed on the same intensity scale for comparison (i.e., all spectra are normalized to the average quiet-Sun continuum intensity). Dashed-gray vertical lines mark four prominent molecular blends identified at 6301.2 \AA , 6302.0 \AA , 6302.9 \AA , and 6303.1 \AA . Columns 2 to 5 (panels c-v) show the full observed Stokes vectors emerging at the same spatial pixels and the best fits found by the coupled inversions (black lines). $\lambda_0 = 6302\text{ \AA}$.

in general. For example, it is expected that this approach will fail at the edges of facular magnetic concentrations, where the opposite polarity weak field lies under the expanding fields of the flux concentrations (see, e.g., Buehler et al. 2015). Similar problems are expected under the canopies surrounding sunspots.

Due to the current lack of an available disambiguation technique that fully accounts for the variation of the magnetic field with height, we opt, in this early phase of MODEST, to provide the magnetic field vector directly as it is obtained by the inversion, with the intrinsic 180° ambiguity. This also means that all quantities are given in the line-of-sight reference frame. Disambiguation codes can be easily found and the user of MODEST can select a map and apply a method of choice, bearing in mind the caveats given above.

5.4. Quality masks

After the inversion of a scan is fully converged, we create quality masks for that scan. Three different types of pixels are marked. These masks are not related to the quality of the fit to

the observed Stokes vector, but rather to the integrity of each Hinode/SOT-SP scan. We define three quality levels:

- (I) Good-quality pixels.
- (II) Medium-quality pixels. In rare events, there are sharp cuts found in the Hinode/SOT-SP data. These pixels in most cases are well fitted on both parts of the sharp cut. However, because of the coupled nature of the inversions, with the signal in nearby pixels being coupled to each other by the PSF, we mark these places to warn the user that the results may be less reliable than for good-quality pixels. An example is shown on Fig. C.1
- (III) Low-quality pixels. In a very small fraction of pixels, there are significant spikes in one of the Stokes profiles. These most likely come from cosmic rays or readout problems. As the inversion still finds the best possible fit to these pixels, including to the spike, unrealistic atmospheric conditions are retrieved in the pixel(s) and, due to the spatial coupling, their surroundings. All these types of pixels must be excluded from any type of analysis. An example is shown on Fig. C.2.

Together, pixels of types II and III make up only 0.07% of all pixels within the catalog.

5.5. Residuals in the atmospheric maps

In some scans we observe a slight discontinuity of the atmospheric parameters for a certain pixel of the slit, resulting in spurious horizontal lines in the maps. These spurious residuals are best seen in the top node of the temperature maps, but they are also visible in the continuum maps. These spurious lines are most often located in the top part of the FOV (cf. Fig. 1 of Tiwari et al. 2013). For some scans, these spurious lines can all be observed directly on the continuum maps of both, the coupled inversions and the standard Level-2 data (yellow marks in Fig. 10a). The dispersion of these residuals in the temperature maps is on the order of a few kelvin, but it is difficult to separate this variation from the observed feature. This pattern highly resembles the Hinode/SOT-SP dark images (see Fig. 2 in Lites & Ichimoto 2013), and is seen more often in scans taken after \sim 2014. This might be an indication of some sort of degradation, but further analysis is needed. The magnitude of the residuals is small, so they could not be detected before the inversions. For the output of the inversion, we avoid removing these residuals ad hoc and leave it up to the user of the catalog to either leave them as they are or apply a filter for their removal.

6. Summary and conclusions

In this paper we have introduced the MODEST catalog, which consists of height-dependent maps of atmospheric parameters and can be used to study a wide range of phenomena in the photosphere of the Sun. The MODEST catalog encompasses all types of photospheric features, from umbral dots to network fields and quiet-Sun regions. In addition, all types of sunspot groups from α spots to complex δ ARs are covered (Fig. 2). The catalog currently contains the outputs of inversions of 944 spatial scans by Hinode/SP of 117 individual sunspot groups, for a total of 1.4×10^8 spatial pixels of the solar photosphere with retrieved height-dependent physical conditions.

The large variety of scans, features, types of ARs, and locations on the solar disk contained in the MODEST catalog can be used to study a range of topics, including:

- The photospheric structure of the penumbra (e.g., Tiwari et al. 2013, 2015) and its formation and temporal evolution on timescales of hours to days (e.g., Scharmer et al. 2008; Schlichenmaier et al. 2010; Bello González et al. 2019), as well as penumbral features such as penumbral grains (e.g., Muller 1973a,b; Sobotka et al. 1999; Sobotka & Puschmann 2022; Sobotka et al. 2024) or orphan penumbrae (e.g., Zirin & Wang 1991, Löptien et al., in prep.).
- Statistics of granular (Vazquez 1973; Lites et al. 1990, 1991; Sobotka et al. 1993; Rouppe van der Voort et al. 2010; Lagg et al. 2014; Schlichenmaier et al. 2016; Griñón-Marín et al. 2021) and filamentary light bridges (Adjabshirzadeh & Koutchmy 1980; Rimmele 2008; Katsukawa et al. 2007; Guglielmino et al. 2017).
- Bipolar light bridges and the super-strong magnetic fields they harbor (Zirin & Wang 1993; Livingston et al. 2006; Okamoto & Sakurai 2018; Wang et al. 2018; Castellanos Durán et al. 2020).
- The 3D structure and evolution (on timescales of hours to days) of the normal Evershed flow (Evershed

1909; Rimmele & Marino 2006) the and counter Evershed flow (e.g., Schlichenmaier et al. 2011; Kleint 2012; Kleint & Sainz Dalda 2013; Louis et al. 2014; Siu-Tapia et al. 2017; Castellanos Durán et al. 2021, 2023)

- Dependence of the properties of sunspots on their size, shape, complexity, and so on (e.g., Collados et al. 1994; Mathew et al. 2007; Rezaei et al. 2012, 2015).
- The physical structure of the umbra–penumbra boundary as a function of various sunspot parameters (Jurčák 2011; Jurčák et al. 2018; Lindner et al. 2020; Löptien et al. 2020b; García-Rivas et al. 2021).
- Properties of the granulation (velocities, contrast, sizes, etc., as a function of height; e.g., Danilovic et al. 2008; Hirzberger et al. 2010; Ishikawa et al. 2020) and of small-scale magnetic features (e.g., Buehler et al. 2015, 2019; Kahil et al. 2017, 2019).
- Changes in sunspot or granulation properties, or the amount of magnetic flux over the \sim 1.5 solar cycles that are currently covered by MODEST (see, e.g., Muller & Roudier 1984; Mathew et al. 2007; Livingston et al. 2012; Buehler et al. 2013; Lites et al. 2014; Kiess et al. 2014).
- The connection between flares and the detailed properties of underlying sunspots (e.g., Shimizu et al. 2014; Toriumi & Wang 2019; Yardley et al. 2022).

Additionally, the large sample of ARs at different μ -values can be used, for example, to train artificial neural networks (Carroll & Staude 2001; Socas-Navarro 2005; Asensio Ramos & Díaz Baso 2019; Milić & Gafeira 2020; Liu et al. 2020; Socas-Navarro & Asensio Ramos 2021; Centeno et al. 2022); or to study the connection between flares and the detailed properties of underlying sunspots (Toriumi & Wang 2019, for review). Finally, thanks to the large number of inverted sunspots with height-dependent information, it may also be possible to extend existing studies.

The spatially coupled inversions effectively retrieve excellent fits to the observed Stokes profiles for all kinds of solar features, almost irrespective of the complexity of the measured Stokes profile. Only in the very cold umbra are the inversions of lower quality, due to the intrinsic problem of molecular lines appearing in the spectral window observed by Hinode/SOT-SP. In addition, recent works have demonstrated the significance of considering the effects of nonlocal thermodynamic equilibrium (non-LTE) on the formation of iron lines in the photosphere (Smitha et al. 2020, 2021b, 2023). Non-LTE Stokes profiles show significant differences compared to LTE-treated Stokes profiles. Additional work is required to fully determine how non-LTE effects impact the retrieved atmospheric conditions.

Besides inverting the Hinode/SOT-SP scans of a larger number of ARs, additional improvements are conceivable. For example, modeling molecular lines and implementing them into the inversion procedure could improve the results obtained for the darkest parts of umbrae. The development and application of a disambiguation technique that covers the height dependence would open up new applications.

Acknowledgements. We are grateful to Rebecca Centeno Elliott for providing the MERLIN input files that were used to obtain synthetic Stokes profiles of standard Level-2 inversions. We thank Stephan Thoma (MPS) for his continuous support and development of a web-application to access the catalog. J. S. Castellanos Durán was funded by the Deutscher Akademischer Austauschdienst (DAAD) and the International Max Planck Research School (IMPRS) for Solar System Science at the University of Göttingen. This project has received funding from the European Research Council (ERC) under the European Union’s Horizon 2020 research and innovation program (grant agreement No. 695075).

Hinode is a Japanese mission developed and launched by ISAS/JAXA, with NAOJ as domestic partner and NASA and UKSA as international partners. It is operated by these agencies in cooperation with ESA and NSC (Norway).

References

- Adjabshirzadeh, A., & Koutchmy, S. 1980, *A&A*, **89**, 88
- Asensio Ramos, A., & Díaz Baso, C. J. 2019, *A&A*, **626**, A102
- Asensio Ramos, A., Trujillo Bueno, J., & Collados, M. 2004, *ApJ*, **603**, L125
- Bello González, N., Jurčák, J., Schlichenmaier, R., & Rezaei, R. 2019, *ASP Conf. Ser.*, **526**, 261
- Bellot Rubio, L. R., Balthasar, H., Collados, M., & Schlichenmaier, R. 2003, *A&A*, **403**, L47
- Berdyugina, S. V. 2011, *ASP Conf. Ser.*, **437**, 219
- Berdyugina, S. V., & Solanki, S. K. 2002, *A&A*, **385**, 701
- Berdyugina, S. V., Solanki, S. K., & Frutiger, C. 2003, *A&A*, **412**, 513
- Berdyugina, S. V., Braun, P. A., Fluri, D. M., & Solanki, S. K. 2005, *A&A*, **444**, 947
- Bianda, M., Solanki, S. K., & Stenflo, J. O. 1998, *A&A*, **331**, 760
- Borrero, J. M., & Ichimoto, K. 2011, *Liv. Rev. Sol. Phys.*, **8**, 4
- Borrero, J. M., Tomczyk, S., Kubo, M., et al. 2011, *Sol. Phys.*, **273**, 267
- Brault, J. W. 1976, *J. Opt. Soc. Am.*, **66**, 1081
- Brault, J. W. 1978, *Future Solar Optical Observations Needs and Constraints*, 106, 33
- Buehler, D., Lagg, A., & Solanki, S. K. 2013, *A&A*, **555**, A33
- Buehler, D., Lagg, A., Solanki, S. K., & van Noort, M. 2015, *A&A*, **576**, A27
- Buehler, D., Lagg, A., van Noort, M., & Solanki, S. K. 2019, *A&A*, **630**, A86
- Carroll, T. A., & Staude, J. 2001, *A&A*, **378**, 316
- Castellanos Durán, J. S. 2022, Ph.D. Thesis, University of Göttingen, Germany
- Castellanos Durán, J. S., Lagg, A., Solanki, S. K., Noort, M. V. 2020, *ApJ*, **895**, 129
- Castellanos Durán, J. S., Lagg, A., & Solanki, S. K. 2021, *A&A*, **651**, L1
- Castellanos Durán, J. S., Korpi-Lagg, A., & Solanki, S. K. 2023, *ApJ*, **952**, 162
- Centeno, R., Flyer, N., Mukherjee, L., et al. 2022, *ApJ*, **925**, 176
- Collados, M., Martínez Pillet, V., Ruiz Cobo, B., del Toro Iniesta, J. C., & Vazquez, M. 1994, *A&A*, **291**, 622
- Community Spectropolarimetric Analysis Center 2006, *Hinode-SpectroPolarimeter (SP) Level 2 (vector magnetic field) Spectral Line Inversions (UCAR/NCAR - HAO/Community Spectropolarimetric Analysis Center)*
- Danilovic, S., Gandorfer, A., Lagg, A., et al. 2008, *A&A*, **484**, L17
- Danilovic, S., van Noort, M., & Rempel, M. 2016, *A&A*, **593**, A93
- de la Cruz Rodríguez, J. 2019, *A&A*, **631**, A153
- de la Cruz Rodríguez, J., & van Noort, M. 2017, *Space. Sci. Rev.*, **210**, 109
- del Toro Iniesta, J. C., & Ruiz Cobo, B. 2016, *Liv. Rev. Sol. Phys.*, **13**, 4
- del Toro Iniesta, J. C., Bellot Rubio, L. R., & Collados, M. 2001, *ApJ*, **549**, L139
- Esteban Pozuelo, S., Bellot Rubio, L. R., & de la Cruz Rodríguez, J. 2016, *ApJ*, **832**, 170
- Evershed, J. 1909, *MNRAS*, **69**, 454
- Fouhey, D. F., Higgins, R. E. L., Antiochos, S. K., et al. 2023, *ApJS*, **264**, 49
- Frutiger, C. 2000, Ph.D. Thesis, ETH, Zürich, Switzerland
- Frutiger, C., Solanki, S. K., Fligge, M., & Bruls, J. H. M. J. 2000, *A&A*, **358**, 1109
- García-Rivas, M., Jurčák, J., & Bello González, N. 2021, *A&A*, **649**, A129
- Grinón-Marín, A. B., Pastor Yabar, A., Centeno, R., & Socas-Navarro, H. 2021, *A&A*, **647**, A148
- Guglielmino, S. L., Romano, P., & Zuccarello, F. 2017, *ApJ*, **846**, L16
- Hale, G. E., Ellerman, F., Nicholson, S. B., & Joy, A. H. 1919, *ApJ*, **49**, 153
- Hirzberger, J., Feller, A., Riethmüller, T. L., et al. 2010, *ApJ*, **723**, L154
- Ichimoto, K., Lites, B., Elmore, D., et al. 2008, *Sol. Phys.*, **249**, 233
- Ishikawa, R. T., Katsukawa, Y., Oba, T., et al. 2020, *ApJ*, **890**, 138
- Jurčák, J. 2011, *A&A*, **531**, A118
- Jurčák, J., & Katsukawa, Y. 2010, *A&A*, **524**, A21
- Jurčák, J., Rezaei, R., González, N. B., Schlichenmaier, R., & Vomlel, J. 2018, *A&A*, **611**, L4
- Kahil, F., Riethmüller, T. L., & Solanki, S. K. 2017, *ApJS*, **229**, 12
- Kahil, F., Riethmüller, T. L., & Solanki, S. K. 2019, *A&A*, **621**, A78
- Katsukawa, Y., & Jurčák, J. 2010, *A&A*, **524**, A20
- Katsukawa, Y., Yokoyama, T., Berger, T. E., et al. 2007, *PASJ*, **59**, S577
- Kiess, C., Rezaei, R., & Schmidt, W. 2014, *A&A*, **565**, A52
- Kleint, L. 2012, *ApJ*, **748**, 138
- Kleint, L., & Sainz Dalda, A. 2013, *ApJ*, **770**, 74
- Kopp, G., & Rabin, D. 1992, *Sol. Phys.*, **141**, 253
- Kosugi, T., Matsuzaki, K., Sakao, T., et al. 2007, *Sol. Phys.*, **243**, 3
- Künzel, H. 1960, *Astron. Nachr.*, **285**, 271
- Künzel, H. 1965, *Astron. Nachr.*, **288**, 177
- Lagg, A., Woch, J., Krupp, N., & Solanki, S. K. 2004, *A&A*, **414**, 1109
- Lagg, A., Ishikawa, R., Merenda, L., et al. 2009, *ASP Conf. Ser.*, **415**, 327
- Lagg, A., Solanki, S. K., van Noort, M., & Danilovic, S. 2014, *A&A*, **568**, A60
- Langhans, K., Schärmer, G. B., Kiselman, D., Löfdahl, M. G., & Berger, T. E. 2005, *A&A*, **436**, 1087
- Leka, K. D., Barnes, G., Crouch, A. D., et al. 2009, *Sol. Phys.*, **260**, 83
- Levenberg, K. 1944, *Quar. Appl. Math.*, **2**, 164
- Lindner, P., Schlichenmaier, R., & Bello González, N. 2020, *A&A*, **638**, A25
- Lites, B. W., & Ichimoto, K. 2013, *Sol. Phys.*, **283**, 601
- Lites, B. W., Schärmer, G. B., & Skumanich, A. 1990, *ApJ*, **355**, 329
- Lites, B. W., Bida, T. A., Johannesson, A., & Schärmer, G. B. 1991, *ApJ*, **373**, 683
- Lites, B. W., Elmore, D. F., Seagraves, P., & Skumanich, A. P. 1993, *ApJ*, **418**, 928
- Lites, B. W., Centeno, R., & McIntosh, S. W. 2014, *PASJ*, **66**, S4
- Liu, H., Xu, Y., Wang, J., et al. 2020, *ApJ*, **894**, 70
- Livingston, W., Harvey, J. W., Malanushenko, O. V., & Webster, L. 2006, *Sol. Phys.*, **239**, 41
- Livingston, W., Penn, M. J., & Svalgaard, L. 2012, *ApJ*, **757**, L8
- Löptien, B., Lagg, A., van Noort, M., & Solanki, S. K. 2018, *A&A*, **619**, A42
- Löptien, B., Lagg, A., van Noort, M., & Solanki, S. K. 2020a, *A&A*, **635**, A202
- Löptien, B., Lagg, A., van Noort, M., & Solanki, S. K. 2020b, *A&A*, **639**, A106
- Louis, R. E., Beck, C., Mathew, S. K., & Venkatakrishnan, P. 2014, *A&A*, **570**, A92
- Marquardt, D. W. 1963, *SIAM J. Appl. Math.*, **11**, 431
- Mathew, S. K., Solanki, S. K., Lagg, A., et al. 2004, *A&A*, **422**, 693
- Mathew, S. K., Martínez Pillet, V., Solanki, S. K., & Krivova, N. A. 2007, *A&A*, **465**, 291
- McIntosh, P. S. 1990, *Sol. Phys.*, **125**, 251
- Milić, I., & Gafeira, R. 2020, *A&A*, **644**, A129
- Milić, I., & van Noort, M. 2018, *A&A*, **617**, A24
- Müller, D., St. Cyr, O. C., Zouganelis, I., , et al. 2020, *A&A*, **642**, A1
- Muller, R. 1973a, *Sol. Phys.*, **29**, 55
- Muller, R. 1973b, *Sol. Phys.*, **32**, 409
- Muller, R., & Roudier, T. 1984, *Sol. Phys.*, **94**, 33
- Okamoto, T. J., & Sakurai, T. 2018, *ApJ*, **852**, L16
- Orozco Suárez, D., Bellot Rubio, L. R., Vögler, A., & Del Toro Iniesta, J. C. 2010, *A&A*, **518**, A2
- Rachkovsky, D. N. 1962, *Izvestiya Ordona Trudovogo Krasnogo Znameni Krymskoj Astrofizicheskoy Observatorii*, **28**, 259
- Rachkovsky, D. N. 1967, *Izvestiya Ordona Trudovogo Krasnogo Znameni Krymskoj Astrofizicheskoy Observatorii*, **37**, 56
- Rezaei, R., Beck, C., & Schmidt, W. 2012, *A&A*, **541**, A60
- Rezaei, R., Beck, C., Lagg, A., et al. 2015, *A&A*, **578**, A43
- Riethmüller, T. L., Solanki, S. K., & Lagg, A. 2008, *ApJ*, **678**, L157
- Riethmüller, T. L., Solanki, S. K., van Noort, M., & Tiwari, S. K. 2013, *A&A*, **554**, A53
- Rimmele, T. 2008, *ApJ*, **672**, 684
- Rimmele, T., & Marino, J. 2006, *ApJ*, **646**, 593
- Rouppé van der Voort, L., Bellot Rubio, L. R., & Ortiz, A. 2010, *ApJ*, **718**, L78
- Rouppé van der Voort, L. H. M., De Pontieu, B., Carlsson, M., et al. 2020, *A&A*, **641**, A146
- Rüedi, I., Solanki, S. K., & Livingston, W. C. 1995, *A&A*, **293**, 252
- Ruiz Cobo, B., & del Toro Iniesta, J. C. 1992, *ApJ*, **398**, 375
- Schärmer, G. B., Nordlund, Å., & Heinemann, T. 2008, *ApJ*, **677**, L149
- Schlichenmaier, R., González, N. B., & Rezaei, R. 2011, in *Physics of Sun and Star Spots*, eds. D. Prasad Choudhary, & K. G. Strassmeier, 273, 134
- Schlichenmaier, R., Rezaei, R., Bello González, N., & Waldmann, T. A. 2010, *A&A*, **512**, L1
- Schlichenmaier, R., von der Lühe, O., Hoch, S., et al. 2016, *A&A*, **596**, A7
- Schmidt, W., Hofmann, A., Balthasar, H., Tarbell, T. D., & Frank, Z. A. 1992, *A&A*, **264**, L27
- Shimizu, T., Lites, B. W., & Bamba, Y. 2014, *PASJ*, **66**, S14
- Sigwarth, M., Balasubramanian, K. S., Knölker, M., & Schmidt, W. 1999, *A&A*, **349**, 941
- Siu-Tapia, A., Lagg, A., Solanki, S. K., van Noort, M., & Jurčák, J. 2017, *A&A*, **607**, A36
- Siu-Tapia, A., Lagg, A., van Noort, M., Rempel, M., & Solanki, S. K. 2019, *A&A*, **631**, A99
- Skiernik, A., & Lites, B. W. 1987, *ApJ*, **322**, 473
- Smitha, H. N., Castellanos Durán, J. S., Solanki, S. K., & Tiwari, S. K. 2021a, *A&A*, **653**, A91
- Smitha, H. N., Holzreuter, R., van Noort, M., & Solanki, S. K. 2020, *A&A*, **633**, A157
- Smitha, H. N., Holzreuter, R., van Noort, M., & Solanki, S. K. 2021b, *A&A*, **647**, A46
- Smitha, H. N., van Noort, M., Solanki, S. K., & Castellanos Durán, J. S. 2023, *A&A*, **669**, A144
- Sobotka, M., & Puschmann, K. G. 2022, *A&A*, **662**, A13

- Sobotka, M., Bonet, J. A., & Vazquez, M. 1993, [ApJ](#), **415**, 832
- Sobotka, M., Brandt, P. N., & Simon, G. W. 1999, [A&A](#), **348**, 621
- Sobotka, M., Jurčák, J., Castellanos Durán, J. S., & García-Rivas, M. 2024, [A&A](#), **682**, A65
- Socas-Navarro, H. 2005, [ApJ](#), **621**, 545
- Socas-Navarro, H., & Asensio Ramos, A. 2021, [A&A](#), **652**, A78
- Socas-Navarro, H., Ruiz Cobo, B., & Trujillo Bueno, J. 1998, [ApJ](#), **507**, 470
- Socas-Navarro, H., Martínez Pillet, V., Sobotka, M., & Vázquez, M. 2004, [ApJ](#), **614**, 448
- Socas-Navarro, H., de la Cruz Rodríguez, J., Asensio Ramos, A., Trujillo Bueno, J., & Ruiz Cobo, B. 2015, [A&A](#), **577**, A7
- Solanki, S. K. 1987, Ph.D. Thesis, ETH, Zürich, Switzerland
- Solanki, S. K. 2003, [A&ARv.](#), **11**, 153
- Solanki, S. K., & Montavon, C. A. P. 1993, [A&A](#), **275**, 283
- Solanki, S. K., & Pahlke, K. D. 1988, [A&A](#), **201**, 143
- Solanki, S. K., & Stenflo, J. O. 1984, [A&A](#), **140**, 185
- Solanki, S. K., & Stenflo, J. O. 1985, [A&A](#), **148**, 123
- Solanki, S. K., Walther, U., & Livingston, W. 1993, [A&A](#), **277**, 639
- Solanki, S. K., del Toro Iniesta, J. C., Woch, J., et al. 2020, [A&A](#), **642**, A11
- Sowmya, K., Lagg, A., Solanki, S. K., & Castellanos Durán, J. S. 2022, [A&A](#), **661**, A122
- Title, A. M., Frank, Z. A., Shine, R. A., et al. 1993, [ApJ](#), **403**, 780
- Tiwari, S. K., van Noort, M., Lagg, A., & Solanki, S. K. 2013, [A&A](#), **557**, A25
- Tiwari, S. K., van Noort, M., Solanki, S. K., & Lagg, A. 2015, [A&A](#), **583**, A119
- Toriumi, S., & Wang, H. 2019, [Liv. Rev. Sol. Phys.](#), **16**, 3
- Tsuneta, S., Ichimoto, K., Katsukawa, Y., et al. 2008, [Sol. Phys.](#), **249**, 167
- Unno, W. 1956, [PASJ](#), **8**, 108
- Valori, G., Löschl, P., Stansby, D., et al. 2022, [Sol. Phys.](#), **297**, 12
- Valori, G., Calchetti, D., Moreno Vacas, A., et al. 2023, [A&A](#), **677**, A25
- van Noort, M. 2012, [A&A](#), **548**, A5
- van Noort, M. 2017, [A&A](#), **608**, A76
- van Noort, M., Lagg, A., Tiwari, S. K., & Solanki, S. K. 2013, [A&A](#), **557**, A24
- Vazquez, M. 1973, [Sol. Phys.](#), **31**, 377
- Vukadinović, D., Smitha, H. N., Korpi-Lagg, A., et al. 2024, [A&A](#), **686**, A262
- Wang, H., Yurchyshyn, V., Liu, C., et al. 2018, [Res. Notes Am. Astron. Soc.](#), **2**, 8
- Yardley, S. L., Green, L. M., James, A. W., Stansby, D., & Mihailescu, T. 2022, [ApJ](#), **937**, 57
- Zirin, H., & Wang, H. 1991, [Adv. Space Res.](#), **11**, 225
- Zirin, H., & Wang, H. 1993, [Sol. Phys.](#), **144**, 37

Appendix A: Spectral stray light and spurious polarization

We tested the influence of the spectral stray light on the atmospheric parameters retrieved by the inversions. We used Hinode/SOT-SP data of the quiet Sun taken at disk center and compared it to the National Solar Observatory/Kitt Peak Fourier Transform Spectrometer (FTS) atlas (Brault 1976, 1978). We found that the spectral stray light is up to $\zeta \sim 3\%$, which is consistent with the nominal values found by Lites & Ichimoto (2013). We chose a test FOV that contains the quiet Sun, a small pore, and parts of the penumbra and the umbra. We calibrated this FOV using the nominal Hinode/SOT-SP data, and created two datacubes: one with the nominal calibration, and another with $\zeta = 3\%$ spectral stray light subtracted. To apply this subtraction, we followed the approach described in Bianda et al. (1998). The corrected Stokes $I(\lambda)$ is given by

$$\left(\frac{I(\lambda)}{I_c} \right) = (1 + \zeta) \frac{I(\lambda)^{\text{corr}}}{I_c} - \zeta, \quad (\text{A.1})$$

where I_c is the continuum intensity. The corresponding Stokes profiles for the linear ($F_{Q,U}(\lambda)$) and circular polarization ($F_V(\lambda)$) are $F_{Q,U,V}(\lambda) = F_{Q,U,V}^{\text{corr}}(\lambda) + k_{Q,U,V} I(\lambda)$. (A.2)

The $k_{Q,U,V}$ is the spurious polarization and is usually well corrected by the sp_prep routines (Lites & Ichimoto 2013). However, it has been shown that $k_{Q,U,V}$ is not negligible in extreme cases (Okamoto & Sakurai 2018). Combining Eqs. (A.1) and (A.2), the corrected Stokes profiles are

$$\left(\frac{F_{Q,U,V}(\lambda)}{I_c} \right)^{\text{corr}} = \frac{F_{Q,U,V}(\lambda)}{I_c \left(1 - \frac{\zeta}{1+\zeta} \right)}. \quad (\text{A.3})$$

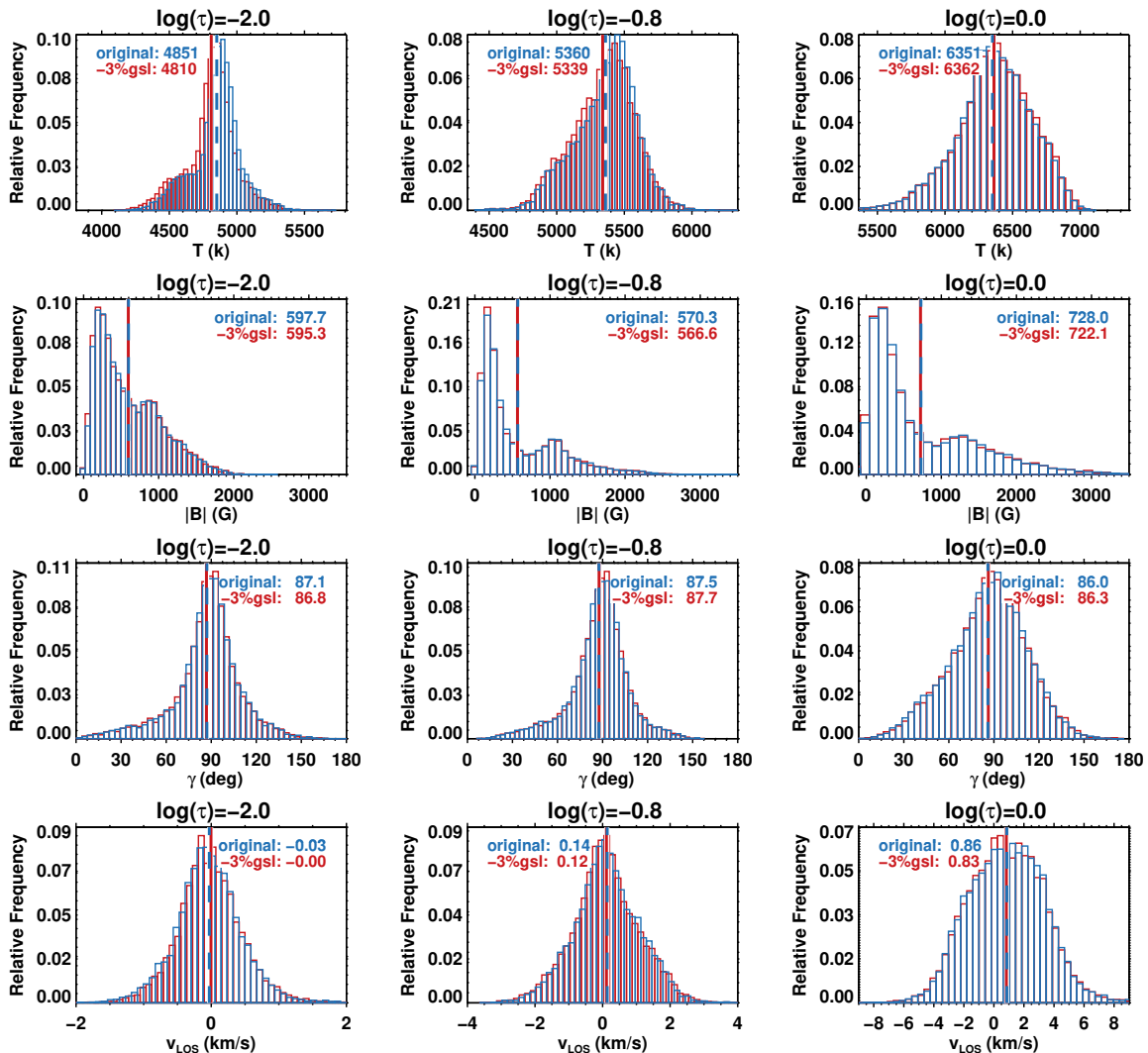


Fig. A.1. Effects of the gray stray light. Each column shows the retrieved atmospheric conditions for each node. From top to bottom we show the retrieved temperature, B , γ , and v_{LOS} . Results obtained from the original Hinode/SOT-SP data are in blue, and data corrected with a 3% level of gray stray light are in red.

Figure A.1 shows the results of this test, where labels “original” and “-3%gsl” mark the two datacubes. Panels in Fig. A.1 show the histograms of the same atmospheric quantity. No strong variation was observed with and without the 3% gray stray light. Based on these findings and as the gray stray light might change over time, no correction of this type was applied.

Appendix B: Effects of tiling the FOV

Splitting the FOV into multiple tiles was necessary to invert large Hinode/SOT-SP scans because of the high-computational demand of the coupled inversions, mainly in terms of memory usage. To mitigate boundary effects, the tiles need to overlap sufficiently. We chose this overlap region to be three times the full width at half maximum of the PSF. In this appendix, we demonstrate that the tiling with this large spatial overlap does not produce any artifacts to the inversion results.

Figure B.1 shows an experiment where the same scan was inverted using two different approaches. The first inversion was performed for the full FOV without any tiling (B.1a). The second inversion used the same tiling scheme as in MODEST, and the FOV was divided into 16 tiles (B.1b). This scan was chosen because all types of features are present (the quiet Sun, penumbras, and umbrae) in the area where the tiles are stitched together. These inversions were carried out following the same steps as in Sects. 3.1–3.3.

The results of these inversions are shown in Fig. B.1. Panels (B.1c) to (B.1f) depict the scatter plots of the retrieved atmospheric conditions for the three nodes combined. The abscissa results of the inversion where the FOV was divided, while the ordinate displays the inversion of the non-tiled FOV. Insets within panels (c)–(f) show the scatter of the difference between the atmospheric quantities from the two inversions for the three-node heights. The differences are Gaussian with a 1σ -level of 43 K for the temperature, 157 G for the magnetic field strength 0.6 km s^{-1} for the line-of-sight velocity, and 11 deg for the line-of-sight inclination of the magnetic field. As expected, the magnetic-field-inclination scatter is the largest. The match between the two inversions reveals that the effect of tiling the FOV is small.

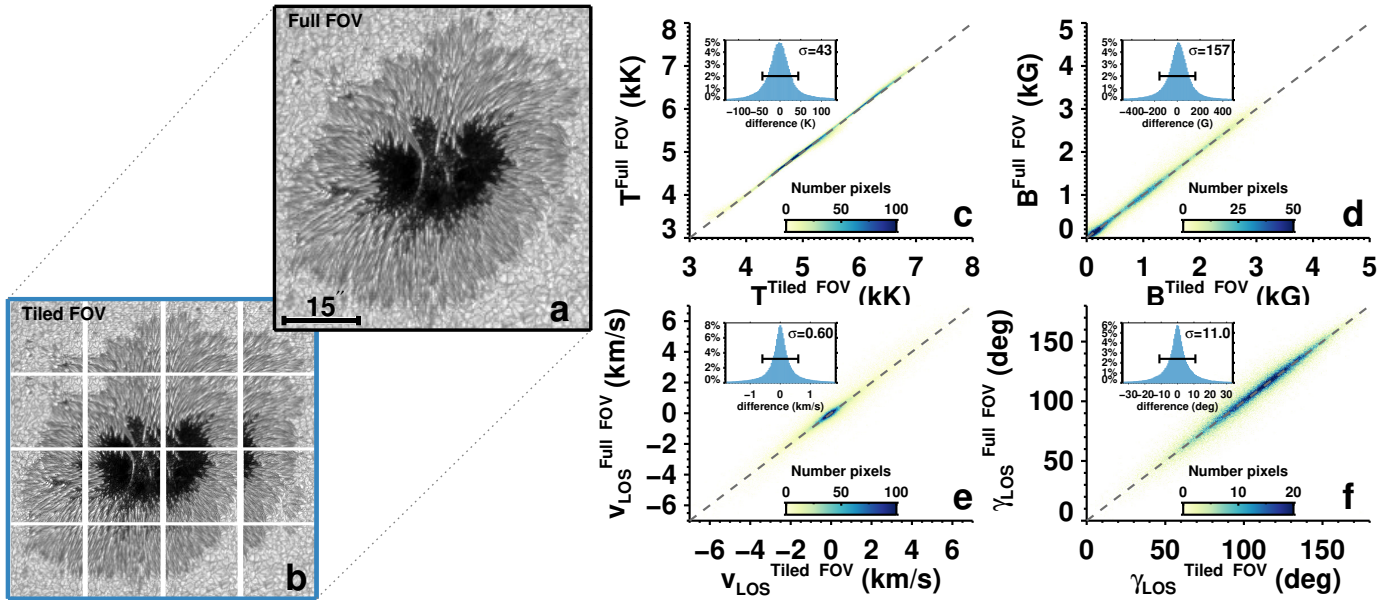


Fig. B.1. Effects of tiling the FOV. Panel (a) shows the full un-tiled continuum image of AR 11748 when it was located close to disk center. Panel (b) shows the FOV broken up into overlapping tiles. The edges of each tile are marked by the white lines FOV. Scatter plots of atmospheric parameters obtained with or without the tiling are displayed in Panels (c)–(d). Data points from all three optical depth nodes are plotted in each panel. The individual panels display the temperature (c), magnetic field strength (d), line-of-sight velocity (e), and line-of-sight inclination of the magnetic field (f). The x-axis displays the inversions performed with the tiled FOV, while the y-axis shows the inversions for the whole FOV inverted in one go for the three-node height. The insets inside panels (c)–(f) show the histograms of differences between the two inversions, where the black bars indicate 1σ .

Appendix C: Medium- and low-quality pixels

Figures C.1 and C.2 show examples of pixels that are likely affected by instrumental or data reduction artifacts, making them of only medium or low quality (see Sect. 5.4). The medium-quality pixels can easily be identified in maps of the Stokes parameters, and also in the corresponding maps of the inverted parameters, as sharp discontinuities in the vertical or horizontal direction.

Figure C.1 shows the atmospheric maps and the fits on both sides of one such discontinuity. The Stokes profiles are well fitted, as is common for medium-quality pixels. However, the fit values are likely not as reliable as for normal pixels due to the coupling of the pixels on both sides of the PSF divide.

Figure C.2 shows an example of a low-quality pixel. There are spikes in the Stokes profiles (black arrows in panels C.21 – C.20). Especially in the polarized Stokes profiles the spike is much larger than the actual solar signals. The inversion still tries to invert this

pixel and its surroundings (red and green profiles), but poor fits and unrealistic atmospheric conditions are retrieved in these pixels and in its surroundings (the latter again, due to the coupling via the PSF).

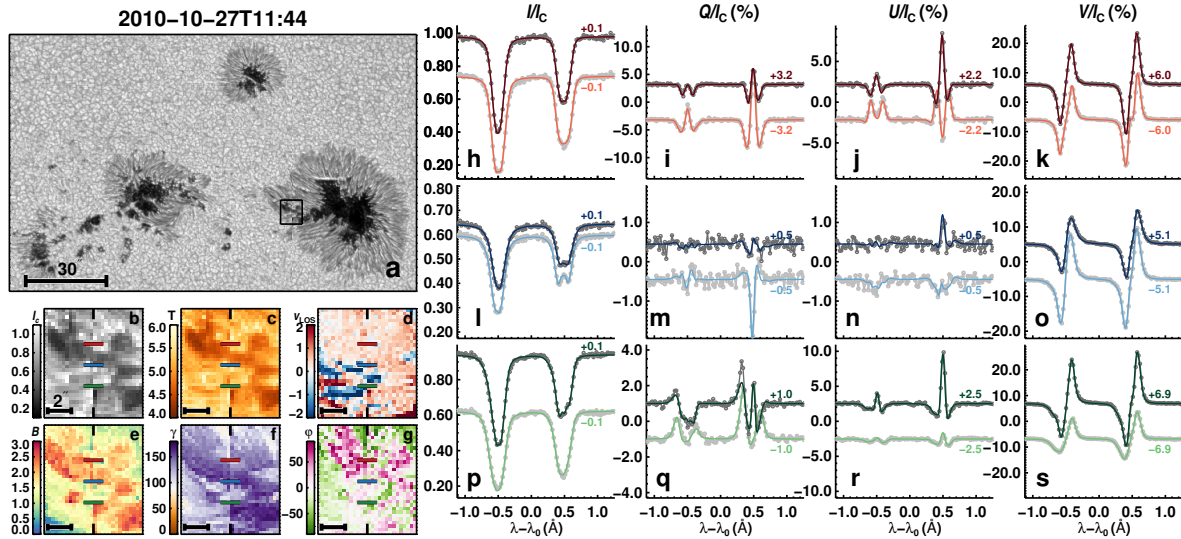


Fig. C.1. Fits obtained by the coupled inversions to the observed Stokes profiles for medium-quality pixels. Panel (a) shows the continuum image of AR 11117 when it was located at $\mu \approx 0.9$. Maps in panels (b) to (g) display the continuum intensity (b), temperature (c), v_{LOS} (d), magnetic field strength (e), inclination (f), and azimuth (g). These maps are from the region outlined by the black rectangle in panel (a). Columns 2 to 5 show the observed Stokes profiles (dotted gray lines) and the best fits obtained by the coupled inversions (colored lines). A vertical shift was added to the Stokes profiles for better representation. The shift values are displayed on the right side of each profile. Each row shows two Stokes vectors coming from neighboring pixels lying immediately to the left (darker lines) and to the right (lighter lines) of a sharp discontinuity in the data (indicated by black vertical tick marks in (b)–(g)). Colored horizontal lines in panels (b) to (g) mark the locations of the profiles. $\lambda_0 = 6302 \text{ \AA}$.

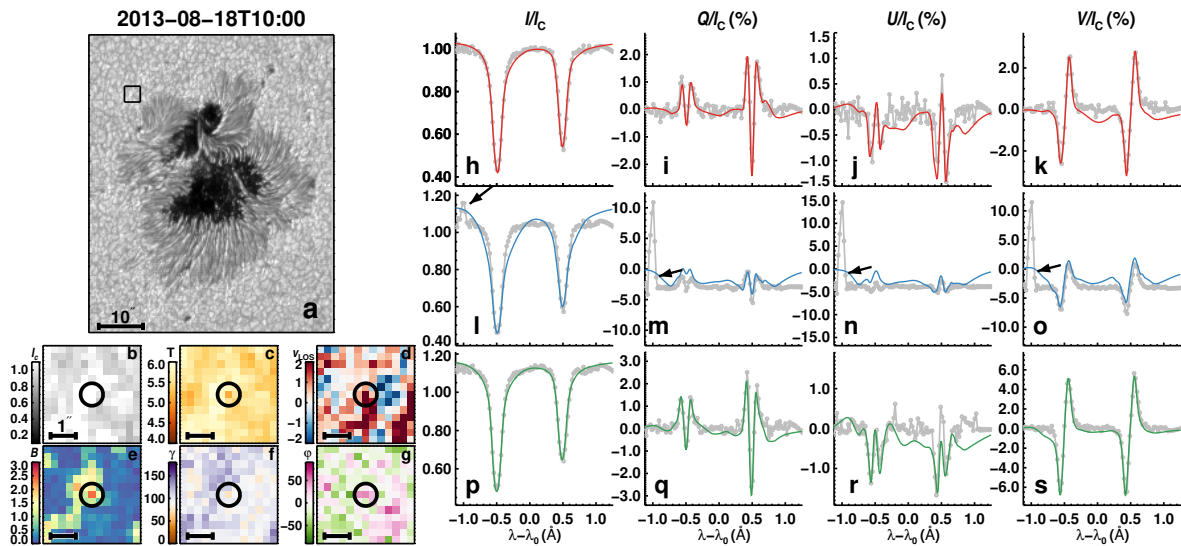


Fig. C.2. Low-quality pixel; the same as Fig. C.1 but for a sunspot group belonging to AR 11818, when it was located at $\mu \approx 0.76$. The open circles mark the location of the low-quality pixel. Black arrows in panels (l) to (o) mark an artifact likely produced by a cosmic ray that strongly influences the fits. $\lambda_0 = 6302 \text{ \AA}$.

Appendix D: Sample of sunspot groups observed by Hinode/SOT-SP and part of the MODEST catalog

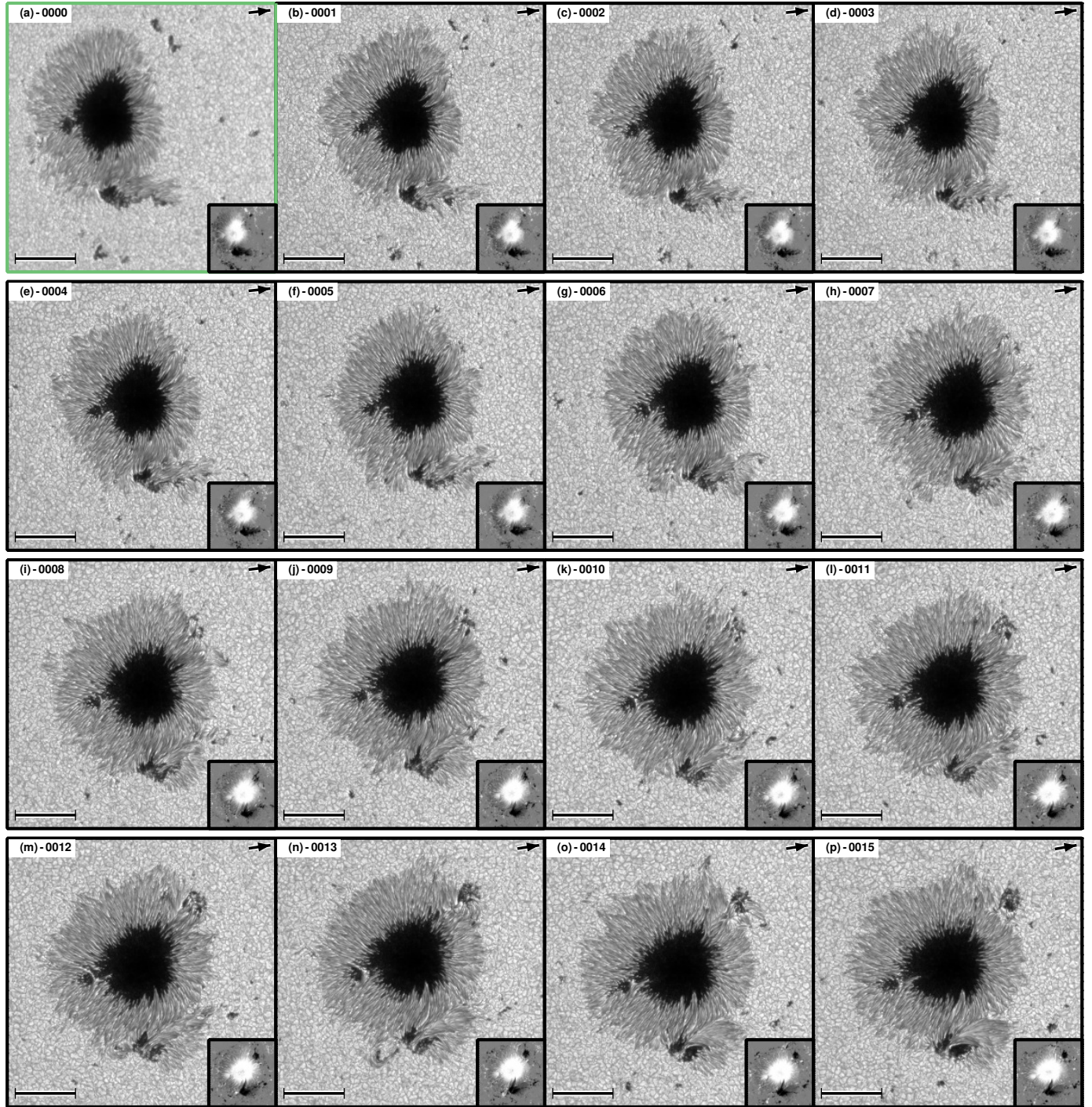


Fig. D.1. Best-fit continuum maps and magnetograms of the sample of sunspots in the MODEST catalog. Numbers on the upper-left part of each panel are the INV_ID of each inversion. INV_IDs can be found on the second column of Table D.1. Bars on the bottom-left corner have a length of $20''$, and arrows on the top-right corner point toward disk center. Insets on the lower-right show the magnetogram ($B \cos(\gamma_{\text{LOS}})$) in the line-of-sight reference frame clipped at 1.5 kG obtained at the middle node. Axes colors display whether the scan was taken in fast (black) or normal mode (green).

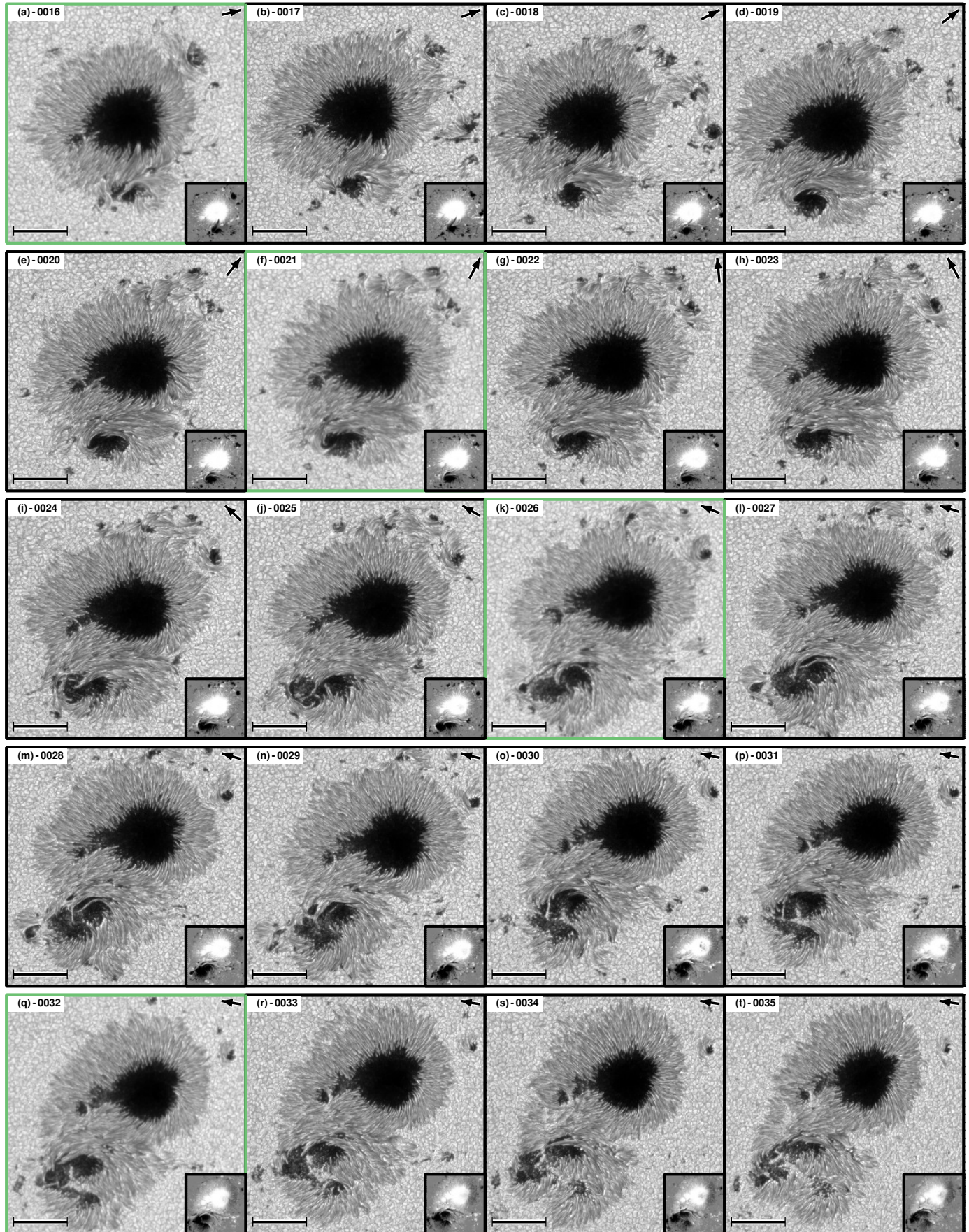


Fig. D.2. Fig. D.1. Continued.

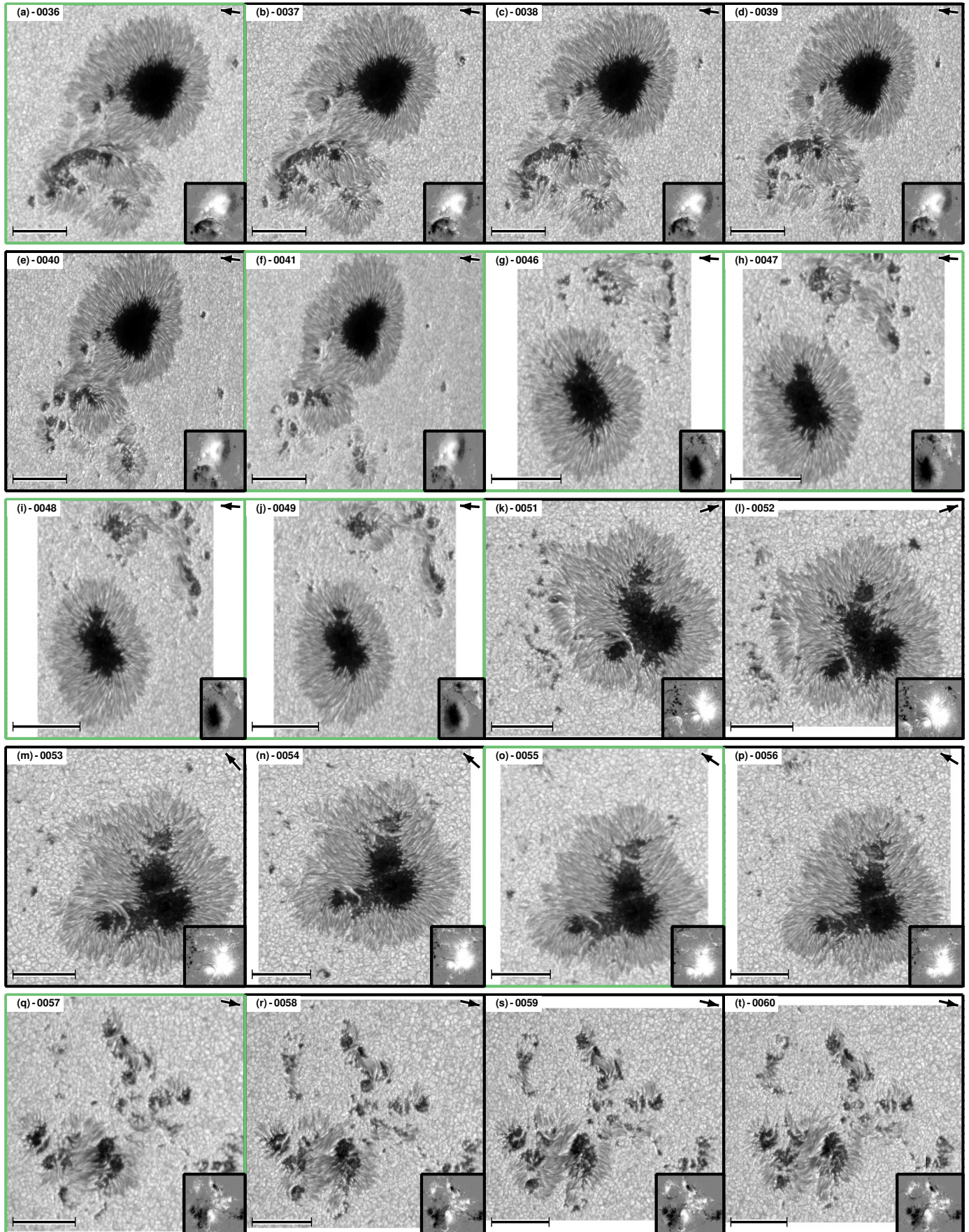


Fig. D.3. Fig. D.1. Continued.

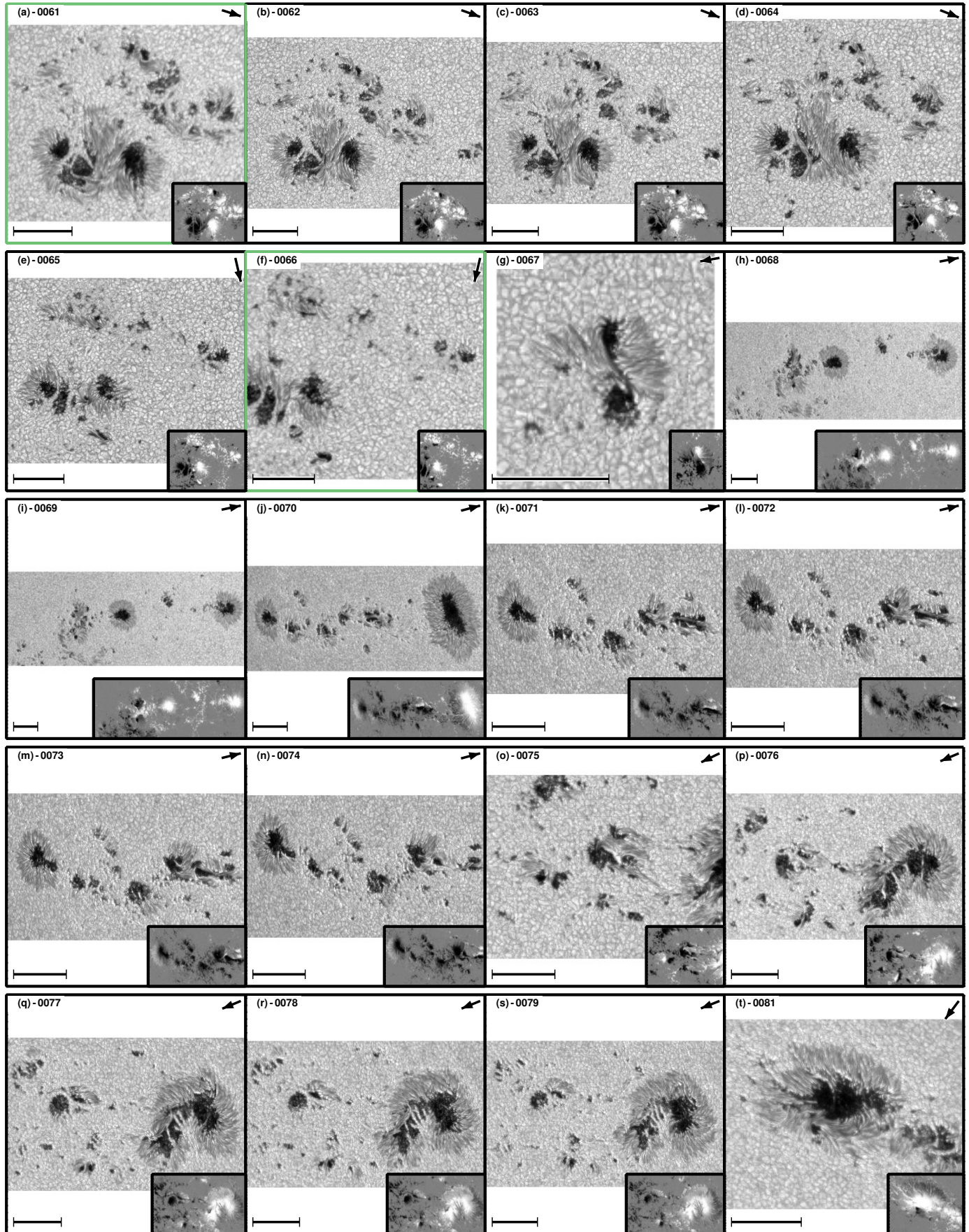


Fig. D.4. Fig. D.1. Continued.

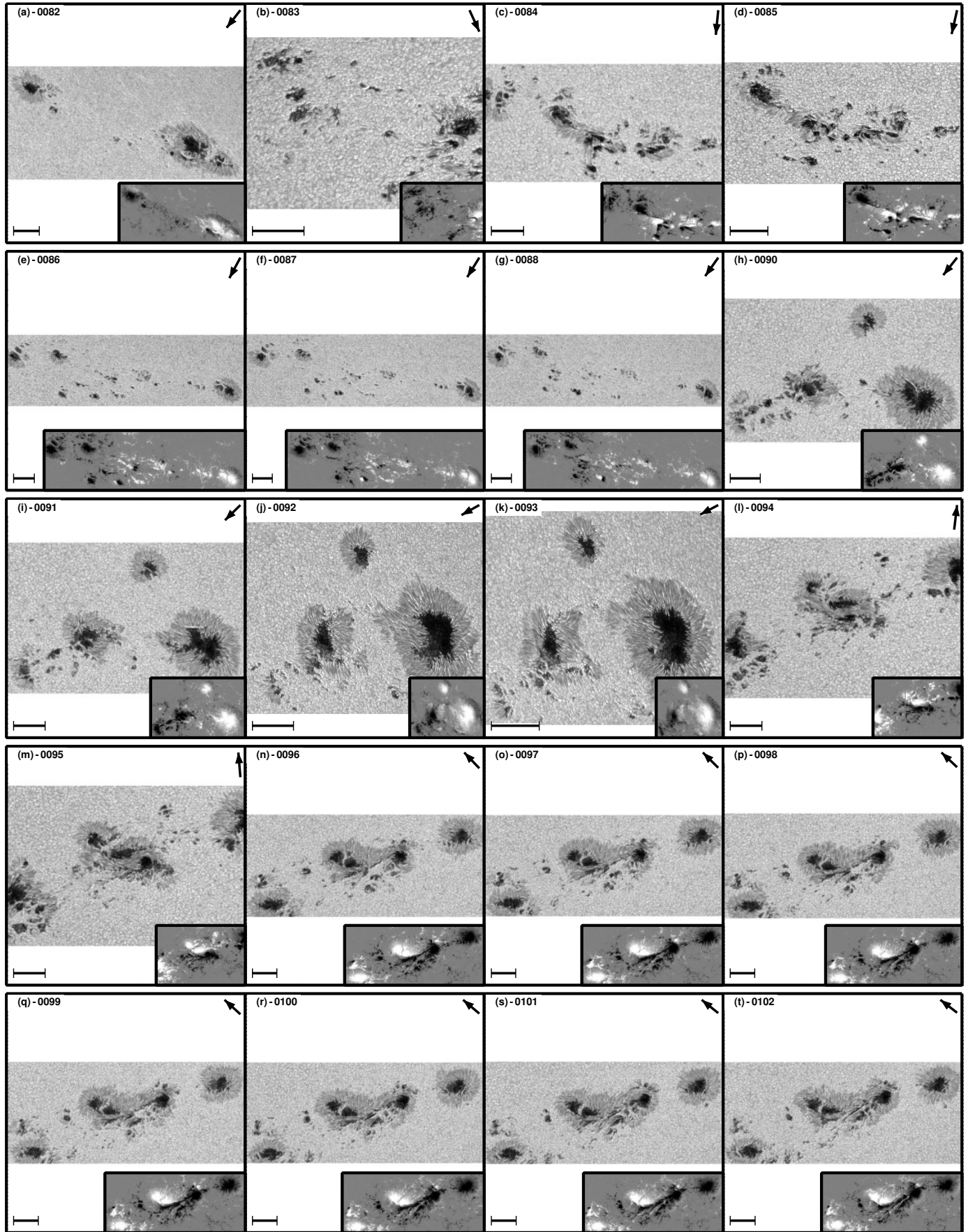


Fig. D.5. Fig. D.1. Continued.

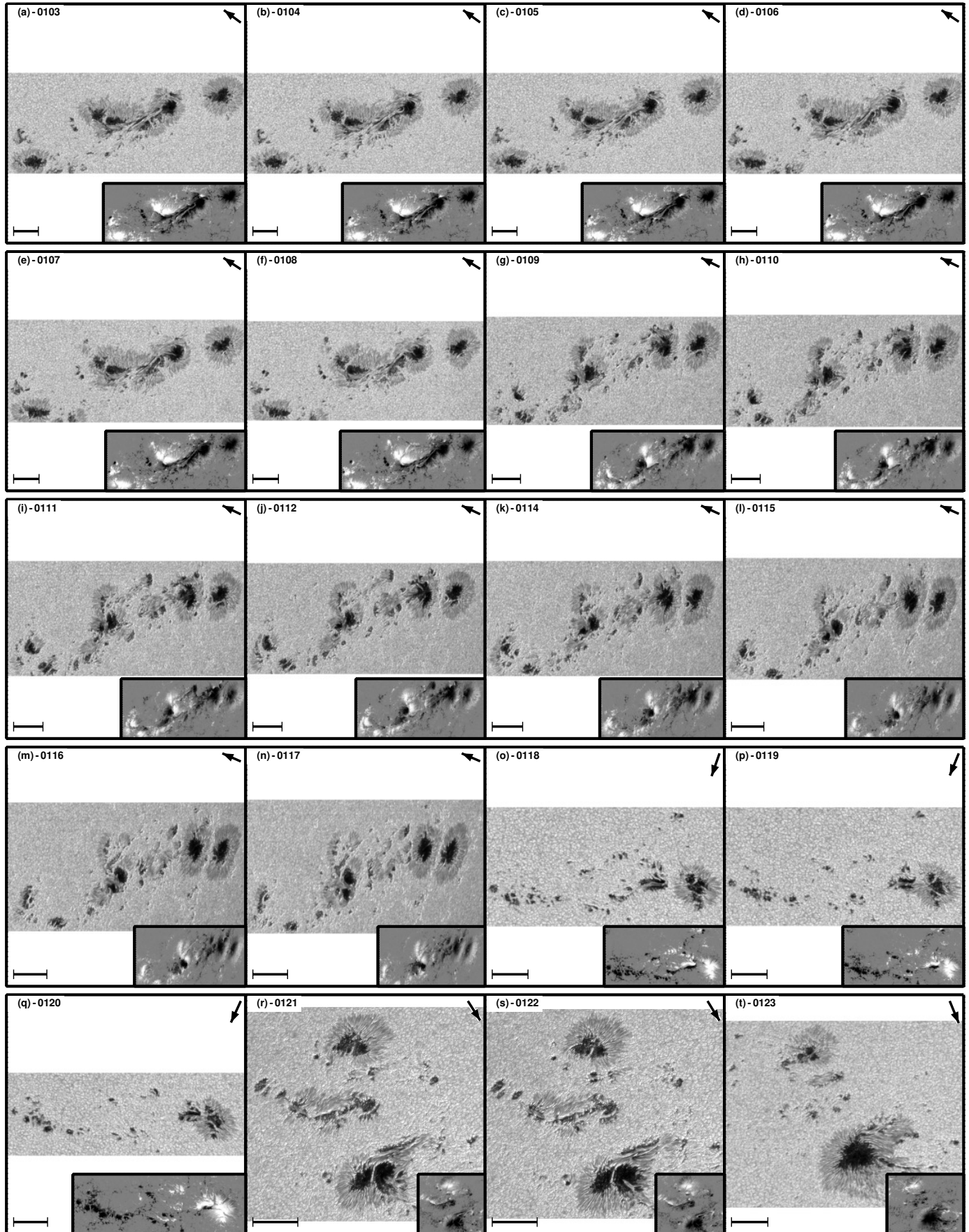


Fig. D.6. Fig. D.1. Continued.

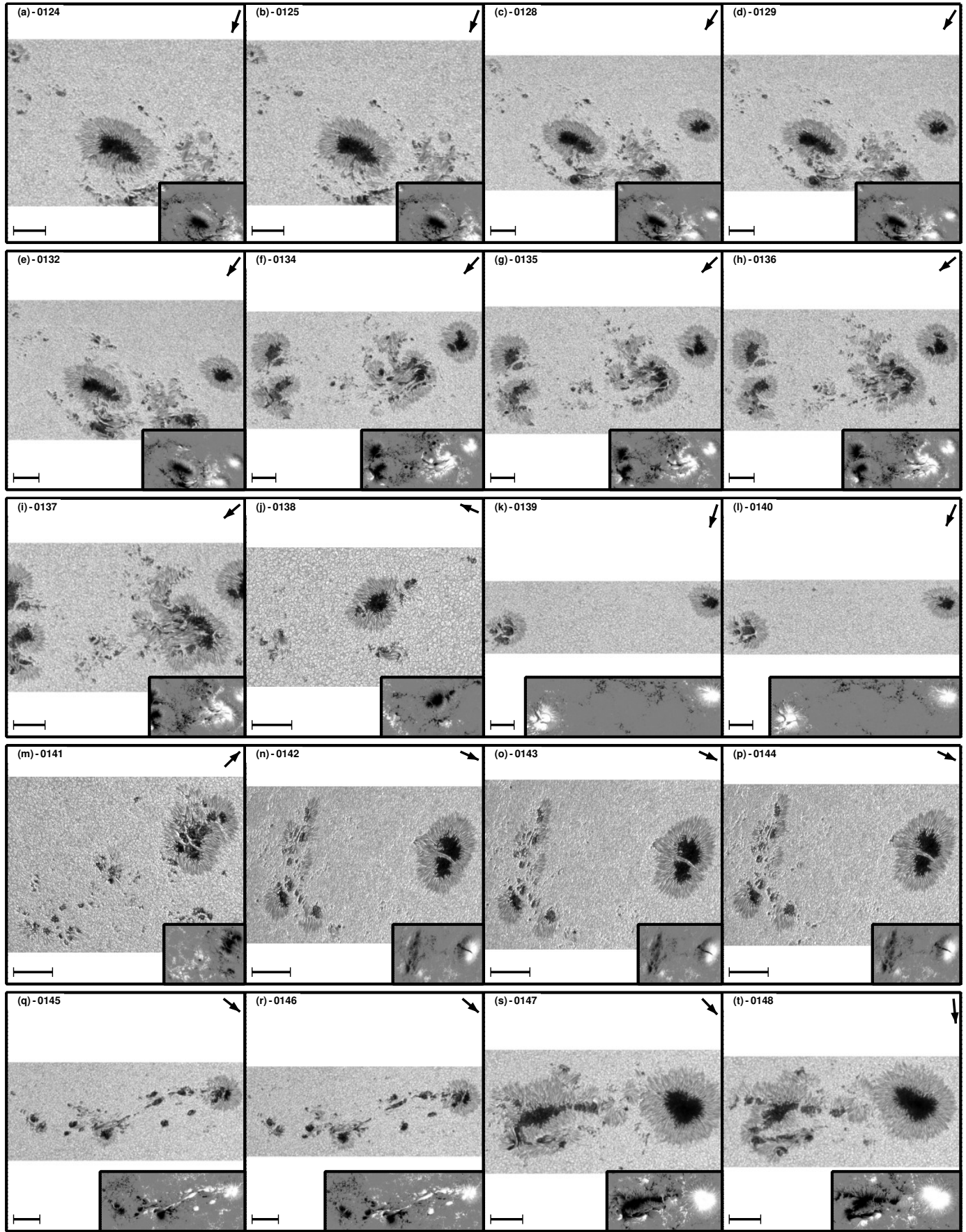


Fig. D.7. Fig. D.1. Continued.

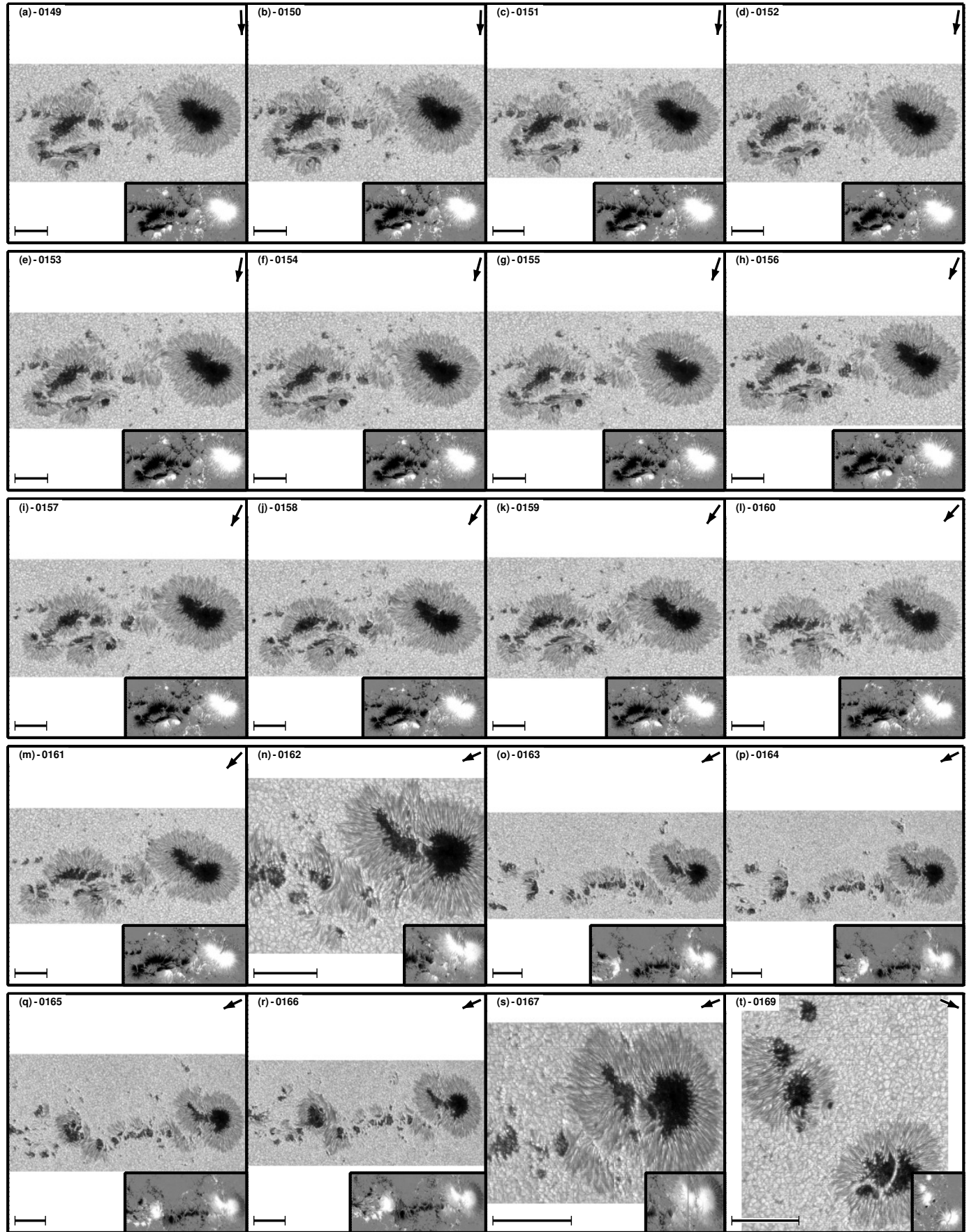


Fig. D.8. Fig. D.1. Continued.

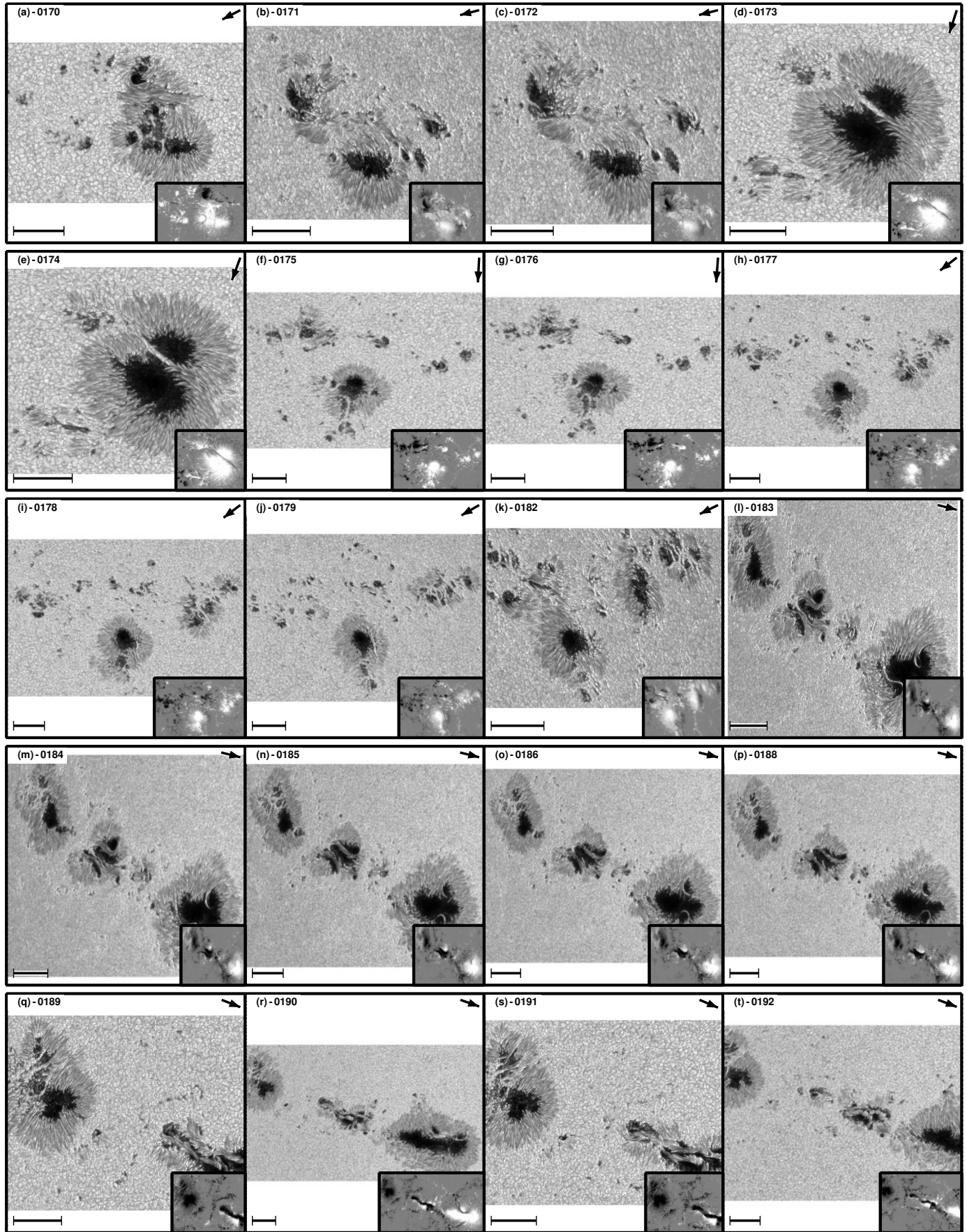


Fig. D.9. Fig. D.1. Continued.

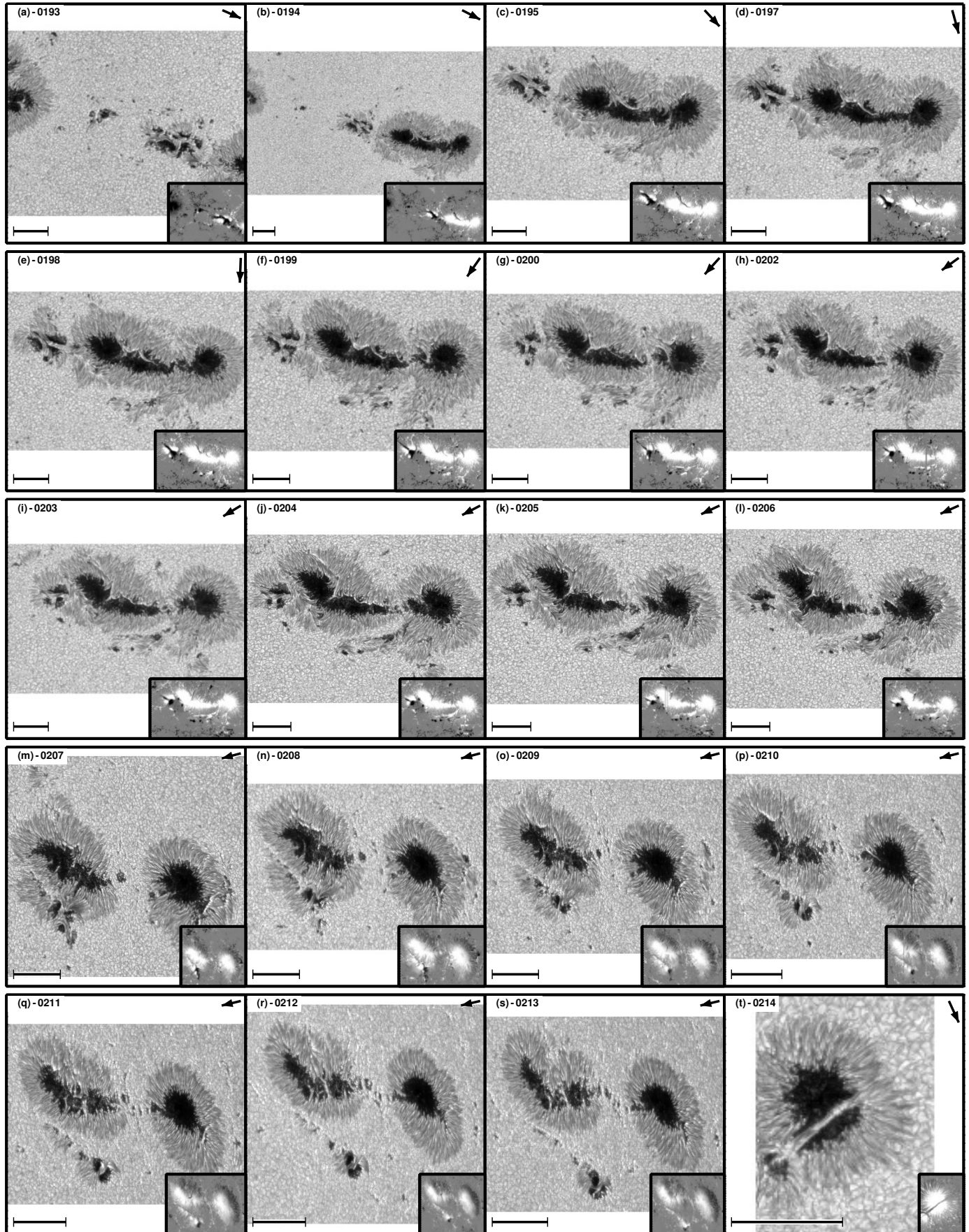


Fig. D.10. Fig. D.1. Continued.

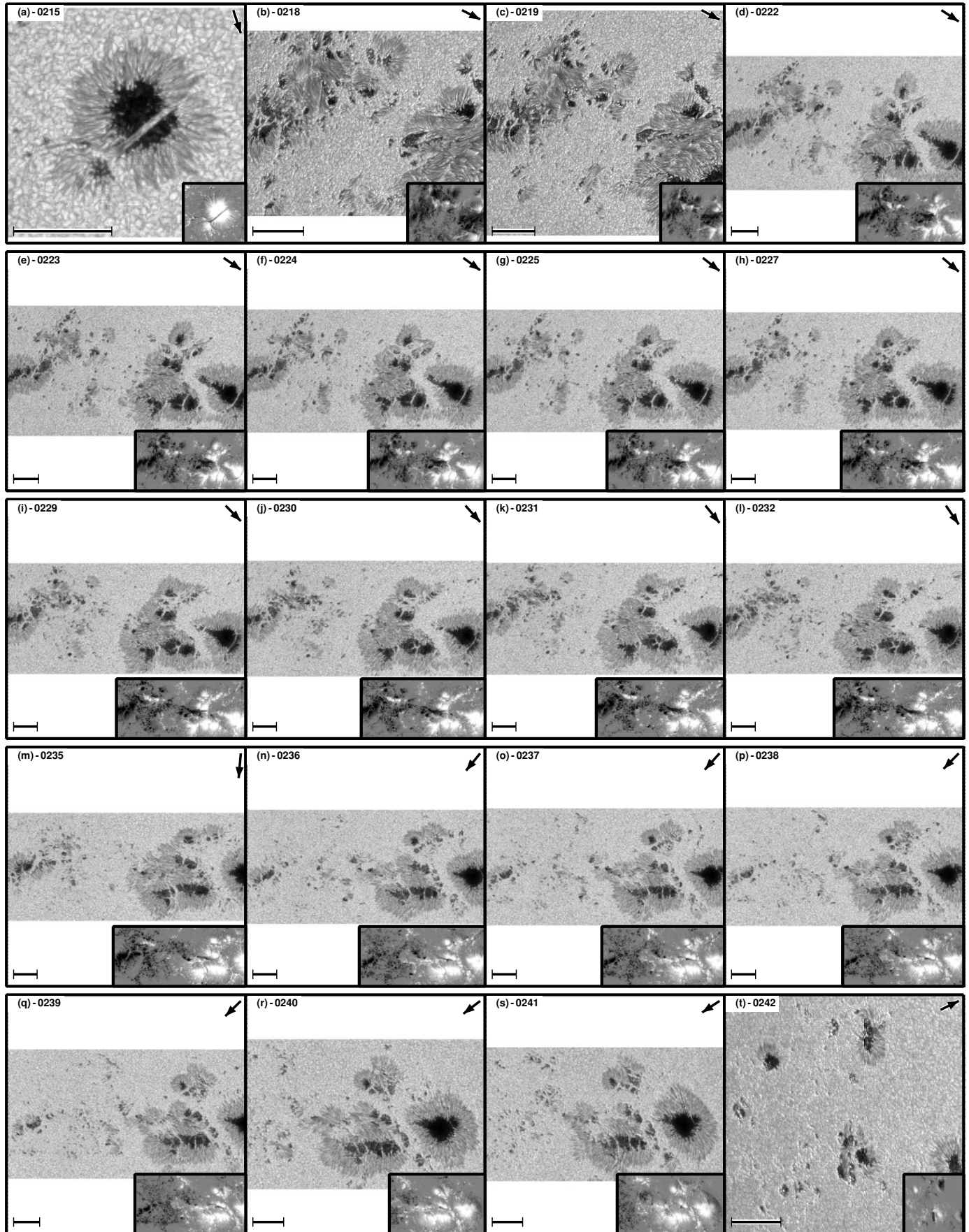


Fig. D.11. Fig. D.1. Continued.

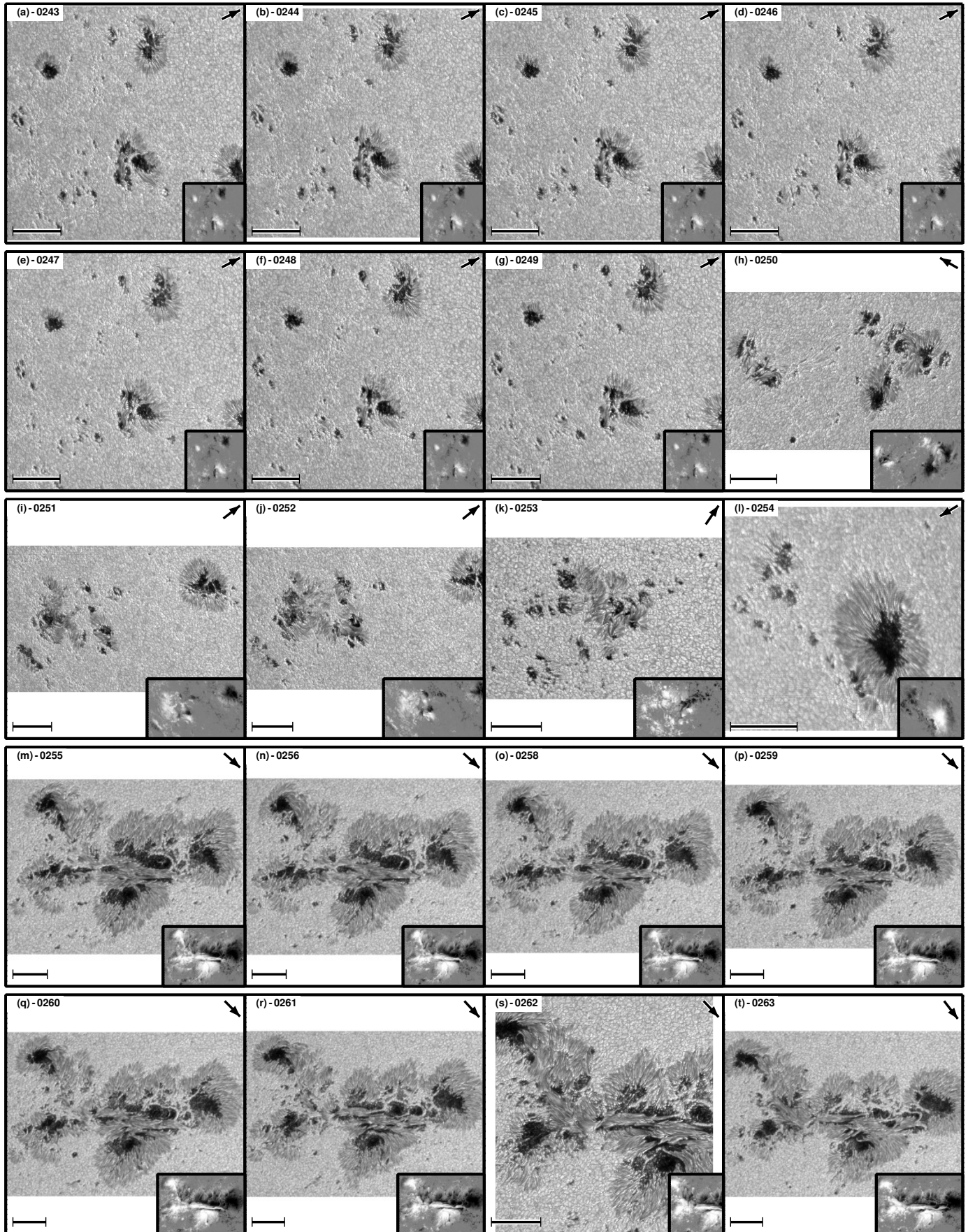


Fig. D.12. Fig. D.1. Continued.

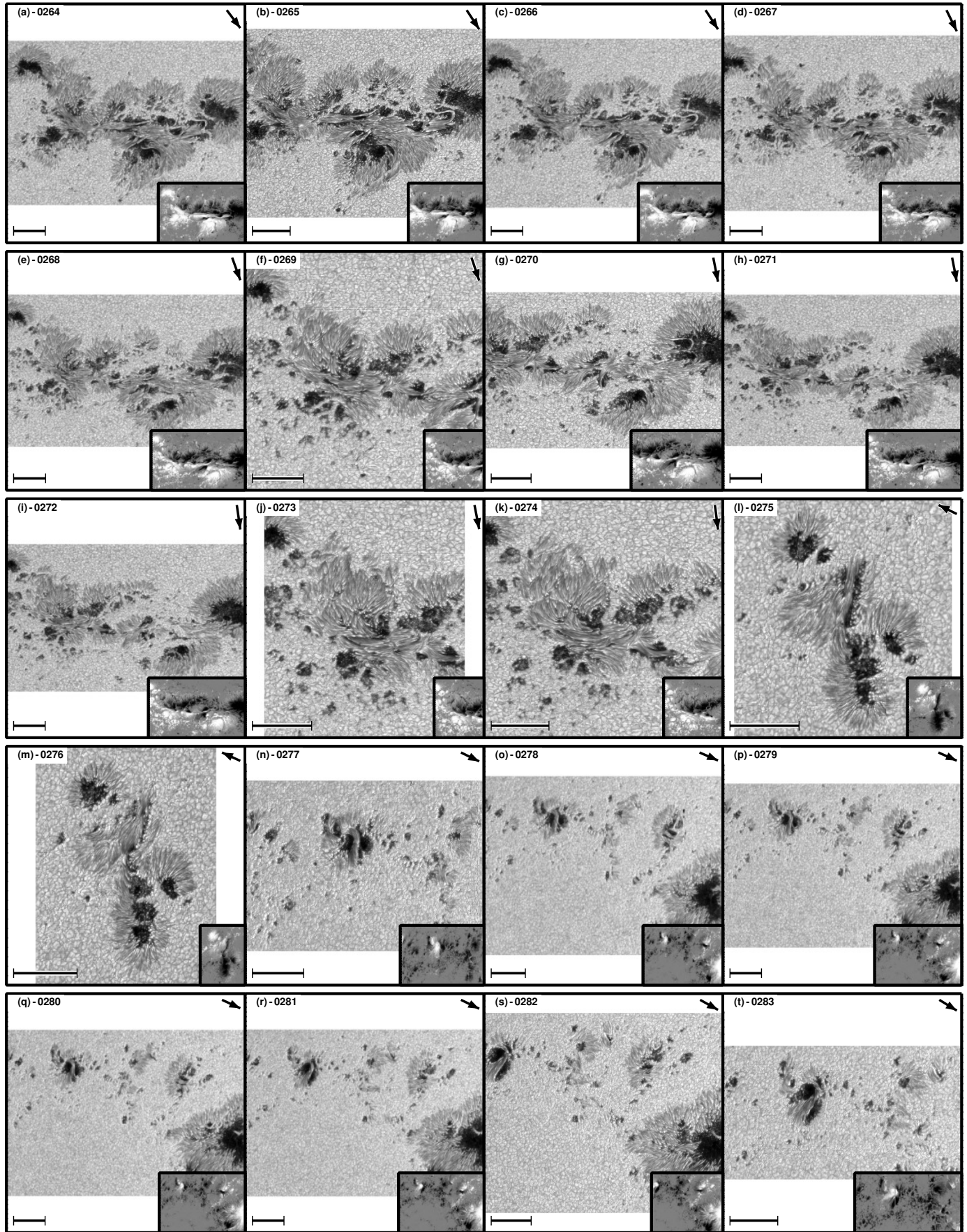


Fig. D.13. Fig. D.1. Continued.

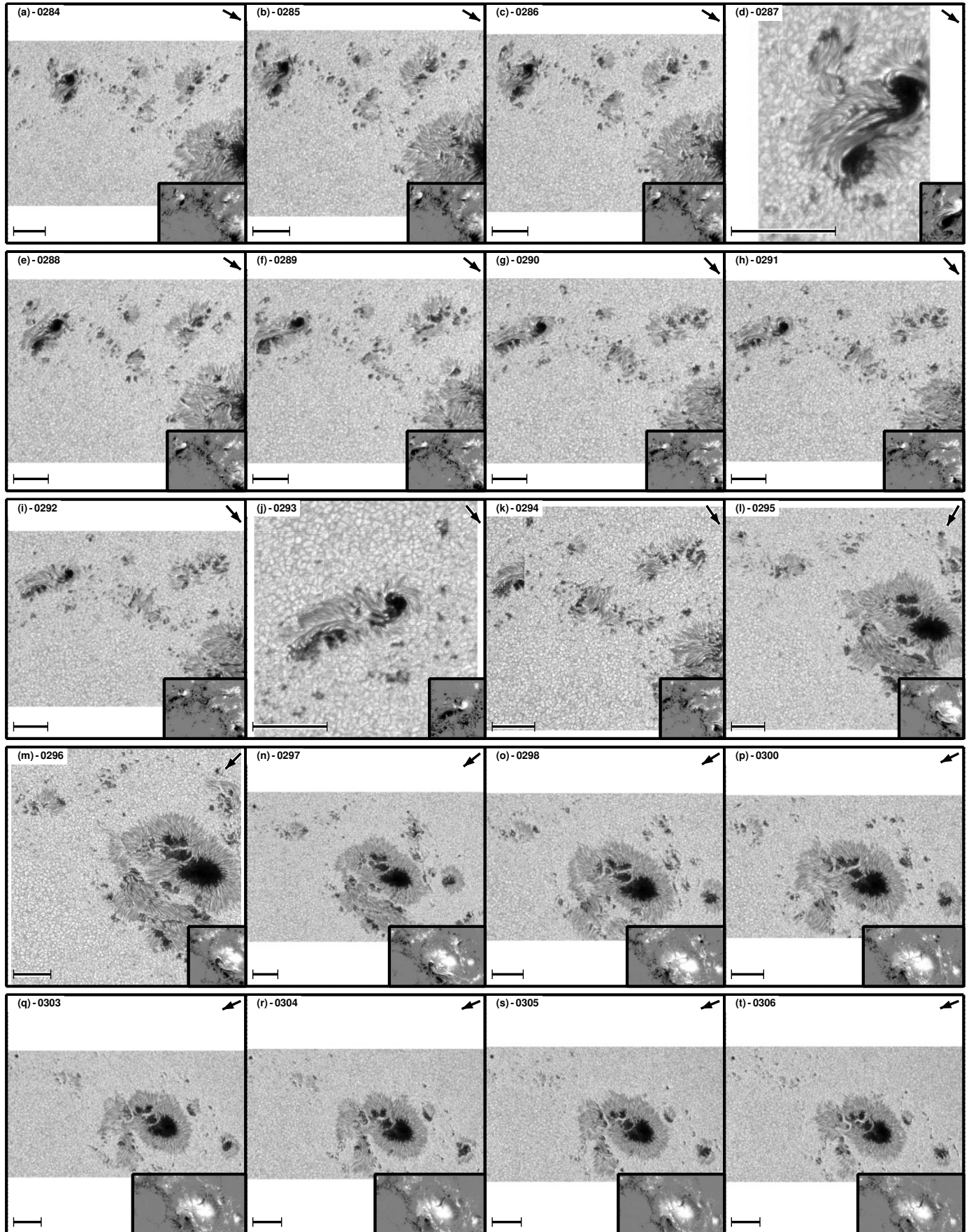


Fig. D.14. Fig. D.1. Continued.

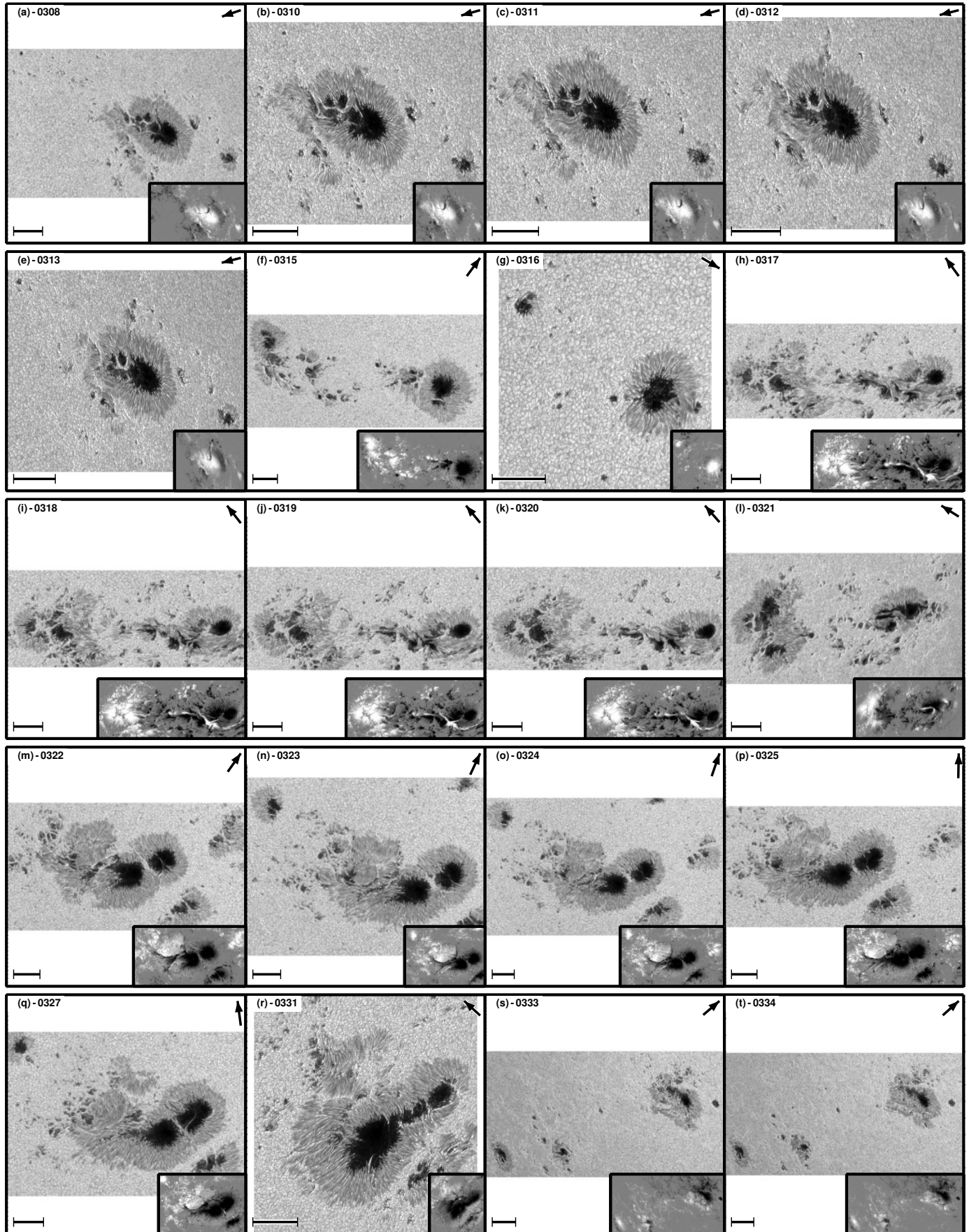


Fig. D.15. Fig. D.1. Continued.

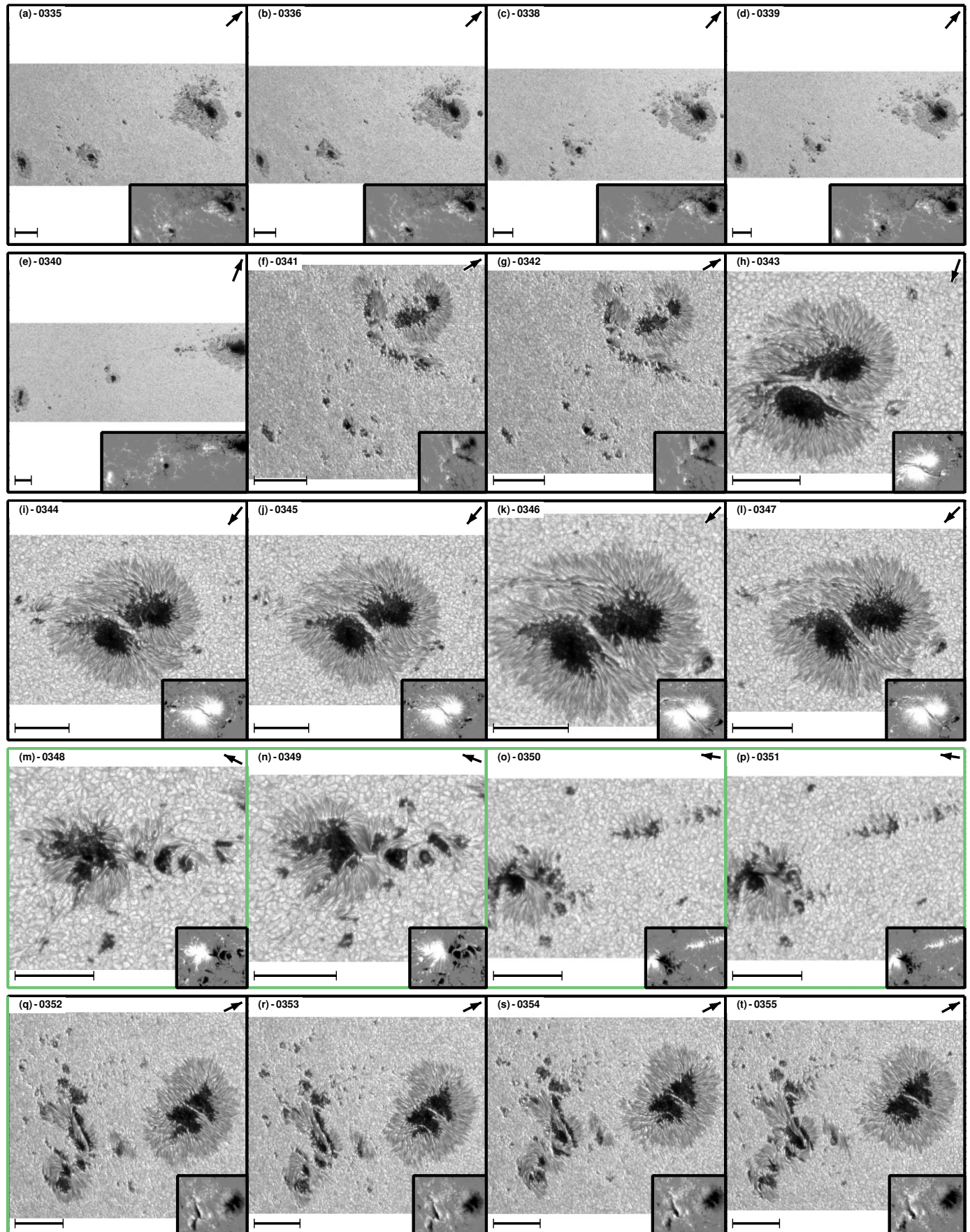


Fig. D.16. Fig. D.1. Continued.

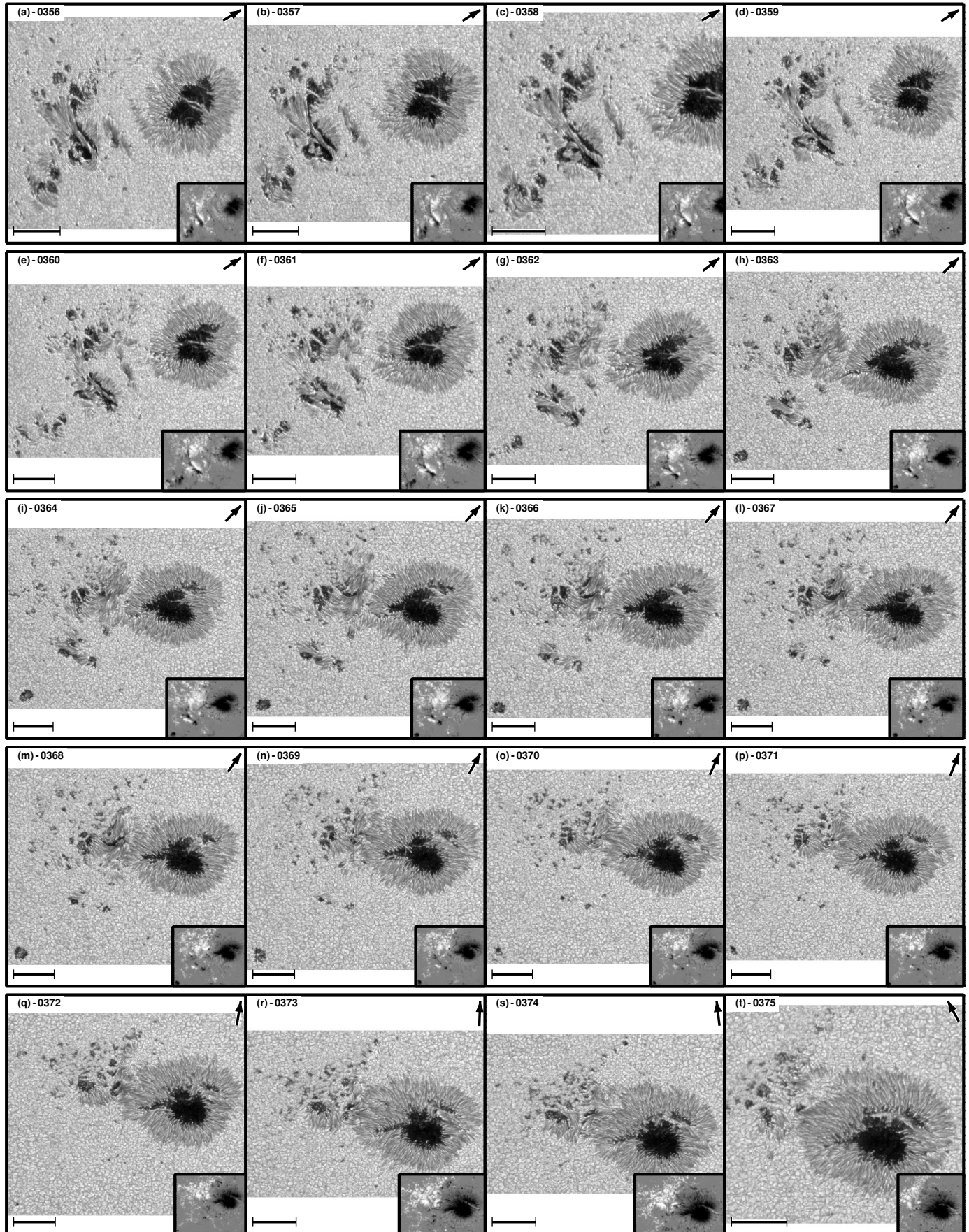


Fig. D.17. Fig. D.1. Continued.

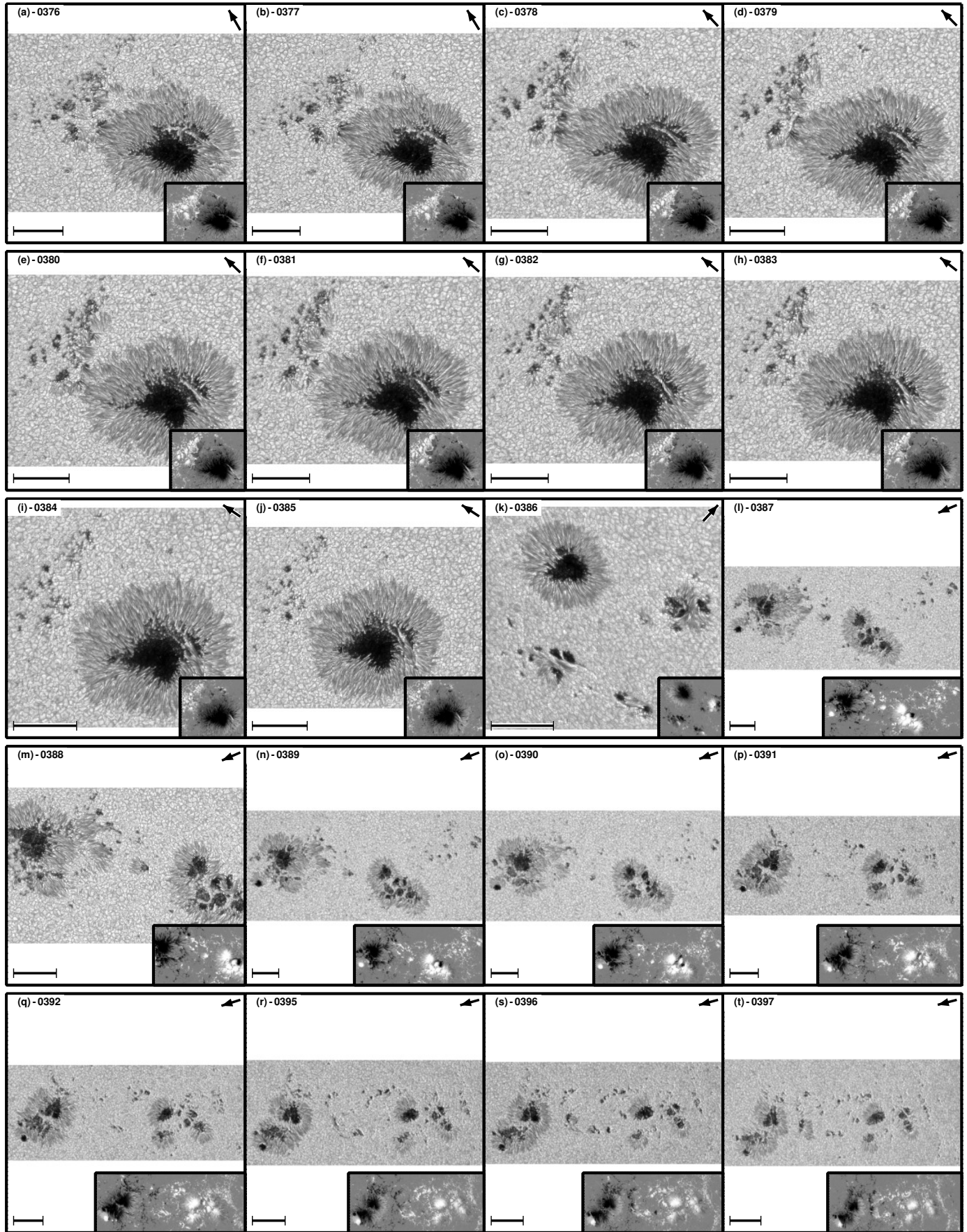


Fig. D.18. Fig. D.1. Continued.

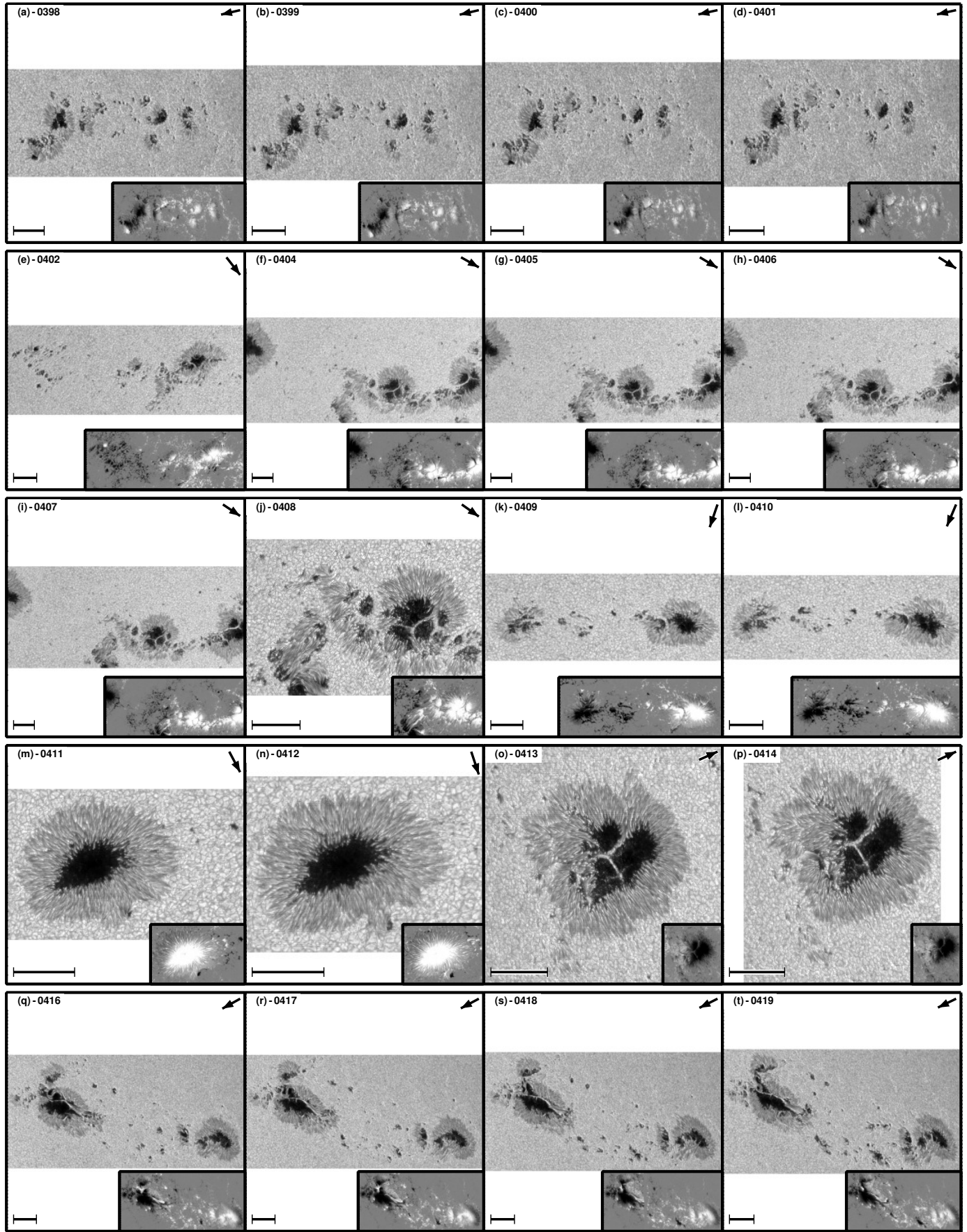


Fig. D.19. Fig. D.1. Continued.

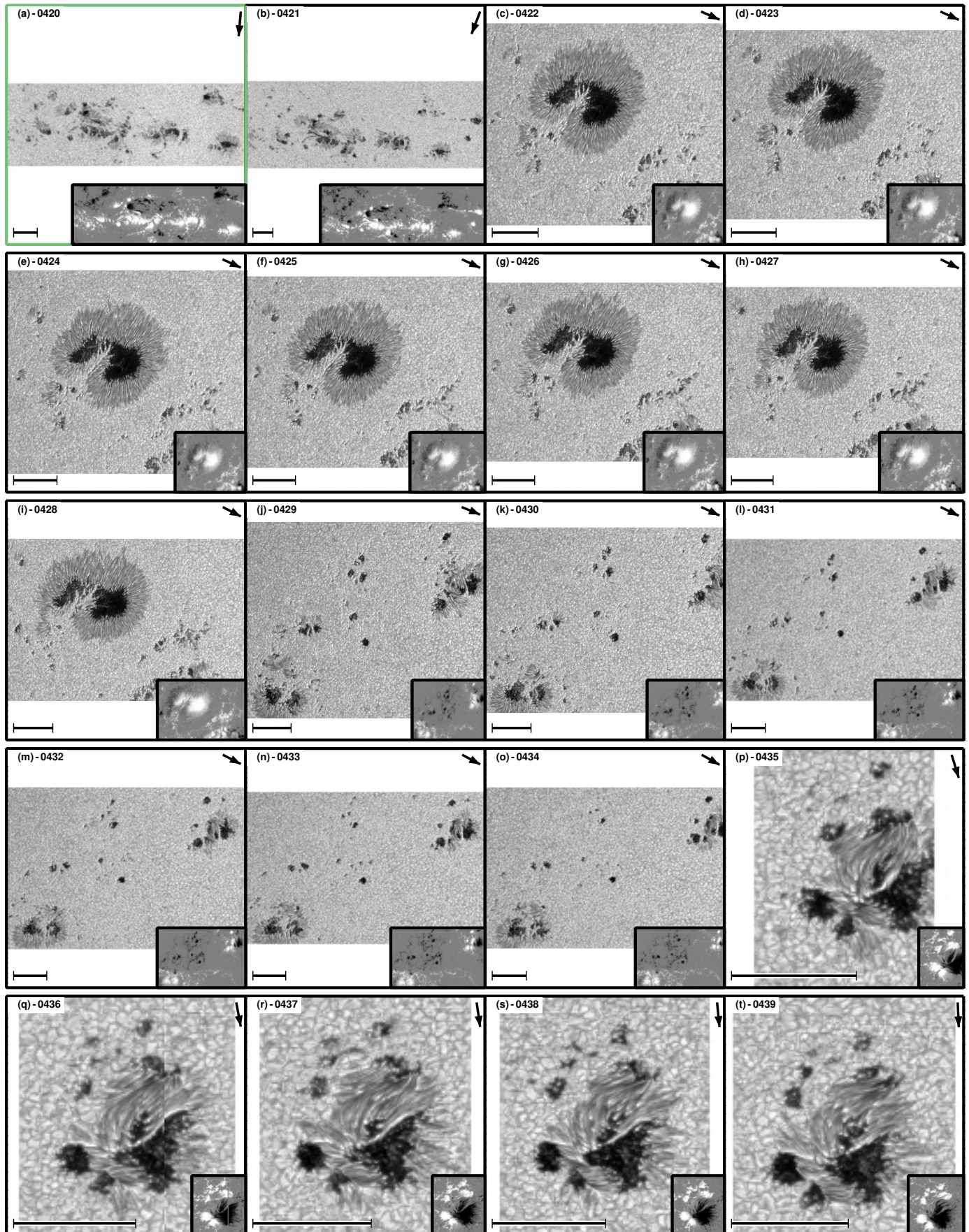


Fig. D.20. Fig. D.1. Continued.

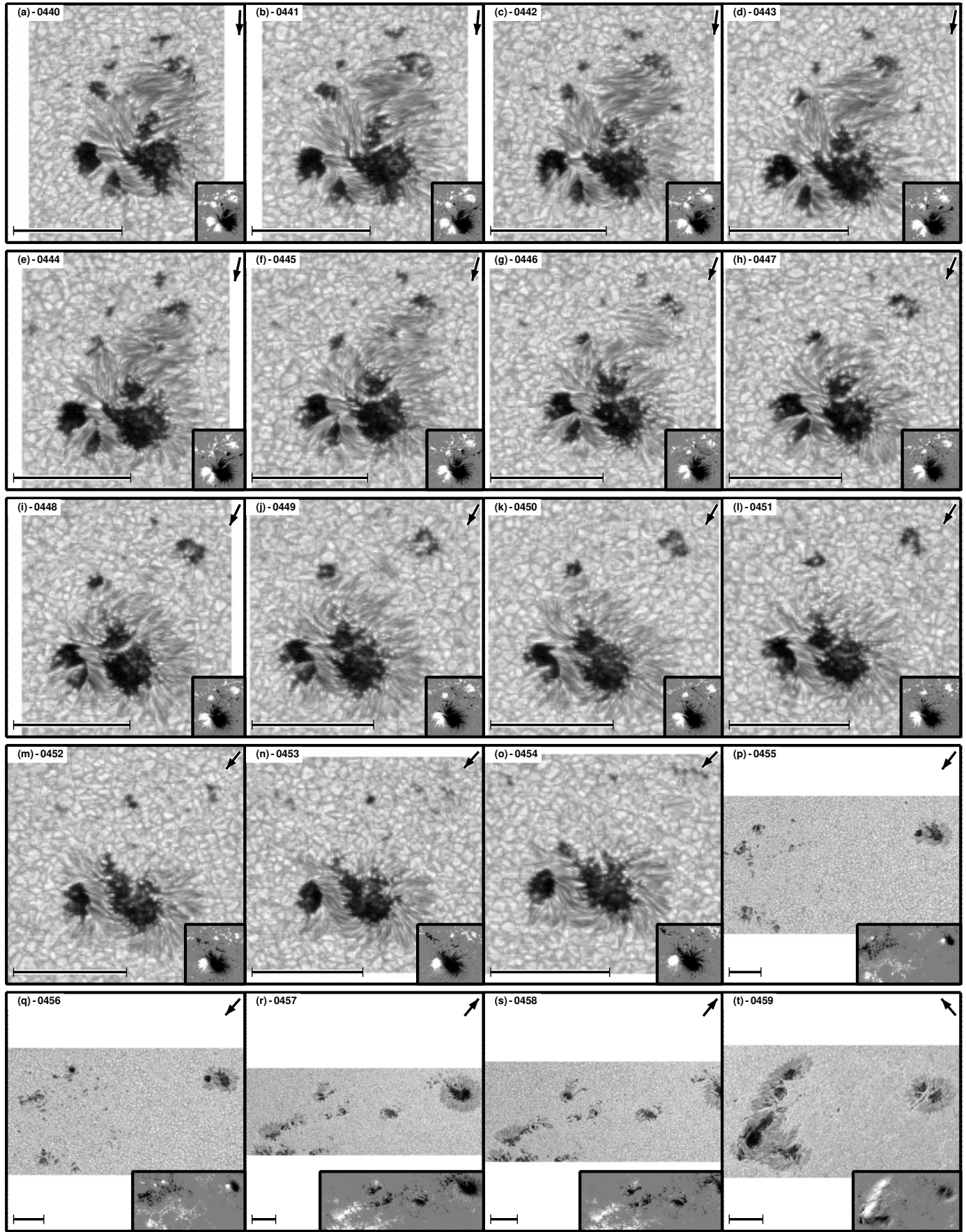


Fig. D.21. Fig. D.1. Continued.

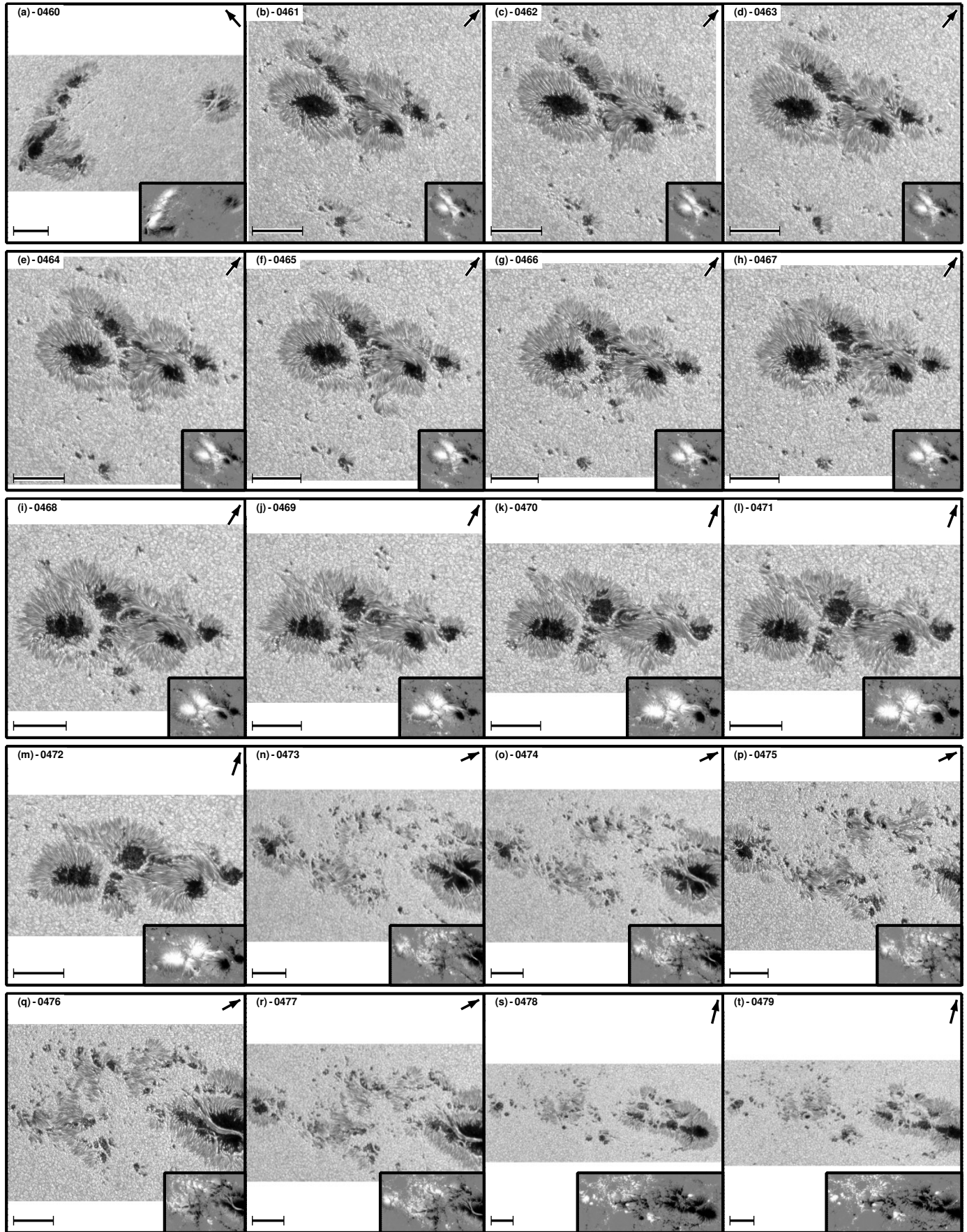


Fig. D.22. Fig. D.1. Continued.

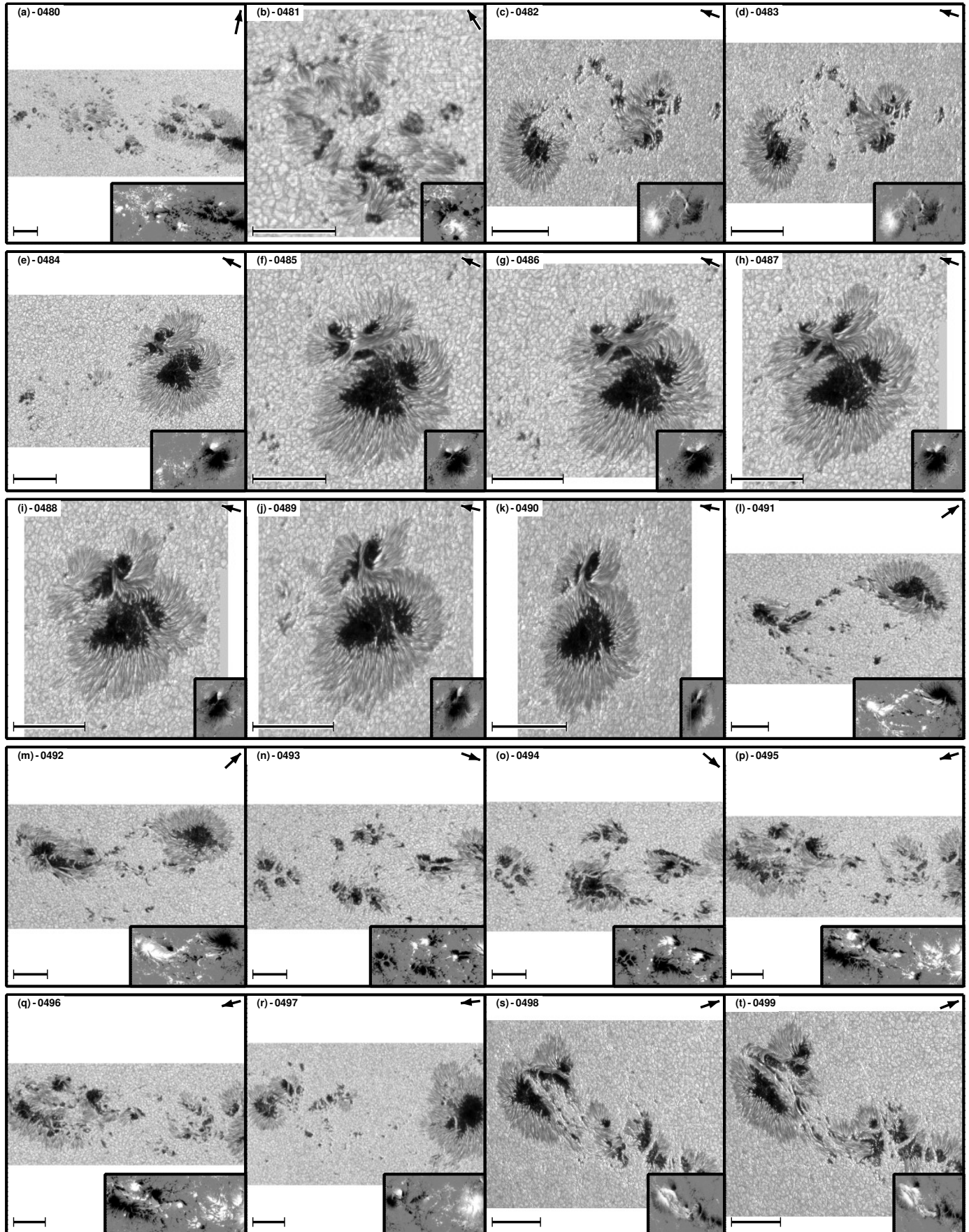


Fig. D.23. Fig. D.1. Continued.

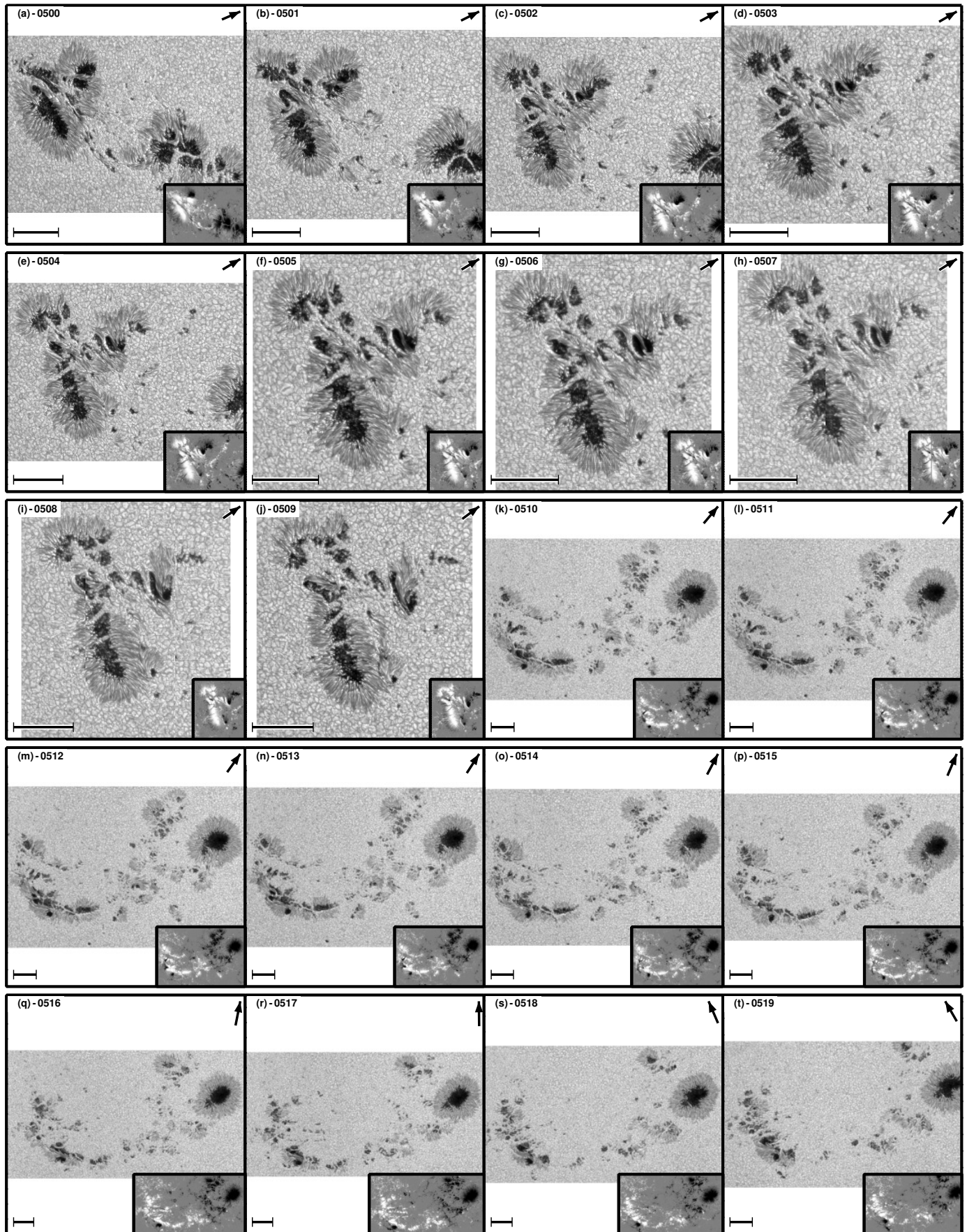


Fig. D.24. – [D.1](#). Continued.

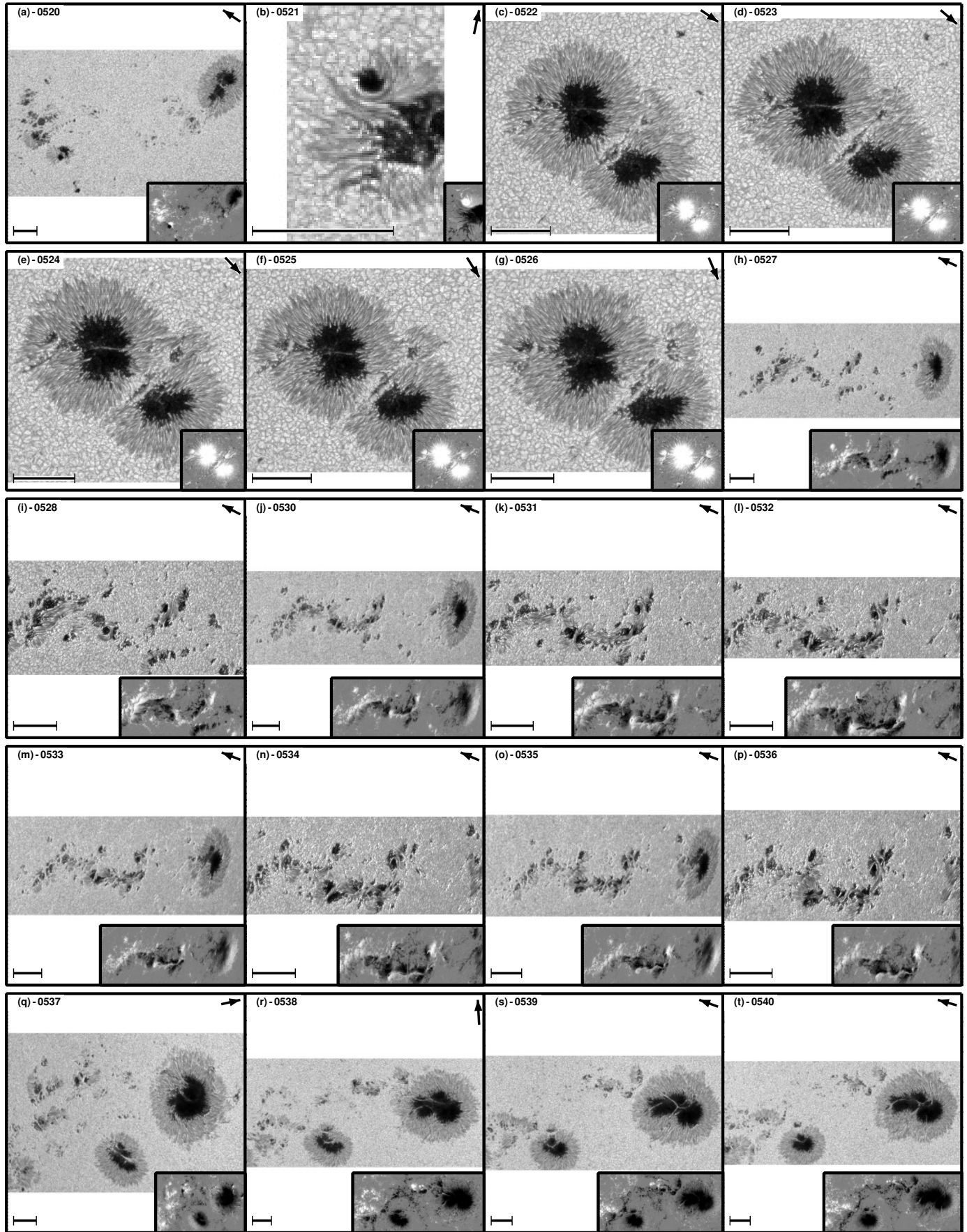


Fig. D.25. – D.1. Continued.

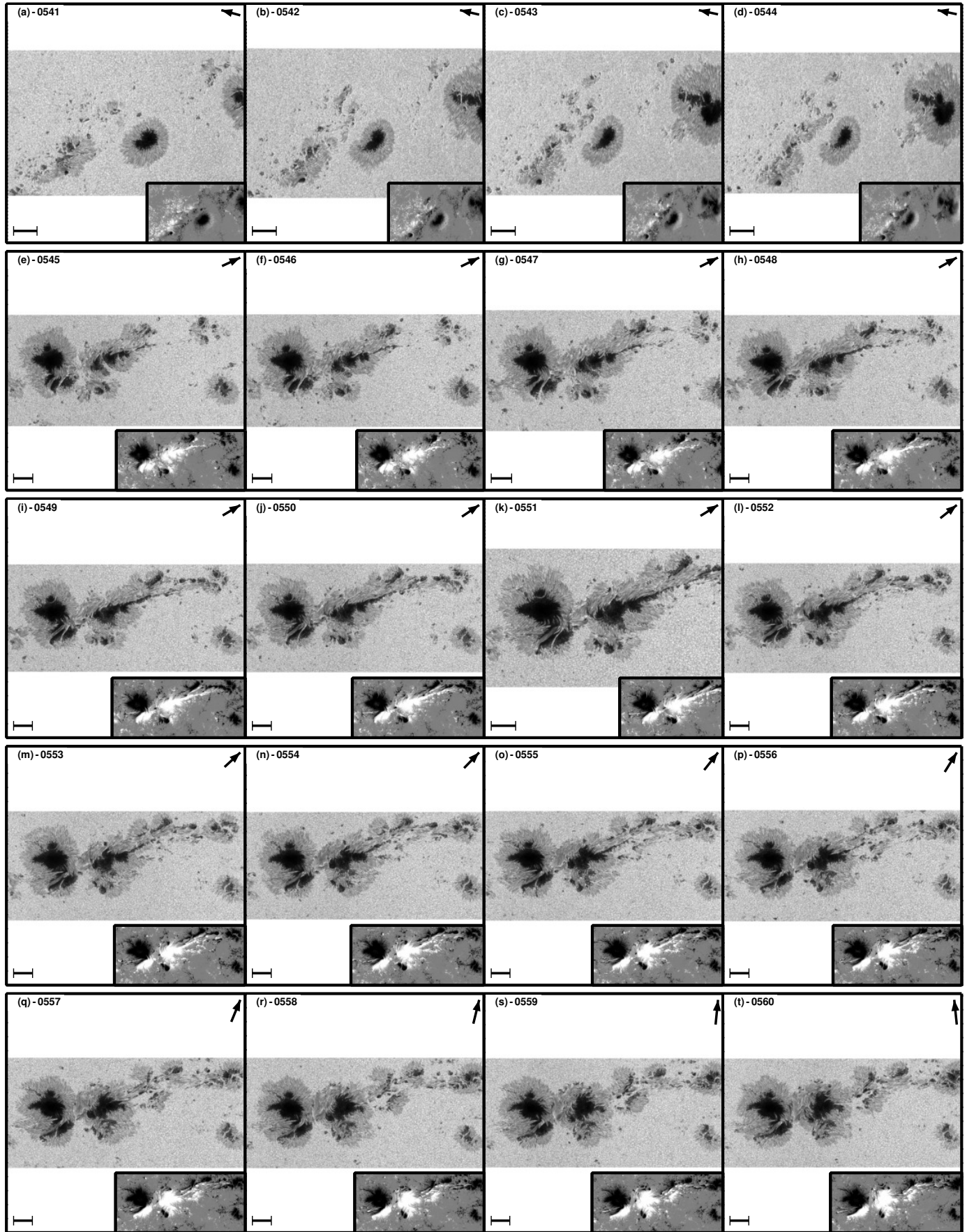


Fig. D.26. – [D.1](#). Continued.

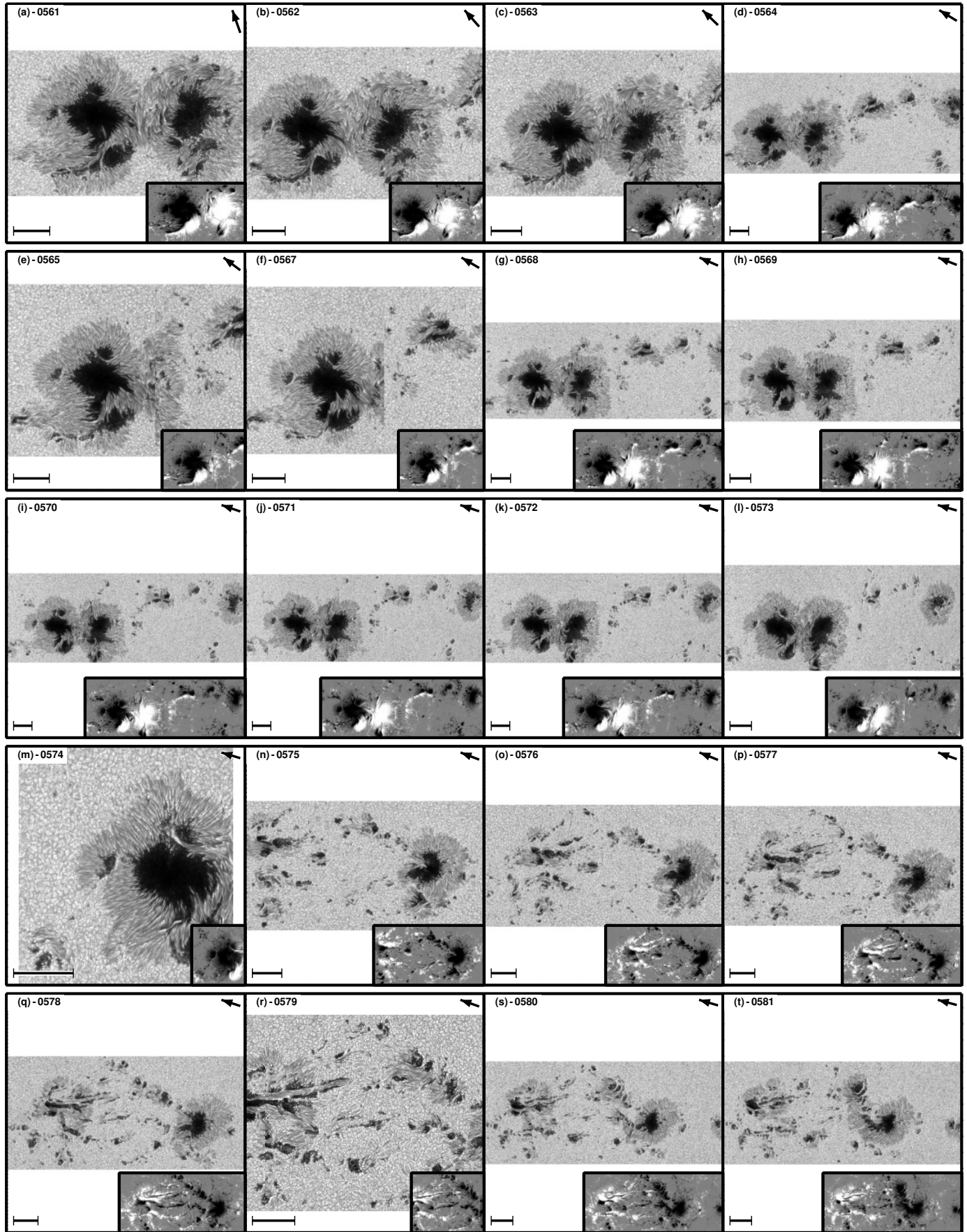


Fig. D.27. – D.1. Continued.

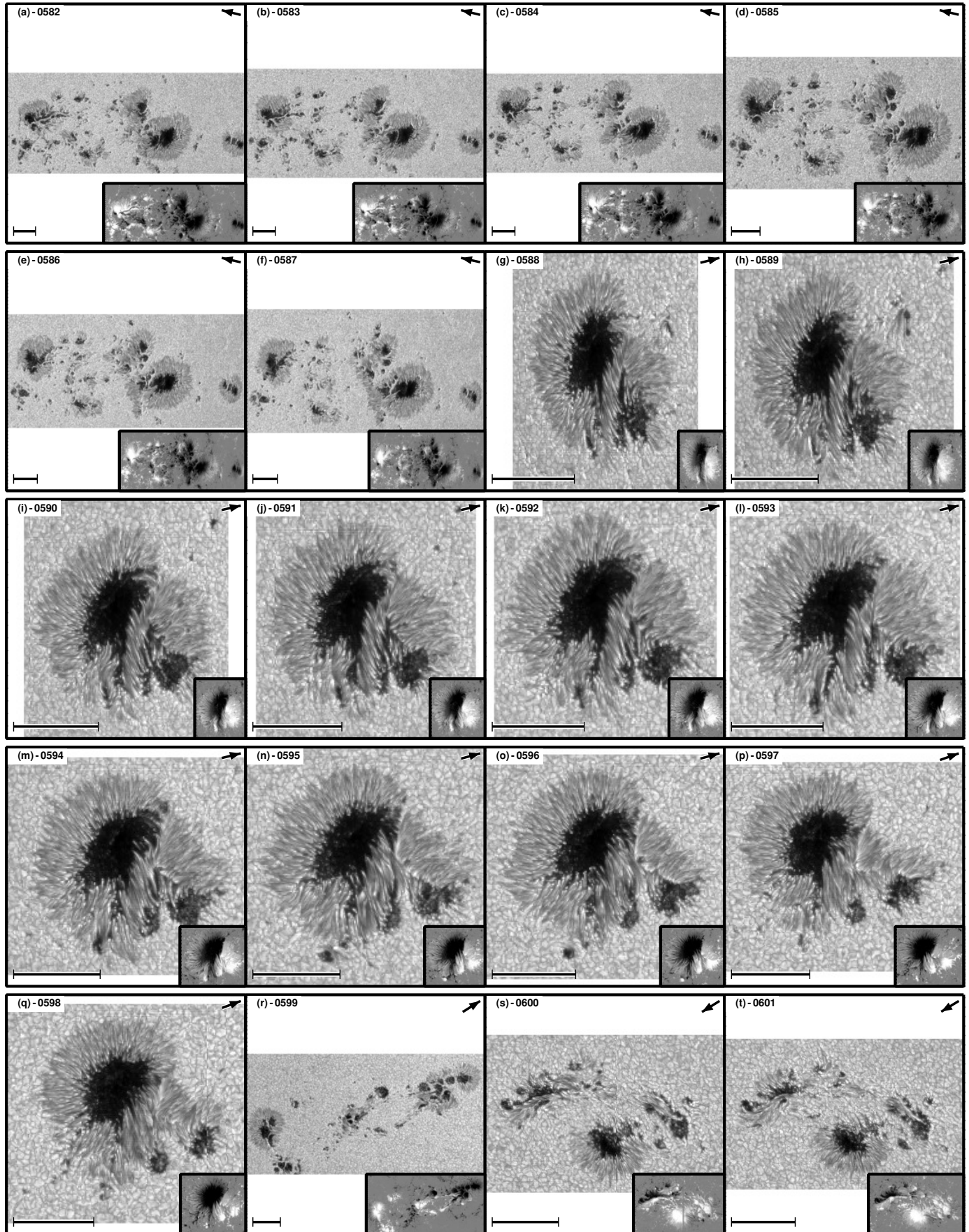


Fig. D.28. – D.1. Continued.

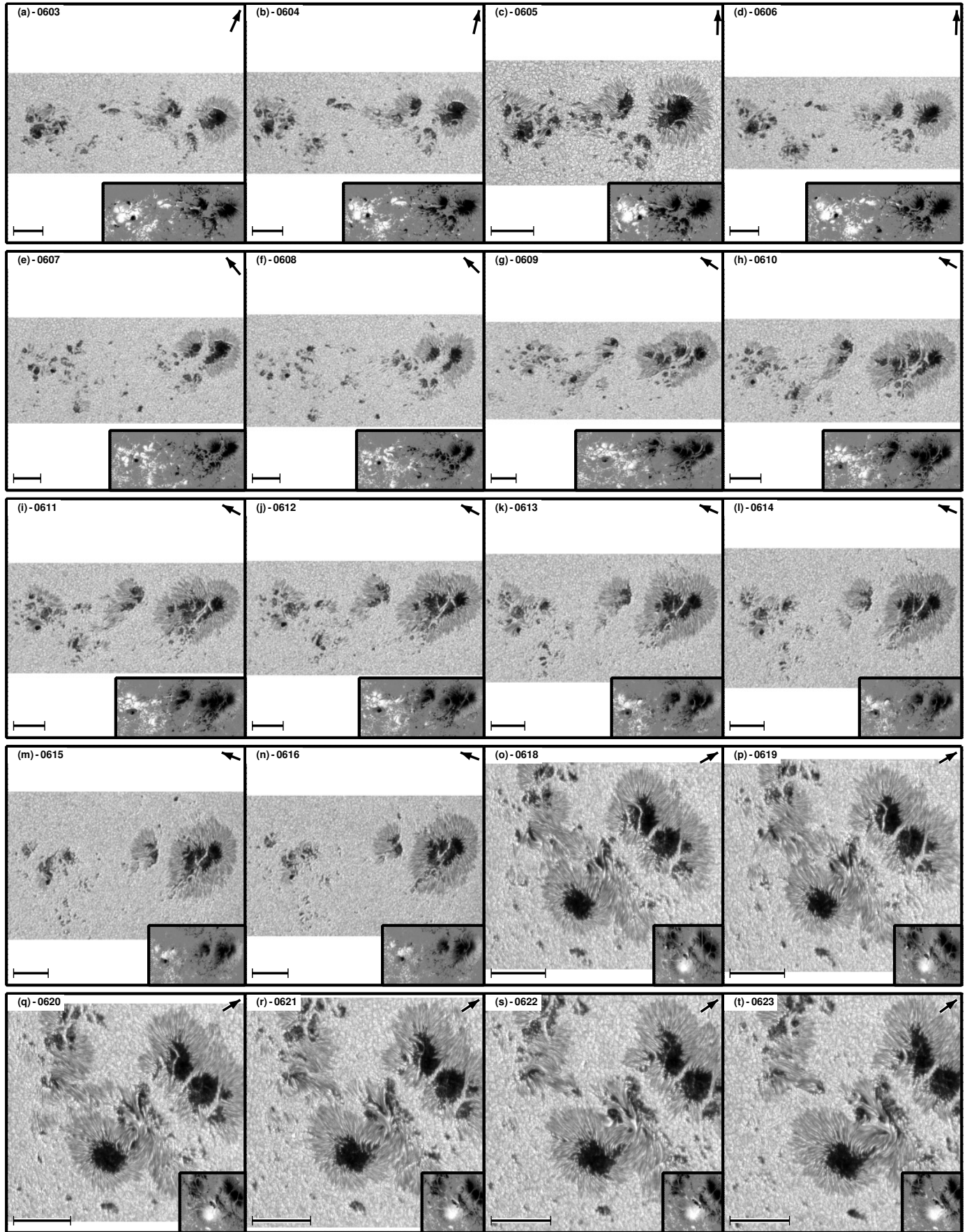


Fig. D.29. – [D.1](#). Continued.

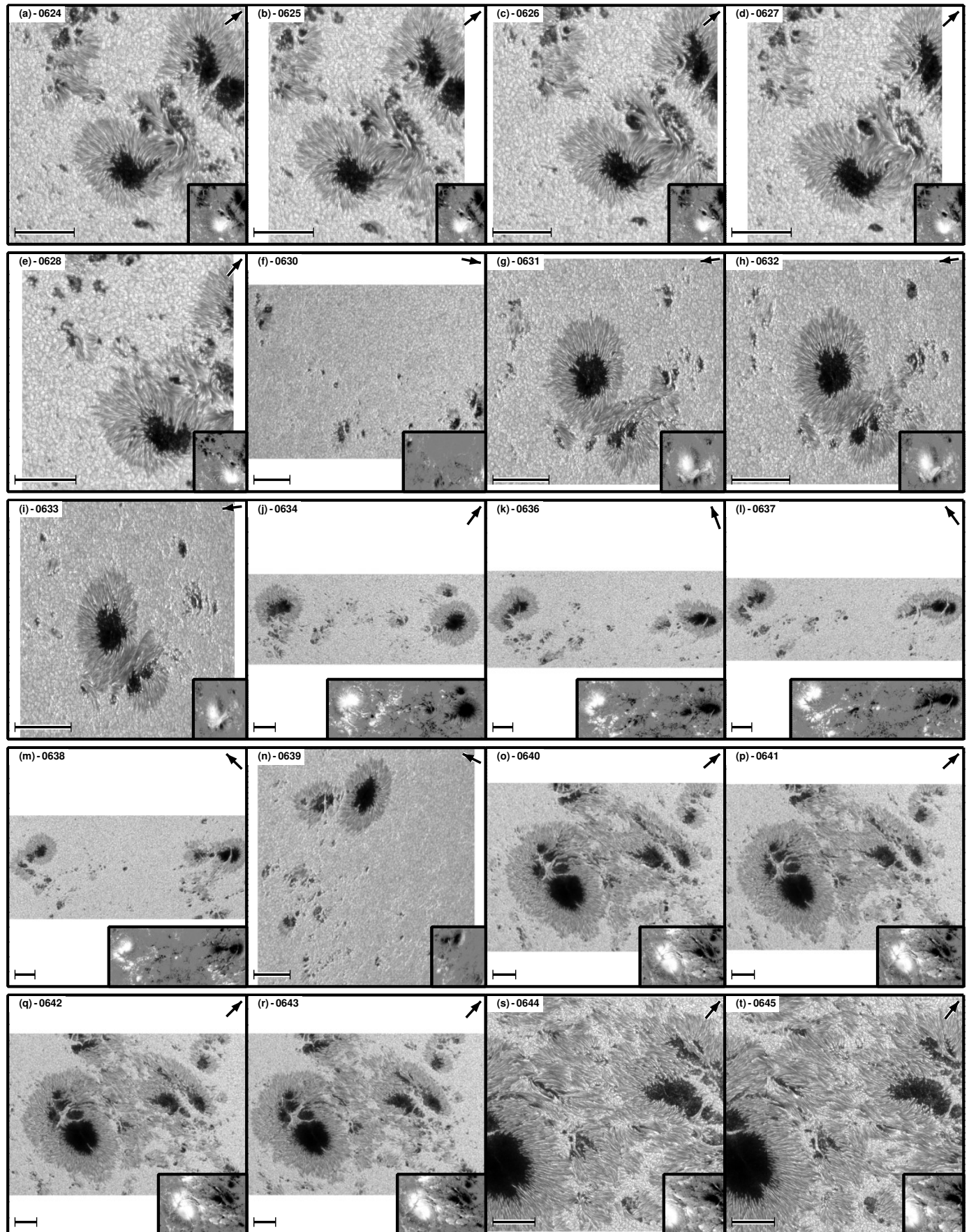


Fig. D.30. – **D.1.** Continued.

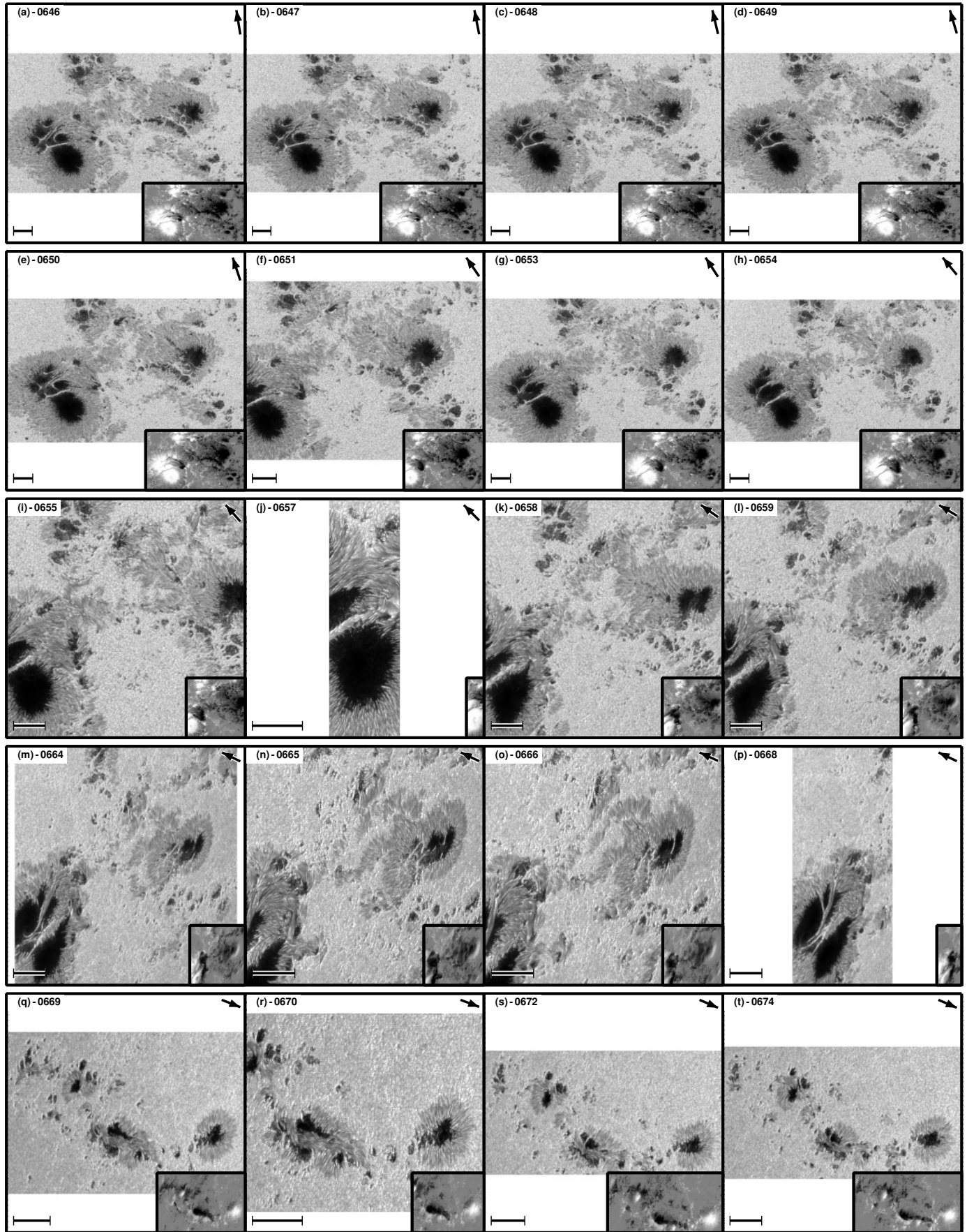


Fig. D.31. – D.1. Continued.

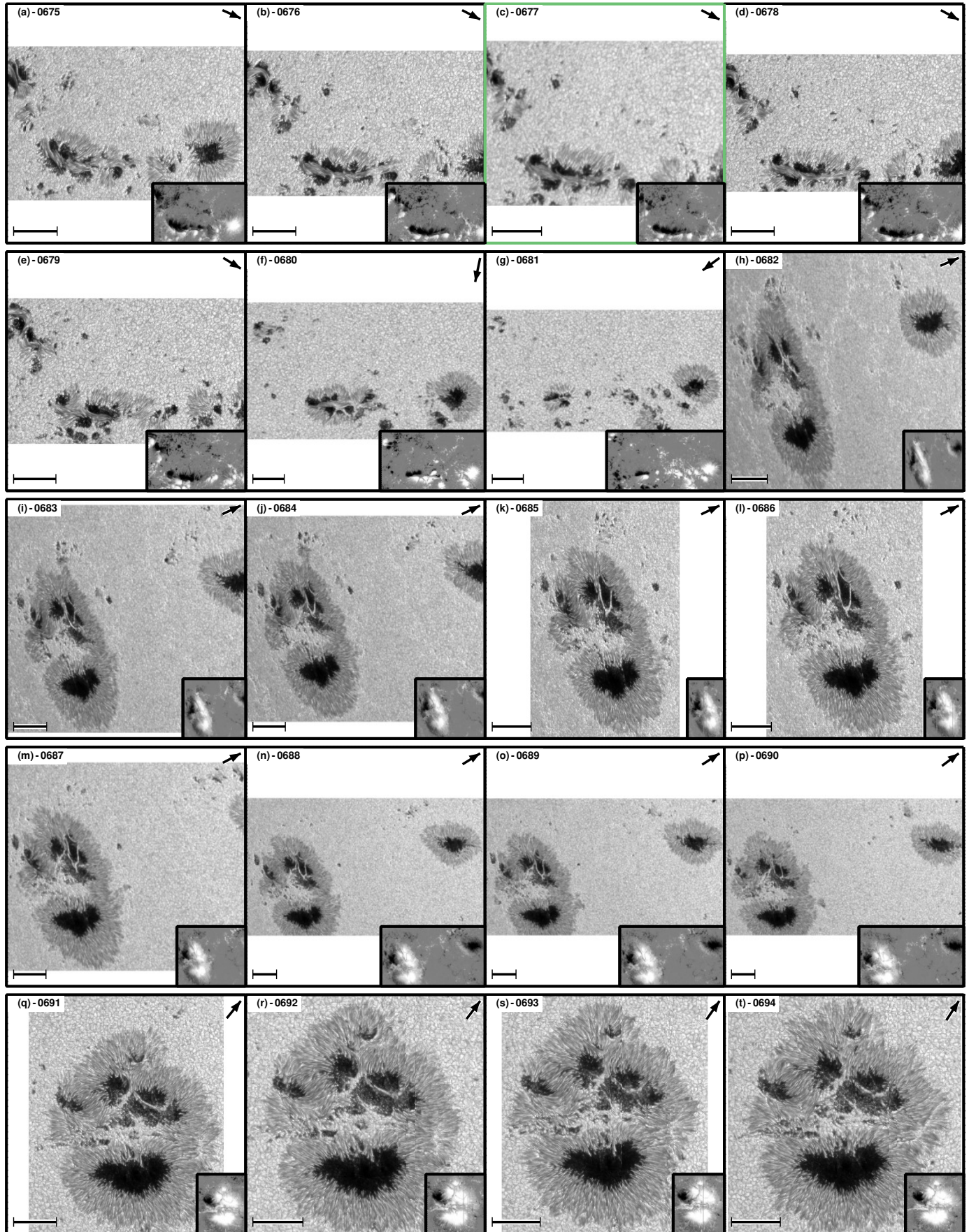


Fig. D.32. – [D.1](#). Continued.

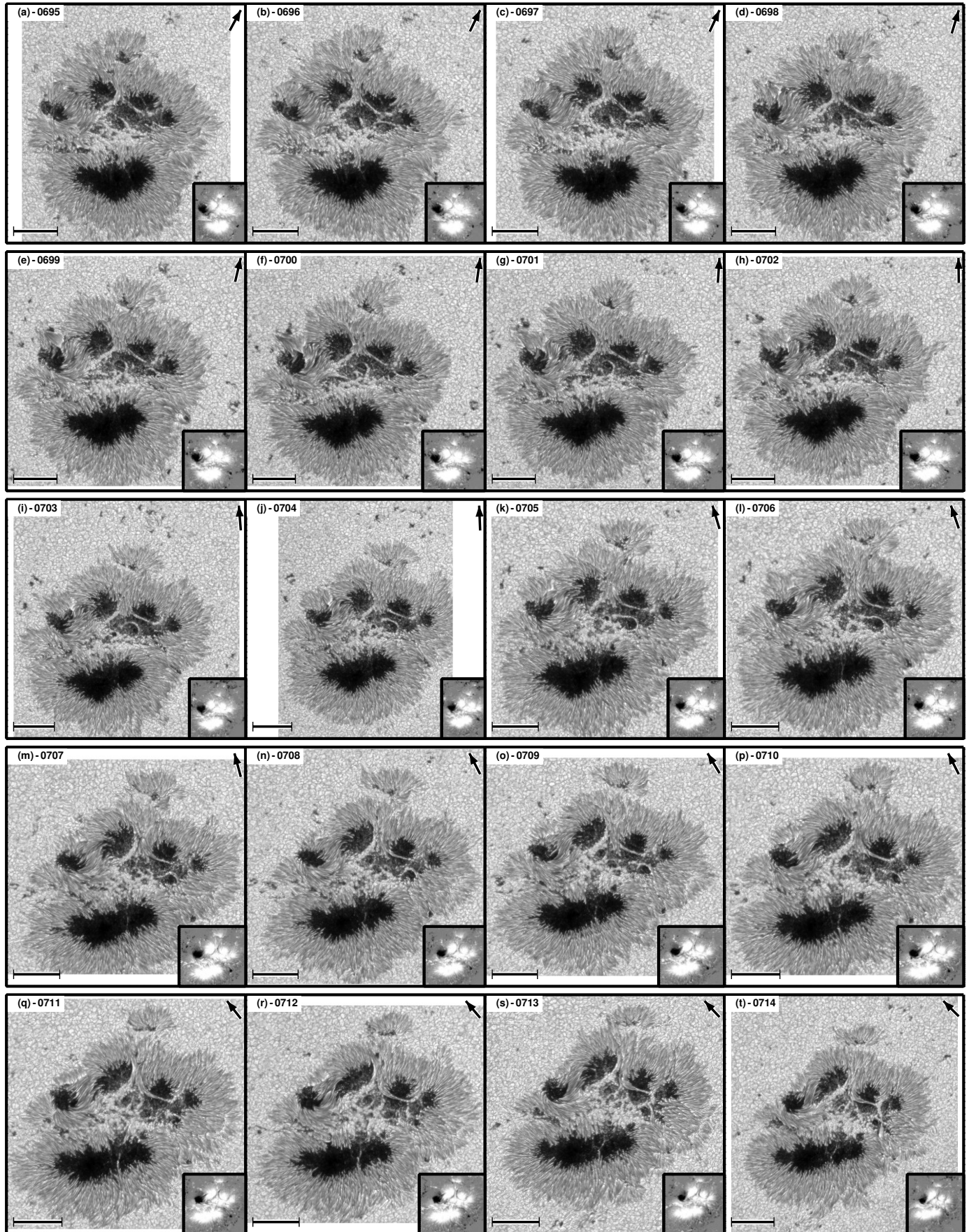


Fig. D.33. – [D.1](#). Continued.

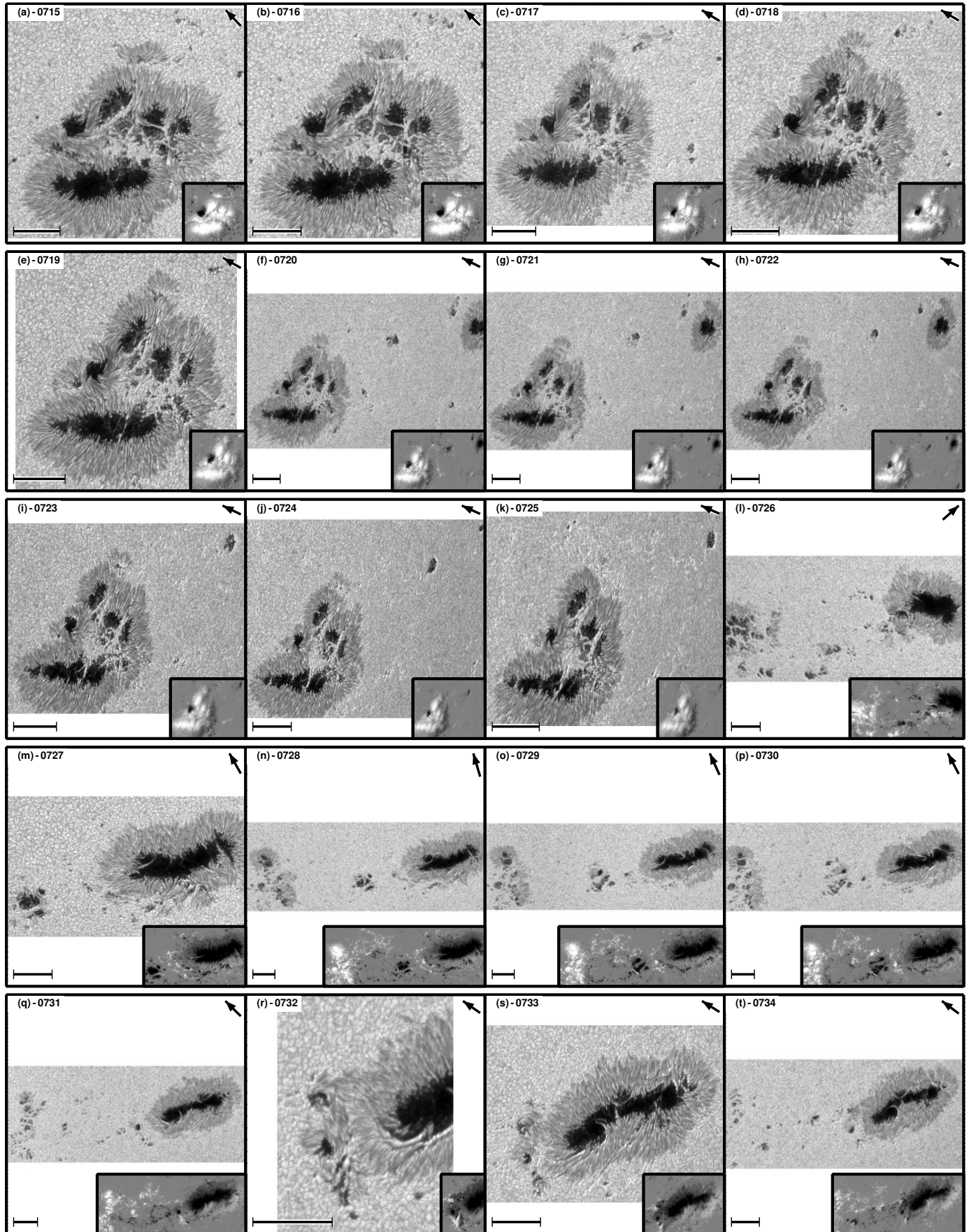


Fig. D.34. – [D.1](#). Continued.

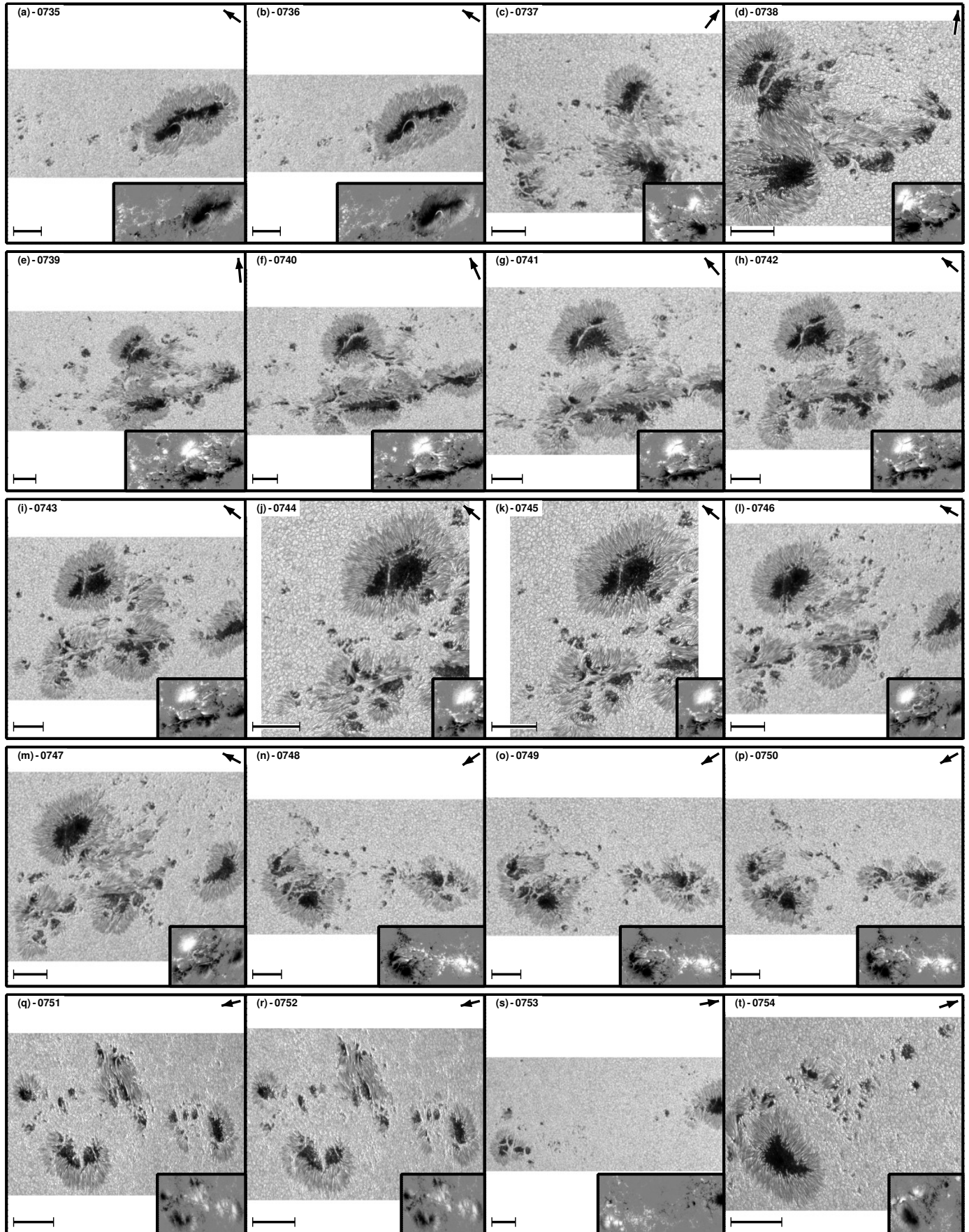


Fig. D.35. – [D.1](#). Continued.

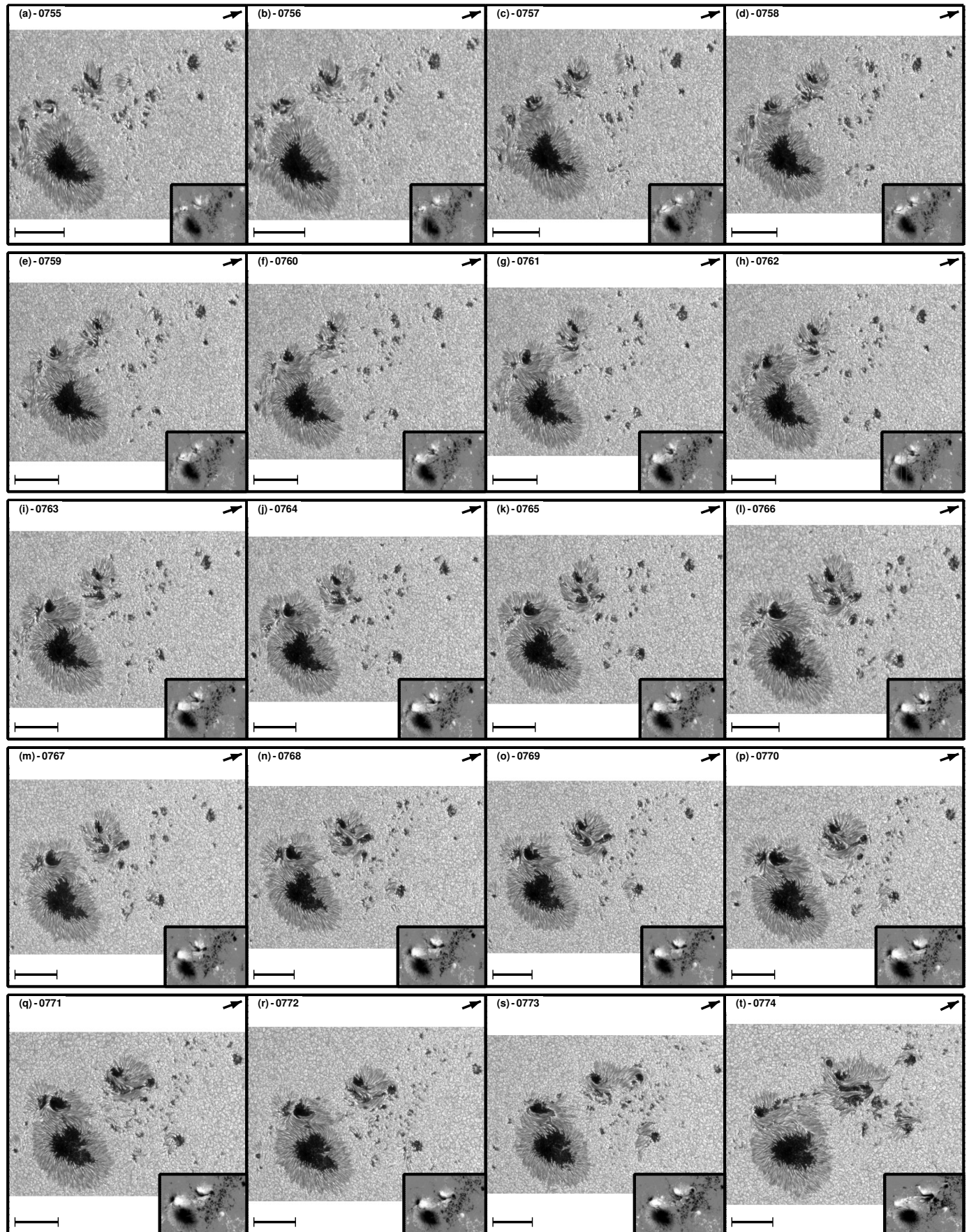


Fig. D.36. – [D.1](#). Continued.

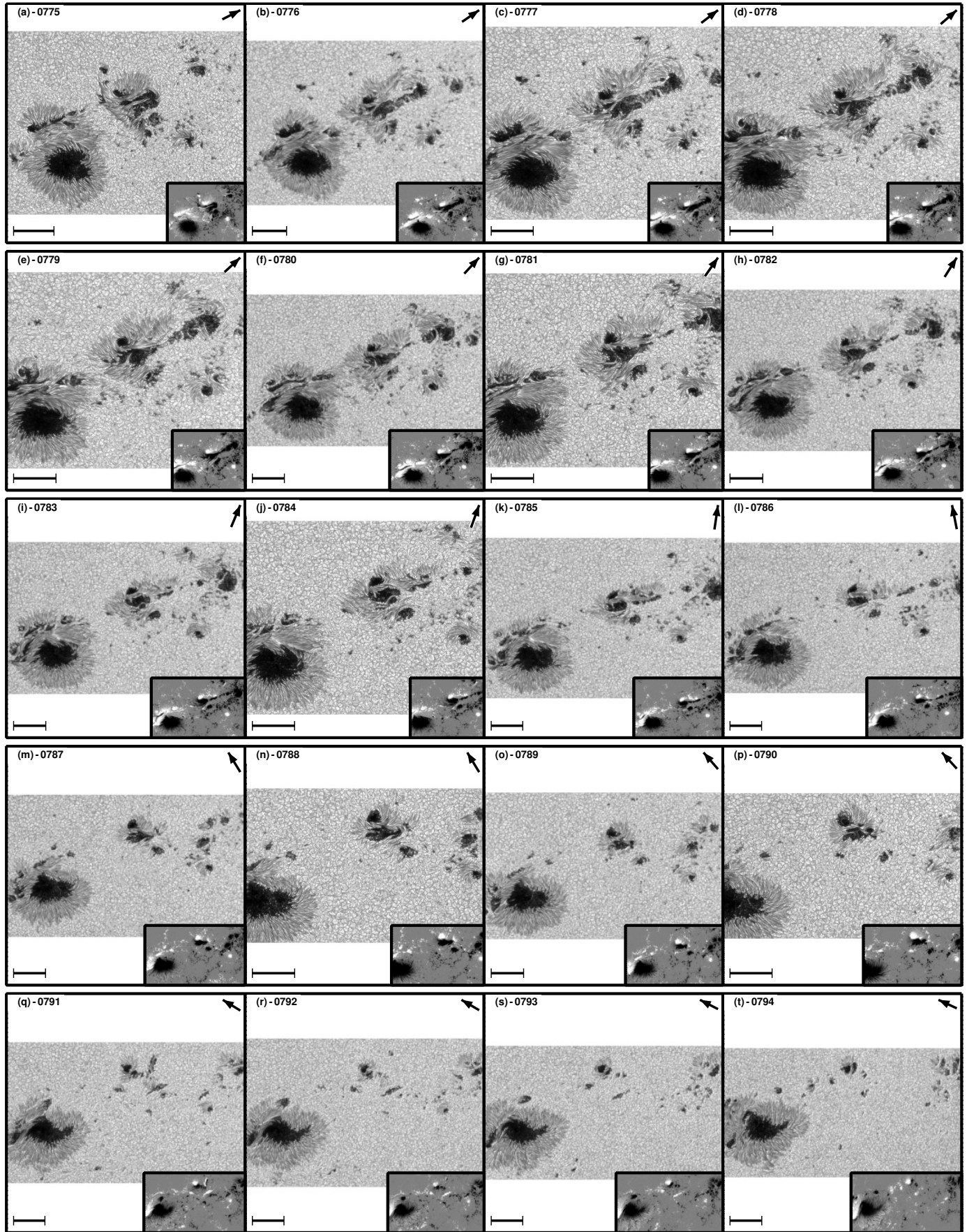


Fig. D.37. – D.1. Continued.

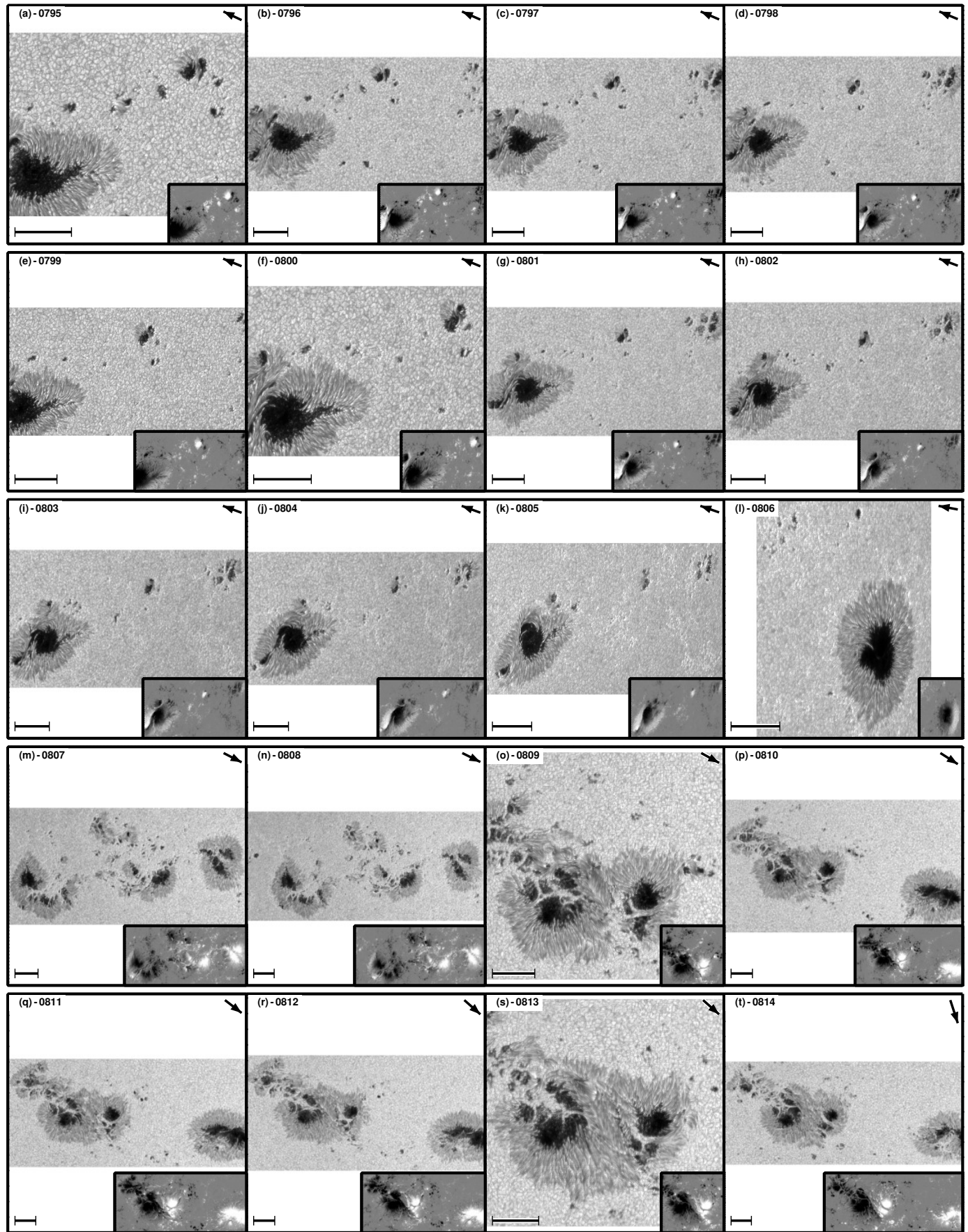


Fig. D.38. – [D.1](#). Continued.

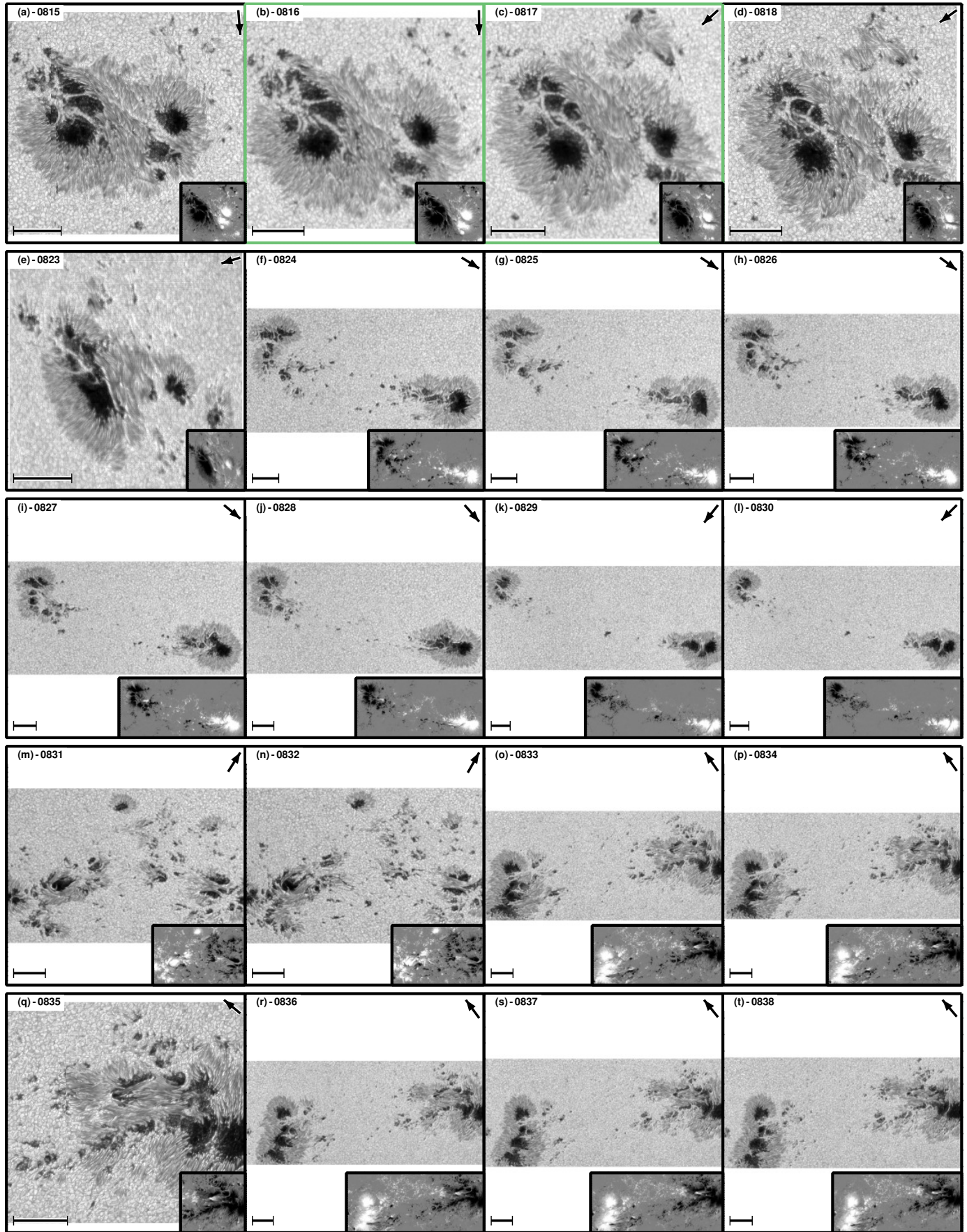


Fig. D.39. – [D.1](#). Continued.

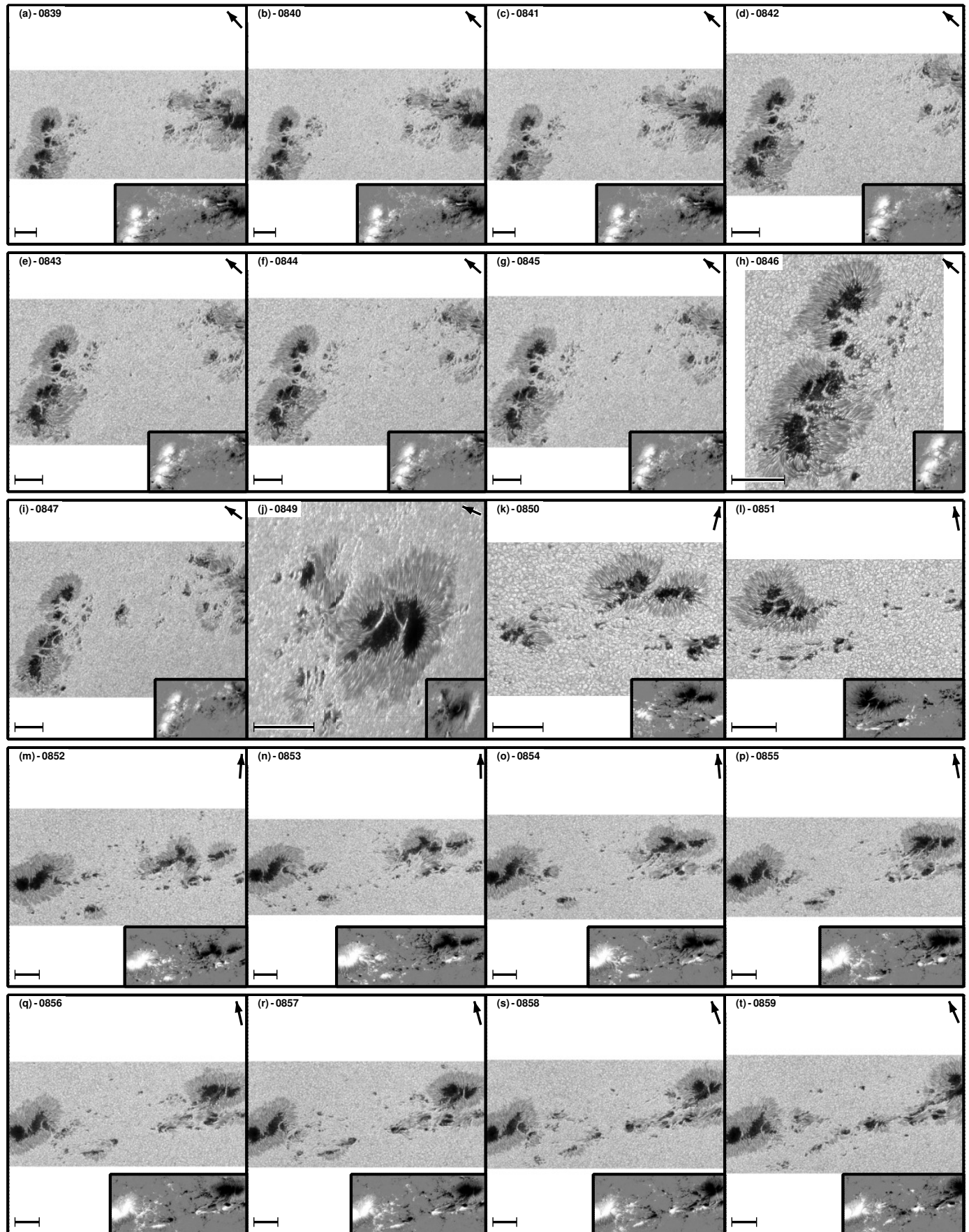


Fig. D.40. – [D.1](#). Continued.

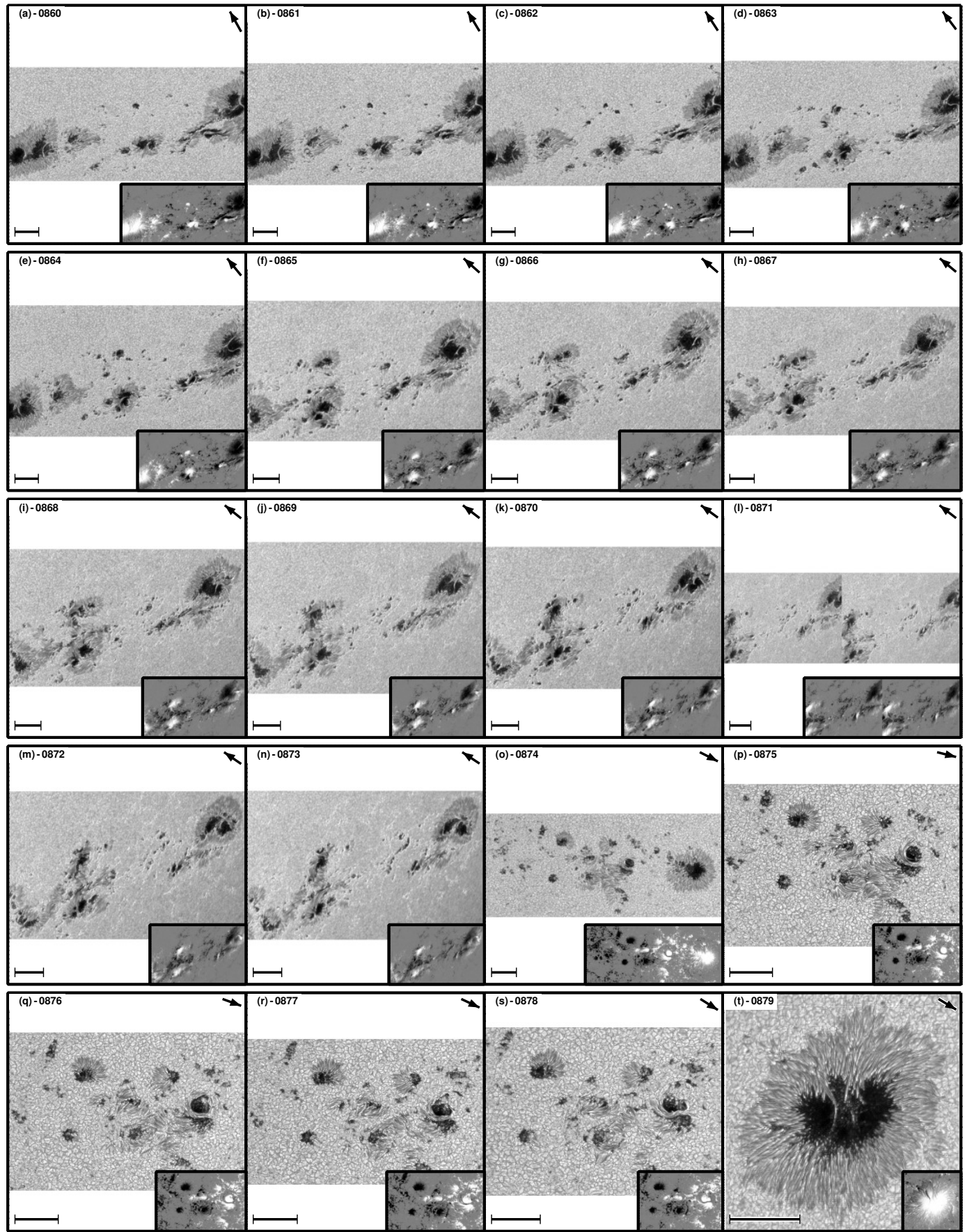


Fig. D.41. – [D.1](#). Continued.

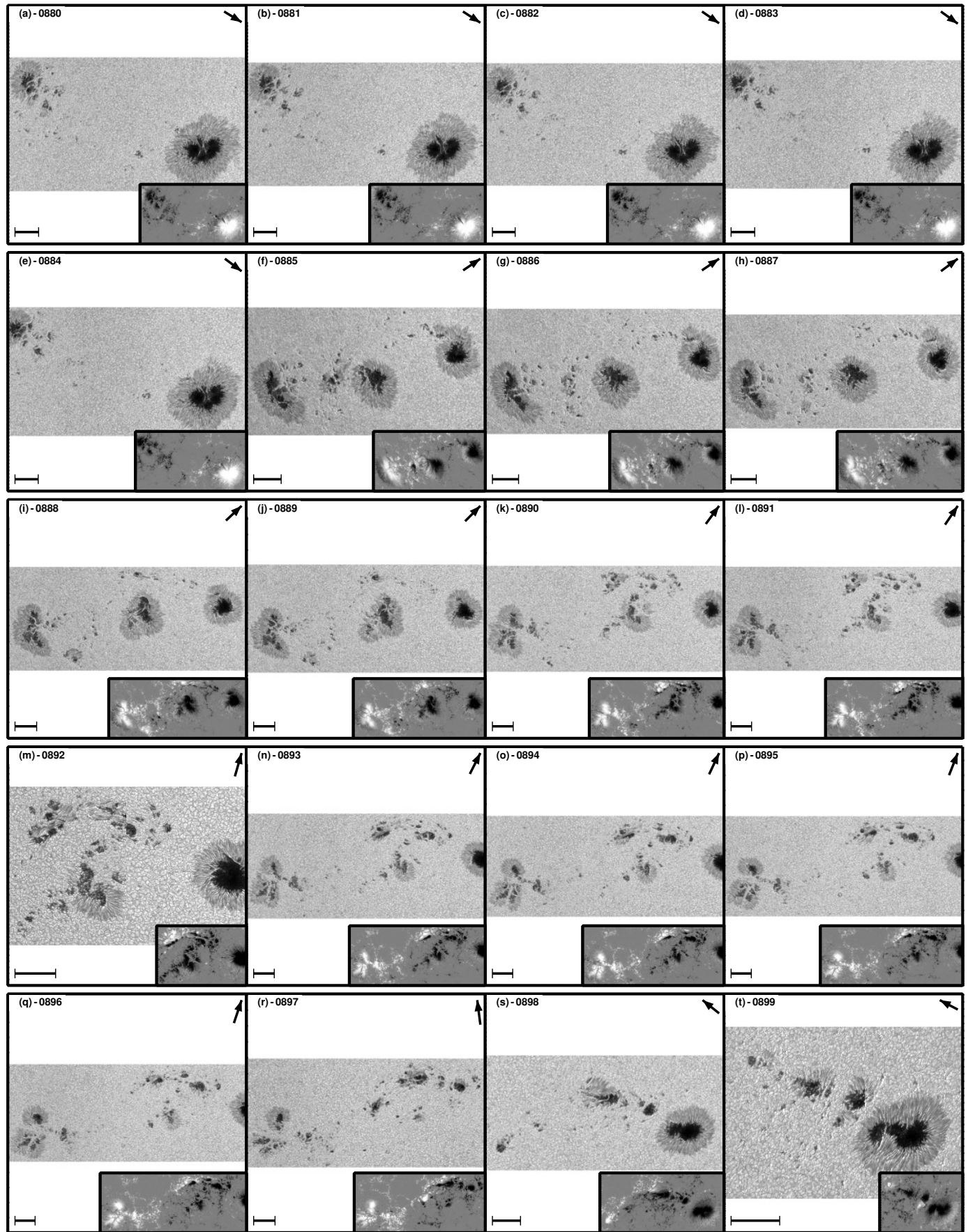


Fig. D.42. – [D.1](#). Continued.

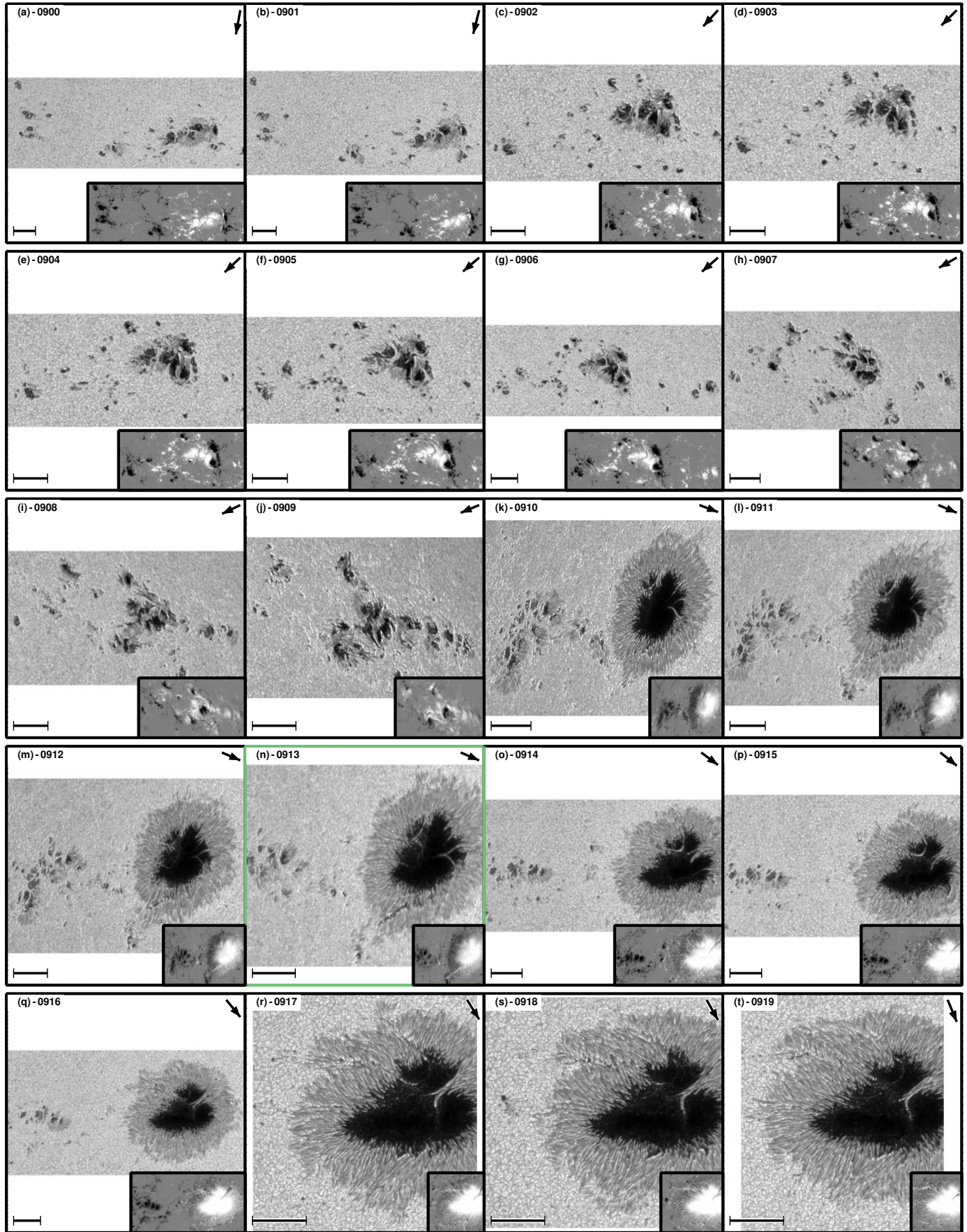


Fig. D.43. – [D.1](#). Continued.

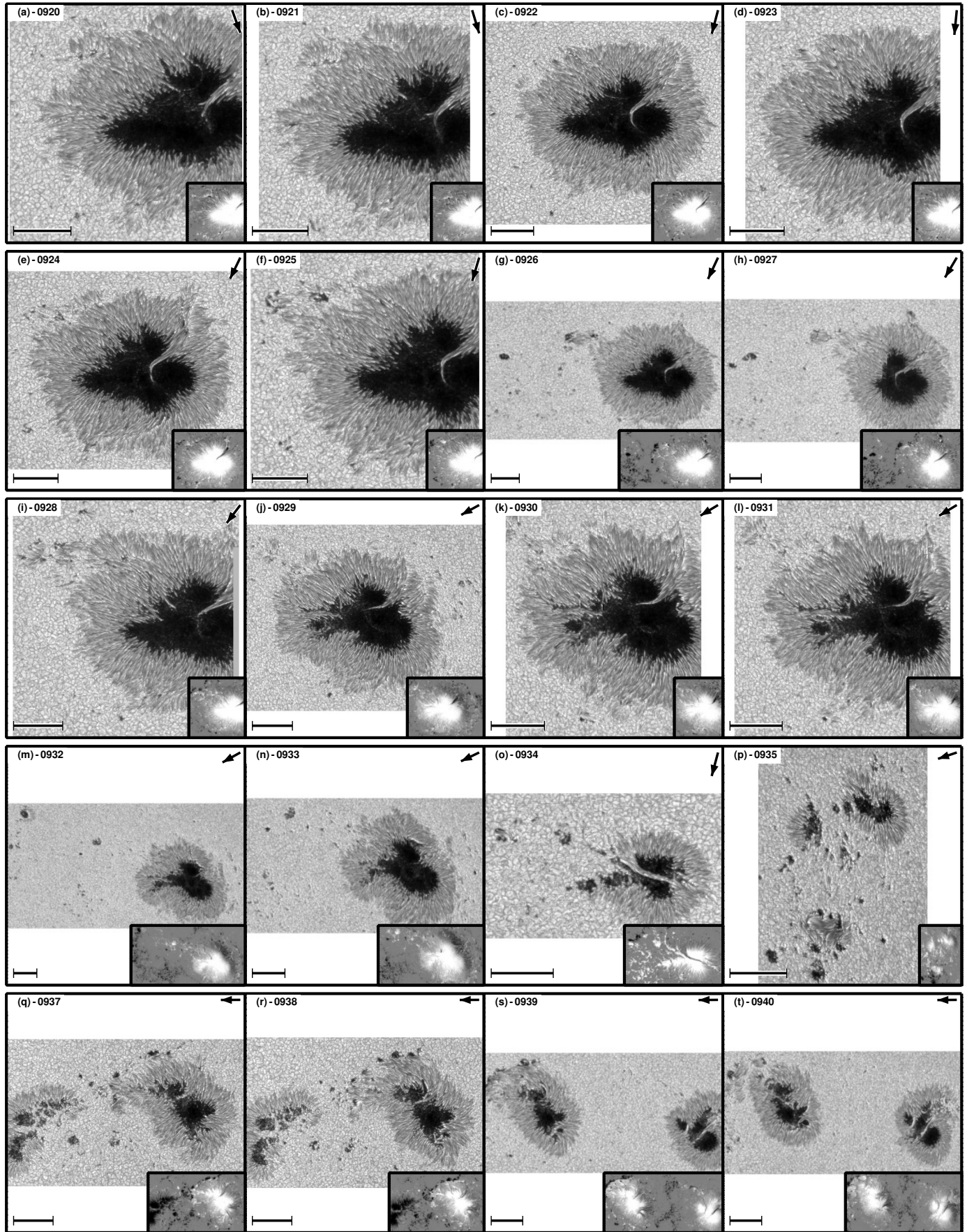


Fig. D.44. – [D.1](#). Continued.

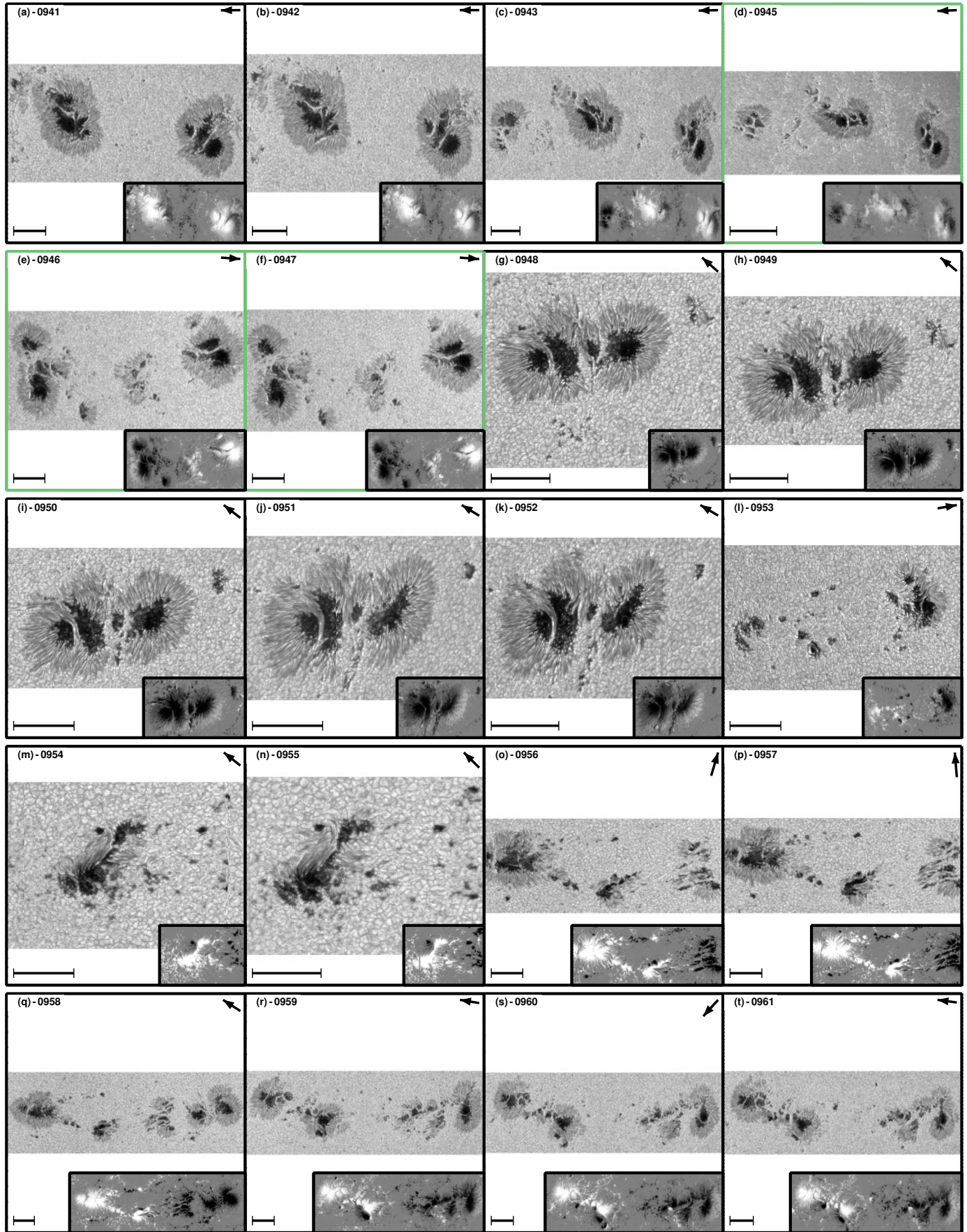


Fig. D.45. – [D.1](#). Continued.

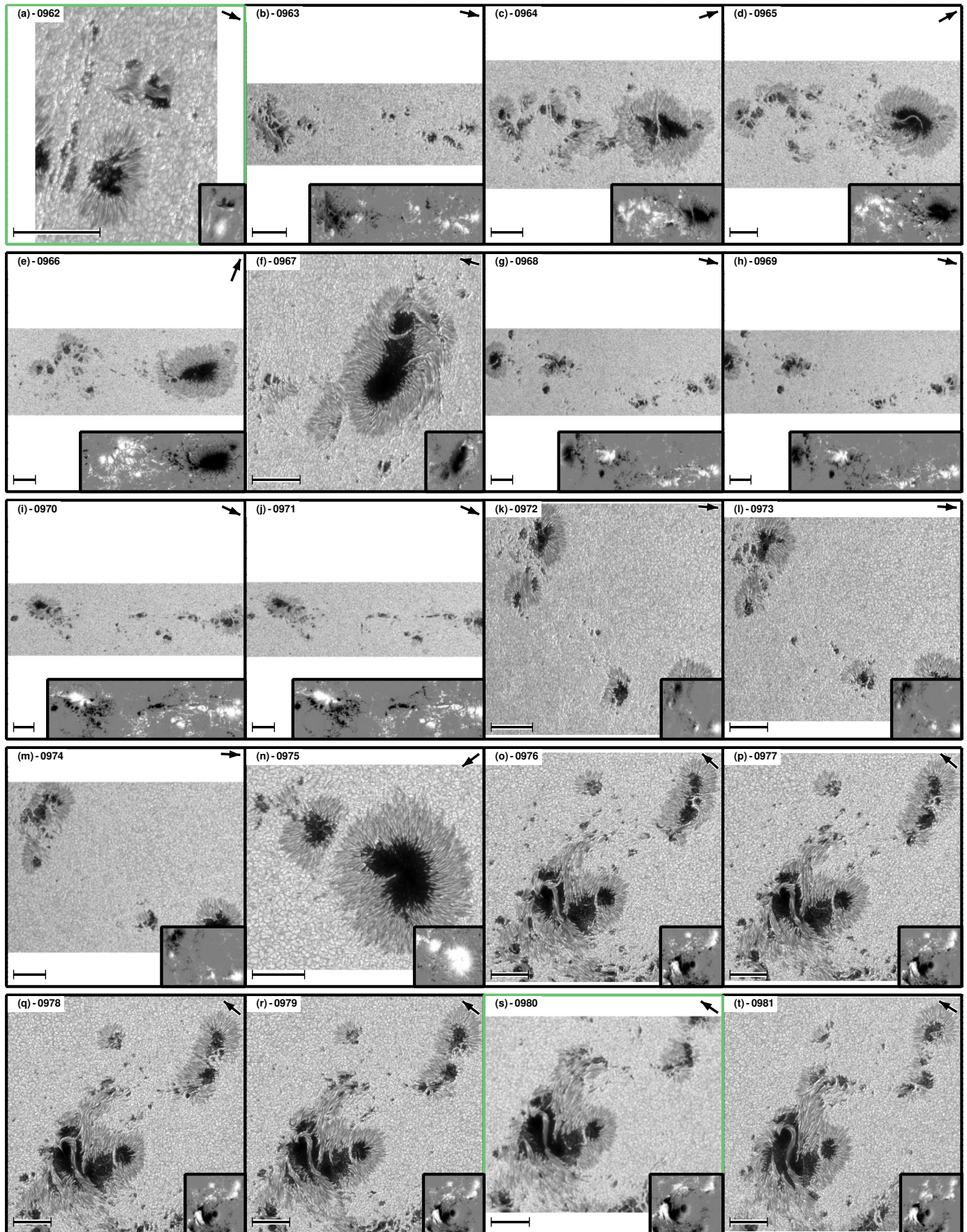


Fig. D.46. – **D.1.** Continued.

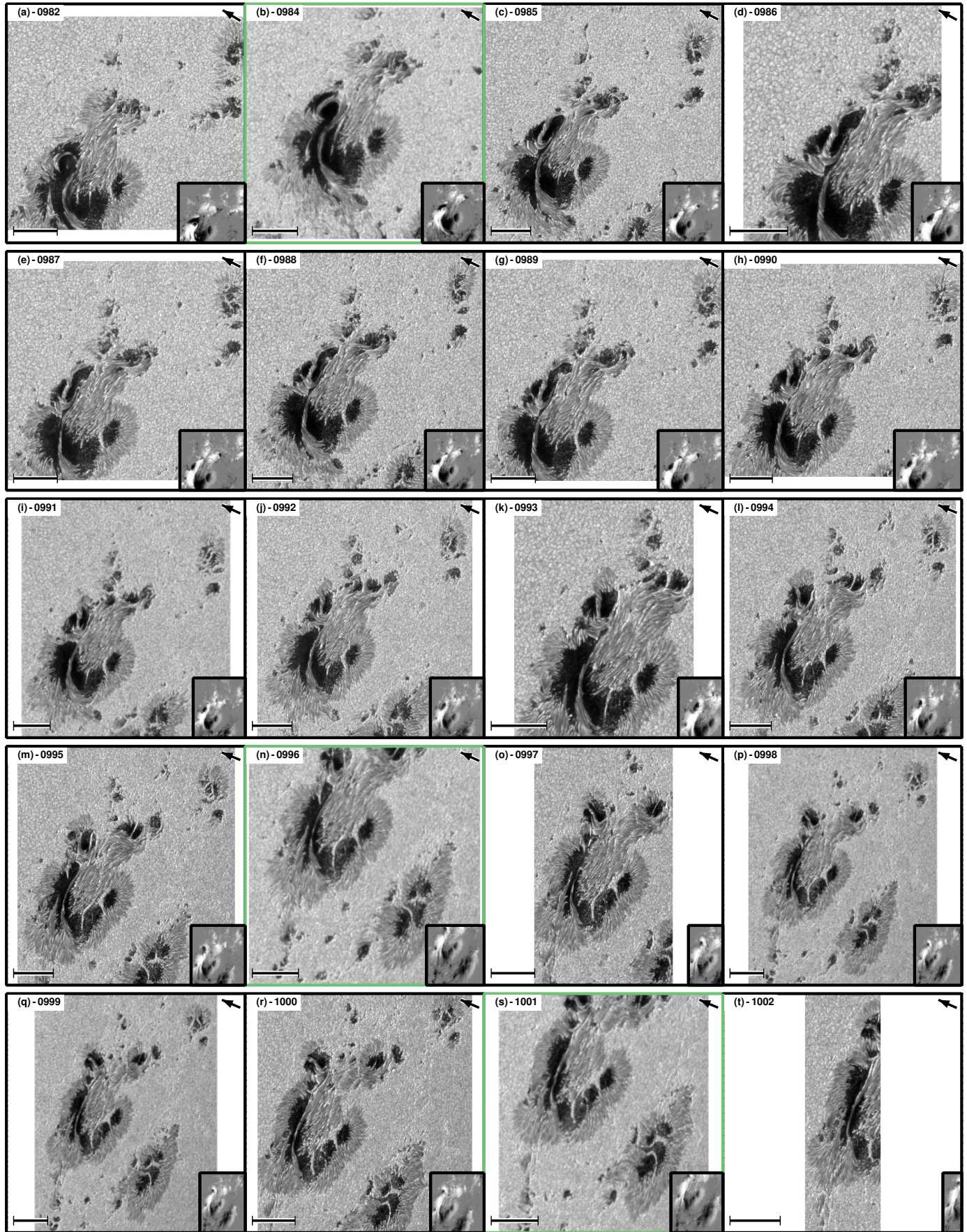
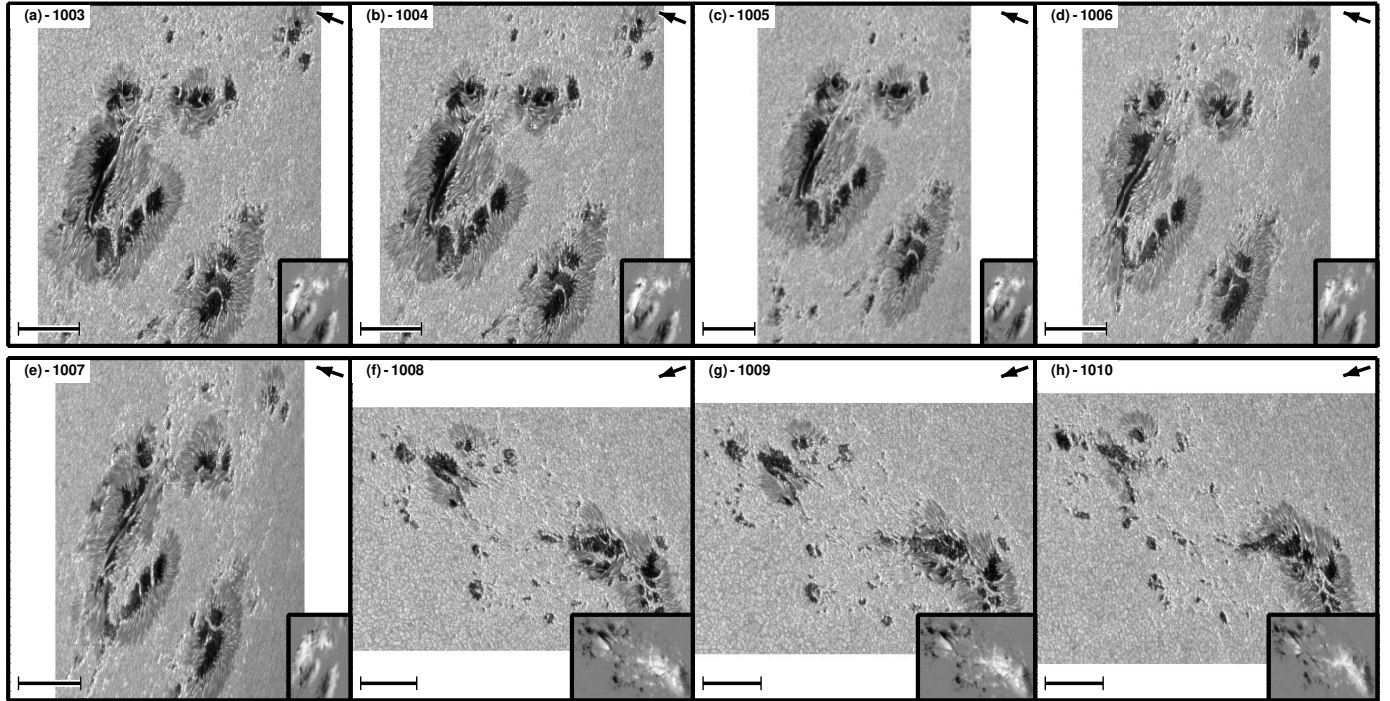


Fig. D.47. – [D.1](#). Continued.

**Fig. D.48.** – **D.1.** Continued.**Table D.1.** Sample of sunspot groups that are part of the MODEST catalog.

index	inv_id	obs_id (date)_ (time)	NOAA AR num	type scan	x_c ('')	y_c ('')	μ	num tiles	size FOV	area (MSH)	Zürich class	magnetic class	Fig. (panel)
1	0000	20061208_061114	10930	Nor.	-797	-72	0.56	100	89'' × 95''	430	Dki	$\beta\gamma\delta$	D.1(a)
2	0001	20061208_105104	10930	Fast	-670	-58	0.60	25	89'' × 95''	430	Dki	$\beta\gamma\delta$	D.1(b)
3	0002	20061208_121357	10930	Fast	-661	-58	0.61	25	89'' × 95''	430	Dki	$\beta\gamma\delta$	D.1(c)
4	0003	20061208_131320	10930	Fast	-634	-57	0.62	25	89'' × 95''	430	Dki	$\beta\gamma\delta$	D.1(d)
5	0004	20061208_145005	10930	Fast	-643	-53	0.63	25	89'' × 95''	430	Dki	$\beta\gamma\delta$	D.1(e)
6	0005	20061208_180506	10930	Fast	-621	-54	0.66	25	89'' × 95''	430	Dki	$\beta\gamma\delta$	D.1(f)
7	0006	20061208_212005	10930	Fast	-598	-54	0.69	25	89'' × 95''	430	Dki	$\beta\gamma\delta$	D.1(g)
8	0007	20061209_034005	10930	Fast	-548	-53	0.74	25	89'' × 95''	430	Dki	$\beta\gamma\delta$	D.1(h)
9	0008	20061209_070005	10930	Fast	-517	-51	0.77	25	89'' × 95''	430	Dki	$\beta\gamma\delta$	D.1(i)
10	0009	20061209_100005	10930	Fast	-493	-54	0.79	25	89'' × 95''	430	Dki	$\beta\gamma\delta$	D.1(j)
11	0010	20061209_112005	10930	Fast	-482	-53	0.80	25	89'' × 95''	430	Dki	$\beta\gamma\delta$	D.1(k)
12	0011	20061209_124005	10930	Fast	-471	-53	0.80	25	89'' × 95''	430	Dki	$\beta\gamma\delta$	D.1(l)
13	0012	20061209_140005	10930	Fast	-459	-53	0.81	25	89'' × 95''	430	Dki	$\beta\gamma\delta$	D.1(m)
14	0013	20061209_171005	10930	Fast	-434	-54	0.83	25	89'' × 95''	430	Dki	$\beta\gamma\delta$	D.1(n)
15	0014	20061209_220004	10930	Fast	-391	-49	0.86	25	89'' × 95''	430	Dki	$\beta\gamma\delta$	D.1(o)
16	0015	20061210_010005	10930	Fast	-363	-51	0.87	25	89'' × 95''	430	Dki	$\beta\gamma\delta$	D.1(p)
17	0016	20061210_105507	10930	Nor.	-270	-51	0.92	100	89'' × 95''	430	Dki	$\beta\gamma\delta$	D.2(a)
18	0017	20061210_210007	10930	Fast	-176	-50	0.95	25	89'' × 95''	430	Dki	$\beta\gamma\delta$	D.2(b)
19	0018	20061211_031004	10930	Fast	-116	-46	0.97	25	89'' × 95''	440	Cki	$\beta\gamma\delta$	D.2(c)
20	0019	20061211_080004	10930	Fast	-72	-43	0.98	25	89'' × 95''	440	Cki	$\beta\gamma\delta$	D.2(d)
21	0020	20061211_111006	10930	Fast	-48	-47	0.98	25	89'' × 95''	440	Cki	$\beta\gamma\delta$	D.2(e)
22	0021	20061211_131009	10930	Nor.	-32	-48	0.99	100	89'' × 95''	440	Cki	$\beta\gamma\delta$	D.2(f)
23	0022	20061211_170008	10930	Fast	5	-48	0.99	25	89'' × 95''	440	Cki	$\beta\gamma\delta$	D.2(g)
24	0023	20061211_200005	10930	Fast	32	-47	0.99	25	89'' × 95''	440	Cki	$\beta\gamma\delta$	D.2(h)
25	0024	20061211_231005	10930	Fast	64	-47	1.00	25	89'' × 95''	440	Cki	$\beta\gamma\delta$	D.2(i)
26	0025	20061212_035005	10930	Fast	107	-48	1.00	25	89'' × 95''	480	Dki	$\beta\gamma\delta$	D.2(j)
27	0026	20061212_101008	10930	Nor.	164	-51	0.99	100	89'' × 95''	480	Dki	$\beta\gamma\delta$	D.2(k)
28	0027	20061212_153008	10930	Fast	206	-52	0.99	25	89'' × 95''	480	Dki	$\beta\gamma\delta$	D.2(l)
29	0028	20061212_174005	10930	Fast	230	-53	0.99	25	89'' × 95''	480	Dki	$\beta\gamma\delta$	D.2(m)
30	0029	20061212_203005	10930	Fast	252	-52	0.98	25	89'' × 95''	480	Dki	$\beta\gamma\delta$	D.2(n)
31	0030	20061213_043005	10930	Fast	324	-58	0.97	25	89'' × 95''	680	Dki	$\beta\gamma\delta$	D.2(o)
32	0031	20061213_075005	10930	Fast	355	-58	0.96	25	89'' × 95''	680	Dki	$\beta\gamma\delta$	D.2(p)

Table D.1. Continued.

index	inv_id	obs_id (date)(time)	NOAA AR num	type scan	x_c (")	y_c (")	μ	num tiles	size FOV	area (MSH)	Zürich class	magnetic class	Fig. (panel)
33	0032	20061213_125104	10930	Nor.	396	-51	0.94	100	89" × 95"	680	Dki	$\beta\gamma\delta$	D.2(q)
34	0033	20061213_162104	10930	Fast	425	-56	0.94	25	89" × 95"	680	Dki	$\beta\gamma\delta$	D.2(r)
35	0034	20061214_002005	10930	Fast	487	-58	0.91	25	89" × 95"	670	Dki	$\beta\gamma\delta$	D.2(s)
36	0035	20061214_050005	10930	Fast	522	-58	0.89	25	89" × 95"	670	Dki	$\beta\gamma\delta$	D.2(t)
37	0036	20061214_112602	10930	Nor.	569	-60	0.87	100	89" × 95"	670	Dki	$\beta\gamma\delta$	D.3(a)
38	0037	20061214_140103	10930	Fast	589	-63	0.86	25	89" × 95"	670	Dki	$\beta\gamma\delta$	D.3(b)
39	0038	20061214_170005	10930	Fast	610	-62	0.84	25	89" × 95"	670	Dki	$\beta\gamma\delta$	D.3(c)
40	0039	20061214_220005	10930	Fast	641	-64	0.82	25	89" × 95"	670	Dki	$\beta\gamma\delta$	D.3(d)
41	0040	20061215_054505	10930	Fast	692	-63	0.79	25	89" × 95"	620	Dkc	$\beta\gamma\delta$	D.3(e)
42	0041	20061215_130205	10930	Nor.	737	-62	0.76	100	89" × 95"	620	Dkc	$\beta\gamma\delta$	D.3(f)
43	0046	20070108_195005	10933	Nor.	665	-33	0.75	48	49" × 74"	180	Hkx	α	D.3(g)
44	0047	20070109_001036	10933	Nor.	744	-33	0.71	56	57" × 73"	230	Cki	β	D.3(h)
45	0048	20070109_063005	10933	Nor.	742	-39	0.68	48	52" × 76"	230	Cki	β	D.3(i)
46	0049	20070109_081505	10933	Nor.	747	-41	0.67	63	54" × 77"	230	Cki	β	D.3(j)
47	0051	20070430_045105	10953	Fast	-283	-71	0.94	25	78" × 82"	500	Dki	$\beta\gamma\delta$	D.3(k)
48	0052	20070430_084005	10953	Fast	-235	-60	0.95	20	77" × 75"	500	Dki	$\beta\gamma\delta$	D.3(l)
49	0053	20070501_163005	10953	Fast	82	-74	1.00	25	76" × 81"	480	Dki	$\beta\gamma\delta$	D.3(m)
50	0054	20070501_193005	10953	Fast	115	-81	1.00	20	72" × 88"	480	Dki	$\beta\gamma\delta$	D.3(n)
51	0055	20070501_210006	10953	Nor.	133	-71	0.99	80	70" × 87"	480	Dki	$\beta\gamma\delta$	D.3(o)
52	0056	20070502_001506	10953	Fast	152	-72	0.99	20	73" × 89"	440	Cko	$\beta\gamma$	D.3(p)
53	0057	20070516_154512	10956	Nor.	-545	87	0.79	81	76" × 80"	130	Dso	$\beta\gamma$	D.3(q)
54	0058	20070516_190522	10956	Fast	-502	89	0.81	25	80" × 82"	130	Dso	$\beta\gamma$	D.3(r)
55	0059	20070516_204206	10956	Fast	-486	90	0.82	20	83" × 79"	130	Dso	$\beta\gamma$	D.3(s)
56	0060	20070516_222006	10956	Fast	-482	88	0.83	25	85" × 83"	130	Dso	$\beta\gamma$	D.3(t)
57	0061	20070517_130101	10956	Nor.	-390	97	0.90	80	81" × 72"	220	Dkc	$\beta\gamma\delta$	D.4(a)
58	0062	20070517_161737	10956	Fast	-338	94	0.91	30	107" × 82"	220	Dkc	$\beta\gamma\delta$	D.4(b)
59	0063	20070517_181820	10956	Fast	-318	96	0.92	24	103" × 75"	220	Dkc	$\beta\gamma\delta$	D.4(c)
60	0064	20070518_034650	10956	Fast	-274	83	0.95	30	92" × 86"	300	Dkc	$\beta\gamma\delta$	D.4(d)
61	0065	20070519_074205	10956	Fast	-25	84	1.00	24	95" × 79"	280	Dko	$\beta\gamma\delta$	D.4(e)
62	0066	20070519_123821	10956	Nor.	25	84	1.00	72	77" × 75"	280	Dko	$\beta\gamma\delta$	D.4(f)
63	0067	20070521_185012	10956	Fast	544	77	0.86	6	37" × 44"	190	Dai	β	D.4(g)
64	0068	20070604_125036	10960	Fast	-584	-88	0.74	55	186" × 81"	540	Fkc	$\beta\gamma\delta$	D.4(h)
65	0069	20070604_224005	10960	Fast	-526	-88	0.80	60	198" × 84"	540	Fkc	$\beta\gamma\delta$	D.4(i)
66	0070	20070710_072505	10963	Fast	-556	-116	0.65	32	139" × 65"	260	Dai	$\beta\gamma$	D.4(j)
67	0071	20070710_122136	10963	Fast	-614	-116	0.64	15	90" × 61"	260	Dai	$\beta\gamma$	D.4(k)
68	0072	20070710_141031	10963	Fast	-603	-116	0.65	15	90" × 56"	260	Dai	$\beta\gamma$	D.4(l)
69	0073	20070710_155025	10963	Fast	-596	-116	0.66	15	90" × 59"	260	Dai	$\beta\gamma$	D.4(m)
70	0074	20070710_191156	10963	Fast	-574	-120	0.69	15	91" × 58"	260	Dai	$\beta\gamma$	D.4(n)
71	0075	20091027_012004	11029	Fast	496	188	0.85	20	76" × 63"	190	Dai	$\beta\gamma$	D.4(o)
72	0076	20091027_104525	11029	Fast	591	198	0.78	24	102" × 67"	190	Dai	$\beta\gamma$	D.4(p)
73	0077	20091027_164506	11029	Fast	629	202	0.75	24	100" × 69"	190	Dai	$\beta\gamma$	D.4(q)
74	0078	20091027_184506	11029	Fast	640	202	0.74	24	102" × 67"	190	Dai	$\beta\gamma$	D.4(r)
75	0079	20091027_212005	11029	Fast	657	204	0.72	24	105" × 69"	190	Dai	$\beta\gamma$	D.4(s)
76	0081	20091217_223005	11035	Fast	495	515	0.72	12	68" × 58"	140	Eac	$\beta\delta$	D.4(t)
77	0082	20091218_140740	11035	Fast	531	534	0.68	55	185" × 94"	210	Eac	β	D.5(a)
78	0083	20100111_013004	11040	Fast	-317	540	0.76	24	92" × 71"	130	Eao	β	D.5(b)
79	0084	20100208_100405	11045	Fast	64	511	0.87	36	148" × 78"	320	Fkc	$\beta\gamma$	D.5(c)
80	0085	20100208_154505	11045	Fast	147	505	0.87	32	126" × 69"	320	Fkc	$\beta\gamma$	D.5(d)
81	0086	20100209_104106	11045	Fast	345	501	0.82	52	230" × 73"	420	Fkc	$\beta\gamma\delta$	D.5(e)
82	0087	20100209_161206	11045	Fast	392	497	0.81	56	241" × 78"	420	Fkc	$\beta\gamma\delta$	D.5(f)
83	0088	20100209_224006	11045	Fast	443	495	0.78	56	238" × 77"	420	Fkc	$\beta\gamma\delta$	D.5(g)
84	0090	20101027_020005	11117	Fast	281	277	0.93	54	158" × 102"	360	Ehi	$\beta\gamma$	D.5(h)
85	0091	20101027_112005	11117	Fast	361	278	0.90	54	151" × 102"	360	Ehi	$\beta\gamma$	D.5(i)
86	0092	20101029_030042	11117	Fast	662	293	0.71	42	116" × 100"	520	Dkc	β	D.5(j)
87	0093	20101029_110005	11117	Fast	724	299	0.66	30	99" × 95"	520	Dkc	β	D.5(k)
88	0094	20110214_000004	11158	Fast	-32	-216	0.97	54	150" × 108"	120	Eac	$\beta\gamma$	D.5(l)
89	0095	20110214_063004	11158	Fast	23	-214	0.97	54	151" × 109"	120	Eac	$\beta\gamma$	D.5(m)
90	0096	20110215_101126	11158	Fast	272	-223	0.93	55	195" × 90"	450	Ekc	$\beta\gamma$	D.5(n)
91	0097	20110215_121106	11158	Fast	288	-224	0.93	56	196" × 89"	450	Ekc	$\beta\gamma$	D.5(o)

Table D.1. Continued.

index	inv_id	obs_id (date)_(time)	NOAA AR num	type scan	x_c (")	y_c (")	μ	num tiles	size FOV	area (MSH)	Zürich class	magnetic class	Fig. (panel)
92	0098	20110215_141106	11158	Fast	306	-224	0.92	55	195" × 92"	450	Ekc	$\beta\gamma$	D.5(p)
93	0099	20110215_154006	11158	Fast	316	-224	0.92	55	192" × 88"	450	Ekc	$\beta\gamma$	D.5(q)
94	0100	20110215_184006	11158	Fast	343	-225	0.91	55	194" × 87"	450	Ekc	$\beta\gamma$	D.5(r)
95	0101	20110215_204005	11158	Fast	359	-224	0.90	55	192" × 88"	450	Ekc	$\beta\gamma$	D.5(s)
96	0102	20110215_233005	11158	Fast	381	-227	0.89	55	192" × 87"	450	Ekc	$\beta\gamma$	D.5(t)
97	0103	20110216_010005	11158	Fast	393	-227	0.89	55	193" × 87"	600	Ekc	$\beta\gamma\delta$	D.6(a)
98	0104	20110216_023005	11158	Fast	404	-228	0.88	55	195" × 88"	600	Ekc	$\beta\gamma\delta$	D.6(b)
99	0105	20110216_043005	11158	Fast	419	-229	0.87	55	192" × 87"	600	Ekc	$\beta\gamma\delta$	D.6(c)
100	0106	20110216_073005	11158	Fast	441	-231	0.86	55	190" × 86"	600	Ekc	$\beta\gamma\delta$	D.6(d)
101	0107	20110216_092005	11158	Fast	454	-231	0.86	55	187" × 86"	600	Ekc	$\beta\gamma\delta$	D.6(e)
102	0108	20110216_113005	11158	Fast	468	-231	0.85	55	187" × 83"	600	Ekc	$\beta\gamma\delta$	D.6(f)
103	0109	20110217_101805	11158	Fast	628	-245	0.73	50	169" × 81"	620	Ekc	$\beta\gamma\delta$	D.6(g)
104	0110	20110217_130005	11158	Fast	648	-247	0.71	50	166" × 83"	620	Ekc	$\beta\gamma\delta$	D.6(h)
105	0111	20110217_170005	11158	Fast	671	-250	0.69	50	162" × 84"	620	Ekc	$\beta\gamma\delta$	D.6(i)
106	0112	20110217_200005	11158	Fast	688	-253	0.67	50	164" × 81"	620	Ekc	$\beta\gamma\delta$	D.6(j)
107	0114	20110218_020005	11158	Fast	722	-257	0.63	45	157" × 81"	290	Eac	$\beta\gamma\delta$	D.6(k)
108	0115	20110218_070005	11158	Fast	745	-261	0.60	45	148" × 80"	290	Eac	$\beta\gamma\delta$	D.6(l)
109	0116	20110218_100505	11158	Fast	763	-263	0.58	40	143" × 83"	290	Eac	$\beta\gamma\delta$	D.6(m)
110	0117	20110218_130005	11158	Fast	787	-265	0.55	40	137" × 82"	290	Eac	$\beta\gamma\delta$	D.6(n)
111	0118	20110219_103406	11162	Fast	190	432	0.89	32	133" × 71"	260	Dai	$\beta\gamma$	D.6(o)
112	0119	20110219_142006	11162	Fast	224	431	0.88	32	134" × 71"	260	Dai	$\beta\gamma$	D.6(p)
113	0120	20110219_181705	11162	Fast	253	429	0.87	24	140" × 52"	260	Dai	$\beta\gamma$	D.6(q)
114	0121	20110301_073504	11164	Fast	-439	539	0.68	36	106" × 102"	350	Ehc	$\beta\gamma$	D.6(r)
115	0122	20110301_090503	11164	Fast	-420	539	0.69	36	106" × 100"	350	Ehc	$\beta\gamma$	D.6(s)
116	0123	20110302_080005	11164	Fast	-284	540	0.78	48	131" × 110"	550	Ekc	$\beta\gamma\delta$	D.6(t)
117	0124	20110304_230505	11164	Fast	242	527	0.80	54	148" × 111"	470	Ekc	$\beta\gamma$	D.7(a)
118	0125	20110305_020005	11164	Fast	265	527	0.80	54	150" × 111"	570	Ekc	$\beta\gamma\delta$	D.7(b)
119	0128	20110305_095308	11164	Fast	403	518	0.77	66	193" × 117"	570	Ekc	$\beta\gamma\delta$	D.7(c)
120	0129	20110305_114006	11164	Fast	416	518	0.76	77	191" × 117"	570	Ekc	$\beta\gamma\delta$	D.7(d)
121	0132	20110305_165006	11164	Fast	455	515	0.74	77	187" × 117"	570	Ekc	$\beta\gamma\delta$	D.7(e)
122	0134	20110310_094136	11166	Fast	315	276	0.92	72	201" × 105"	630	Ekc	$\beta\gamma\delta$	D.7(f)
123	0135	20110310_144005	11166	Fast	358	274	0.91	72	199" × 113"	630	Ekc	$\beta\gamma\delta$	D.7(g)
124	0136	20110310_225505	11166	Fast	428	274	0.88	66	191" × 104"	630	Ekc	$\beta\gamma\delta$	D.7(h)
125	0137	20110311_033108	11166	Fast	413	272	0.87	54	151" × 101"	750	Ekc	$\beta\gamma$	D.7(i)
126	0138	20110330_140005	11176	Fast	486	-165	0.89	28	120" × 75"	210	Fsi	$\beta\gamma$	D.7(j)
127	0139	20110506_012650	11203+11204	Fast	140	343	0.92	48	203" × 66"	80+120	Hsx+Cao	$\alpha+\beta$	D.7(k)
128	0140	20110506_090106	11203+11204	Fast	192	342	0.91	48	203" × 68"	80+120	Hsx+Cao	$\alpha+\beta$	D.7(l)
129	0141	20110531_125814	11226	Fast	-464	-358	0.75	35	122" × 96"	360	Dki	$\beta\gamma$	D.7(m)
130	0142	20110616_111806	11236	Fast	-655	232	0.59	35	124" × 88"	350	Ehi	$\beta\delta$	D.7(n)
131	0143	20110616_130006	11236	Fast	-641	232	0.61	35	121" × 93"	350	Ehi	$\beta\delta$	D.7(o)
132	0144	20110616_143906	11236	Fast	-633	231	0.62	35	122" × 89"	350	Ehi	$\beta\delta$	D.7(p)
133	0145	20110728_124012	11260	Fast	-358	220	0.89	55	181" × 80"	110	Dsi	$\beta\gamma$	D.7(q)
134	0146	20110728_142336	11260	Fast	-345	226	0.90	44	181" × 73"	110	Dsi	$\beta\gamma$	D.7(r)
135	0147	20110802_112411	11263	Fast	-227	184	0.95	45	149" × 83"	460	Dki	$\beta\gamma\delta$	D.7(s)
136	0148	20110803_113623	11263	Fast	-21	181	0.98	36	151" × 75"	560	Eki	$\beta\gamma\delta$	D.7(t)
137	0149	20110803_130305	11263	Fast	-8	180	0.98	36	147" × 78"	560	Eki	$\beta\gamma\delta$	D.8(a)
138	0150	20110803_144135	11263	Fast	7	179	0.98	36	147" × 77"	560	Eki	$\beta\gamma\delta$	D.8(b)
139	0151	20110803_163635	11263	Fast	21	183	0.99	36	153" × 75"	560	Eki	$\beta\gamma\delta$	D.8(c)
140	0152	20110803_182805	11263	Fast	39	184	0.98	45	151" × 80"	560	Eki	$\beta\gamma\delta$	D.8(d)
141	0153	20110803_195005	11263	Fast	45	184	0.98	36	146" × 76"	560	Eki	$\beta\gamma\delta$	D.8(e)
142	0154	20110803_212735	11263	Fast	64	183	0.98	36	148" × 78"	560	Eki	$\beta\gamma\delta$	D.8(f)
143	0155	20110803_230235	11263	Fast	78	184	0.98	36	146" × 78"	560	Eki	$\beta\gamma\delta$	D.8(g)
144	0156	20110804_021034	11263	Fast	100	181	0.98	36	150" × 73"	600	Dki	$\beta\gamma\delta$	D.8(h)
145	0157	20110804_034904	11263	Fast	114	181	0.98	36	150" × 79"	600	Dki	$\beta\gamma\delta$	D.8(i)
146	0158	20110804_070605	11263	Fast	143	184	0.98	36	151" × 79"	600	Dki	$\beta\gamma\delta$	D.8(j)
147	0159	20110804_084405	11263	Fast	158	182	0.97	45	149" × 81"	600	Dki	$\beta\gamma\delta$	D.8(k)
148	0160	20110804_153706	11263	Fast	212	186	0.96	36	149" × 77"	600	Dki	$\beta\gamma\delta$	D.8(l)
149	0161	20110804_171305	11263	Fast	228	189	0.96	36	149" × 77"	600	Dki	$\beta\gamma\delta$	D.8(m)
150	0162	20110806_072004	11263	Fast	519	189	0.82	15	75" × 59"	570	Ekc	$\beta\gamma\delta$	D.8(n)

Table D.1. Continued.

index	inv_id	obs_id (date)_ (time)	NOAA AR num	type scan	x_c (")	y_c (")	μ	num tiles	size FOV	area (MSH)	Zürich class	magnetic class	Fig. (panel)
151	0163	20110806_120558	11263	Fast	514	215	0.82	40	164" × 78"	570	Ekc	$\beta\gamma\delta$	D.8(o)
152	0164	20110806_170006	11263	Fast	547	216	0.79	50	161" × 80"	570	Ekc	$\beta\gamma\delta$	D.8(p)
153	0165	20110806_220006	11263	Fast	578	216	0.76	45	156" × 82"	570	Ekc	$\beta\gamma\delta$	D.8(q)
154	0166	20110807_024006	11263	Fast	606	214	0.74	36	153" × 72"	440	Ekc	$\beta\gamma\delta$	D.8(r)
155	0167	20110807_110005	11263	Fast	692	215	0.65	12	60" × 49"	440	Ekc	$\beta\gamma\delta$	D.8(s)
156	0169	20110819_083005	11271	Fast	-471	158	0.85	16	61" × 76"	290	Ehc	β	D.8(t)
157	0170	20110907_050002	11283	Fast	341	138	0.93	24	94" × 68"	200	Eai	$\beta\gamma\delta$	D.9(a)
158	0171	20110909_113005	11283	Fast	794	160	0.62	20	82" × 71"	200	Cao	$\beta\gamma\delta$	D.9(b)
159	0172	20110909_130125	11283	Fast	801	161	0.61	20	76" × 70"	200	Cao	$\beta\gamma\delta$	D.9(c)
160	0173	20110913_103405	11289	Fast	111	271	0.96	20	85" × 76"	300	Cko	β	D.9(d)
161	0174	20110913_120405	11289	Fast	126	269	0.96	20	81" × 75"	300	Cko	β	D.9(e)
162	0175	20110918_051205	11295	Fast	14	234	0.97	48	141" × 99"	210	Dai	β	D.9(f)
163	0176	20110918_065504	11295	Fast	22	237	0.97	40	142" × 93"	210	Dai	β	D.9(g)
164	0177	20110920_072004	11295	Fast	441	267	0.89	54	160" × 109"	300	Dhc	$\beta\gamma$	D.9(h)
165	0178	20110920_092339	11295	Fast	458	270	0.88	54	154" × 109"	300	Dhc	$\beta\gamma$	D.9(i)
166	0179	20110921_082351	11295	Fast	622	286	0.77	48	143" × 108"	310	Dhc	$\beta\gamma$	D.9(j)
167	0182	20110922_114005	11295	Fast	718	279	0.60	20	90" × 73"	380	Ehc	$\beta\gamma$	D.9(k)
168	0183	20110924_104905	11302	Fast	-768	152	0.55	56	123" × 138"	840	Ekc	$\beta\gamma$	D.9(l)
169	0184	20110924_130005	11302	Fast	-749	148	0.56	64	139" × 139"	840	Ekc	$\beta\gamma$	D.9(m)
170	0185	20110924_222528	11302	Fast	-703	139	0.64	72	155" × 141"	840	Ekc	$\beta\gamma$	D.9(n)
171	0186	20110925_012335	11302	Fast	-693	135	0.66	80	162" × 141"	1300	Fkc	$\beta\gamma\delta$	D.9(o)
172	0188	20110925_043921	11302	Fast	-675	137	0.68	80	166" × 136"	1300	Fkc	$\beta\gamma\delta$	D.9(p)
173	0189	20110926_065034	11302	Fast	-558	169	0.81	30	99" × 87"	980	Ekc	$\beta\gamma\delta$	D.9(q)
174	0190	20110926_110209	11302	Fast	-470	128	0.87	84	205" × 126"	980	Ekc	$\beta\gamma\delta$	D.9(r)
175	0191	20110926_130004	11302	Fast	-506	165	0.84	30	105" × 87"	980	Ekc	$\beta\gamma\delta$	D.9(s)
176	0192	20110926_184634	11302	Fast	-432	125	0.89	63	158" × 125"	980	Ekc	$\beta\gamma\delta$	D.9(t)
177	0193	20110927_010005	11302	Fast	-391	134	0.91	48	139" × 115"	950	Ekc	$\beta\gamma$	D.10(a)
178	0194	20110927_104259	11302	Fast	-268	108	0.96	104	218" × 140"	950	Ekc	$\beta\gamma$	D.10(b)
179	0195	20110927_140006	11302	Fast	-118	101	0.98	40	141" × 97"	950	Ekc	$\beta\gamma$	D.10(c)
180	0197	20110927_223605	11302	Fast	-36	103	0.99	40	139" × 95"	950	Ekc	$\beta\gamma$	D.10(d)
181	0198	20110928_031135	11302	Fast	5	101	0.99	40	136" × 97"	980	Fkc	$\beta\gamma\delta$	D.10(e)
182	0199	20110928_110005	11302	Fast	89	101	1.00	40	129" × 93"	980	Fkc	$\beta\gamma\delta$	D.10(f)
183	0200	20110928_150006	11302	Fast	117	103	1.00	40	134" × 93"	980	Fkc	$\beta\gamma\delta$	D.10(g)
184	0202	20110928_213705	11302	Fast	180	102	0.99	40	133" × 95"	980	Fkc	$\beta\gamma\delta$	D.10(h)
185	0203	20110929_004505	11302	Fast	220	104	0.99	40	137" × 92"	1070	Fkc	$\beta\gamma\delta$	D.10(i)
186	0204	20110929_041004	11302	Fast	251	103	0.98	35	125" × 95"	1070	Fkc	$\beta\gamma\delta$	D.10(j)
187	0205	20110929_073004	11302	Fast	283	104	0.98	35	123" × 95"	1070	Fkc	$\beta\gamma\delta$	D.10(k)
188	0206	20110929_101606	11302	Fast	286	100	0.97	42	125" × 100"	1070	Fkc	$\beta\gamma\delta$	D.10(l)
189	0207	20111001_050403	11302	Fast	643	133	0.80	36	102" × 101"	750	Fkc	$\beta\gamma\delta$	D.10(m)
190	0208	20111001_110406	11302	Fast	678	140	0.77	24	102" × 76"	750	Fkc	$\beta\gamma\delta$	D.10(n)
191	0209	20111001_180235	11302	Fast	724	145	0.73	30	103" × 80"	750	Fkc	$\beta\gamma\delta$	D.10(o)
192	0210	20111002_010504	11302	Fast	769	151	0.68	24	95" × 79"	700	Fkc	$\beta\gamma\delta$	D.10(p)
193	0211	20111002_070514	11302	Fast	741	138	0.65	20	91" × 74"	700	Fkc	$\beta\gamma\delta$	D.10(q)
194	0212	20111002_113449	11302	Fast	818	149	0.61	25	90" × 89"	700	Fkc	$\beta\gamma\delta$	D.10(r)
195	0213	20111002_151148	11302	Fast	785	146	0.59	20	86" × 75"	700	Fkc	$\beta\gamma\delta$	D.10(s)
196	0214	20111006_152406	11309	Fast	-189	322	0.90	6	32" × 46"	160	Dso	β	D.10(t)
197	0215	20111007_023104	11309	Fast	-134	321	0.93	9	48" × 50"	170	Cso	β	D.11(a)
198	0218	20111004_233139	11339	Fast	-680	271	0.65	24	94" × 78"	1400	Ekc	$\beta\gamma\delta$	D.11(b)
199	0219	20111005_034209	11339	Fast	-654	272	0.68	42	112" × 113"	1540	Fkc	$\beta\gamma\delta$	D.11(c)
200	0222	20111005_210005	11339	Fast	-522	267	0.80	66	181" × 109"	1540	Fkc	$\beta\gamma\delta$	D.11(d)
201	0223	20111006_010506	11339	Fast	-488	263	0.82	66	191" × 111"	1250	Ekc	$\beta\gamma\delta$	D.11(e)
202	0224	20111006_042005	11339	Fast	-456	262	0.84	72	202" × 111"	1250	Ekc	$\beta\gamma\delta$	D.11(f)
203	0225	20111006_080205	11339	Fast	-429	263	0.86	72	202" × 111"	1250	Ekc	$\beta\gamma\delta$	D.11(g)
204	0227	20111006_120041	11339	Fast	-396	263	0.87	72	202" × 106"	1250	Ekc	$\beta\gamma\delta$	D.11(h)
205	0229	20111006_200005	11339	Fast	-332	264	0.90	72	201" × 100"	1250	Ekc	$\beta\gamma\delta$	D.11(i)
206	0230	20111007_000005	11339	Fast	-300	262	0.91	72	202" × 105"	1230	Fkc	$\beta\gamma\delta$	D.11(j)
207	0231	20111007_034004	11339	Fast	-270	260	0.92	72	201" × 101"	1230	Fkc	$\beta\gamma\delta$	D.11(k)
208	0232	20111007_081004	11339	Fast	-231	262	0.93	72	201" × 100"	1230	Fkc	$\beta\gamma\delta$	D.11(l)
209	0235	20111008_160006	11339	Fast	29	258	0.97	60	203" × 98"	1240	Fkc	$\beta\gamma\delta$	D.11(m)

Table D.1. Continued.

index	inv_id	obs_id (date)(time)	NOAA AR num	type scan	x_c (")	y_c (")	μ	num tiles	size FOV	area (MSH)	Zürich class	magnetic class	Fig. (panel)
210	0236	20111109_200005	11339	Fast	274	263	0.92	72	200" × 102"	940	Ekc	$\beta\gamma$	D.11(n)
211	0237	20111109_231005	11339	Fast	300	262	0.91	72	198" × 104"	940	Ekc	$\beta\gamma$	D.11(o)
212	0238	20111110_021005	11339	Fast	330	262	0.90	72	199" × 105"	1030	Fkc	$\beta\gamma$	D.11(p)
213	0239	20111110_051005	11339	Fast	345	263	0.90	66	183" × 106"	1030	Fkc	$\beta\gamma$	D.11(q)
214	0240	20111110_100239	11339	Fast	450	266	0.86	54	155" × 104"	1030	Fkc	$\beta\gamma$	D.11(r)
215	0241	20111111_000005	11339	Fast	528	273	0.80	45	157" × 94"	1020	Fkc	$\beta\gamma$	D.11(s)
216	0242	20111119_113006	11354	Fast	-744	-283	0.55	36	96" × 104"	210	Dso	β	D.11(t)
217	0243	20111119_123006	11354	Fast	-738	-284	0.56	36	99" × 104"	210	Dso	β	D.12(a)
218	0244	20111119_133005	11354	Fast	-733	-284	0.57	36	99" × 102"	210	Dso	β	D.12(b)
219	0245	20111119_143006	11354	Fast	-728	-285	0.57	36	100" × 106"	210	Dso	β	D.12(c)
220	0246	20111119_163005	11354	Fast	-718	-286	0.59	36	99" × 105"	210	Dso	β	D.12(d)
221	0247	20111119_181506	11354	Fast	-708	-286	0.60	36	100" × 109"	210	Dso	β	D.12(e)
222	0248	20111119_192005	11354	Fast	-701	-288	0.61	36	100" × 108"	210	Dso	β	D.12(f)
223	0249	20111119_195245	11354	Fast	-698	-286	0.61	36	96" × 105"	210	Dso	β	D.12(g)
224	0250	20111227_120042	11387	Fast	729	-330	0.63	24	103" × 73"	130	Dai	$\beta\gamma$	D.12(h)
225	0251	20111231_004005	11389	Fast	-622	-375	0.59	35	123" × 81"	500	Ekc	$\beta\gamma$	D.12(i)
226	0252	20111231_085005	11389	Fast	-582	-372	0.64	28	117" × 75"	500	Ekc	$\beta\gamma$	D.12(j)
227	0253	20120102_032504	11389	Fast	-315	-362	0.84	24	95" × 69"	420	Fko	β	D.12(k)
228	0254	20120223_224505	11420	Fast	774	360	0.61	16	71" × 72"	30	Hrx	α	D.12(l)
229	0255	20120306_100006	11429	Fast	-560	388	0.71	48	138" × 108"	770	Dkc	$\beta\delta$	D.12(m)
230	0256	20120306_120006	11429	Fast	-542	390	0.73	48	140" × 111"	770	Dkc	$\beta\delta$	D.12(n)
231	0258	20120306_140104	11429	Fast	-528	391	0.74	48	143" × 111"	770	Dkc	$\beta\delta$	D.12(o)
232	0259	20120306_155006	11429	Fast	-515	396	0.75	54	145" × 106"	770	Dkc	$\beta\delta$	D.12(p)
233	0260	20120306_173006	11429	Fast	-503	397	0.76	54	145" × 106"	770	Dkc	$\beta\delta$	D.12(q)
234	0261	20120306_221040	11429	Fast	-472	399	0.78	54	147" × 110"	770	Dkc	$\beta\delta$	D.12(r)
235	0262	20120307_020006	11429	Fast	-460	384	0.79	30	87" × 104"	1120	Dkc	$\beta\gamma\delta$	D.12(s)
236	0263	20120307_080005	11429	Fast	-399	407	0.82	54	149" × 111"	1120	Dkc	$\beta\gamma\delta$	D.12(t)
237	0264	20120307_090005	11429	Fast	-391	405	0.82	54	150" × 111"	1120	Dkc	$\beta\gamma\delta$	D.13(a)
238	0265	20120307_140005	11429	Fast	-338	404	0.85	42	126" × 107"	1120	Dkc	$\beta\gamma\delta$	D.13(b)
239	0266	20120307_160005	11429	Fast	-333	405	0.85	54	151" × 115"	1120	Dkc	$\beta\gamma\delta$	D.13(c)
240	0267	20120308_012005	11429	Fast	-255	406	0.88	63	149" × 117"	1270	Dkc	$\beta\gamma\delta$	D.13(d)
241	0268	20120308_080004	11429	Fast	-197	421	0.89	54	149" × 101"	1270	Dkc	$\beta\gamma\delta$	D.13(e)
242	0269	20120308_131128	11429	Fast	-181	425	0.89	36	93" × 100"	1270	Dkc	$\beta\gamma\delta$	D.13(f)
243	0270	20120308_163652	11429	Fast	-106	422	0.91	35	119" × 83"	1270	Dkc	$\beta\gamma\delta$	D.13(g)
244	0271	20120308_183006	11429	Fast	-105	421	0.91	54	151" × 103"	1270	Dkc	$\beta\gamma\delta$	D.13(h)
245	0272	20120308_213005	11429	Fast	-78	424	0.91	54	150" × 100"	1270	Dkc	$\beta\gamma\delta$	D.13(i)
246	0273	20120308_230005	11429	Fast	-108	436	0.91	20	67" × 86"	1270	Dkc	$\beta\gamma\delta$	D.13(j)
247	0274	20120309_023602	11429	Fast	-68	433	0.91	25	82" × 88"	950	Ekc	$\beta\gamma\delta$	D.13(k)
248	0275	20120426_130548	11465	Fast	535	-207	0.82	16	62" × 74"	280	Dko	β	D.13(l)
249	0276	20120426_220006	11465	Fast	606	-218	0.78	15	56" × 80"	280	Dko	β	D.13(m)
250	0277	20120508_095806	11476	Fast	-678	258	0.66	24	93" × 71"	810	Fkc	$\beta\gamma$	D.13(n)
251	0278	20120508_114506	11476	Fast	-640	218	0.70	48	139" × 112"	810	Fkc	$\beta\gamma$	D.13(o)
252	0279	20120508_132006	11476	Fast	-626	217	0.72	54	151" × 111"	810	Fkc	$\beta\gamma$	D.13(p)
253	0280	20120508_150506	11476	Fast	-613	217	0.73	54	151" × 113"	810	Fkc	$\beta\gamma$	D.13(q)
254	0281	20120508_200505	11476	Fast	-579	219	0.76	54	151" × 113"	810	Fkc	$\beta\gamma$	D.13(r)
255	0282	20120508_232005	11476	Fast	-508	221	0.79	42	119" × 107"	810	Fkc	$\beta\gamma$	D.13(s)
256	0283	20120509_010005	11476	Fast	-563	267	0.77	18	100" × 60"	940	Fkc	$\beta\gamma\delta$	D.13(t)
257	0284	20120509_040340	11476	Fast	-521	221	0.80	54	150" × 111"	940	Fkc	$\beta\gamma\delta$	D.14(a)
258	0285	20120509_072005	11476	Fast	-464	221	0.83	48	130" × 109"	940	Fkc	$\beta\gamma\delta$	D.14(b)
259	0286	20120509_090005	11476	Fast	-456	222	0.84	48	134" × 107"	940	Fkc	$\beta\gamma\delta$	D.14(c)
260	0287	20120509_121526	11476	Fast	-490	278	0.82	6	32" × 49"	940	Fkc	$\beta\gamma\delta$	D.14(d)
261	0288	20120509_140021	11476	Fast	-422	223	0.86	48	137" × 112"	940	Fkc	$\beta\gamma\delta$	D.14(e)
262	0289	20120509_222005	11476	Fast	-351	224	0.89	48	135" × 111"	940	Fkc	$\beta\gamma\delta$	D.14(f)
263	0290	20120510_080005	11476	Fast	-272	225	0.92	48	138" × 114"	1050	Fkc	$\beta\gamma\delta$	D.14(g)
264	0291	20120510_093906	11476	Fast	-260	226	0.93	48	139" × 112"	1050	Fkc	$\beta\gamma\delta$	D.14(h)
265	0292	20120510_111405	11476	Fast	-251	226	0.93	48	140" × 110"	1050	Fkc	$\beta\gamma\delta$	D.14(i)
266	0293	20120510_130006	11476	Fast	-279	271	0.92	16	60" × 69"	1050	Fkc	$\beta\gamma\delta$	D.14(j)
267	0294	20120510_144006	11476	Fast	-200	226	0.95	42	112" × 113"	1050	Fkc	$\beta\gamma\delta$	D.14(k)
268	0295	20120512_023835	11476	Fast	135	183	0.97	72	144" × 143"	1040	Fkc	$\beta\gamma\delta$	D.14(l)
269	0296	20120512_091334	11476	Fast	228	182	0.96	56	123" × 138"	1040	Fkc	$\beta\gamma\delta$	D.14(m)

Table D.1. Continued.

index	inv_id	obs_id (date)(time)	NOAA AR num	type scan	x_c (")	y_c (")	μ	num tiles	size FOV	area (MSH)	Zürich class	magnetic class	Fig. (panel)
270	0297	20120512_123050	11476	Fast	306	191	0.94	77	191" × 128"	1040	Fkc	$\beta\gamma\delta$	D.14(n)
271	0298	20120512_223006	11476	Fast	381	188	0.92	54	154" × 102"	1040	Fkc	$\beta\gamma\delta$	D.14(o)
272	0300	20120513_081505	11476	Fast	474	186	0.88	45	149" × 95"	960	Fkc	$\beta\gamma\delta$	D.14(p)
273	0303	20120513_183005	11476	Fast	514	184	0.84	50	173" × 98"	960	Fkc	$\beta\gamma\delta$	D.14(q)
274	0304	20120513_213005	11476	Fast	543	183	0.82	50	167" × 97"	960	Fkc	$\beta\gamma\delta$	D.14(r)
275	0305	20120514_004505	11476	Fast	567	181	0.80	60	164" × 99"	810	Fki	$\beta\gamma\delta$	D.14(s)
276	0306	20120514_040005	11476	Fast	589	180	0.79	60	168" × 102"	810	Fki	$\beta\gamma\delta$	D.14(t)
277	0308	20120514_103004	11476	Fast	625	166	0.76	60	164" × 110"	810	Fki	$\beta\gamma\delta$	D.15(a)
278	0310	20120514_171605	11476	Fast	746	163	0.69	30	106" × 97"	810	Fki	$\beta\gamma\delta$	D.15(b)
279	0311	20120514_203239	11476	Fast	769	162	0.66	30	103" × 90"	810	Fki	$\beta\gamma\delta$	D.15(c)
280	0312	20120515_030004	11476	Fast	807	161	0.62	30	97" × 93"	600	Fko	$\beta\gamma$	D.15(d)
281	0313	20120515_061504	11476	Fast	795	158	0.61	42	114" × 103"	600	Fko	$\beta\gamma$	D.15(e)
282	0315	20120613_110505	11504	Fast	-282	-301	0.87	55	195" × 98"	310	Eki	β	D.15(f)
283	0316	20120629_224835	11513	Fast	-417	193	0.83	25	79" × 96"	90	Dso	$\beta\gamma$	D.15(g)
284	0317	20120704_224035	11515	Fast	325	-349	0.86	40	165" × 70"	570	Fkc	$\beta\gamma\delta$	D.15(h)
285	0318	20120705_015535	11515	Fast	350	-348	0.85	40	164" × 71"	640	Fkc	$\beta\gamma\delta$	D.15(i)
286	0319	20120705_034535	11515	Fast	365	-349	0.84	40	164" × 76"	640	Fkc	$\beta\gamma\delta$	D.15(j)
287	0320	20120705_065135	11515	Fast	388	-347	0.83	36	161" × 74"	640	Fkc	$\beta\gamma\delta$	D.15(k)
288	0321	20120706_190513	11515	Fast	688	-339	0.61	50	163" × 95"	670	Ekc	$\beta\gamma\delta$	D.15(l)
289	0322	20120710_231041	11520	Fast	-336	-371	0.85	66	181" × 103"	1370	Fkc	$\beta\gamma\delta$	D.15(m)
290	0323	20120711_173528	11520	Fast	-210	-352	0.89	80	172" × 137"	1370	Fkc	$\beta\gamma\delta$	D.15(n)
291	0324	20120711_202646	11520	Fast	-154	-357	0.90	91	216" × 134"	1370	Fkc	$\beta\gamma\delta$	D.15(o)
292	0325	20120712_111228	11520	Fast	-10	-372	0.92	66	187" × 102"	1320	Fkc	$\beta\gamma\delta$	D.15(p)
293	0327	20120713_004708	11520	Fast	63	-375	0.91	63	159" × 118"	1460	Fkc	$\beta\gamma\delta$	D.15(q)
294	0331	20120715_045105	11520	Fast	514	-365	0.75	36	99" × 115"	990	Fkc	$\beta\gamma\delta$	D.15(r)
295	0333	20120729_020305	11532	Fast	-609	-407	0.59	72	204" × 115"	510	Fho	β	D.15(s)
296	0334	20120729_052005	11532	Fast	-590	-411	0.62	91	214" × 118"	510	Fho	β	D.15(t)
297	0335	20120729_083605	11532	Fast	-575	-413	0.63	78	213" × 117"	510	Fho	β	D.16(a)
298	0336	20120729_120005	11532	Fast	-559	-416	0.65	91	222" × 117"	510	Fho	β	D.16(b)
299	0338	20120730_024005	11532	Fast	-480	-423	0.73	98	248" × 124"	500	Fko	β	D.16(c)
300	0339	20120730_060005	11532	Fast	-462	-425	0.74	105	257" × 122"	500	Fko	β	D.16(d)
301	0340	20120731_113345	11532	Fast	-240	-453	0.83	119	292" × 129"	350	Dkc	β	D.16(e)
302	0341	20120809_052420	11542	Fast	-641	-305	0.57	25	91" × 87"	160	Dai	β	D.16(f)
303	0342	20120809_070119	11542	Fast	-644	-300	0.59	30	93" × 85"	160	Dai	β	D.16(g)
304	0343	20120814_000004	11543	Fast	113	243	0.96	16	71" × 64"	250	Dko	$\beta\gamma$	D.16(h)
305	0344	20120814_143505	11543	Fast	261	260	0.94	20	88" × 67"	250	Dko	$\beta\gamma$	D.16(i)
306	0345	20120814_180906	11543	Fast	285	265	0.93	20	87" × 67"	250	Dko	$\beta\gamma$	D.16(j)
307	0346	20120815_003105	11543	Fast	307	253	0.91	12	63" × 61"	250	Cko	$\beta\gamma$	D.16(k)
308	0347	20120815_013142	11543	Fast	344	270	0.91	20	80" × 65"	250	Cko	$\beta\gamma$	D.16(l)
309	0348	20120902_090505	11560	Nor.	164	-65	0.98	42	60" × 55"	220	Dai	$\beta\gamma$	D.16(m)
310	0349	20120902_130005	11560	Nor.	204	-61	0.98	35	58" × 48"	220	Dai	$\beta\gamma$	D.16(n)
311	0350	20120903_113004	11560	Nor.	406	-48	0.90	48	69" × 56"	260	Ehi	$\beta\gamma$	D.16(o)
312	0351	20120903_130004	11560	Nor.	418	-50	0.89	48	69" × 57"	260	Ehi	$\beta\gamma$	D.16(p)
313	0352	20121023_150006	11598	Fast	-684	-255	0.58	30	99" × 92"	370	Dhi	β	D.16(q)
314	0353	20121023_181635	11598	Fast	-665	-255	0.61	30	104" × 92"	370	Dhi	β	D.16(r)
315	0354	20121023_212005	11598	Fast	-646	-262	0.63	30	102" × 90"	370	Dhi	β	D.16(s)
316	0355	20121024_003005	11598	Fast	-617	-262	0.66	30	102" × 87"	420	Dki	$\beta\delta$	D.16(t)
317	0356	20121024_034005	11598	Fast	-597	-272	0.68	30	102" × 97"	420	Dki	$\beta\delta$	D.17(a)
318	0357	20121024_065005	11598	Fast	-577	-272	0.70	30	105" × 92"	420	Dki	$\beta\delta$	D.17(b)
319	0358	20121024_091322	11598	Fast	-601	-275	0.70	25	90" × 90"	420	Dki	$\beta\delta$	D.17(c)
320	0359	20121024_120026	11598	Fast	-565	-274	0.73	35	110" × 86"	420	Dki	$\beta\delta$	D.17(d)
321	0360	20121024_151505	11598	Fast	-540	-278	0.75	35	116" × 90"	420	Dki	$\beta\delta$	D.17(e)
322	0361	20121024_190005	11598	Fast	-499	-274	0.78	35	111" × 84"	420	Dki	$\beta\delta$	D.17(f)
323	0362	20121025_010005	11598	Fast	-450	-277	0.81	35	111" × 94"	360	Dki	$\beta\delta$	D.17(g)
324	0363	20121025_110506	11598	Fast	-367	-280	0.86	42	113" × 100"	360	Dki	$\beta\delta$	D.17(h)
325	0364	20121025_141505	11598	Fast	-350	-280	0.87	35	121" × 98"	360	Dki	$\beta\delta$	D.17(i)
326	0365	20121025_164005	11598	Fast	-328	-282	0.88	42	112" × 99"	360	Dki	$\beta\delta$	D.17(j)
327	0366	20121025_195005	11598	Fast	-300	-283	0.89	42	112" × 100"	360	Dki	$\beta\delta$	D.17(k)
328	0367	20121025_230005	11598	Fast	-280	-285	0.90	42	117" × 102"	360	Dki	$\beta\delta$	D.17(l)
329	0368	20121026_021005	11598	Fast	-251	-285	0.91	42	117" × 103"	370	Dko	$\beta\delta$	D.17(m)

Table D.1. Continued.

index	inv_id	obs_id (date)(time)	NOAA AR num	type scan	x_c (")	y_c (")	μ	num tiles	size FOV	area (MSH)	Zürich class	magnetic class	Fig. (panel)
330	0369	20121026_083005	11598	Fast	-197	-288	0.92	42	114" × 106"	370	Dko	$\beta\delta$	D.17(n)
331	0370	20121026_121006	11598	Fast	-166	-288	0.93	42	118" × 103"	370	Dko	$\beta\delta$	D.17(o)
332	0371	20121026_145006	11598	Fast	-138	-285	0.94	42	121" × 102"	370	Dko	$\beta\delta$	D.17(p)
333	0372	20121026_231006	11598	Fast	-61	-285	0.95	42	114" × 104"	370	Dko	$\beta\delta$	D.17(q)
334	0373	20121027_034505	11598	Fast	-11	-264	0.95	35	110" × 82"	340	Dko	$\beta\delta$	D.17(r)
335	0374	20121027_091505	11598	Fast	38	-257	0.95	28	109" × 79"	340	Dko	$\beta\delta$	D.17(s)
336	0375	20121027_210005	11598	Fast	179	-260	0.95	25	86" × 84"	340	Dko	$\beta\delta$	D.17(t)
337	0376	20121027_234005	11598	Fast	185	-253	0.94	24	96" × 77"	340	Dko	$\beta\delta$	D.18(a)
338	0377	20121028_014005	11598	Fast	199	-254	0.94	30	100" × 80"	330	Dkc	$\beta\delta$	D.18(b)
339	0378	20121028_104005	11598	Fast	297	-252	0.92	20	84" × 72"	330	Dkc	$\beta\delta$	D.18(c)
340	0379	20121028_124005	11598	Fast	314	-249	0.92	20	87" × 74"	330	Dkc	$\beta\delta$	D.18(d)
341	0380	20121028_144004	11598	Fast	329	-246	0.91	20	85" × 73"	330	Dkc	$\beta\delta$	D.18(e)
342	0381	20121028_164004	11598	Fast	356	-246	0.90	20	83" × 70"	330	Dkc	$\beta\delta$	D.18(f)
343	0382	20121028_193004	11598	Fast	373	-244	0.90	20	83" × 70"	330	Dkc	$\beta\delta$	D.18(g)
344	0383	20121028_213004	11598	Fast	395	-243	0.89	20	83" × 67"	330	Dkc	$\beta\delta$	D.18(h)
345	0384	20121029_034504	11598	Fast	454	-240	0.87	20	75" × 74"	240	Dac	β	D.18(i)
346	0385	20121029_053004	11598	Fast	472	-240	0.86	20	87" × 71"	240	Dac	β	D.18(j)
347	0386	20121113_111206	11613	Fast	-505	-425	0.67	20	76" × 76"	170	Dso	β	D.18(k)
348	0387	20121123_073005	11618	Fast	370	121	0.95	55	192" × 89"	350	Ekc	$\beta\gamma\delta$	D.18(l)
349	0388	20121123_121122	11618	Fast	315	108	0.94	28	111" × 78"	350	Ekc	$\beta\gamma\delta$	D.18(m)
350	0389	20121123_130123	11618	Fast	422	127	0.93	55	181" × 89"	350	Ekc	$\beta\gamma\delta$	D.18(n)
351	0390	20121123_192205	11618	Fast	480	129	0.91	50	177" × 88"	350	Ekc	$\beta\gamma\delta$	D.18(o)
352	0391	20121124_122005	11618	Fast	591	138	0.83	40	169" × 75"	450	Ekc	$\beta\gamma\delta$	D.18(p)
353	0392	20121124_150005	11618	Fast	596	145	0.82	40	162" × 69"	450	Ekc	$\beta\gamma\delta$	D.18(q)
354	0395	20121125_003005	11618	Fast	684	148	0.76	36	145" × 69"	340	Ekc	$\beta\gamma\delta$	D.18(r)
355	0396	20121125_034005	11618	Fast	711	148	0.74	36	149" × 68"	340	Ekc	$\beta\gamma\delta$	D.18(s)
356	0397	20121125_070005	11618	Fast	734	148	0.72	36	154" × 74"	340	Ekc	$\beta\gamma\delta$	D.18(t)
357	0398	20121125_131505	11618	Fast	774	141	0.67	36	155" × 75"	340	Ekc	$\beta\gamma\delta$	D.19(a)
358	0399	20121125_154505	11618	Fast	792	148	0.66	36	144" × 74"	340	Ekc	$\beta\gamma\delta$	D.19(b)
359	0400	20121125_190005	11618	Fast	813	143	0.63	36	146" × 79"	340	Ekc	$\beta\gamma\delta$	D.19(c)
360	0401	20121125_221005	11618	Fast	828	143	0.61	32	138" × 79"	340	Ekc	$\beta\gamma\delta$	D.19(d)
361	0402	20130109_203505	11652	Fast	-408	410	0.79	60	206" × 82"	210	Fac	$\beta\gamma$	D.19(e)
362	0404	20130112_133006	11654	Fast	-449	198	0.86	78	229" × 108"	1100	Fki	$\beta\gamma$	D.19(f)
363	0405	20130112_160006	11654	Fast	-427	199	0.88	78	229" × 108"	1100	Fki	$\beta\gamma$	D.19(g)
364	0406	20130112_191506	11654	Fast	-400	200	0.89	78	229" × 107"	1100	Fki	$\beta\gamma$	D.19(h)
365	0407	20130112_210505	11654	Fast	-385	200	0.90	78	229" × 104"	1100	Fki	$\beta\gamma$	D.19(i)
366	0408	20130112_215759	11654	Fast	-358	200	0.90	24	99" × 70"	1100	Fki	$\beta\gamma$	D.19(j)
367	0409	20130210_143004	11670	Fast	183	422	0.91	27	149" × 58"	150	Dsi	$\beta\gamma$	D.19(k)
368	0410	20130210_190004	11670	Fast	228	421	0.90	24	143" × 54"	150	Dsi	$\beta\gamma$	D.19(l)
369	0411	20130314_120112	11692	Fast	-193	283	0.92	15	78" × 53"	190	Cso	β	D.19(m)
370	0412	20130314_210005	11692	Fast	-122	285	0.94	12	66" × 52"	190	Cso	β	D.19(n)
371	0413	20130402_161006	11711	Fast	-584	-203	0.71	25	84" × 90"	480	Cki	β	D.19(o)
372	0414	20130402_173505	11711	Fast	-575	-208	0.71	20	71" × 93"	480	Cki	β	D.19(p)
373	0416	20130423_105459	11726	Fast	626	271	0.73	72	208" × 106"	550	Ekc	$\beta\gamma\delta$	D.19(q)
374	0417	20130423_143005	11726	Fast	653	270	0.70	72	209" × 107"	550	Ekc	$\beta\gamma\delta$	D.19(r)
375	0418	20130423_173805	11726	Fast	674	266	0.68	72	201" × 107"	550	Ekc	$\beta\gamma\delta$	D.19(s)
376	0419	20130423_210505	11726	Fast	698	263	0.66	66	195" × 109"	550	Ekc	$\beta\gamma\delta$	D.19(t)
377	0420	20130430_215439	11731	Nor.	26	238	0.98	185	202" × 75"	350	Ekc	$\beta\gamma$	D.20(a)
378	0421	20130501_061517	11731	Fast	116	238	0.97	70	239" × 93"	380	Ekc	$\beta\gamma\delta$	D.20(b)
379	0422	20130513_103605	11745	Fast	-631	218	0.66	30	104" × 94"	600	Ekc	$\beta\gamma$	D.20(c)
380	0423	20130513_121739	11745	Fast	-621	219	0.67	30	107" × 91"	600	Ekc	$\beta\gamma$	D.20(d)
381	0424	20130513_135528	11745	Fast	-615	219	0.68	42	110" × 100"	600	Ekc	$\beta\gamma$	D.20(e)
382	0425	20130513_153428	11745	Fast	-603	221	0.69	35	112" × 96"	600	Ekc	$\beta\gamma$	D.20(f)
383	0426	20130513_165426	11745	Fast	-592	220	0.70	35	112" × 90"	600	Ekc	$\beta\gamma$	D.20(g)
384	0427	20130513_202929	11745	Fast	-568	222	0.73	35	114" × 87"	600	Ekc	$\beta\gamma$	D.20(h)
385	0428	20130513_234629	11745	Fast	-542	222	0.75	35	122" × 88"	600	Ekc	$\beta\gamma$	D.20(i)
386	0429	20130516_154529	11748	Fast	-589	190	0.71	42	125" × 110"	260	Dki	$\beta\gamma\delta$	D.20(j)
387	0430	20130516_235827	11748	Fast	-535	193	0.76	42	123" × 102"	260	Dki	$\beta\gamma\delta$	D.20(k)
388	0431	20130517_025928	11748	Fast	-509	193	0.78	48	141" × 103"	270	Dki	$\beta\gamma\delta$	D.20(l)
389	0432	20130517_061806	11748	Fast	-481	194	0.80	54	144" × 104"	270	Dki	$\beta\gamma\delta$	D.20(m)

Table D.1. Continued.

index	inv_id	obs_id (date)(time)	NOAA AR num	type scan	x_c (")	y_c (")	μ	num tiles	size FOV	area (MSH)	Zürich class	magnetic class	Fig. (panel)
390	0433	20130517_094005	11748	Fast	-458	194	0.82	54	145" × 99"	270	Dki	$\beta\gamma\delta$	D.20(n)
391	0434	20130517_130305	11748	Fast	-438	194	0.83	48	140" × 101"	270	Dki	$\beta\gamma\delta$	D.20(o)
392	0435	20130518_065702	11748	Fast	-99	253	0.94	4	28" × 41"	220	Dai	$\beta\gamma\delta$	D.20(p)
393	0436	20130518_115505	11748	Fast	-62	253	0.95	4	35" × 42"	220	Dai	$\beta\gamma\delta$	D.20(q)
394	0437	20130518_133303	11748	Fast	-46	251	0.95	6	35" × 43"	220	Dai	$\beta\gamma\delta$	D.20(r)
395	0438	20130518_150304	11748	Fast	-31	250	0.95	6	36" × 45"	220	Dai	$\beta\gamma\delta$	D.20(s)
396	0439	20130518_165005	11748	Fast	-13	254	0.96	6	38" × 44"	220	Dai	$\beta\gamma\delta$	D.20(t)
397	0440	20130518_200305	11748	Fast	11	249	0.96	6	35" × 47"	220	Dai	$\beta\gamma\delta$	D.21(a)
398	0441	20130518_213306	11748	Fast	29	252	0.97	6	34" × 43"	220	Dai	$\beta\gamma\delta$	D.21(b)
399	0442	20130518_231505	11748	Fast	41	251	0.97	6	38" × 44"	220	Dai	$\beta\gamma\delta$	D.21(c)
400	0443	20130519_004505	11748	Fast	58	252	0.97	6	38" × 43"	140	Dao	$\beta\delta$	D.21(d)
401	0444	20130519_022005	11748	Fast	71	252	0.97	6	35" × 43"	140	Dao	$\beta\delta$	D.21(e)
402	0445	20130519_041005	11748	Fast	87	250	0.97	6	39" × 44"	140	Dao	$\beta\delta$	D.21(f)
403	0446	20130519_071505	11748	Fast	116	248	0.98	9	40" × 45"	140	Dao	$\beta\delta$	D.21(g)
404	0447	20130519_085405	11748	Fast	133	248	0.98	9	41" × 45"	140	Dao	$\beta\delta$	D.21(h)
405	0448	20130519_105005	11748	Fast	158	250	0.98	6	35" × 44"	140	Dao	$\beta\delta$	D.21(i)
406	0449	20130519_122005	11748	Fast	171	249	0.98	4	37" × 42"	140	Dao	$\beta\delta$	D.21(j)
407	0450	20130519_134905	11748	Fast	182	250	0.98	4	37" × 41"	140	Dao	$\beta\delta$	D.21(k)
408	0451	20130519_154205	11748	Fast	198	249	0.98	9	39" × 42"	140	Dao	$\beta\delta$	D.21(l)
409	0452	20130519_221223	11748	Fast	253	247	0.97	9	42" × 45"	140	Dao	$\beta\delta$	D.21(m)
410	0453	20130520_011905	11748	Fast	281	247	0.97	6	43" × 41"	110	Fao	$\beta\gamma\delta$	D.21(n)
411	0454	20130520_043605	11748	Fast	308	247	0.97	6	40" × 39"	110	Fao	$\beta\gamma\delta$	D.21(o)
412	0455	20130520_112004	11748	Fast	189	193	0.97	45	150" × 93"	110	Fao	$\beta\gamma\delta$	D.21(p)
413	0456	20130520_162004	11748	Fast	218	192	0.96	45	157" × 90"	110	Fao	$\beta\gamma\delta$	D.21(q)
414	0457	20130524_104005	11756	Fast	-333	-317	0.86	48	202" × 79"	250	Ehi	$\beta\gamma$	D.21(r)
415	0458	20130524_122306	11756	Fast	-329	-317	0.87	55	179" × 80"	250	Ehi	$\beta\gamma$	D.21(s)
416	0459	20130604_121436	11762	Fast	529	-476	0.65	40	142" × 84"	300	Dki	$\beta\gamma\delta$	D.21(t)
417	0460	20130604_135306	11762	Fast	540	-477	0.64	40	137" × 84"	300	Dki	$\beta\gamma\delta$	D.22(a)
418	0461	20130618_110138	11775	Fast	-535	-459	0.62	36	92" × 102"	380	Dko	$\beta\delta$	D.22(b)
419	0462	20130618_142006	11775	Fast	-521	-461	0.64	30	88" × 102"	380	Dko	$\beta\delta$	D.22(c)
420	0463	20130618_192638	11775	Fast	-483	-462	0.67	36	93" × 103"	380	Dko	$\beta\delta$	D.22(d)
421	0464	20130618_224137	11775	Fast	-465	-460	0.68	30	94" × 96"	380	Dko	$\beta\delta$	D.22(e)
422	0465	20130619_032837	11775	Fast	-434	-462	0.71	30	98" × 97"	410	Dkc	β	D.22(f)
423	0466	20130619_064537	11775	Fast	-411	-460	0.72	30	101" × 97"	410	Dkc	β	D.22(g)
424	0467	20130619_100236	11775	Fast	-387	-459	0.74	30	97" × 92"	410	Dkc	β	D.22(h)
425	0468	20130619_131937	11775	Fast	-345	-442	0.76	20	90" × 76"	410	Dkc	β	D.22(i)
426	0469	20130619_200505	11775	Fast	-295	-438	0.78	24	97" × 74"	410	Dkc	β	D.22(j)
427	0470	20130620_040405	11775	Fast	-230	-440	0.81	24	96" × 64"	360	Dkc	$\beta\delta$	D.22(k)
428	0471	20130620_054305	11775	Fast	-214	-437	0.81	18	92" × 60"	360	Dkc	$\beta\delta$	D.22(l)
429	0472	20130620_092306	11775	Fast	-191	-439	0.82	18	95" × 60"	360	Dkc	$\beta\delta$	D.22(m)
430	0473	20130704_223846	11785	Fast	-604	-215	0.72	40	142" × 97"	570	Fkc	$\beta\gamma$	D.22(n)
431	0474	20130705_014935	11785	Fast	-593	-220	0.74	54	149" × 103"	630	Fkc	$\beta\gamma\delta$	D.22(o)
432	0475	20130705_050632	11785	Fast	-583	-216	0.75	35	125" × 95"	630	Fkc	$\beta\gamma\delta$	D.22(p)
433	0476	20130705_081348	11785	Fast	-502	-214	0.79	35	120" × 95"	630	Fkc	$\beta\gamma\delta$	D.22(q)
434	0477	20130705_114005	11785	Fast	-526	-212	0.79	45	151" × 94"	630	Fkc	$\beta\gamma\delta$	D.22(r)
435	0478	20130707_093903	11785	Fast	-73	-233	0.95	65	217" × 96"	650	Ekc	$\beta\gamma\delta$	D.22(s)
436	0479	20130707_143916	11785	Fast	-80	-236	0.96	60	199" × 95"	650	Ekc	$\beta\gamma\delta$	D.22(t)
437	0480	20130707_162405	11785	Fast	-65	-235	0.96	60	201" × 96"	650	Ekc	$\beta\gamma\delta$	D.23(a)
438	0481	20130708_221858	11785	Fast	203	-247	0.94	12	57" × 59"	610	Ekc	$\beta\gamma\delta$	D.23(b)
439	0482	20130727_084736	11800	Fast	710	-204	0.63	20	85" × 63"	160	Dai	$\beta\gamma$	D.23(c)
440	0483	20130727_102859	11800	Fast	787	-192	0.61	24	92" × 66"	160	Dai	$\beta\gamma$	D.23(d)
441	0484	20130817_101750	11818	Fast	454	-181	0.89	28	112" × 76"	330	Dki	$\beta\gamma\delta$	D.23(e)
442	0485	20130817_184136	11818	Fast	509	-187	0.84	16	65" × 70"	330	Dki	$\beta\gamma\delta$	D.23(f)
443	0486	20130817_201708	11818	Fast	504	-181	0.84	16	67" × 64"	330	Dki	$\beta\gamma\delta$	D.23(g)
444	0487	20130817_220443	11818	Fast	593	-166	0.82	13	57" × 71"	330	Dki	$\beta\gamma\delta$	D.23(h)
445	0488	20130818_092928	11818	Fast	702	-160	0.76	13	57" × 72"	300	Dko	$\beta\gamma\delta$	D.23(i)
446	0489	20130818_210006	11818	Fast	781	-147	0.69	12	53" × 63"	300	Dko	$\beta\gamma\delta$	D.23(j)
447	0490	20130819_093505	11818	Fast	867	-138	0.59	12	46" × 69"	260	Cko	$\beta\delta$	D.23(k)
448	0491	20131010_191608	11861	Fast	-408	-223	0.84	32	129" × 76"	60	Cao	β	D.23(l)
449	0492	20131011_063405	11861	Fast	-310	-230	0.89	32	141" × 79"	200	Eac	β	D.23(m)

Table D.1. Continued.

index	inv_id	obs_id (date)(time)	NOAA AR num	type scan	x_c (")	y_c (")	μ	num tiles	size FOV	area (MSH)	Zürich class	magnetic class	Fig. (panel)
450	0493	20131022_183221	11875	Fast	-169	47	0.98	32	141" × 79"	250	Ekc	$\beta\gamma\delta$	D.23(n)
451	0494	20131023_061805	11875	Fast	-63	42	1.00	40	141" × 82"	420	Ekc	$\beta\gamma\delta$	D.23(o)
452	0495	20131024_060011	11875	Fast	187	44	0.98	36	151" × 68"	610	Ekc	$\beta\gamma\delta$	D.23(p)
453	0496	20131024_103406	11875	Fast	228	48	0.97	36	150" × 69"	610	Ekc	$\beta\gamma\delta$	D.23(q)
454	0497	20131026_061556	11875	Fast	593	51	0.79	45	151" × 96"	660	Ekc	$\beta\gamma\delta$	D.23(r)
455	0498	20131026_223109	11882	Fast	-693	-183	0.60	30	99" × 83"	280	Dko	$\beta\gamma\delta$	D.23(s)
456	0499	20131027_080005	11882	Fast	-626	-190	0.67	30	97" × 90"	300	Dki	$\beta\gamma\delta$	D.23(t)
457	0500	20131027_170005	11882	Fast	-583	-196	0.73	30	106" × 84"	300	Dki	$\beta\gamma\delta$	D.24(a)
458	0501	20131028_040005	11882	Fast	-494	-194	0.79	30	99" × 84"	390	Dkc	$\beta\gamma\delta$	D.24(b)
459	0502	20131028_100004	11882	Fast	-450	-189	0.82	24	99" × 78"	390	Dkc	$\beta\gamma\delta$	D.24(c)
460	0503	20131028_113628	11882	Fast	-469	-211	0.82	20	82" × 73"	390	Dkc	$\beta\gamma\delta$	D.24(d)
461	0504	20131028_140520	11882	Fast	-413	-192	0.84	24	96" × 77"	390	Dkc	$\beta\gamma\delta$	D.24(e)
462	0505	20131028_144914	11882	Fast	-446	-211	0.84	16	67" × 77"	390	Dkc	$\beta\gamma\delta$	D.24(f)
463	0506	20131028_151910	11882	Fast	-440	-209	0.84	16	63" × 76"	390	Dkc	$\beta\gamma\delta$	D.24(g)
464	0507	20131028_154459	11882	Fast	-436	-214	0.84	16	62" × 76"	390	Dkc	$\beta\gamma\delta$	D.24(h)
465	0508	20131028_190020	11882	Fast	-376	-203	0.86	20	69" × 86"	390	Dkc	$\beta\gamma\delta$	D.24(i)
466	0509	20131029_000004	11882	Fast	-351	-204	0.88	20	70" × 84"	330	Dkc	$\beta\gamma\delta$	D.24(j)
467	0510	20131107_094107	11890	Fast	-273	-254	0.90	96	208" × 151"	910	Ekc	$\beta\gamma\delta$	D.24(k)
468	0511	20131107_111006	11890	Fast	-260	-255	0.91	96	207" × 151"	910	Ekc	$\beta\gamma\delta$	D.24(l)
469	0512	20131107_150005	11890	Fast	-233	-255	0.92	96	210" × 152"	910	Ekc	$\beta\gamma\delta$	D.24(m)
470	0513	20131107_164506	11890	Fast	-212	-256	0.92	104	213" × 153"	910	Ekc	$\beta\gamma\delta$	D.24(n)
471	0514	20131107_214005	11890	Fast	-169	-252	0.93	104	214" × 151"	910	Ekc	$\beta\gamma\delta$	D.24(o)
472	0515	20131108_021005	11890	Fast	-137	-248	0.94	104	217" × 143"	920	Ehc	$\beta\gamma\delta$	D.24(p)
473	0516	20131108_113005	11890	Fast	-62	-243	0.96	98	236" × 136"	920	Ehc	$\beta\gamma\delta$	D.24(q)
474	0517	20131108_190005	11890	Fast	3	-236	0.96	98	235" × 131"	920	Ehc	$\beta\gamma\delta$	D.24(r)
475	0518	20131109_074004	11890	Fast	135	-244	0.96	104	228" × 140"	920	Ehc	$\beta\gamma\delta$	D.24(s)
476	0519	20131109_104806	11890	Fast	186	-251	0.95	104	213" × 140"	920	Ehc	$\beta\gamma\delta$	D.24(t)
477	0520	20131110_183005	11890	Fast	492	-255	0.87	84	203" × 134"	660	Ekc	$\beta\gamma\delta$	D.25(a)
478	0521	20131115_214505	11897	Fast	-91	-333	0.87	3	22" × 36"	310	Fkc	$\beta\gamma$	D.25(b)
479	0522	20131214_094105	11921	Fast	-276	146	0.94	25	80" × 80"	350	Cko	β	D.25(c)
480	0523	20131214_150005	11921	Fast	-224	149	0.96	20	81" × 76"	350	Cko	β	D.25(d)
481	0524	20131214_200005	11921	Fast	-181	147	0.97	20	78" × 78"	350	Cko	β	D.25(e)
482	0525	20131215_020005	11921	Fast	-121	151	0.98	20	81" × 74"	380	Cko	β	D.25(f)
483	0526	20131215_064235	11921	Fast	-83	155	0.99	20	76" × 69"	380	Cko	β	D.25(g)
484	0527	20131221_190404	11928	Fast	668	-241	0.72	60	200" × 85"	400	Ekc	$\beta\gamma$	D.25(h)
485	0528	20131221_200353	11928	Fast	618	-247	0.73	21	110" × 56"	400	Ekc	$\beta\gamma$	D.25(i)
486	0530	20131222_080005	11928	Fast	753	-243	0.65	40	177" × 74"	460	Ekc	$\beta\gamma$	D.25(j)
487	0531	20131222_085954	11928	Fast	700	-248	0.64	21	113" × 48"	460	Ekc	$\beta\gamma$	D.25(k)
488	0532	20131222_151010	11928	Fast	735	-250	0.60	14	112" × 40"	460	Ekc	$\beta\gamma$	D.25(l)
489	0533	20131222_163103	11928	Fast	803	-243	0.58	40	169" × 75"	460	Ekc	$\beta\gamma$	D.25(m)
490	0534	20131222_190412	11928	Fast	758	-250	0.57	21	111" × 48"	460	Ekc	$\beta\gamma$	D.25(n)
491	0535	20131222_213103	11928	Fast	820	-241	0.55	36	156" × 71"	460	Ekc	$\beta\gamma$	D.25(o)
492	0536	20131222_223054	11928	Fast	775	-252	0.55	21	113" × 56"	460	Ekc	$\beta\gamma$	D.25(p)
493	0537	20140105_000405	11944	Fast	-608	-108	0.77	96	209" × 150"	1470	Fkc	$\beta\gamma\delta$	D.25(q)
494	0538	20140107_212006	11944	Fast	5	-82	1.00	105	251" × 122"	1415	Fkc	$\beta\gamma\delta$	D.25(r)
495	0539	20140109_040506	11944	Fast	299	-84	0.95	78	227" × 117"	1560	Fkc	$\beta\gamma\delta$	D.25(s)
496	0540	20140109_160024	11944	Fast	380	-85	0.92	84	235" × 110"	1560	Fkc	$\beta\gamma\delta$	D.25(t)
497	0541	20140110_144924	11944	Fast	565	-119	0.84	84	203" × 133"	1420	Fkc	$\beta\gamma\delta$	D.26(a)
498	0542	20140111_065506	11944	Fast	693	-126	0.75	84	199" × 134"	1300	Fkc	$\beta\gamma\delta$	D.26(b)
499	0543	20140111_154006	11944	Fast	754	-130	0.69	84	198" × 129"	1300	Fkc	$\beta\gamma\delta$	D.26(c)
500	0544	20140111_190006	11944	Fast	775	-130	0.66	84	199" × 126"	1300	Fkc	$\beta\gamma\delta$	D.26(d)
501	0545	20140201_104205	11967	Fast	-378	-137	0.91	105	248" × 123"	1000	Fkc	$\beta\gamma\delta$	D.26(e)
502	0546	20140201_140005	11967	Fast	-356	-136	0.92	98	246" × 124"	1000	Fkc	$\beta\gamma\delta$	D.26(f)
503	0547	20140201_165405	11967	Fast	-341	-135	0.92	98	233" × 126"	1000	Fkc	$\beta\gamma\delta$	D.26(g)
504	0548	20140201_201319	11967	Fast	-305	-134	0.94	105	253" × 126"	1000	Fkc	$\beta\gamma\delta$	D.26(h)
505	0549	20140201_231906	11967	Fast	-280	-130	0.95	105	254" × 122"	1000	Fkc	$\beta\gamma\delta$	D.26(i)
506	0550	20140202_022005	11967	Fast	-249	-131	0.96	105	252" × 123"	1410	Fkc	$\beta\gamma\delta$	D.26(j)
507	0551	20140202_041505	11967	Fast	-264	-128	0.95	77	195" × 121"	1410	Fkc	$\beta\gamma\delta$	D.26(k)
508	0552	20140202_071205	11967	Fast	-206	-129	0.97	105	252" × 124"	1410	Fkc	$\beta\gamma\delta$	D.26(l)
509	0553	20140202_102005	11967	Fast	-178	-128	0.97	105	251" × 123"	1410	Fkc	$\beta\gamma\delta$	D.26(m)
510	0554	20140202_130005	11967	Fast	-157	-127	0.98	105	253" × 122"	1410	Fkc	$\beta\gamma\delta$	D.26(n)

Table D.1. Continued.

index	inv_id	obs_id (date)(time)	NOAA AR num	type scan	x_c (")	y_c (")	μ	num tiles	size FOV	area (MSH)	Zürich class	magnetic class	Fig. (panel)
511	0555	20140202_160005	11967	Fast	-128	-128	0.98	105	254" × 125"	1410	Fkc	$\beta\gamma\delta$	D.26(o)
512	0556	20140202_192005	11967	Fast	-101	-128	0.99	105	252" × 126"	1410	Fkc	$\beta\gamma\delta$	D.26(p)
513	0557	20140202_223004	11967	Fast	-67	-127	0.99	105	253" × 125"	1410	Fkc	$\beta\gamma\delta$	D.26(q)
514	0558	20140203_013005	11967	Fast	-39	-127	0.99	105	252" × 125"	1510	Fkc	$\beta\gamma\delta$	D.26(r)
515	0559	20140203_044004	11967	Fast	-15	-126	0.99	105	256" × 125"	1510	Fkc	$\beta\gamma\delta$	D.26(s)
516	0560	20140203_075004	11967	Fast	16	-126	0.99	105	254" × 124"	1510	Fkc	$\beta\gamma\delta$	D.26(t)
517	0561	20140203_182306	11967	Fast	48	-107	0.99	40	131" × 86"	1510	Fkc	$\beta\gamma\delta$	D.27(a)
518	0562	20140204_003801	11967	Fast	122	-108	0.99	54	145" × 99"	1490	Fkc	$\beta\gamma\delta$	D.27(b)
519	0563	20140204_034005	11967	Fast	143	-108	0.98	54	157" × 103"	1490	Fkc	$\beta\gamma\delta$	D.27(c)
520	0564	20140204_070214	11967	Fast	228	-109	0.97	90	256" × 116"	1490	Fkc	$\beta\gamma\delta$	D.27(d)
521	0565	20140204_100005	11967	Fast	187	-111	0.97	48	133" × 103"	1490	Fkc	$\beta\gamma\delta$	D.27(e)
522	0567	20140204_154250	11967	Fast	244	-112	0.96	54	146" × 109"	1490	Fkc	$\beta\gamma\delta$	D.27(f)
523	0568	20140204_190005	11967	Fast	322	-108	0.94	84	246" × 106"	1490	Fkc	$\beta\gamma\delta$	D.27(g)
524	0569	20140205_011005	11967	Fast	368	-112	0.92	79	230" × 105"	1580	Fkc	$\beta\gamma\delta$	D.27(h)
525	0570	20140205_073005	11967	Fast	433	-115	0.89	90	259" × 103"	1580	Fkc	$\beta\gamma\delta$	D.27(i)
526	0571	20140205_104005	11967	Fast	460	-118	0.87	90	258" × 101"	1580	Fkc	$\beta\gamma\delta$	D.27(j)
527	0572	20140205_145005	11967	Fast	495	-120	0.85	90	257" × 103"	1580	Fkc	$\beta\gamma\delta$	D.27(k)
528	0573	20140206_000004	11967	Fast	556	-125	0.81	78	222" × 105"	1500	Fkc	$\beta\gamma\delta$	D.27(l)
529	0574	20140206_032004	11967	Fast	533	-125	0.83	20	71" × 86"	1500	Fkc	$\beta\gamma\delta$	D.27(m)
530	0575	20140213_103140	11974	Fast	332	-99	0.95	50	162" × 94"	460	Fkc	$\beta\gamma\delta$	D.27(n)
531	0576	20140213_143006	11974	Fast	318	-100	0.95	66	191" × 105"	460	Fkc	$\beta\gamma\delta$	D.27(o)
532	0577	20140213_193104	11974	Fast	368	-103	0.93	66	192" × 103"	460	Fkc	$\beta\gamma\delta$	D.27(p)
533	0578	20140214_000005	11974	Fast	404	-101	0.92	66	195" × 99"	780	Fkc	$\beta\gamma\delta$	D.27(q)
534	0579	20140214_030859	11974	Fast	386	-105	0.91	42	112" × 99"	780	Fkc	$\beta\gamma\delta$	D.27(r)
535	0580	20140214_063104	11974	Fast	473	-106	0.89	78	221" × 102"	780	Fkc	$\beta\gamma\delta$	D.27(s)
536	0581	20140214_120005	11974	Fast	519	-109	0.86	78	221" × 102"	780	Fkc	$\beta\gamma\delta$	D.27(t)
537	0582	20140214_200005	11974	Fast	585	-115	0.82	65	218" × 98"	780	Fkc	$\beta\gamma\delta$	D.28(a)
538	0583	20140215_003005	11974	Fast	623	-118	0.79	72	212" × 104"	990	Fkc	$\beta\gamma\delta$	D.28(b)
539	0584	20140215_040005	11974	Fast	645	-120	0.77	60	210" × 93"	990	Fkc	$\beta\gamma\delta$	D.28(c)
540	0585	20140215_090005	11974	Fast	658	-124	0.76	60	167" × 99"	990	Fkc	$\beta\gamma\delta$	D.28(d)
541	0586	20140215_103600	11974	Fast	687	-124	0.74	72	202" × 103"	990	Fkc	$\beta\gamma\delta$	D.28(e)
542	0587	20140215_154106	11974	Fast	718	-126	0.71	66	194" × 108"	990	Fkc	$\beta\gamma\delta$	D.28(f)
543	0588	20140226_235108	11990	Fast	-667	-132	0.60	12	44" × 62"	210	Dkc	$\beta\delta$	D.28(g)
544	0589	20140227_030005	11990	Fast	-646	-127	0.63	9	50" × 59"	210	Dkc	$\beta\delta$	D.28(h)
545	0590	20140227_120038	11990	Fast	-666	-120	0.68	9	48" × 60"	210	Dkc	$\beta\delta$	D.28(i)
546	0591	20140227_133005	11990	Fast	-656	-118	0.69	9	49" × 57"	210	Dkc	$\beta\delta$	D.28(j)
547	0592	20140227_181805	11990	Fast	-623	-113	0.72	9	48" × 55"	210	Dkc	$\beta\delta$	D.28(k)
548	0593	20140227_233505	11990	Fast	-589	-111	0.76	9	50" × 56"	250	Dkc	$\beta\delta$	D.28(l)
549	0594	20140228_021505	11990	Fast	-573	-109	0.77	9	55" × 54"	250	Dkc	$\beta\delta$	D.28(m)
550	0595	20140228_113006	11990	Fast	-499	-108	0.83	9	54" × 58"	250	Dkc	$\beta\delta$	D.28(n)
551	0596	20140228_140005	11990	Fast	-483	-105	0.84	12	57" × 57"	250	Dkc	$\beta\delta$	D.28(o)
552	0597	20140228_233534	11990	Fast	-362	-100	0.89	12	61" × 57"	250	Dkc	$\beta\delta$	D.28(p)
553	0598	20140301_022804	11990	Fast	-347	-100	0.90	12	59" × 58"	250	Dkc	$\beta\delta$	D.28(q)
554	0599	20140311_143005	12002	Fast	-433	-213	0.85	50	174" × 94"	150	Dac	$\beta\gamma\delta$	D.28(r)
555	0600	20140329_150006	12017	Fast	605	295	0.80	12	72" × 51"	150	Dao	$\beta\delta$	D.28(s)
556	0601	20140329_170006	12017	Fast	615	292	0.79	15	75" × 50"	150	Dao	$\beta\delta$	D.28(t)
557	0603	20140607_145319	12080	Fast	-115	-201	0.96	40	162" × 73"	160	Dai	$\beta\gamma\delta$	D.29(a)
558	0604	20140607_195436	12080	Fast	-60	-203	0.96	36	157" × 71"	160	Dai	$\beta\gamma\delta$	D.29(b)
559	0605	20140607_231505	12080	Fast	-5	-199	0.97	28	112" × 63"	160	Dai	$\beta\gamma\delta$	D.29(c)
560	0606	20140608_022356	12080	Fast	-7	-203	0.97	40	166" × 69"	230	Dac	$\beta\gamma\delta$	D.29(d)
561	0607	20140609_043534	12080	Fast	226	-215	0.96	50	175" × 83"	340	Dkc	$\beta\gamma\delta$	D.29(e)
562	0608	20140609_093452	12080	Fast	276	-213	0.95	50	173" × 87"	340	Dkc	$\beta\gamma\delta$	D.29(f)
563	0609	20140610_001635	12080	Fast	414	-217	0.90	55	191" × 83"	300	Ekc	$\beta\gamma\delta$	D.29(g)
564	0610	20140610_033335	12080	Fast	451	-203	0.88	36	154" × 71"	300	Ekc	$\beta\gamma\delta$	D.29(h)
565	0611	20140610_082905	12080	Fast	495	-206	0.86	36	153" × 76"	300	Ekc	$\beta\gamma\delta$	D.29(i)
566	0612	20140610_114536	12080	Fast	512	-211	0.85	36	154" × 79"	300	Ekc	$\beta\gamma\delta$	D.29(j)
567	0613	20140610_231505	12080	Fast	618	-210	0.78	40	142" × 82"	300	Ekc	$\beta\gamma\delta$	D.29(k)
568	0614	20140611_023135	12080	Fast	639	-211	0.77	40	139" × 87"	320	Dkc	$\beta\gamma\delta$	D.29(l)
569	0615	20140611_090858	12085	Fast	692	-209	0.72	40	137" × 91"	460	Ekc	$\beta\gamma$	D.29(m)
570	0616	20140611_122235	12085	Fast	712	-211	0.70	40	134" × 84"	460	Ekc	$\beta\gamma$	D.29(n)

Table D.1. Continued.

index	inv_id	obs_id (date)(time)	NOAA AR num	type scan	x_c (")	y_c (")	μ	num tiles	size FOV	area (MSH)	Zürich class	magnetic class	Fig. (panel)
571	0618	20140701_194405	12104	Fast	-554	-249	0.68	25	87" × 81"	350	Dkc	$\beta\gamma\delta$	D.29(o)
572	0619	20140701_212105	12104	Fast	-544	-252	0.69	25	87" × 83"	350	Dkc	$\beta\gamma\delta$	D.29(p)
573	0620	20140702_003105	12104	Fast	-519	-252	0.71	25	83" × 82"	410	Dkc	$\beta\gamma\delta$	D.29(q)
574	0621	20140702_034805	12104	Fast	-496	-256	0.73	25	82" × 84"	410	Dkc	$\beta\gamma\delta$	D.29(r)
575	0622	20140702_070505	12104	Fast	-471	-258	0.74	25	80" × 86"	410	Dkc	$\beta\gamma\delta$	D.29(s)
576	0623	20140702_102205	12104	Fast	-453	-259	0.76	25	79" × 86"	410	Dkc	$\beta\gamma\delta$	D.29(t)
577	0624	20140702_120005	12104	Fast	-436	-260	0.77	25	78" × 86"	410	Dkc	$\beta\gamma\delta$	D.30(a)
578	0625	20140702_140005	12104	Fast	-410	-260	0.78	20	65" × 86"	410	Dkc	$\beta\gamma\delta$	D.30(b)
579	0626	20140702_170605	12104	Fast	-399	-264	0.80	25	76" × 88"	410	Dkc	$\beta\gamma\delta$	D.30(c)
580	0627	20140702_202200	12104	Fast	-362	-262	0.81	20	65" × 86"	410	Dkc	$\beta\gamma\delta$	D.30(d)
581	0628	20140703_074304	12104	Fast	-281	-264	0.86	20	69" × 84"	470	Dkc	$\beta\gamma\delta$	D.30(e)
582	0630	20140824_011822	12149	Fast	-698	112	0.65	48	132" × 103"	120	Eac	$\beta\gamma$	D.30(f)
583	0631	20140826_105321	12146	Fast	733	70	0.67	25	85" × 86"	290	Dki	$\beta\delta$	D.30(g)
584	0632	20140826_141206	12146	Fast	751	73	0.65	25	82" × 83"	290	Dki	$\beta\delta$	D.30(h)
585	0633	20140826_212506	12148	Fast	796	77	0.59	25	76" × 91"	60	Cao	β	D.30(i)
586	0634	20140925_142206	12172	Fast	-259	-273	0.90	65	222" × 90"	440	Ekc	$\beta\gamma$	D.30(j)
587	0636	20140927_110005	12172	Fast	137	-287	0.94	84	240" × 104"	500	Ekc	$\beta\gamma$	D.30(k)
588	0637	20140928_011505	12172	Fast	268	-288	0.91	70	240" × 89"	460	Ekc	$\beta\gamma$	D.30(l)
589	0638	20140928_134005	12172	Fast	381	-290	0.87	84	238" × 111"	460	Ekc	$\beta\gamma$	D.30(m)
590	0639	20140929_220004	12172	Fast	790	-309	0.61	56	119" × 142"	460	Ekc	$\beta\gamma$	D.30(n)
591	0640	20141021_130127	12192	Fast	-465	-318	0.81	108	209" × 158"	2180	Fkc	$\beta\gamma\delta$	D.30(o)
592	0641	20141021_154005	12192	Fast	-437	-319	0.82	108	212" × 158"	2180	Fkc	$\beta\gamma\delta$	D.30(p)
593	0642	20141021_190005	12192	Fast	-414	-321	0.84	117	220" × 160"	2180	Fkc	$\beta\gamma\delta$	D.30(q)
594	0643	20141021_220005	12192	Fast	-374	-323	0.85	117	220" × 160"	2180	Fkc	$\beta\gamma\delta$	D.30(r)
595	0644	20141022_013937	12192	Fast	-344	-324	0.87	49	113" × 119"	2410	Fkc	$\beta\gamma\delta$	D.30(s)
596	0645	20141022_041102	12192	Fast	-322	-324	0.88	49	112" × 120"	2410	Fkc	$\beta\gamma\delta$	D.30(t)
597	0646	20141024_003106	12192	Fast	68	-327	0.94	135	256" × 161"	2740	Fkc	$\beta\gamma\delta$	D.31(a)
598	0647	20141024_021005	12192	Fast	82	-327	0.94	135	257" × 159"	2740	Fkc	$\beta\gamma\delta$	D.31(b)
599	0648	20141024_040005	12192	Fast	98	-326	0.93	135	256" × 159"	2740	Fkc	$\beta\gamma\delta$	D.31(c)
600	0649	20141024_070006	12192	Fast	124	-326	0.93	135	255" × 160"	2740	Fkc	$\beta\gamma\delta$	D.31(d)
601	0650	20141024_084505	12192	Fast	139	-326	0.93	135	248" × 160"	2740	Fkc	$\beta\gamma\delta$	D.31(e)
602	0651	20141024_203004	12192	Fast	283	-322	0.90	108	199" × 159"	2740	Fkc	$\beta\gamma\delta$	D.31(f)
603	0653	20141024_234105	12192	Fast	267	-321	0.90	126	247" × 159"	2740	Fkc	$\beta\gamma\delta$	D.31(g)
604	0654	20141025_074004	12192	Fast	337	-319	0.88	135	251" × 160"	2510	Fkc	$\beta\gamma\delta$	D.31(h)
605	0655	20141025_110049	12192	Fast	367	-320	0.86	81	149" × 162"	2510	Fkc	$\beta\gamma\delta$	D.31(i)
606	0657	20141025_230021	12192	Fast	400	-315	0.85	12	28" × 102"	2510	Fkc	$\beta\gamma\delta$	D.31(j)
607	0658	20141026_110005	12192	Fast	553	-308	0.75	81	151" × 160"	2570	Fkc	$\beta\gamma\delta$	D.31(k)
608	0659	20141026_233004	12192	Fast	639	-301	0.68	81	151" × 160"	2570	Fkc	$\beta\gamma\delta$	D.31(l)
609	0664	20141027_191004	12192	Fast	752	-289	0.55	72	138" × 160"	2750	Fkc	$\beta\gamma\delta$	D.31(m)
610	0665	20141027_221951	12192	Fast	771	-287	0.52	49	112" × 119"	2750	Fkc	$\beta\gamma\delta$	D.31(n)
611	0666	20141028_025431	12192	Fast	793	-284	0.49	49	112" × 120"	2380	Fkc	$\beta\gamma\delta$	D.31(o)
612	0668	20141028_044051	12192	Fast	758	-283	0.54	36	62" × 161"	2380	Fkc	$\beta\gamma\delta$	D.31(p)
613	0669	20141106_062834	12205	Fast	-751	228	0.54	40	130" × 95"	250	Ekc	$\beta\gamma\delta$	D.31(q)
614	0670	20141106_072825	12205	Fast	-769	224	0.57	30	95" × 85"	250	Ekc	$\beta\gamma\delta$	D.31(r)
615	0672	20141106_170111	12205	Fast	-702	232	0.60	32	142" × 79"	250	Ekc	$\beta\gamma\delta$	D.31(s)
616	0674	20141106_203419	12205	Fast	-693	231	0.63	45	150" × 89"	250	Ekc	$\beta\gamma\delta$	D.31(t)
617	0675	20141107_040201	12205	Fast	-651	226	0.70	28	109" × 75"	360	Ekc	$\beta\gamma\delta$	D.32(a)
618	0676	20141107_182005	12205	Fast	-553	223	0.79	28	111" × 72"	360	Ekc	$\beta\gamma\delta$	D.32(b)
619	0677	20141107_184601	12205	Nor.	-547	222	0.79	88	97" × 71"	360	Ekc	$\beta\gamma\delta$	D.32(c)
620	0678	20141107_222544	12205	Fast	-521	222	0.81	28	112" × 69"	360	Ekc	$\beta\gamma\delta$	D.32(d)
621	0679	20141108_063905	12205	Fast	-460	219	0.85	28	112" × 73"	410	Ekc	$\beta\gamma\delta$	D.32(e)
622	0680	20141110_075739	12205	Fast	52	201	0.98	45	152" × 93"	350	Ekc	$\beta\gamma\delta$	D.32(f)
623	0681	20141111_183840	12205	Fast	353	205	0.93	45	153" × 84"	280	Dkc	$\beta\gamma\delta$	D.32(g)
624	0682	20141115_102421	12209	Fast	-818	-273	0.43	64	133" × 143"	680	Eac	$\beta\gamma$	D.32(h)
625	0683	20141115_231101	12209	Fast	-762	-276	0.53	72	144" × 147"	680	Fkc	$\beta\gamma$	D.32(i)
626	0684	20141116_014605	12209	Fast	-754	-277	0.55	72	147" × 136"	800	Fkc	$\beta\gamma\delta$	D.32(j)
627	0685	20141116_080039	12209	Fast	-755	-280	0.55	35	76" × 132"	800	Fkc	$\beta\gamma\delta$	D.32(k)
628	0686	20141116_110005	12209	Fast	-735	-280	0.57	35	78" × 129"	800	Fkc	$\beta\gamma\delta$	D.32(l)
629	0687	20141116_150004	12209	Fast	-682	-282	0.64	72	147" × 138"	800	Fkc	$\beta\gamma\delta$	D.32(m)
630	0688	20141116_200048	12209	Fast	-582	-284	0.70	84	202" × 125"	800	Fkc	$\beta\gamma\delta$	D.32(n)

Table D.1. Continued.

index	inv_id	obs_id (date)(time)	NOAA AR num	type scan	x_c (")	y_c (")	μ	num tiles	size FOV	area (MSH)	Zürich class	magnetic class	Fig. (panel)
631	0689	20141116_230004	12209	Fast	-558	-285	0.72	84	200" × 123"	800	Fkc	$\beta\gamma\delta$	D.32(o)
632	0690	20141117_090004	12209	Fast	-489	-286	0.78	84	204" × 125"	940	Fkc	$\beta\gamma\delta$	D.32(p)
633	0691	20141118_120006	12209	Fast	-316	-302	0.86	35	90" × 119"	990	Fkc	$\beta\gamma\delta$	D.32(q)
634	0692	20141118_133006	12209	Fast	-292	-302	0.87	36	94" × 103"	990	Fkc	$\beta\gamma\delta$	D.32(r)
635	0693	20141118_160506	12209	Fast	-273	-302	0.87	30	85" × 107"	990	Fkc	$\beta\gamma\delta$	D.32(s)
636	0694	20141118_193006	12209	Fast	-248	-302	0.89	36	95" × 105"	990	Fkc	$\beta\gamma\delta$	D.32(t)
637	0695	20141118_224006	12209	Fast	-211	-304	0.90	36	94" × 117"	990	Fkc	$\beta\gamma\delta$	D.33(a)
638	0696	20141119_013005	12209	Fast	-187	-304	0.91	36	104" × 113"	990	Fkc	$\beta\gamma\delta$	D.33(b)
639	0697	20141119_031505	12209	Fast	-177	-304	0.91	36	95" × 112"	1100	Fkc	$\beta\gamma\delta$	D.33(c)
640	0698	20141119_100005	12209	Fast	-117	-304	0.93	36	108" × 116"	1100	Fkc	$\beta\gamma\delta$	D.33(d)
641	0699	20141119_130005	12209	Fast	-93	-305	0.93	42	110" × 113"	1100	Fkc	$\beta\gamma\delta$	D.33(e)
642	0700	20141119_164505	12209	Fast	-53	-302	0.94	42	112" × 116"	1100	Fkc	$\beta\gamma\delta$	D.33(f)
643	0701	20141119_200005	12209	Fast	-25	-304	0.94	42	111" × 117"	1100	Fkc	$\beta\gamma\delta$	D.33(g)
644	0702	20141119_231005	12209	Fast	4	-303	0.95	42	110" × 113"	1100	Fkc	$\beta\gamma\delta$	D.33(h)
645	0703	20141120_021005	12209	Fast	30	-304	0.95	49	110" × 126"	930	Fko	$\beta\gamma\delta$	D.33(i)
646	0704	20141120_070048	12209	Fast	15	-294	0.95	35	89" × 132"	930	Fko	$\beta\gamma\delta$	D.33(j)
647	0705	20141120_120048	12209	Fast	116	-304	0.95	36	97" × 111"	930	Fko	$\beta\gamma\delta$	D.33(k)
648	0706	20141120_140005	12209	Fast	132	-302	0.95	36	99" × 109"	930	Fko	$\beta\gamma\delta$	D.33(l)
649	0707	20141120_195942	12209	Fast	105	-303	0.94	36	103" × 100"	930	Fko	$\beta\gamma\delta$	D.33(m)
650	0708	20141120_221104	12209	Fast	198	-301	0.94	36	105" × 111"	930	Fko	$\beta\gamma\delta$	D.33(n)
651	0709	20141121_011005	12209	Fast	230	-302	0.94	36	105" × 103"	970	Fko	$\beta\gamma\delta$	D.33(o)
652	0710	20141121_044536	12209	Fast	196	-302	0.93	30	98" × 96"	970	Fko	$\beta\gamma\delta$	D.33(p)
653	0711	20141121_091903	12209	Fast	303	-301	0.92	36	98" × 102"	970	Fko	$\beta\gamma\delta$	D.33(q)
654	0712	20141121_121804	12209	Fast	329	-301	0.92	36	103" × 101"	970	Fko	$\beta\gamma\delta$	D.33(r)
655	0713	20141121_211048	12209	Fast	343	-289	0.89	36	101" × 108"	970	Fko	$\beta\gamma\delta$	D.33(s)
656	0714	20141122_001504	12209	Fast	376	-290	0.88	42	106" × 121"	900	Fko	$\beta\gamma\delta$	D.33(t)
657	0715	20141122_005652	12209	Fast	362	-296	0.88	36	103" × 106"	900	Fko	$\beta\gamma\delta$	D.34(a)
658	0716	20141122_033802	12209	Fast	389	-297	0.87	36	99" × 102"	900	Fko	$\beta\gamma\delta$	D.34(b)
659	0717	20141122_220054	12209	Fast	609	-292	0.78	42	109" × 101"	900	Fko	$\beta\gamma\delta$	D.34(c)
660	0718	20141123_023004	12209	Fast	637	-291	0.76	36	100" × 101"	950	Fko	$\beta\gamma\delta$	D.34(d)
661	0719	20141123_062123	12209	Fast	654	-289	0.75	30	85" × 100"	950	Fko	$\beta\gamma\delta$	D.34(e)
662	0720	20141123_110004	12209	Fast	735	-288	0.68	70	175" × 121"	950	Fko	$\beta\gamma\delta$	D.34(f)
663	0721	20141123_160004	12209	Fast	766	-286	0.65	70	172" × 121"	950	Fko	$\beta\gamma\delta$	D.34(g)
664	0722	20141123_210004	12209	Fast	794	-285	0.61	70	173" × 122"	950	Fko	$\beta\gamma\delta$	D.34(h)
665	0723	20141124_020043	12209	Fast	753	-284	0.61	35	111" × 95"	1000	Fki	$\beta\gamma\delta$	D.34(i)
666	0724	20141124_080004	12209	Fast	798	-283	0.55	42	124" × 111"	1000	Fki	$\beta\gamma\delta$	D.34(j)
667	0725	20141124_140006	12209	Fast	821	-281	0.52	30	101" × 97"	1000	Fki	$\beta\gamma\delta$	D.34(k)
668	0726	20141129_224005	12224	Fast	-498	-344	0.78	50	166" × 94"	10	Bxo	β	D.34(l)
669	0727	20141202_211505	12222	Fast	244	-338	0.92	28	124" × 78"	650	Eki	$\beta\gamma$	D.34(m)
670	0728	20141203_001505	12222	Fast	129	-348	0.92	65	217" × 87"	620	Eki	$\beta\gamma$	D.34(n)
671	0729	20141203_081505	12222	Fast	200	-348	0.91	65	217" × 84"	620	Eki	$\beta\gamma$	D.34(o)
672	0730	20141203_111005	12222	Fast	235	-347	0.91	60	209" × 83"	620	Eki	$\beta\gamma$	D.34(p)
673	0731	20141204_141506	12222	Fast	446	-342	0.82	60	199" × 86"	570	Ekc	$\beta\gamma$	D.34(q)
674	0732	20141204_210005	12222	Fast	616	-336	0.78	12	44" × 64"	570	Ekc	$\beta\gamma$	D.34(r)
675	0733	20141205_030005	12222	Fast	675	-331	0.73	24	99" × 79"	770	Ekc	$\beta\gamma$	D.34(s)
676	0734	20141205_075005	12222	Fast	594	-343	0.73	50	172" × 84"	770	Ekc	$\beta\gamma$	D.34(t)
677	0735	20141205_105005	12222	Fast	614	-337	0.72	50	171" × 83"	770	Ekc	$\beta\gamma$	D.35(a)
678	0736	20141205_163408	12222	Fast	658	-330	0.68	40	172" × 75"	770	Ekc	$\beta\gamma$	D.35(b)
679	0737	20141216_110511	12242	Fast	-290	-299	0.89	48	142" × 114"	360	Dkc	$\beta\gamma\delta$	D.35(c)
680	0738	20141217_100116	12242	Fast	-53	-296	0.95	42	111" × 102"	630	Dkc	$\beta\gamma\delta$	D.35(d)
681	0739	20141217_233104	12242	Fast	36	-294	0.95	78	214" × 115"	630	Dkc	$\beta\gamma\delta$	D.35(e)
682	0740	20141218_151342	12242	Fast	170	-292	0.94	66	193" × 110"	700	Ekc	$\beta\gamma\delta$	D.35(f)
683	0741	20141218_223006	12242	Fast	318	-293	0.92	63	156" × 117"	700	Ekc	$\beta\gamma\delta$	D.35(g)
684	0742	20141219_100006	12242	Fast	442	-293	0.88	60	163" × 115"	970	Ekc	$\beta\gamma\delta$	D.35(h)
685	0743	20141219_150006	12242	Fast	487	-293	0.86	63	161" × 118"	970	Ekc	$\beta\gamma\delta$	D.35(i)
686	0744	20141219_223124	12242	Fast	434	-292	0.85	30	88" × 109"	970	Ekc	$\beta\gamma\delta$	D.35(j)
687	0745	20141220_003053	12242	Fast	459	-293	0.85	30	83" × 115"	1080	Ekc	$\beta\gamma\delta$	D.35(k)
688	0746	20141220_101605	12242	Fast	665	-294	0.77	56	142" × 121"	1080	Ekc	$\beta\gamma\delta$	D.35(l)
689	0747	20141220_154505	12242	Fast	705	-293	0.74	56	143" × 121"	1080	Ekc	$\beta\gamma\delta$	D.35(m)
690	0748	20150109_092006	12257	Fast	340	183	0.93	60	166" × 100"	170	Dai	β	D.35(n)
691	0749	20150109_132307	12257	Fast	376	184	0.92	60	165" × 102"	170	Dai	β	D.35(o)

Table D.1. Continued.

index	inv_id	obs_id (date)(time)	NOAA AR num	type scan	x_c (")	y_c (")	μ	num tiles	size FOV	area (MSH)	Zürich class	magnetic class	Fig. (panel)
692	0750	20150109_182020	12257	Fast	419	183	0.90	60	166" × 101"	170	Dai	β	D.35(p)
693	0751	20150111_210105	12257	Fast	826	159	0.59	35	119" × 87"	470	Ekc	$\beta\delta$	D.35(q)
694	0752	20150111_234445	12262	Fast	820	161	0.59	35	113" × 87"	20	Cro	β	D.35(r)
695	0753	20150126_000204	12268	Fast	-534	-74	0.79	72	202" × 103"	360	Eki	$\beta\gamma$	D.35(s)
696	0754	20150309_025047	12297	Fast	-758	-200	0.57	30	94" × 81"	260	Dhc	$\beta\gamma\delta$	D.35(t)
697	0755	20150309_051505	12297	Fast	-743	-199	0.59	30	97" × 82"	260	Dhc	$\beta\gamma\delta$	D.36(a)
698	0756	20150309_070504	12297	Fast	-733	-197	0.60	30	94" × 80"	260	Dhc	$\beta\gamma\delta$	D.36(b)
699	0757	20150309_103622	12297	Fast	-704	-179	0.63	30	102" × 87"	260	Dhc	$\beta\gamma\delta$	D.36(c)
700	0758	20150309_123006	12297	Fast	-693	-175	0.64	30	106" × 84"	260	Dhc	$\beta\gamma\delta$	D.36(d)
701	0759	20150309_140005	12297	Fast	-686	-176	0.65	35	109" × 87"	260	Dhc	$\beta\gamma\delta$	D.36(e)
702	0760	20150309_154006	12297	Fast	-672	-173	0.67	35	109" × 86"	260	Dhc	$\beta\gamma\delta$	D.36(f)
703	0761	20150309_171106	12297	Fast	-664	-171	0.68	30	108" × 81"	260	Dhc	$\beta\gamma\delta$	D.36(g)
704	0762	20150309_184806	12297	Fast	-654	-170	0.69	35	109" × 86"	260	Dhc	$\beta\gamma\delta$	D.36(h)
705	0763	20150309_204806	12297	Fast	-642	-172	0.70	35	111" × 88"	260	Dhc	$\beta\gamma\delta$	D.36(i)
706	0764	20150309_223805	12297	Fast	-630	-168	0.71	35	114" × 84"	260	Dhc	$\beta\gamma\delta$	D.36(j)
707	0765	20150310_000005	12297	Fast	-623	-168	0.72	35	112" × 85"	260	Dac	$\beta\delta$	D.36(k)
708	0766	20150310_010006	12297	Fast	-623	-167	0.72	30	101" × 86"	260	Dac	$\beta\delta$	D.36(l)
709	0767	20150310_024006	12297	Fast	-605	-168	0.74	35	113" × 89"	260	Dac	$\beta\delta$	D.36(m)
710	0768	20150310_043005	12297	Fast	-595	-169	0.75	35	118" × 86"	260	Dac	$\beta\delta$	D.36(n)
711	0769	20150310_061705	12297	Fast	-583	-171	0.76	35	122" × 94"	260	Dac	$\beta\delta$	D.36(o)
712	0770	20150310_074505	12297	Fast	-582	-162	0.76	35	111" × 81"	260	Dac	$\beta\delta$	D.36(p)
713	0771	20150310_093005	12297	Fast	-568	-162	0.78	35	110" × 81"	260	Dac	$\beta\delta$	D.36(q)
714	0772	20150310_110406	12297	Fast	-540	-162	0.79	35	114" × 90"	260	Dac	$\beta\delta$	D.36(r)
715	0773	20150310_165005	12297	Fast	-500	-159	0.82	35	121" × 86"	260	Dac	$\beta\delta$	D.36(s)
716	0774	20150311_031505	12297	Fast	-425	-157	0.87	35	116" × 95"	280	Dkc	$\beta\gamma\delta$	D.36(t)
717	0775	20150311_081005	12297	Fast	-382	-153	0.89	35	118" × 97"	280	Dkc	$\beta\gamma\delta$	D.37(a)
718	0776	20150311_220105	12297	Fast	-279	-149	0.94	48	139" × 103"	280	Dkc	$\beta\gamma\delta$	D.37(b)
719	0777	20150311_223546	12297	Fast	-279	-167	0.94	35	113" × 98"	280	Dkc	$\beta\gamma\delta$	D.37(c)
720	0778	20150312_032226	12297	Fast	-238	-161	0.95	35	111" × 97"	350	Dkc	$\beta\gamma\delta$	D.37(d)
721	0779	20150312_044309	12297	Fast	-226	-161	0.96	42	112" × 99"	350	Dkc	$\beta\gamma\delta$	D.37(e)
722	0780	20150312_103721	12297	Fast	-174	-146	0.97	54	149" × 101"	350	Dkc	$\beta\gamma\delta$	D.37(f)
723	0781	20150312_135257	12297	Fast	-145	-163	0.97	35	112" × 98"	350	Dkc	$\beta\gamma\delta$	D.37(g)
724	0782	20150312_155021	12297	Fast	-119	-148	0.98	54	145" × 105"	350	Dkc	$\beta\gamma\delta$	D.37(h)
725	0783	20150312_210006	12297	Fast	-77	-146	0.98	54	148" × 101"	350	Dkc	$\beta\gamma\delta$	D.37(i)
726	0784	20150312_214800	12297	Fast	-75	-164	0.98	35	113" × 98"	350	Dkc	$\beta\gamma\delta$	D.37(j)
727	0785	20150313_030121	12297	Fast	-27	-147	0.98	54	151" × 109"	340	Dkc	$\beta\gamma\delta$	D.37(k)
728	0786	20150313_103036	12297	Fast	38	-151	0.98	54	151" × 102"	340	Dkc	$\beta\gamma\delta$	D.37(l)
729	0787	20150313_200005	12297	Fast	122	-156	0.98	45	149" × 95"	340	Dkc	$\beta\gamma\delta$	D.37(m)
730	0788	20150313_204115	12297	Fast	127	-165	0.98	28	112" × 78"	340	Dkc	$\beta\gamma\delta$	D.37(n)
731	0789	20150314_015020	12297	Fast	170	-153	0.97	45	147" × 97"	420	Dkc	$\beta\gamma\delta$	D.37(o)
732	0790	20150314_042951	12297	Fast	195	-167	0.96	28	113" × 74"	420	Dkc	$\beta\gamma\delta$	D.37(p)
733	0791	20150315_001106	12297	Fast	362	-172	0.91	45	152" × 96"	320	Ekc	$\beta\gamma\delta$	D.37(q)
734	0792	20150315_030005	12297	Fast	384	-174	0.90	54	150" × 100"	320	Ekc	$\beta\gamma\delta$	D.37(r)
735	0793	20150315_093005	12297	Fast	435	-173	0.87	45	151" × 91"	320	Ekc	$\beta\gamma\delta$	D.37(s)
736	0794	20150315_200005	12297	Fast	513	-183	0.82	45	150" × 87"	320	Ekc	$\beta\gamma\delta$	D.37(t)
737	0795	20150315_224638	12297	Fast	518	-189	0.82	20	84" × 69"	320	Ekc	$\beta\gamma\delta$	D.38(a)
738	0796	20150316_000020	12297	Fast	537	-185	0.81	40	139" × 84"	370	Ekc	$\beta\gamma\delta$	D.38(b)
739	0797	20150316_030005	12297	Fast	564	-189	0.79	45	151" × 90"	370	Ekc	$\beta\gamma\delta$	D.38(c)
740	0798	20150316_100004	12297	Fast	610	-195	0.75	45	151" × 92"	370	Ekc	$\beta\gamma\delta$	D.38(d)
741	0799	20150316_104729	12297	Fast	616	-195	0.74	28	113" × 65"	370	Ekc	$\beta\gamma\delta$	D.38(e)
742	0800	20150316_125916	12297	Fast	613	-198	0.74	20	82" × 63"	370	Ekc	$\beta\gamma\delta$	D.38(f)
743	0801	20150316_140019	12297	Fast	643	-197	0.72	45	150" × 86"	370	Ekc	$\beta\gamma\delta$	D.38(g)
744	0802	20150316_230004	12297	Fast	687	-202	0.67	40	140" × 87"	370	Ekc	$\beta\gamma\delta$	D.38(h)
745	0803	20150317_020004	12297	Fast	706	-204	0.65	40	138" × 86"	380	Ekc	$\beta\gamma\delta$	D.38(i)
746	0804	20150317_082405	12297	Fast	734	-210	0.61	40	137" × 82"	380	Ekc	$\beta\gamma\delta$	D.38(j)
747	0805	20150317_170554	12297	Fast	827	-224	0.55	35	121" × 82"	380	Ekc	$\beta\gamma\delta$	D.38(k)
748	0806	20150331_160005	12315	Fast	882	-130	0.55	24	71" × 105"	30	Cro	β	D.38(l)
749	0807	20150508_101508	12339	Fast	-597	239	0.71	72	206" × 108"	730	Fkc	$\beta\gamma$	D.38(m)
750	0808	20150508_120005	12339	Fast	-620	241	0.71	84	232" × 114"	730	Fkc	$\beta\gamma$	D.38(n)

Table D.1. Continued.

index	inv_id	obs_id (date)(time)	NOAA AR num	type scan	x_c (")	y_c (")	μ	num tiles	size FOV	area (MSH)	Zürich class	magnetic class	Fig. (panel)
751	0809	20150620_102106	12371	Fast	-400	173	0.89	42	112" × 115"	1020	Ekc	$\beta\gamma\delta$	D.38(o)
752	0810	20150620_144749	12371	Fast	-291	145	0.93	91	223" × 133"	1020	Ekc	$\beta\gamma\delta$	D.38(p)
753	0811	20150620_194105	12371	Fast	-253	152	0.94	78	228" × 111"	1020	Ekc	$\beta\gamma\delta$	D.38(q)
754	0812	20150621_003746	12371	Fast	-211	145	0.96	91	226" × 117"	1120	Ekc	$\beta\gamma\delta$	D.38(r)
755	0813	20150621_061125	12371	Fast	-234	161	0.96	36	103" × 105"	1120	Ekc	$\beta\gamma\delta$	D.38(s)
756	0814	20150621_184013	12371	Fast	-62	149	0.99	84	235" × 109"	1120	Ekc	$\beta\gamma\delta$	D.38(t)
757	0815	20150622_062148	12371	Fast	-16	152	0.99	36	100" × 100"	1180	Fkc	$\beta\gamma\delta$	D.39(a)
758	0816	20150622_074504	12371	Nor.	-2	158	0.99	110	92" × 87"	1180	Fkc	$\beta\gamma\delta$	D.39(b)
759	0817	20150623_082141	12371	Nor.	214	154	0.96	100	88" × 92"	1070	Fkc	$\beta\gamma\delta$	D.39(c)
760	0818	20150623_145506	12371	Fast	271	153	0.95	30	88" × 99"	1070	Fkc	$\beta\gamma\delta$	D.39(d)
761	0823	20150625_180921	12371	Fast	670	162	0.71	25	79" × 88"	740	Fkc	$\beta\gamma$	D.39(e)
762	0824	20150707_100806	12381	Fast	-345	166	0.90	66	181" × 100"	350	Ekc	$\beta\gamma$	D.39(f)
763	0825	20150707_150606	12381	Fast	-309	161	0.92	66	186" × 101"	350	Ekc	$\beta\gamma$	D.39(g)
764	0826	20150707_200754	12381	Fast	-276	158	0.93	72	203" × 103"	350	Ekc	$\beta\gamma$	D.39(h)
765	0827	20150708_005701	12381	Fast	-234	153	0.95	72	210" × 107"	450	Ekc	$\beta\gamma$	D.39(i)
766	0828	20150708_090505	12381	Fast	-164	146	0.97	78	222" × 111"	450	Ekc	$\beta\gamma$	D.39(j)
767	0829	20150709_211604	12381	Fast	136	135	0.98	90	251" × 117"	550	Eko	β	D.39(k)
768	0830	20150710_020434	12381	Fast	173	135	0.97	105	253" × 119"	500	Eko	β	D.39(l)
769	0831	20150822_144608	12403	Fast	-275	-338	0.87	54	150" × 104"	350	Dkc	$\beta\gamma$	D.39(m)
770	0832	20150822_181735	12403	Fast	-244	-339	0.88	54	151" × 105"	350	Dkc	$\beta\gamma$	D.39(n)
771	0833	20150825_103138	12403	Fast	323	-366	0.86	78	219" × 107"	930	Fkc	$\beta\gamma\delta$	D.39(o)
772	0834	20150825_120006	12403	Fast	332	-366	0.86	78	218" × 104"	930	Fkc	$\beta\gamma\delta$	D.39(p)
773	0835	20150825_134505	12403	Fast	540	-348	0.82	25	88" × 87"	930	Fkc	$\beta\gamma\delta$	D.39(q)
774	0836	20150825_145006	12403	Fast	345	-365	0.85	78	228" × 106"	930	Fkc	$\beta\gamma\delta$	D.39(r)
775	0837	20150825_182005	12403	Fast	375	-363	0.84	78	224" × 109"	930	Fkc	$\beta\gamma\delta$	D.39(s)
776	0838	20150825_200005	12403	Fast	395	-362	0.83	78	215" × 107"	930	Fkc	$\beta\gamma\delta$	D.39(t)
777	0839	20150825_231006	12403	Fast	415	-361	0.82	78	223" × 109"	930	Fkc	$\beta\gamma\delta$	D.40(a)
778	0840	20150826_022005	12403	Fast	443	-360	0.80	78	221" × 111"	1190	Fki	$\beta\gamma\delta$	D.40(b)
779	0841	20150826_053005	12403	Fast	466	-359	0.79	78	216" × 108"	1190	Fki	$\beta\gamma\delta$	D.40(c)
780	0842	20150826_083510	12403	Fast	517	-374	0.78	60	172" × 110"	1190	Fki	$\beta\gamma\delta$	D.40(d)
781	0843	20150826_100505	12403	Fast	533	-373	0.77	60	173" × 113"	1190	Fki	$\beta\gamma\delta$	D.40(e)
782	0844	20150826_113005	12403	Fast	543	-372	0.76	60	170" × 112"	1190	Fki	$\beta\gamma\delta$	D.40(f)
783	0845	20150826_130005	12403	Fast	560	-371	0.75	60	171" × 116"	1190	Fki	$\beta\gamma\delta$	D.40(g)
784	0846	20150826_171351	12403	Fast	537	-369	0.77	25	75" × 97"	1190	Fki	$\beta\gamma\delta$	D.40(h)
785	0847	20150826_234235	12403	Fast	637	-364	0.69	70	170" × 119"	1190	Fki	$\beta\gamma\delta$	D.40(i)
786	0849	20150827_192810	12403	Fast	810	-281	0.50	25	79" × 85"	1100	Fkc	$\beta\gamma\delta$	D.40(j)
787	0850	20150916_110553	12415	Fast	-137	-427	0.87	24	95" × 65"	150	Cai	$\beta\gamma$	D.40(k)
788	0851	20150917_102655	12415	Fast	102	-418	0.87	18	107" × 58"	190	Dac	$\beta\gamma$	D.40(l)
789	0852	20150926_180815	12422	Fast	-44	-421	0.88	67	196" × 103"	310	Eko	$\beta\gamma$	D.40(m)
790	0853	20150927_000005	12422	Fast	8	-428	0.88	60	207" × 89"	410	Ekc	$\beta\gamma\delta$	D.40(n)
791	0854	20150927_050004	12422	Fast	50	-431	0.88	60	203" × 95"	410	Ekc	$\beta\gamma\delta$	D.40(o)
792	0855	20150927_110515	12422	Fast	99	-420	0.87	60	196" × 87"	410	Ekc	$\beta\gamma\delta$	D.40(p)
793	0856	20150927_140004	12422	Fast	124	-422	0.87	60	197" × 92"	410	Ekc	$\beta\gamma\delta$	D.40(q)
794	0857	20150927_170004	12422	Fast	152	-426	0.86	60	199" × 95"	410	Ekc	$\beta\gamma\delta$	D.40(r)
795	0858	20150927_230004	12422	Fast	199	-429	0.85	60	200" × 98"	410	Ekc	$\beta\gamma\delta$	D.40(s)
796	0859	20150928_051504	12422	Fast	249	-432	0.84	66	193" × 103"	650	Ekc	$\beta\gamma\delta$	D.40(t)
797	0860	20150928_110523	12422	Fast	299	-416	0.82	72	200" × 102"	650	Ekc	$\beta\gamma\delta$	D.41(a)
798	0861	20150928_140004	12422	Fast	322	-419	0.82	72	197" × 108"	650	Ekc	$\beta\gamma\delta$	D.41(b)
799	0862	20150928_171504	12422	Fast	346	-418	0.81	72	202" × 111"	650	Ekc	$\beta\gamma\delta$	D.41(c)
800	0863	20150929_000003	12422	Fast	398	-417	0.78	72	203" × 116"	690	Fkc	$\beta\gamma\delta$	D.41(d)
801	0864	20150929_044003	12422	Fast	432	-417	0.76	84	203" × 119"	690	Fkc	$\beta\gamma\delta$	D.41(e)
802	0865	20150929_181615	12422	Fast	565	-395	0.69	66	183" × 115"	690	Fkc	$\beta\gamma\delta$	D.41(f)
803	0866	20150929_210042	12422	Fast	583	-396	0.68	66	183" × 113"	690	Fkc	$\beta\gamma\delta$	D.41(g)
804	0867	20150930_001534	12422	Fast	605	-391	0.66	66	195" × 112"	950	Fkc	$\beta\gamma\delta$	D.41(h)
805	0868	20150930_033005	12422	Fast	623	-388	0.64	66	182" × 113"	950	Fkc	$\beta\gamma\delta$	D.41(i)
806	0869	20150930_064004	12422	Fast	645	-389	0.62	70	175" × 119"	950	Fkc	$\beta\gamma\delta$	D.41(j)
807	0870	20150930_120004	12422	Fast	670	-385	0.59	60	176" × 113"	950	Fkc	$\beta\gamma\delta$	D.41(k)
808	0871	20150930_132025	12422	Fast	636	-385	0.63	65	227" × 92"	950	Fkc	$\beta\gamma\delta$	D.41(l)
809	0872	20150930_183541	12422	Fast	702	-379	0.55	60	166" × 111"	950	Fkc	$\beta\gamma\delta$	D.41(m)
810	0873	20150930_233004	12422	Fast	726	-375	0.52	60	167" × 112"	950	Fkc	$\beta\gamma\delta$	D.41(n)

Table D.1. Continued.

index	inv_id	obs_id (date)(time)	NOAA AR num	type scan	x_c (")	y_c (")	μ	num tiles	size FOV	area (MSH)	Zürich class	magnetic class	Fig. (panel)
811	0874	20151103_141549	12443	Fast	-153	60	0.98	55	191" × 89"	590	Fkc	$\beta\delta$	D.41(o)
812	0875	20151103_160105	12443	Fast	-196	38	0.98	35	111" × 81"	590	Fkc	$\beta\delta$	D.41(p)
813	0876	20151103_210505	12443	Fast	-149	41	0.99	28	109" × 78"	590	Fkc	$\beta\delta$	D.41(q)
814	0877	20151103_225005	12443	Fast	-130	47	0.99	24	108" × 71"	590	Fkc	$\beta\delta$	D.41(r)
815	0878	20151104_011005	12443	Fast	-91	44	0.99	24	97" × 74"	560	Fkc	$\beta\delta$	D.41(s)
816	0879	20151216_170513	12470	Fast	-475	221	0.83	16	66" × 73"	610	Eko	β	D.41(t)
817	0880	20151216_200611	12470	Fast	-534	251	0.80	84	201" × 121"	610	Eko	β	D.42(a)
818	0881	20151217_002935	12470	Fast	-504	254	0.82	72	208" × 115"	530	Eko	β	D.42(b)
819	0882	20151217_040005	12470	Fast	-478	258	0.84	72	209" × 115"	530	Eko	β	D.42(c)
820	0883	20151217_065605	12470	Fast	-458	257	0.85	72	202" × 117"	530	Eko	β	D.42(d)
821	0884	20151217_083304	12470	Fast	-444	259	0.86	84	205" × 118"	530	Eko	β	D.42(e)
822	0885	20151224_092605	12473	Fast	-612	-325	0.65	60	173" × 99"	420	Ekc	$\beta\gamma$	D.42(f)
823	0886	20151224_150016	12473	Fast	-604	-322	0.68	66	182" × 102"	420	Ekc	$\beta\gamma$	D.42(g)
824	0887	20151224_182135	12473	Fast	-556	-321	0.71	55	189" × 96"	420	Ekc	$\beta\gamma$	D.42(h)
825	0888	20151225_110004	12473	Fast	-443	-325	0.80	78	220" × 102"	500	Ekc	$\beta\gamma$	D.42(i)
826	0889	20151225_153204	12473	Fast	-411	-322	0.82	78	226" × 110"	500	Ekc	$\beta\gamma$	D.42(j)
827	0890	20151226_061533	12473	Fast	-298	-318	0.87	78	229" × 109"	570	Ekc	$\beta\gamma$	D.42(k)
828	0891	20151226_090003	12473	Fast	-277	-319	0.88	84	233" × 109"	570	Ekc	$\beta\gamma$	D.42(l)
829	0892	20151226_120003	12473	Fast	-108	-292	0.91	35	117" × 83"	570	Ekc	$\beta\gamma$	D.42(m)
830	0893	20151226_181332	12473	Fast	-202	-313	0.91	84	231" × 109"	570	Ekc	$\beta\gamma$	D.42(n)
831	0894	20151226_210003	12473	Fast	-185	-308	0.91	84	234" × 106"	570	Ekc	$\beta\gamma$	D.42(o)
832	0895	20151227_000003	12473	Fast	-157	-310	0.92	84	236" × 106"	590	Fkc	$\beta\gamma\delta$	D.42(p)
833	0896	20151227_030703	12473	Fast	-131	-306	0.92	84	236" × 103"	590	Fkc	$\beta\gamma\delta$	D.42(q)
834	0897	20151228_003002	12473	Fast	50	-307	0.94	78	223" × 109"	530	Fhc	$\beta\delta$	D.42(r)
835	0898	20151229_113620	12473	Fast	449	-280	0.87	50	169" × 87"	510	Fhc	$\beta\delta$	D.42(s)
836	0899	20151230_080545	12473	Fast	691	-281	0.75	24	98" × 76"	470	Fhc	β	D.42(t)
837	0900	20160211_224006	12497	Fast	81	345	0.95	65	217" × 88"	240	Eac	$\beta\gamma$	D.43(a)
838	0901	20160212_013506	12497	Fast	109	343	0.94	60	200" × 93"	180	Eac	$\beta\gamma\delta$	D.43(b)
839	0902	20160212_195805	12497	Fast	393	336	0.90	32	140" × 73"	180	Eac	$\beta\gamma\delta$	D.43(c)
840	0903	20160212_231005	12497	Fast	428	334	0.89	32	136" × 71"	180	Eac	$\beta\gamma\delta$	D.43(d)
841	0904	20160213_021005	12497	Fast	451	331	0.88	32	139" × 71"	250	Eac	$\beta\gamma\delta$	D.43(e)
842	0905	20160213_070005	12497	Fast	498	333	0.87	32	136" × 65"	250	Eac	$\beta\gamma\delta$	D.43(f)
843	0906	20160213_101204	12497	Fast	479	328	0.85	44	181" × 74"	250	Eac	$\beta\gamma\delta$	D.43(g)
844	0907	20160214_110104	12497	Fast	677	301	0.72	45	158" × 84"	220	Eac	$\beta\gamma\delta$	D.43(h)
845	0908	20160215_001040	12497	Fast	767	288	0.64	40	139" × 83"	200	Eac	$\beta\gamma\delta$	D.43(i)
846	0909	20160215_120103	12497	Fast	862	284	0.54	28	109" × 79"	200	Eac	$\beta\gamma\delta$	D.43(j)
847	0910	20160410_000205	12529	Fast	-783	229	0.51	42	120" × 105"	820	Ehi	β	D.43(k)
848	0911	20160410_120405	12529	Fast	-728	237	0.61	48	135" × 107"	820	Ehi	β	D.43(l)
849	0912	20160410_150604	12529	Fast	-707	237	0.63	48	140" × 110"	820	Ehi	β	D.43(m)
850	0913	20160410_183420	12529	Nor.	-678	226	0.67	143	111" × 100"	820	Ehi	β	D.43(n)
851	0914	20160412_000504	12529	Fast	-469	272	0.84	45	154" × 91"	850	Eki	β	D.43(o)
852	0915	20160412_042303	12529	Fast	-433	272	0.86	45	150" × 96"	850	Eki	β	D.43(p)
853	0916	20160412_123504	12529	Fast	-284	271	0.89	60	177" × 99"	850	Eki	β	D.43(q)
854	0917	20160412_180021	12529	Fast	-215	273	0.92	25	82" × 95"	850	Eki	β	D.43(r)
855	0918	20160412_210905	12529	Fast	-198	274	0.93	25	89" × 92"	850	Eki	β	D.43(s)
856	0919	20160413_001305	12529	Fast	-146	272	0.94	25	75" × 95"	800	Eho	β	D.43(t)
857	0920	20160413_032105	12529	Fast	-129	276	0.94	25	80" × 89"	800	Eho	β	D.44(a)
858	0921	20160413_050705	12529	Fast	-108	277	0.95	25	75" × 92"	800	Eho	β	D.44(b)
859	0922	20160413_183219	12529	Fast	90	269	0.96	42	112" × 103"	800	Eho	β	D.44(c)
860	0923	20160413_201103	12529	Fast	35	277	0.96	20	71" × 95"	800	Eho	β	D.44(d)
861	0924	20160414_022103	12529	Fast	172	276	0.97	30	107" × 95"	780	Eko	β	D.44(e)
862	0925	20160414_053304	12529	Fast	105	276	0.97	25	82" × 93"	780	Eko	β	D.44(f)
863	0926	20160414_124504	12529	Fast	163	274	0.96	60	169" × 105"	780	Eko	β	D.44(g)
864	0927	20160414_181520	12529	Fast	207	274	0.96	45	152" × 97"	780	Eko	β	D.44(h)
865	0928	20160415_000104	12529	Fast	260	269	0.94	31	91" × 104"	790	Eki	β	D.44(i)
866	0929	20160416_031518	12529	Fast	595	257	0.84	42	119" × 99"	740	Eki	$\beta\gamma$	D.44(j)
867	0930	20160416_060302	12529	Fast	544	256	0.84	20	73" × 96"	740	Eki	$\beta\gamma$	D.44(k)
868	0931	20160416_070005	12529	Fast	541	257	0.83	25	82" × 98"	740	Eki	$\beta\gamma$	D.44(l)
869	0932	20160416_184203	12529	Fast	587	255	0.80	72	205" × 115"	740	Eki	$\beta\gamma$	D.44(m)
870	0933	20160416_220005	12529	Fast	675	256	0.76	45	146" × 88"	740	Eki	$\beta\gamma$	D.44(n)

Table D.1. Continued.

index	inv_id	obs_id (date)_(time)	NOAA AR num	type scan	x_c (")	y_c (")	μ	num tiles	size FOV	area (MSH)	Zürich class	magnetic class	Fig. (panel)
871	0934	20160510_080133	12542	Fast	84	248	0.98	15	76" × 50"	150	Dai	$\beta\gamma$	D.44(o)
872	0935	20160513_130705	12542	Fast	664	175	0.72	20	59" × 90"	160	Dai	$\beta\gamma$	D.44(p)
873	0937	20160720_010205	12567	Fast	385	0	0.91	28	120" × 79"	390	Dki	$\beta\gamma$	D.44(q)
874	0938	20160720_041105	12565+12567	Fast	411	1	0.90	35	120" × 81"	300+390	Cko+Dki	$\beta+\beta\gamma$	D.44(r)
875	0939	20160720_091551	12565+12567	Fast	519	4	0.83	45	151" × 81"	300+390	Cko+Dki	$\beta+\beta\gamma$	D.44(s)
876	0940	20160720_223047	12565+12567	Fast	616	4	0.76	45	150" × 83"	300+390	Cko+Dki	$\beta+\beta\gamma$	D.44(t)
877	0941	20160721_000005	12565+12567	Fast	628	5	0.74	36	149" × 79"	310+510	Cko+Dki	$\beta+\beta$	D.45(a)
878	0942	20160721_014005	12565+12567	Fast	637	0	0.74	40	139" × 86"	310+510	Cko+Dki	$\beta+\beta$	D.45(b)
879	0943	20160721_181004	12565+12567	Fast	796	14	0.65	50	166" × 84"	310+510	Cko+Dki	$\beta+\beta$	D.45(c)
880	0945	20160722_233504	12565+12567	Nor.	879	31	0.43	60	102" × 95"	250+380	Hkx+Dki	$\alpha+\beta\gamma$	D.45(d)
881	0946	20160903_074908	12585	Nor.	-593	34	0.77	162	152" × 81"	460	Ekc	$\beta\gamma$	D.45(e)
882	0947	20160903_104306	12585	Nor.	-571	34	0.79	162	150" × 82"	460	Ekc	$\beta\gamma$	D.45(f)
883	0948	20161011_144054	12599	Fast	502	-346	0.80	20	81" × 71"	250	Cko	β	D.45(g)
884	0949	20161011_160006	12599	Fast	508	-326	0.80	15	82" × 55"	250	Cko	β	D.45(h)
885	0950	20161011_192106	12599	Fast	533	-320	0.78	15	79" × 49"	250	Cko	β	D.45(i)
886	0951	20161012_132104	12599	Fast	656	-313	0.69	12	68" × 50"	270	Cko	β	D.45(j)
887	0952	20161012_152005	12599	Fast	673	-314	0.68	12	70" × 51"	270	Cko	β	D.45(k)
888	0953	20161130_130006	12615	Fast	-646	-88	0.69	18	94" × 61"	30	Dsi	β	D.45(l)
889	0954	20161203_184119	12615	Fast	129	-80	0.99	15	79" × 59"	110	Dao	β	D.45(m)
890	0955	20161204_001834	12615	Fast	106	-82	0.99	12	69" × 55"	140	Dai	β	D.45(n)
891	0956	20170401_061405	12645	Fast	-19	-50	1.00	36	151" × 64"	380	Ekc	$\beta\gamma$	D.45(o)
892	0957	20170401_090005	12645	Fast	5	-53	1.00	36	150" × 64"	380	Ekc	$\beta\gamma$	D.45(p)
893	0958	20170401_110049	12645	Fast	79	-39	1.00	65	229" × 84"	380	Ekc	$\beta\gamma$	D.45(q)
894	0959	20170403_100542	12645	Fast	495	-62	0.87	65	218" × 82"	600	Ehc	$\beta\gamma\delta$	D.45(r)
895	0960	20170403_173711	12645	Fast	40	34	1.00	52	216" × 78"	600	Ehc	$\beta\gamma\delta$	D.45(s)
896	0961	20170404_000104	12645	Fast	602	-62	0.80	48	205" × 77"	700	Ekc	$\beta\gamma\delta$	D.45(t)
897	0962	20170420_071538	12651	Nor.	-762	257	0.55	35	42" × 59"	110	Dao	β	D.46(a)
898	0963	20170603_190143	12661	Fast	-576	102	0.71	24	140" × 51"	200	Dao	β	D.46(b)
899	0964	20170708_230346	12665	Fast	-593	-156	0.74	45	151" × 87"	310	Ekc	β	D.46(c)
900	0965	20170709_233834	12665	Fast	-404	-177	0.87	60	174" × 99"	480	Ekc	β	D.46(d)
901	0966	20170711_114358	12665	Fast	-90	-177	0.97	65	217" × 84"	690	Ekc	$\beta\gamma$	D.46(e)
902	0967	20170714_232204	12665	Fast	748	-169	0.69	36	97" × 107"	440	Ehi	β	D.46(f)
903	0968	20170817_160006	12671	Fast	-615	114	0.76	65	223" × 87"	380	Ehc	$\beta\gamma\delta$	D.46(g)
904	0969	20170817_203005	12671	Fast	-579	113	0.79	65	228" × 85"	380	Ehc	$\beta\gamma\delta$	D.46(h)
905	0970	20170819_083144	12671	Fast	-232	84	0.96	56	234" × 76"	410	Fkc	$\beta\gamma$	D.46(i)
906	0971	20170819_115106	12671	Fast	-192	64	0.97	52	216" × 72"	410	Fkc	$\beta\gamma$	D.46(j)
907	0972	20170822_171104	12672	Fast	-732	38	0.60	49	115" × 120"	160	Dao	β	D.46(k)
908	0973	20170823_061405	12672	Fast	-650	31	0.70	48	126" × 116"	270	Dao	β	D.46(l)
909	0974	20170823_224005	12672	Fast	-502	20	0.81	54	148" × 114"	270	Dao	β	D.46(m)
910	0975	20170905_030404	12674	Fast	135	79	0.99	25	91" × 84"	740	Fhi	β	D.46(n)
911	0976	20170905_105108	12673	Fast	352	-254	0.90	56	128" × 132"	680	Dkc	$\beta\gamma\delta$	D.46(o)
912	0977	20170905_140006	12673	Fast	378	-252	0.88	56	128" × 131"	680	Dkc	$\beta\gamma\delta$	D.46(p)
913	0978	20170905_160006	12673	Fast	400	-250	0.88	56	127" × 136"	680	Dkc	$\beta\gamma\delta$	D.46(q)
914	0979	20170905_180902	12673	Fast	417	-250	0.87	56	128" × 135"	680	Dkc	$\beta\gamma\delta$	D.46(r)
915	0980	20170906_000205	12673	Nor.	470	-247	0.84	180	125" × 110"	880	Dkc	$\beta\gamma\delta$	D.46(s)
916	0981	20170906_061405	12673	Fast	512	-244	0.81	56	127" × 134"	880	Dkc	$\beta\gamma\delta$	D.46(t)
917	0982	20170906_090339	12673	Fast	516	-242	0.80	42	109" × 104"	880	Dkc	$\beta\gamma\delta$	D.47(a)
918	0984	20170906_120847	12673	Nor.	547	-240	0.79	144	105" × 110"	880	Dkc	$\beta\gamma\delta$	D.47(b)
919	0985	20170906_161754	12673	Fast	593	-237	0.76	49	119" × 130"	880	Dkc	$\beta\gamma\delta$	D.47(c)
920	0986	20170906_174028	12673	Fast	558	-237	0.77	20	68" × 89"	880	Dkc	$\beta\gamma\delta$	D.47(d)
921	0987	20170906_181045	12673	Fast	586	-236	0.75	36	109" × 107"	880	Dkc	$\beta\gamma\delta$	D.47(e)
922	0988	20170906_183650	12673	Fast	605	-235	0.75	49	115" × 127"	880	Dkc	$\beta\gamma\delta$	D.47(f)
923	0989	20170906_191722	12673	Fast	592	-236	0.74	36	108" × 107"	880	Dkc	$\beta\gamma\delta$	D.47(g)
924	0990	20170907_000129	12673	Fast	623	-233	0.72	42	112" × 107"	960	Ekc	$\beta\gamma\delta$	D.47(h)
925	0991	20170907_002734	12673	Fast	646	-231	0.71	56	113" × 140"	960	Ekc	$\beta\gamma\delta$	D.47(i)
926	0992	20170907_031405	12673	Fast	662	-229	0.70	42	108" × 129"	960	Ekc	$\beta\gamma\delta$	D.47(j)
927	0993	20170907_050218	12673	Fast	633	-228	0.71	20	64" × 92"	960	Ekc	$\beta\gamma\delta$	D.47(k)
928	0994	20170907_064318	12673	Fast	688	-226	0.67	42	109" × 124"	960	Ekc	$\beta\gamma\delta$	D.47(l)
929	0995	20170907_100004	12673	Fast	705	-224	0.65	49	109" × 129"	960	Ekc	$\beta\gamma\delta$	D.47(m)

Table D.1. Continued.

index	inv_id	obs_id (date)_(time)	NOAA AR num	type scan	x_c (")	y_c (")	μ	num tiles	size FOV	area (MSH)	Zürich class	magnetic class	Fig. (panel)
930	0996	20170907_112906	12673	Nor.	697	-249	0.64	144	99" × 111"	960	Ekc	$\beta\gamma\delta$	D.47(n)
931	0997	20170907_143319	12673	Fast	693	-246	0.63	28	63" × 118"	960	Ekc	$\beta\gamma\delta$	D.47(o)
932	0998	20170907_144813	12673	Fast	722	-246	0.61	56	111" × 152"	960	Ekc	$\beta\gamma\delta$	D.47(p)
933	0999	20170907_164809	12673	Fast	734	-244	0.60	48	106" × 150"	960	Ekc	$\beta\gamma\delta$	D.47(q)
934	1000	20170907_182845	12673	Fast	734	-242	0.58	42	100" × 120"	960	Ekc	$\beta\gamma\delta$	D.47(r)
935	1001	20170907_185450	12673	Nor.	740	-241	0.59	120	88" × 109"	960	Ekc	$\beta\gamma\delta$	D.47(s)
936	1002	20170907_202403	12673	Fast	710	-240	0.62	12	30" × 102"	960	Ekc	$\beta\gamma\delta$	D.47(t)
937	1003	20170908_001907	12673	Fast	767	-238	0.54	42	93" × 121"	1000	Ekc	$\beta\gamma\delta$	D.48(a)
938	1004	20170908_004457	12673	Fast	785	-237	0.54	42	93" × 121"	1000	Ekc	$\beta\gamma\delta$	D.48(b)
939	1005	20170908_011519	12673	Fast	783	-234	0.54	40	82" × 142"	1000	Ekc	$\beta\gamma\delta$	D.48(c)
940	1006	20170908_090038	12673	Fast	816	-229	0.47	35	81" × 120"	1000	Ekc	$\beta\gamma\delta$	D.48(d)
941	1007	20170908_163731	12673	Fast	845	-221	0.42	35	79" × 118"	1000	Ekc	$\beta\gamma\delta$	D.48(e)
942	1008	20190322_002307	12736	Fast	703	201	0.67	35	122" × 93"	210	Dac	$\beta\gamma\delta$	D.48(f)
943	1009	20190322_010205	12736	Fast	789	221	0.66	35	117" × 92"	210	Dac	$\beta\gamma\delta$	D.48(g)
944	1010	20190322_061746	12736	Fast	744	189	0.62	42	118" × 100"	210	Dac	$\beta\gamma\delta$	D.48(h)